Normandie Université

THESE

Pour obtenir le diplôme de doctorat

Spécialité CHIMIE

Préparée au sein de l'ENSICAEN et de l'UNICAEN

Trirutiles and multiferroic properties : exploring tellurates

Présentée et soutenue par MATSUBARA Nami

Thèse soutenue publiquement le 28/09/2018 devant le jury composé de		
M. Werner PAULUS	Professeur. Université de Montpellier	Rapporteur
Mme. Valérie PAUL-BONCOUR	Directeur de Recherche CNRS à Institut de Chimie et des Matériaux Paris-Est	Rapporteur
M. Laurent CARIO	Directeur de Recherche CNRS à Institut des Matériaux Jean Rouxel	Examinateur
M. Takashi TERANISHI	Professeur Associé à Okayama University	Examinateur
Mme. Françoise DAMAY	Directeur de Recherche CNRS au Laboratoire Léon Brillouin	Codirecteur de thèse
Mme. Christine MARTIN	Directeur de Recherche CNRS au CRISMAT	Directeur de thèse

Thèse dirigée par Dr. Christine MARTIN, laboratoire CRISMAT et Dr. Françoise DAMAY, LLB.

UNIVERSITÉ CAEN NORMANDIE

ENSICAEN
ÉCOLE PUBLIQUE D'INGÉNIEURS
CENTRE DE RECHERCHE

ED PSIME

RISM

LLB Orphée Laboratoire Léon Brillouin

永らえば
　またこの頃や
　　しのばれむ
憂いしと見し世ぞ
　今は恋しき

Acknowledgments

I would first and foremost like to express thanks to my supervisors, Françoise DAMAY and Christine MARTIN who have been an unequivocal resource of guidance and academic support, as well as excellent social partisans.
Thanks to you I got to travel to many different places, try a lot of things for the first time and meet many great people who inspired me both personally and scientifically. It was a pleasure working with both of you.

I am also sincerely thankful to all members of my jury for taking the time to critically evaluate my thesis.

A special "thank you" also goes to Antoine MAIGNAN, Nicola BARRIER, Oleg I. LEBEDEV, Philippe BOULLAY, Sylvie MALO, Vincent HARDY, Natalia E. MORDVINOVA, Denis PELLOQUIN, Yassine EL MENDILI, Jonas SOTTMANN, Laura CHAIX, Sophie DUFOURD, Fabien VEILLON, Stéphanie GASCOIN, Sylvie COLLIN, Jérôme LECOURT, Véronique BACLET, Benoît HERVIEU, Eric LECOURT, Sandrine SOCHARD and Marie SAVARY for all their support during my thesis. Your support and advice helped me greatly over the past three years. Thank you very much.

Travel has been an important and pertinent part of my academic career. For that I would like to acknowledge the Association Française de Cristallographie, International Union of Crystallography, CNRS, Écoles doctorales and particularly CEA and Région Basse-Normandie for their financial support, not forgetting all for accompanying me on some of the most amazing travel adventures (conferences) anyone could hope for.

I would also like to thank the worldwide network and the large scale facilities, who facilitated the research mobility scheme allowing me to study and have an excellent experiment at WISH (ISIS, UK) with Pascal MANUEL, Dmitry KHALYAVIN and Fabio ORLANDI, at BL04-MSPD (ALBA, Spain) with François Fauth, at CRISTAL (SOLEIL, Saclay) with Erik Elkaïm, at ODE (SOLEIL, Saclay) with Lucie NATAF, at D2B (ILL, Grenoble) with Emmanuelle SUARD, at GREENMAT (Université de Liège, Belgium) with Bénédicte VERTRUYEN, Stéphane CAUBERGH and Thomas JUNGERS. This proved to be an incredible opportunity to not only experience academia but also make some lifelong relationships with those who made my stay so enjoyable.

My friends and colleagues within the CRISMAT, the LLB, the Université de Caen too have been fantastically supportive, special thanks for Stefan, Florent, Clarisse, Evan,

Jonas, Robin, Bruno, Tristan, Chantal, Rodolphe, Alexandre, Natalia, Fabien, David, Yohann, Adrian, Jean-Baptiste, Cedric, Laurine, Emmanuel, Yassine, Deepak, Maria, Tathamay, Flora, Elisabeth, Melanie, Stanislav, Hichem, Luz, Kamila, Stijn, Ghinwa, Manila, Dalila, Laura, Joseph, Jaehong, David, Lucie, Afonso, Yvan, Sylvain, Philippe, Jean-Michel and all those I might have forgotten.

Special thanks to all my friends outside the lab who constantly support me – especially: Brad, Lola, Simon, Damian.

I would like to thank Florian and his family for their unwavering support through the whole adventure; I could not have done it without you!

心細いフランスの生活の中で、カン・パリにいる日本人の皆さん、特に蔵馬くん、永沼先生（東北大）と話して愚痴りあってストレスを解消させてもらいました。いざという時、助けていただいて本当にありがとうございました。

遠い日本から、いつも気をかけてくれて応援してくれて、いつもエネルギーをくれた大切な友達、特に萌、彩、瞳、奈保理、麻美子、佐起ちゃん、梨香ちゃん、はるお、浩志、高校ソフト部のみんな、田路くん、Elza、早紀さん、Farid、ハリン、本当にありがとう。　どこで何をやっていても、いつでもみんなが帰るところを作ってくれていることが私のこの 3 年間＋α の留学生活の支えでした。ここには書ききれないほどたくさんの友人に支えられて、この博論を仕上げることができました。

岡山大学の先生の皆様、特に、寺西先生、岸本先生、林先生、狩野先生、Bernard 先生、米田先生、宇根山先生、池田先生、卒業した後もさまざまな面で多くの刺激と示唆をいただきました。感謝の意を表します。

そして、最後に，これまで私を温かく応援してくれた家族，熊本のばあちゃん、じいちゃん、親戚のみんな、そして、先日志半ば若くして亡くなられた美保子叔母さん、なんだかんだ言っても私をいつも見守ってくれて心配してくれたお父さん、お母さん，くだらないことで笑いあえる素敵な兄弟達、弥生、優太郎に心から感謝します。

本当にありがとうございました。
Thank you very much!
Merci beaucoup!
Danke schön!

Abbreviations

ABF	Annular Bright Field
ac	Alternating Current
ACMS	AC Measurement System
AFM	Antiferromagnet, -ic, -ism, (s)
APBs	Antiphase boundaries
CRISMAT	Laboratoire de Cristallographie et Sciences des Matériaux
dc	Direct Current
EDS	Energy Dispersive Spectroscopy
EDT	Electron Diffraction Tomography
f.u.	Formula unit
fcc(w)	field-cooled cooling (Warning)
FM	Ferromagnet, -ic, -ism, (s)
GREENMAT	Groupe de Recherche en Energie et Environnement à partir des Matériaux
HAADF	High Angle Annular Dark Field
HC	Honeycomb
hcp	Hexagonal close-packed
HRTEM	High-Resolution Transmission Electron Microscopy
HT	High-Temperature
HTT	High-temperature tetragonal
i.d.	inner diameter
IC	Incommensurate
ICP-OES	Inductively Coupled Plasma Optical Emission Spectroscopy
ILL	Institute Laue-Langevin
Irrep(s)	Irreducible representation(s)
LLB	Laboratoire Léon Brillouin
LTM	Low-temperature monoclinic
ME	Magnetoelectric
NPD	Neutron Powder Diffraction
NTE	Negative thermal expansion
OO	Orbital ordering
PED(T)	Precession Electron Diffraction (Tomography)
PPMS	Physical Property Measurement System
RTM	Room-temperature monoclinic
SAED	Selected-Area Electron Diffraction
SEM	Scanning Electron Microscopy
SG	Space Group
SQUID	Superconducting Quantum Interference Device

STEM	Scanning Transmission Electron Microscopy
SXRPD	Synchrotron X-ray Powder Diffraction
T.O.F	Time Of Flight
TEM	Transmission Electron Microscopy
TGA-DTA	ThermoGravimetry and Differential Thermal Analysis
WP	Wyckoff Position
XANES	X-ray Absorption Near-Edge Spectroscopy
XRPD	X-Ray Powder Diffraction
zfcw	Zero-Field-Cooled Warming

Symbols

$<d>$	Average inter atomic distance
a	Lattice constant
b	Lattice constant
$B_{(iso)}$	Isotropic thermal displacement
C	Capacitance
$\boldsymbol{C}$	Curie constant
c	Lattice constant
Cp	Specific heat
d	distance between electrodes
d_{hkl}	Separating distance between parallel planes
E_0	External electric field
E_1	Depolarizing field
F	Formula molar mass (g/mol)
f	Frequency
G	Lower symmetry phase
G_0	Higher symmetry phase
G_k	Little group
H	Magnetic field strength
h_{ac}	AC magnetic field
h_{dc}	DC magnetic field
$\boldsymbol{k}$	Propagation vector
k_B	Boltzmann's constant = 1.38062×10^{-23} J/K
M	Magnetization
m	Mass
N_A	Avogadro's number = 6.02217×10^{23} /mol
P	Polarization
Q	Reciprocal space unit

$\boldsymbol{Q}$	Order parameter
R_{Bragg}	Agreement factor
S	Electrode area
T	Temperature
T_C	Curie temperature
T_N	Néel temperature
T_{pulse}	Temperature pulse
T_S	Structural transition temperature
V	Volume
Z	Atomic number per unit cells
$\boldsymbol{Z}$	Atomic number in periodic table
$\Delta(AO_6)$	Distortion parameter of A octahedra
Γ_{mag}	Global magnetic representation
Γ_n	Magnetic representation
α	Linear thermal expansion coefficient
β	Lattice constant
χ	Magnetic susceptibility per unit mass
χ^2	Agreement factor
ε'	Dielectric permittivity
ε_0	Dielectric permittivity in vacuum
γ	Lattice constant
λ	Wavelength
$\mu_0 H$	Applied magnetic field
μ_B	Bohr Magneton = 9.2732 x 10^{-24} J/T
μ_{eff}	Effective magnetic moment
μ_0	Magnetic field constant
θ	Bragg angle
θ_{CW}	Weiss constant
ψ_n	Basis vector

Abstract

Magnetoelectric (ME) materials, which present simultaneously two coupled properties, i.e. ferromagnetism and ferroelectricity in our case, have attracted attention for the past decade, not only in the perspective of applications, as next-generation magnetic RAM, but also for their rich physics background. The inverse trirutile structure is of particular interest, since some compounds of this family were reported to exhibit ME properties.
The main focus of this thesis is therefore the study of the chemistry, physical and structural properties of inverse trirutile compounds. Its motivation lays in the discovery of new potential multiferroic transition metal oxides, and in the understanding of the relationships between crystal structures - through structural and magnetic transitions- and physical properties.
In the inverse trirutile family, little was known regarding the inverse trirutile Mn_2TeO_6, which was our main motivation to study it in details.

First a very a short state of the art is presented in the crystallography field, with the history of rutile derivative oxides and the structures in which they crystallize, followed by a brief review of physical properties essential to this study.

Chapter 2 is devoted to the experimental methods: synthesis, structural characterizations and measurements of the physical properties. Particular attention is paid to the powder diffraction techniques (X-ray and neutron), including crystal and magnetic structures refinement procedures.

The main chapter is Chapter 3, which presents a thorough investigation of the crystal and magnetic structures and physical properties of Mn_2TeO_6 in the temperature range 700°C -1.5K. The complexity of the phenomena observed in this compound required a combination of X-ray diffraction (laboratory and synchrotron), neutron diffraction (including in-situ), electron microscopy, ac and dc magnetic susceptibility, specific heat, and dielectric measurements techniques, performed on different samples obtained varying the synthesis conditions. The emerging picture is that of a compound in which

a complex orbital ordering sets in as high as 400°C. It is followed at lower temperature (≅ 53K) by a first order structural transition involving an even more complex orbital ordering pattern, which is thought to govern the subsequent magnetic orderings and the cascade of magnetic transitions that are observed below.

Chapter 4 concerns the Cr for Mn substitution, with its effect on crystal and magnetic structures and magnetization properties. It also confirms the conclusions of the previous chapter.

A conclusion and perspectives part ends this work, with a more general overview of tellurium oxides and their solid state chemistry, with an emphasis on their polymorphism and their crystallographic wealth.

Table of contents

Acknowledgments ii
Abbreviations iv
Symbols v
Abstract vii
Table of contents ix
List of Tables xi
List of Figures xiii
Chapter 1. Introduction 2
1.1 Rutile-type Structures 2
1.2 Tellurium based oxides 5
1.3 Multiferroic and Magnetoelectric Effects 11
1.4 Problematic of the thesis 14
Chapter 2. Experimental methods 17
2.1 Sample Preparation 17
2.1.1 Solid State Synthesis 18
2.1.2 Spray Drying Method 18
2.1.3 TGA-DTA 21
2.2 Structural Characterizations 21
2.2.1 Powder Diffraction 21
2.2.2 Symmetry analysis 25
2.2.3 Structure Refinements 28
2.2.4 X-ray Absorption Spectroscopy 29
2.2.5 Electron Microscopy 31
2.3 Physical Properties 32
2.3.1 Magnetic Properties 33
2.3.2 Dielectric constant and Polarization 35
2.3.3 Heat capacity measurement 36
Chapter 3. Study of inverse trirutile Mn_2TeO_6 39
3.1 Synthesis and Structural Characterization above RT 39
3.1.1 Previous results from the literature about Mn_2TeO_6 39

3.1.2 Determination of synthesis conditions 40
3.1.3 Preliminary Structural Study 46
3.1.4 XRPD vs. T 48
3.1.5 NPD vs. T 50
3.1.6 Precession electron diffraction tomography 52
3.1.7 Structure refinement using SXRPD data and AMPLIMODES 54
3.1.8 RT-TEM study: SAED and images 62
3.1.9 Tetragonal to monoclinic transition: from 700°C to RT 66
3.2 Low-temperature structures and properties 68
3.2.1 Previous reports 68
3.2.2 Preliminary physical characterizations 69
3.2.3 LT-SXRPD study 73
3.2.4 LT-NPD study 80
3.2.5 Effect of applied magnetic field 87
3.2.6 Structural and magnetic behavior of different Mn_2TeO_6 samples 89
3.3 Discussion 91
3.4 Conclusion and perspective 103
Chapter 4. Study of Cr-substitution effect in Mn_2TeO_6 105
4.1 Synthesis and Preliminary Structural Characterizations 105
4.1.1 Sample preparation 105
4.1.2 Laboratory XRPD analysis 106
4.2 Comparison of the χ(T)curves of Mn_2TeO_6 and Cr_2TeO_6 109
4.3 Neutron diffraction study of Cr_2TeO_6 110
4.4 $Cr_{0.2}Mn_{1.8}TeO_6$ 114
4.4.1 Preliminary magnetic characterization 114
4.4.2 T evolution of the crystal structure of $Cr_{0.2}Mn_{1.8}TeO_6$ 115
4.4.3 Neutron diffraction study 120
4.5 Properties along the $Cr_xMn_{2-x}TeO_6$ series and discussion 125
Chapter 5. Conclusion & Perspectives 129
Bibliography 139

List of Tables

Table 1-1 Examples of inverse trirutile compounds with their lattice parameters. 4

Table 1-2 Magnetic characteristics of a few inverse trirutile compounds. A and G labels correspond to the arrangements of the spins (described in the later).....4

Table 1-3 Structures of A_2TeO_6 compounds versus the ionic radius of A^{3+} in VI coordination –taken in ref (27). 6

Table 1-4 Structural characteristics of $ABTeO_6$ compounds: space group, lattice parameters, cation coordination (O and P are for octahedron and prism, respectively), cationic ordering (yes, no or partial), n° refers to the labels used in the text and Figure 1-5, and references.....9

Table 2-1 Comparison of scattering lengths between X-ray and Neutron (69) 23

Table 2-2 Working condition for the NPD experiments.....24

Table 2-3 Summaries of electron microscopy techniques 32

Table 3-1 Synthesis conditions and cell parameters of Mn_2TeO_6 at RT 40

Table 3-2 Synthesis conditions of the 3 Mn_2TeO_6 samples (S1-S3) characterized in this study.....46

Table 3-3 Crystallographic parameters and corresponding interatomic distances in Mn_2TeO_6 ($P4_2/mnm$) at 700°C, from Rietveld refinement of NPD data.....51

Table 3-4 Summary of the mode decomposition showing the different distortion components and isotropy subgroups.....55

Table 3-5 Summary of the basis modes involved in the distortion of Mn_2TeO_6, distributed per type of WP in $P4_2/mnm$. The numbers in parentheses indicate the number of modes for each Irrep.....55

Table 3-6 Normalized polarization vectors for the Σ_3 distortion components of Mn_2TeO_6, expressed as displacements in relative units for the asymmetric cell of the structure (Normalization unit: 1 Å).....57

Table 3-7 Atomic coordinates and thermal displacement parameters (from SXRPD data) of Mn_2TeO_6 at RT. SG: $P2_1/c$, a = 9.1030(1) Å, b = 13.0463(1) Å, c = 6.4659(1) Å, β = 90.0331(4) °. Agreement factors: R_{Bragg} = 3.29 %, χ^2 = 8.45. 59

Table 3-8 Selected inter-atomic distances (in Å) in Mn_2TeO_6 ($P2_1/c$) at RT 61

Table 4-1 Crystallographic parameters and corresponding interatomic distances in Cr_2TeO_6 ($P4_2/mnm$), obtained from Rietveld refinements of XRPD data at 300K. 111

Table 4-2 Basis functions for axial vectors bound to the Wyckoff site 4e, within the irreducible representations of the propagation vector group for **k** = (0 0 0) in $P4_2/mnm$.....112

Table 4-3 Crystallographic parameters and corresponding interatomic distances in $Cr_{0.2}Mn_{1.8}TeO_6$ ($P4_2/mnm$), obtained from Rietveld refinements of SXRPD (BL04 at ALBA) data at 300 and 10 K. 118

Table 4-4 Basis functions for axial vectors bound to the Wyckoff site (4e), within the irreducible representations of the propagation vector group for **k** = (0 0 1/2) in $P4_2/mnm$. 121

List of Figures

Figure 1-1 Dra wing of rutile-type structures (only cations are shown) and O_6 octahedra for the (a) panel. 3

Figure 1-2 Drawing of the magnetic structures: (a) A-type in $Cr_2W(Mo)O_6$, (b) G-type in Cr_2TeO_6 and (c) G-type in Fe_2TeO_6. The red ellipse show the magnetic bi-unit made of two edge-sharing octahedra, while the blue ellipse shows corner sharing octahedra. 5

Figure 1-3 Polyhedral presentation of the crystal structures of (a) Nd_2WO_6-type ($P2_12_12_1$) and (b) Na_2SiF_6-type (P321). 7

Figure 1-4 Polyhedral presentation of the structures of (a) Na_2SiF_6 and (b) Li_2ZrF_6. In top and middle panels, the two (z = 0 and 1/2) layers are shown separately and their staking is given below. Orange: AO_6 units, green: TeO_6 units. 8

Figure 1-5 Polyhedral representation of known structures in the $ABTeO_6$ family....11

Figure 1-6 (a) Representation of the ferroic orders and their links (36). (b) The relationship between multiferroic and magnetoelectric materials. Ferromagnets (ferroelectrics) form a subset of magnetically (electrically) polarizable materials such as paramagnets and antiferromagnets (paraelectrics and antiferroelectrics). The intersection (yellow circle) represents materials that are multiferroic. Magnetoelectric coupling (blue circle) is an independent phenomenon that can sometimes arise in any of the materials that are both magnetically and electrically polarizable. (37) 12

Figure 2-1 Process of spray drying method 20

Figure 2-2 Spray drying system at GREENMAT (Université de Liège)....20

Figure 2-3 (Left) Schema of the phase transition from cubic to tetragonal (in decreasing temperature) generating the spontaneous polarization in $BaTiO_3$. (Right) Group-subgroup relationship between Pm-3m and P4mm. 26

Figure 2-4 Examples of order parameter **Q** (on 2D lattice); **k** is the propagation vector of high symmetry phase. (81) 27

Figure 2-5 Part of the PCR file (for FullProf) exported from AMPLIMODE routine in the Bilbao crystallographic server (Phase transition from cubic to tetragonal in $BaTiO_3$) 29

Figure 2-6 ODE Beamline at SOLEIL synchrotron facility, enlargement showing the diamond cell and its sample holder....30

Figure 2-7 Collinear antiferromagnetic structures. The circles are magnetic ions, the relative orientation of the spins is given by + (red) and – (blue) symbols. 34

Figure 2-8 (Left) Induced charge on a dielectric placed between the plates of a charged capacitor. (Right) Dependence of the relative dielectric constant on frequency. Contributions of the dipoles, ions and electrons in the total polarization are determined. (106) 36

Figure 3-1 Thermogravimetric and differential thermal analysis data in air (TGA(a)-DTA(b)) and in O2 (TGA(c)-DTA(d)) starting from ($MnC_2O_4 \cdot 2H_2O + H_6TeO_6$) from RT to 750°C. The weight changes corresponding to dehydration and decarbonation are indicated by the black arrows on the TGA curve. Red dot vertical lines corresponding to the DTA peaks are guides to the eyes. 41

Figure 3-2 In-situ XRPD patterns of the Mn, Te, O system as a function of temperature in O_2, from 400 to 670°C. Selected diffraction patterns are presented on the right side. 42

Figure 3-3 Phases involved during the synthesis of the inverse trirutile (versus temperature), extracted from the in-situ XRPD patterns presented in Figure 3-2, the reported temperature range for each phase is only approximate..... 43

Figure 3-4 Le Bail fits of XRPD patterns recorded during in-situ synthesis of Mn_2TeO_6, at 510°C (a) and 550°C (b) in air, showing the coexistence of tetragonal inverse trirutile Mn_2TeO_6 with (a) the Na_2SiF_6-type structure and (b) the Li_2ZrF_6-type structure. Corresponding cell parameters and crystal structures are summarized on the right side. 44

Figure 3-5 SEM micrographs of Mn_2TeO_6 at different steps of the synthesis process. 45

Figure 3-6 SXRPD patterns (in selected Q-ranges) of the three Mn_2TeO_6 samples..... 47

Figure 3-7 SEM micrographs of the three Mn_2TeO_6 samples (a) S1, (b) S2 and (c, d) S3 48

Figure 3-8 Crystal structure of the tetragonal ($P4_2/mnm$) inverse trirutile Mn_2TeO_6 projected (left) along [010] and (right) along [001]..... 49

Figure 3-9 Rietveld refinement of the Mn_2TeO_6 structure from XRPD data recorded at 640°C using $P4_2/mnm$: experimental data (open red circles); calculated pattern (black line); allowed Bragg reflections (green vertical marks). The difference between the experimental and calculated profiles is displayed at the bottom of the graph as a blue line. In following sections, unless otherwise mentioned, Rietveld refinements of powder diffraction patterns will be described in this manner..... 49

Figure 3-10 (left) Temperature evolution of the NPD patterns of Mn_2TeO_6, in the 2.65–3.17 $Å^{-1}$ selected Q range (from 50 to 700°C and then back to 50°C). The horizontal black dotted lines indicate the structural transition at 400°C during both the heating and cooling processes. (right) NPD data of Mn_2TeO_6 at 700 and 50°C (S1 and S2). The insets indicate additional small peaks (thin black arrows) and the splitting of peaks (thick red arrows) in the 50°C patterns. Indexation given in the 700°C pattern is based on the tetragonal unit cell..... 50

Figure 3-11 NPD pattern of Mn_2TeO_6 at 700°C, Rietveld refinement performed in $P4_2/mnm$..... 51

Figure 3-12 (a) [hk0], (b) [0kl], (c) [h0l], and (d) [h1l] reciprocal space sections reconstructed from the PEDT data obtained at RT on a S2 crystalline. Rows of extra reflections (green arrows) show the existence of a superstructure with respect to the HTT (highlighted by a red dashed grid). These extra reflections can be

accounted for by considering lattice parameters a ≅ 9.1 Å, b ≅ 13.0 Å, and c ≅ 6.5 Å.....53

Figure 3-13 Comparison between the HTT (blue) and RTM (black) unit cells of Mn_2TeO_6. 53

Figure 3-14 SXRPD data (CRISTAL, SOLEIL) of Mn_2TeO_6 at RT. The inset shows an enlarged view of extra peaks induced by the doubling of the b parameter (with respect to the HTT form). 54

Figure 3-15 Symmetry relations for the transformation from $P4_2/mnm$ to $P2_1/c$ via five possible subgroup paths. The irrep labels (blue) indicate the active irrep components of each subgroup. Σ_3 is highlighted in red. Numbers in brackets denote SG numbers according to the international tables for crystallography. Corresponding cell parameters and transformation matrixes, which relate the coordinate system of the subgroup to that of the super-group, are also given.....55

Figure 3-16 Rietveld refinement of the SXRPD data of Mn_2TeO_6 at RT. The inset shows an enlarged view of peaks indexed in $P2_1/c$ with a = 9.103 Å, b = 13.046 Å, c = 6.466 Å, β = 90.03°.....56

Figure 3-17 Description of the Σ_3 distortion components of Mn_2TeO_6 through the polarization vectors of the Mn and Te cations, projected along [001]. The atomic displacements correspond to the direction of the arrows, and their relative length is proportional to the mode amplitude. 58

Figure 3-18 Description of the Σ_3 distortion components (polarization vectors) of all atoms in Mn_2TeO_6, using projections chosen to single out each octahedra chain separately for clarity. 58

Figure 3-19 Representation of the $P2_1/c$ distorted inverse trirutile structure of Mn_2TeO_6 at RT projected (a) along [100], (b) along [001] and (c) along [010] and [001]. The parent HTT cell is shown in (a) as a black line. In (b) both types of chains are represented, and the full/dotted black lines highlight the compressed/elongated Mn–O distances of the MnO_6 octahedra. For clarity, only one type of chain is shown in each projection in (c). (d) Mn–O and Te–O interatomic distances (Å) are given for each of in the six octahedra building Mn_2TeO_6. 60

Figure 3-20 SAED patterns along the main zone axes [100], [001], and [010] and corresponding [100] and [001] HRTEM images and associated FT patterns. The indexation corresponds to the RTM (white) and HTT (italic yellow) structures. ..62

Figure 3-21 (Left) High-resolution HAADF-STEM images and corresponding FT pattern of main zone axes along (a) [010], (b) [100] and (c) [001]. On the enlarged images, color-coded atoms are overlapped (Mn, Te, and O in orange, green and blue, respectively), and simulated patterns are given in the inset. (d) [001] ABF-STEM image acquired simultaneously with HAADF-STEM image given in (c) and its FT pattern. For simplicity, only O atoms are shown in the enlarged image. (Right) Projection along [001] of the RTM of Mn_2TeO_6, deduced from the SXRPD refinement results, highlighting the atomic oxygen arrangement along b (blue ellipses) (for comparison with (d)). 63

Figure 3-22 [001] HADDF-STEM image highlighting the area corresponding to the 020 spots in the FT and ED patterns (red arrow). The intensity plot profile along the Te row of the selected area (white rectangle) is also given in insert. 64

Figure 3-23 [001] HAADF-STEM image of an area with two types of defects. The (A) and (B) regions are enlarged (right panels), and corresponding structural models are proposed in the bottom left panel. 65

Figure 3-24 Temperature evolution between RT and 700°C of the lattice parameters and cell volume of Mn_2TeO_6, from NPD data upon heating (full symbols) and cooling (open symbols). 66

Figure 3-25 Mn K-edge XANES spectra of Mn_2TeO_6 (S3 and S1) and Mn_2O_3 as a reference sample for Mn^{3+} at RT. The highest absorbance of each spectrum was normalized to unity. 68

Figure 3-26 Zero field-cooling warming (zfcw) and field-cooling warming (fcw) $\chi(T)$ curves (left axis) of Mn_2TeO_6 (S2 sample) and $\chi^{-1}(T)$ (right axis) in 100 Oe. The dotted black line show the linear fit to a Curie-Weiss regime. 69

Figure 3-27 (a) $\chi(T)$ curves (of S2 sample) recorded upon warming and cooling (1-zfcw, 2-fcc, and 3-fcw modes) in 100 Oe (left axis) and corresponding $\Delta\chi/\Delta T$ vs. T curves (right axis);(b) In addition to 2- and 3-curves of panel of (a), $\chi(T)$ curves recorded in 5T in 4-fcc and 5-fcw modes; (c) Ac susceptibility $\chi'(T)$ upon warming and cooling in h_{ac} = 10 Oe at different frequencies in the 100 – 10k Hz range. 70

Figure 3-28 T dependence of the dielectric constant (ε') at 10k Hz upon warming and cooling between 100 and 10K, and in inset, from 10 to 200K upon warming measured at different frequencies from 5k to 100k Hz. 71

Figure 3-29 Cp(T) curves of the Mn_2TeO_6 (S2 sample) shows at least 6 transitions including T_s, T_{N1} and T_{N2}. First and second order transitions are indicated by red and black triangles, respectively. 72

Figure 3-30 SXRPD data of Mn_2TeO_6 (S3 sample) at 295 and 205K in the 1.2 – 3.0 $Å^{-1}$ Q range and in insets selected Bragg peaks at higher-Q ranges. 74

Figure 3-31 Temperature evolution of the SXRPD data of Mn_2TeO_6 (S3 sample) recorded from 70 to 25K (cooling) and from 25 to 70K (warming) in temperature sweeping mode 75

Figure 3-32 Temperature evolution of the SXRPD data of Mn_2TeO_6 (S3 sample) from 10 to 200K. The temperature range covered by dashed area (100 – 40K) corresponds to the coexistence of two phases. Pink arrows (on the top of figure) point out selected Bragg peaks belonging to RTM phase, while green arrows (on the bottom of figure) are for the LT phase. Two enlarged Q ranges are shown: on the right to highlight new small peaks compared with the RTM phase (indicated by green stars) and on the left to visualize the LT-RTM phase transition. 75

Figure 3-33 Rietveld refinement of the SXRPD data of Mn_2TeO_6 (S3 sample) at 120K in $P2_1/c$ with a = 9.101 Å, b = 13.035 Å, c = 6.453 Å and β = 90.64°. The insets show chosen Q ranges to highlight (a) small peaks corresponding to the doubling

along b (compared with the HTT phase), (b) Bragg peaks characteristic of the monoclinic distortion, (c) the quality of the fit at high angles.....76

Figure 3-34 SXRPD data of Mn_2TeO_6 (S3 sample) recorded at 295K (red) and 10K (blue). The inset shows a Q-range chosen to highlight the small "satellite" peaks existing at RT (pink triangles) and only at LT (green wedge triangles).....77

Figure 3-35 Temperature evolution of lattice parameters and cell volume of Mn_2TeO_6, from SXRPD data (Le Bail fit). Between 295 and 205K the parameters are extracted from data (Figure 3-30) recorded upon cooling, while between 200 and 10K they are obtained upon warming (Figure 3-32). The grey area indicates the temperature range where the two phases (RTM and LTM) coexist. 78

Figure 3-36 Le Bail fit of the SXRPD data of Mn_2TeO_6 at 10K. The inset shows a Q-range chosen to show the small peaks (pink arrows: RTM-like b doubling, green arrows: LTM), indexed in the monoclinic structure ($P2_1/c$, a = 9.0386 (1) Å, b = 13.0498 (1) Å, c = 6.5048 (1) Å, β = 90.285 (1) °) with **k** = (1/2 0 1/4).....79

Figure 3-37 Temperature evolution of the NPD patterns of Mn_2TeO_6 (S2 sample), in a selected Q range, from 1.5 to 250 K upon warming (WISH@ISIS). The dashed area corresponds to the two-phase temperature range. The horizontal red dot line indicates Ts. 81

Figure 3-38 Temperature evolution of the NPD patterns (G4.1) of Mn_2TeO_6 (S2 sample) (a) between 1.5 K and 200 K, in the 0.2 - 3 $Å^{-1}$ range (b) between 1.5 and 80 K, in the 0.2-1.8 $Å^{-1}$ range. T_S is marked in yellow, T_{N1} in purple and T_{N2} in red. Main magnetic Bragg peaks and their corresponding propagation vectors are also shown (circles and squares for $\mathbf{k_1}$ and $\mathbf{k_2}$ respectively).....82

Figure 3-39 Le Bail fitting of the LT crystal structure of Mn_2TeO_6 at 27 K (WISH): $P2_1/c$ with a = 9.0354 (2) Å, b = 13.0478 (3) Å, c = 6.5039 (1) Å, β = 90.2302 (2) ° and the magnetic peaks indexed with $\mathbf{k_1}$ = (1/2 0 0) and $\mathbf{k_2}$ = (0 1/2 0). Weak additional magnetic peaks are outlined by grey stars. 83

Figure 3-40 Upper panel: Temperature evolution (below T_{N1}) of the integrated intensities of a few magnetic Bragg peaks (G4.1 data, see indexation on Figure 3-39 with the 27K pattern). The vertical arrow shows the maximum of intensity for the (-1 -2 1) (-1 2 1) + $\mathbf{k_1}$ Bragg peak. Lower panel: NPD patterns in selected T - range and Q - range used to build the plot above. 84

Figure 3-41: Views along b and c-axis of the magnetic model for the tetragonal Mn_2TeO_6; as proposed by Fruchart (7) in (a) and derived from the Γ_3 representation in (b) The red ellipses show the magnetic bi-unit made of two edge-sharing octahedra, while the blue ellipse show corner sharing octahedra. 86

Figure 3-42 Magnetic field dependence of magnetization of Mn_2TeO_6 recorded at 5, 10, 20, 30, 40, 50 and 60K. A small hysteresis is seen in the M(H) curve at 5 and 10K. 87

Figure 3-43 Magnetic field dependence of dielectric constant measured in Mn_2TeO_6 recorded at f =100 kHz at 10K. M(H) curve (10K) is also shown for comparison. 88

Figure 3-44 Temperature dependence of the zfc (left axis) susceptibility and (right axis) inverse susceptibility curves of S1 sample (inverse triangle) and S2 like samples (triangle, square and circle) of Mn_2TeO_6 recorded under 100 Oe. 89

Figure 3-45 Temperature evolution (from 6 to 250K) of the NPD patterns (selected Bragg peaks) of Mn_2TeO_6 (Left: S1, Right: S2 sample) recorded upon warming. Green triangles (top of figure) and pink triangles (bottom of figure) point out Bragg peaks belonging to RTM and LT phase, respectively. The horizontal yellow and black dotted lines indicate the T_{N1} and T_{N2} magnetic transition, respectively.90

Figure 3-46 Evolution of the cell parameters of Mn_2TeO_6 between 973 and 1.5K. 92

Figure 3-47 Transformation of the RTM to LTM phase versus temperature in warming and cooling; the biphasic areas in red (warming) and blue (cooling) are determined using a 10% threshold (lower panel) and corresponding $\chi(T)$ curves (upper panel). 93

Figure 3-48 The two Jahn-Teller distortions of the manganese (III) octahedron (high-spin configuration), (left) compressed and (right) elongated. Both distortions lower the energies of one electron in the eg level. (62) 94

Figure 3-49 Sketches explaining the transition from HTT to RTM, by decomposing the distortions. The sequence follows the blue arrows. The red lines indicate the change at each step (elongation, compression, rotation…). 96

Figure 3-50 (010) projection of RTM structure ($\beta \cong 90°$) and simulated structure model with shorter c-axis and bigger β angle ($\beta \leq 95°$). 97

Figure 3-51 Relationships between structural parameters V and β (a), magnetic properties illustrated by $\chi(T)$ and $\Delta\chi/\Delta T(T)$ curves (b) and the temperature evolution of the intensity of chosen magnetic Bragg peaks (c) from 1.5 to 100K 99

Figure 3-52 Coefficients of the linear thermal expansion α (ppm/K) for the cell volume. Parameters at each temperature (V, T) are used to calculate α_V using 10K parameters as the reference (V_0, T_0). The dashed area indicates the temperature range where the two phases coexist. 100

Figure 4-1 (a) Selected room-temperature XRPD patterns in the $Cr_xMn_{2-x}TeO_6$ series, from x = 0 to x = 2. A minor amount of Cr_2O_3 is observed in the x =1 and 1.5 samples (shown with black stars). The main peak indicating the doubling of the unit cell along b (in the RTM setting) is indicated by a triangle. Indexations using the tetragonal unit cell are given. (b) Enlargement of (110) Bragg peak around Q = 1.95 $Å^{-1}$ 106

Figure 4-2 Variation of lattice parameters and cell volume of $Cr_xMn_{2-x}TeO_6$ as a function of the Cr-content x, obtained from the Le Bail fitting of laboratory XRPD data. 108

Figure 4-3 Magnetic susceptibility vs. temperature curves (zfc and fc) for (left axis) Mn_2TeO_6 in 100Oe and (right axis) Cr_2TeO_6 in 3000Oe. The inset shows the corresponding $\chi^{-1}(T)$ curve of Cr_2TeO_6. The black dot line is for the Curie-Weiss fitting. 109

Figure 4-4 (left) Temperature evolution of the NPD (G4.1@LLB) patterns of Cr_2TeO_6, in the 1.25–3.5 $Å^{-1}$ selected Q range (from 1.6 to 289 K). The horizontal white dot line indicates the magnetic transition at 90K. (right) NPD data of Cr_2TeO_6 at 289, 105 and 1.6K, the inset on the pattern at 105K emphases the diffuse scattering signal observed at this temperature.....110

Figure 4-5 Rietveld refinement of the NPD data of Cr_2TeO_6 at 1.6K within the $P4_2/mnm$ space group and **k** = (0 0 0). Stars indicate main magnetic peaks. 112

Figure 4-6 (a) Structure of Cr_2TeO_6 with the labels corresponding to the four (symmetrically equivalent) Cr-sites. The red ellipse shows the magnetic bi-unit made of two edge-sharing octahedra, while the blue ellipse shows corner sharing octahedra. Magnetic structure of Cr_2TeO_6 (Γ_9 with ψ_1) projected along (b) [010] and (c) [001].....113

Figure 4-7 Magnetic susceptibility vs. T curves (left axis) (zfc and fc) for $Cr_{0.2}Mn_{1.8}TeO_6$ and χ^{-1}(T) (right axis) in 100 Oe. The black dotted line is the Curie-Weiss fitting. The inset shows the ac susceptibility χ'(T) in h_{ac} = 10Oe at different frequencies in the 10 - 10kHz range. 115

Figure 4-8 Laboratory XRPD patterns of $Cr_{0.2}Mn_{1.8}TeO_6$ at 473K (red line) and 873K (black line) in air.....116

Figure 4-9 Two views of the crystal structure of the tetragonal ($P4_2/mnm$) inverse trirutile structure of $Cr_{0.2}Mn_{1.8}TeO_6$, showing the 2:1 cationic ordering of Mn/Cr (orange/dark green) and Te (green) species. O species are light blue. (Cr/Mn)-O distances corresponding to RT structure are given and the longest apical bond along <110> direction is highlighted in thick orange line. 116

Figure 4-10 Rietveld refinement of the SXRPD data of $Cr_{0.2}Mn_{1.8}TeO_6$ at 300 and 10K ($P4_2/mnm$ space group). Orange stars indicate the main peak of Mn_2O_3. 117

Figure 4-11 Temperature evolution of the lattice parameters and cell volume of $Cr_{0.2}Mn_{1.8}TeO_6$ obtained from Le Bail fitting of laboratory XRPD data recorded in air (right, from 300 to 873K) and NPD (G4.1@LLB) data (left, 2K to 300K) upon warming. Characterized samples and measurement conditions are not same, explaining the discrepancy at 300K between the two plots.....119

Figure 4-12 Neutron diffraction patterns of $Cr_{0.2}Mn_{1.8}TeO_6$ at 40 and 2K and of Mn_2TeO_6 at 28K, for which the main $\mathbf{k_1}$ magnetic reflections are indicated by pink arrows.....120

Figure 4-13 Refinement of the NPD data of $Cr_{0.2}Mn_{1.8}TeO_6$ at 2 K (G4.1@LLB). Magnetic peaks indexation is shown for propagation vector **k** = (0 0 1/2) with $P4_2/mnm$ space group. The inset shows an enlargement of the magnetic Bragg peaks profiles. This refinement corresponds to model I; model II gives identical magnetic structure factors.....122

Figure 4-14 Models of magnetic structures for $Cr_{0.2}Mn_{1.8}TeO_6$ projected along (a) [010] and (b) [001]. 123

Figure 4-15 Temperature dependence of the magnetization curves (zfc, fc) of $Cr_{0.025}Mn_{1.975}TeO_6$ in an applied field of 0.01, 1, 3 and 5T. 126

Figure 4-16 Magnetic field dependence of the magnetization of $Cr_{0.025}Mn_{1.975}TeO_6$ recorded at 5, 35, and 100K. Hysteresis features are seen in the MH curve at 5 and 35K. The inset shows the enlargement of the selected range. 126

Figure 4-17 Extracted μ_{eff}, θ_{cw} and transition temperatures (T_{peak}) as a function of x in the $Cr_xMn_{2-x}TeO_6$. T_N, T_{peak} and T_{peak2} are shown when compounds show two peaks on susceptibility curve. 127

Figure 5-1 Le Bail fitting of the SXRPD (CRISTAL@Soleil) and NPD (D2B@ILL) data of HC-MTO phase recorded at RT. Both patterns are indexed in a trigonal structure (SG: P-31m with a ≅ 5.00Å, c ≅ 4.65Å and γ = 120°) 132

Figure 5-2 Le Bail fits of the XRPD patterns of the HC-MTO phase and the inverse trirutile Mn_2TeO_6 recorded at RT. The HC-MTO pattern is indexed in the trigonal structure (SG: P-31m with a ≅ 5.00Å, c ≅4.65Å and γ = 120°), while the inverse trirutile Mn_2TeO_6 pattern is indexed in the RTM structure (SG: $P2_1/c$ with a ≅ 9.10Å, b ≅ 13.05Å, c ≅ 6.47Å and β ≅ 90.07°)..... 133

Figure 5-3 Drawing of the structures (lower panel) and showing each time only one octahedral layer (higher and middle panels) (a) inverse trirutile ($P4_2/mnm$), (b) honeycomb with P-31m and (c) honeycomb with P321 from (157). In (b) and (c), red and blue arrows show cation shifts layer to layer (z = 0 ↔ z = 1/2) to highlight the relationship between structures. Cations move from dot rectangles to solid rectangles. 134

Figure 5-4 Relationships between the ionic radius of A^{3+}_{ave} (average ionic radius of A and A' in VI coordination (27)) and the reduced cell volume V/Z in AA'TeO_6 compounds. Grey triangles, pink triangles, green circles, and blue squares are for Nd_2WO_6 (i), Li_2ZrF_6, Na_2SiF_6 (ii) and inverse trirutile–types (iii), respectively. Some corresponding A^{3+} cations are indicated. The areas at the borderline between two regimes are highlighted by a colored background. 135

Figure 5-5 Relationship between structure of diagram of AA'TeO_6 compounds, among trirutile, Li_2ZrF_6 and Na_2SiF_6 families..... 137

Trirutile and multiferroic properties : exploring tellurates

Chapter 1. Introduction

This chapter aims at covering briefly the research history about oxides which exhibit structures derived from the rutile one. A particular attention will be paid to the so-called inverse trirutile structure that is involved in a large part of this work. We will then present a short review dealing with tellurium-based oxides. Three structures, Nd_2WO_6, Na_2SiF_6 and Li_2ZrF_6 types, reported for ternary and quaternary tellurates (A_2TeO_6, $ABTeO_6$) systems, will be described. At the end, a few generalities about multiferroics and magnetoelectric effects are presented to explain the motivation of this PhD thesis.

1.1 *Rutile-type Structures*

Rutile-type compounds can be classified into three groups: $A^{4+}O_2$, $A^{2+}B_2^{5+}O_6$ and $A_2^{3+}B^{6+}O_6$.

The prototype $A^{4+}O_2$ compound is rutile, TiO_2 crystallizing in $P4_2/mnm$ with a = 4.53Å and c = 2.93Å (*1*). Its tetragonal crystal structure is built of a chain of edge-sharing TiO_6 octahedra along the c-axis. These chains are then joined together by corners in the *ab*-plane (Figure 1-1a, b). $A^{3+}B^{5+}O_4$ compounds belong to the same class as they keep the same unit cell due to a statistical distribution of the cations on the lattice. Examples include tantalates such as $CrTaO_4$ and antimonates such as $AlSbO_4$.

$A^{2+}B_2^{5+}O_6$ compounds (Figure 1-1c) correspond to a rutile superstructure, reported for the first time for two minerals -tapiolite ($FeTa_2O_6$) and mossite ($FeNb_2O_6$)- by Goldschmidt (*2*). He established that their structure is derived from the rutile one by ordering the metal ions in the chain of edge-sharing octahedra in a regular way $1A^{2+}$:

$2B^{5+}$ (Figure 1-1c). The rutile and trirutile structures are both tetragonal and have the same crystal symmetry, i.e., space group (SG) $P4_2/mnm$, and the relationships between unit cells are $a_{trirutile} = a_{rutile}$ and $c_{trirutile} = 3c_{rutile}$ (*3*, *4*). Until 1960, the only known $A^{2+}B_2^{5+}O_6$ compounds with a trirutile-type structure were for A = Mg, Ni, Co, Fe, etc., and B = Nb, Ta, Sb.

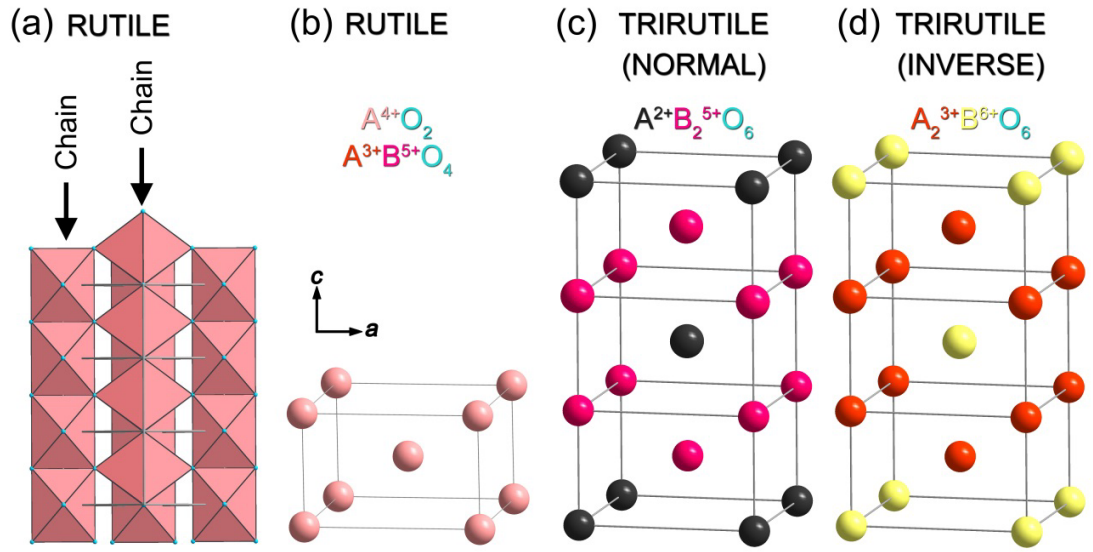


Figure 1-1 Dra wing of rutile-type structures (only cations are shown) and O_6 octahedra for the (a) panel.

In 1960, Bayer (*5*) first synthesized Cr_2WO_6, a ternary oxide with composition A_2BO_6 (Figure 1-1d), where A and B correspond to trivalent and hexavalent ion, respectively. There is one cation with a high oxidation state for two cations with a lower oxidation state, in contrast with $A^{2+}B_2^{5+}O_6$ trirutiles. The positions of A and B are therefore interchanged on the lattice, with a $2A^{3+}$:$1B^{6+}$ order in the chain of edge-sharing octahedra. It is why Bayer called this structure "inverse trirutile structure." In 1962, he synthesized the A_2TeO_6 series with A = A1, Cr, Ga or Fe (*6*). Then, new inverse trirutile compounds were discovered with different A cations : Mn, V (*7*). Recently, chromium-based inverse trirutiles with molybdenum or rhenium were synthesized under high pressure (*8*, *9*). Space groups and cell parameters of these inverse trirutile compounds are summarized in Table 1-1. They all crystallize in the tetragonal unit cell, $P4_2/mnm$ (136), with $a \cong 4.5$ Å and $c \cong 9.0$ Å, as well as the trirutile structure.

Composition	*a* (Å)	*c* (Å)	Ref
Al_2TeO_6	4.445(10)	8.70(1)	*10*
Cr_2MoO_6	4.587(1)	8.811(1)	*8*
Cr_2ReO_6	4.552(1)	8.893(1)	*9*
Cr_2TeO_6	4.546(2)	9.014(1)	*11–13*
Cr_2WO_6	4.582(2)	8.870(3)	*11–13*
Fe_2TeO_6	4.601(2)	9.087(3)	*11*, *13*, *14*
Ga_2TeO_6	4.559(1)	8.970(1)	*10*
V_2WO_6	4.629	8.912	*7*

Table 1-1 Examples of inverse trirutile compounds with their lattice parameters.

Transition metal based inverse trirutiles are all reported as antiferromagnets (AFM). This AFM behavior was confirmed by neutron powder diffraction (NPD) for Cr_2WO_6, Cr_2TeO_6, Fe_2TeO_6, Cr_2MoO_6, Cr_2ReO_6 and V_2WO_6 as summarized in Table 1-2.

Composition	T_N (K)	*k*-vector	Mag SG	Ordering	Ref
Cr_2MoO_6	93	(0 0 0)	*Pn'nm*	A	*8*
Cr_2ReO_6	67	(1/2 0 1/2)	$Pa2_1/c$		*9*
Cr_2TeO_6	93	(0 0 0)	*Pn'nm*	G	*11–13*, *15*
Cr_2WO_6	45	(0 0 0)	*Pn'nm*	A	*11*, *15–17*
Fe_2TeO_6	207	(0 0 0)	$P4_2/m'n'm'$	G	*11*, *13*, *14*
V_2WO_6	117	(0 0 0)	*Pn'nm*	A	*7*

Table 1-2 Magnetic characteristics of a few inverse trirutile compounds. A and G labels correspond to the arrangements of the spins (described in the later).

Cr_2MoO_6 and Cr_2WO_6 exhibit an A-type antiferromagnetic structure, as visualized in Figure 1-2a; Cr^{3+} spins are aligned in the same direction in the *ab*-basal plane, in each pair of CrO_6 octahedra sharing edges the coupling (red ellipse in Figure 1-2) is AFM (along *c*) and the coupling is ferromagnetic (FM) in the pairs sharing coners. The magnetic structure of V_2WO_6 is similar. In contrast, as shown in Figure 1-2b, Cr_2TeO_6 has a G-type antiferromagnetic structure; Cr^{3+} spins are aligned in parallel in the *ab*-plane as well but are antiparallel in between octahedra sharing corners (blue ellipse in Figure 1-2). As shown in Figure 1-2c, the magnetic structure of Fe_2TeO_6 is also a G type order, but the direction of the Fe^{3+} spins are along the *c*-axis. Cr_2ReO_6 has a

drastically different magnetic structure since the rhenium spins also order, thus we do not mention more details here (see (*9*) for more information).

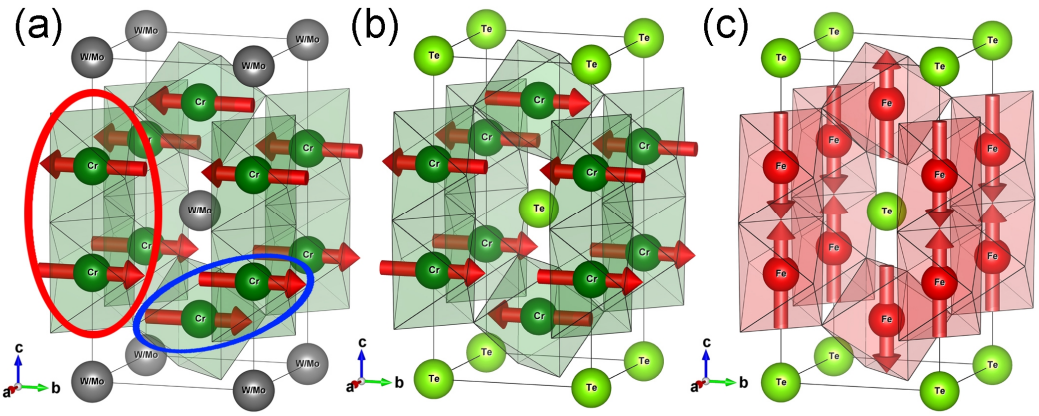


Figure 1-2 Drawing of the magnetic structures: (a) A-type in $Cr_2W(Mo)O_6$, (b) G-type in Cr_2TeO_6 and (c) G-type in Fe_2TeO_6. The red ellipse show the magnetic bi-unit made of two edge-sharing octahedra, while the blue ellipse shows corner sharing octahedra.

1.2 *Tellurium based oxides*

As tellurium exhibits several oxidation states (Te^{4+} or Te^{6+}), there are numerous Te-based oxides corresponding to a large variety of structures, depending on the conditions of synthesis (temperature, atmosphere, pressure). Both oxidation states can also coexist in a same structure, even if the coordination polyhedra are different for Te^{6+} and Te^{4+}. Te^{6+} is more often in rather regular O_6 octahedra with usual short Te-O bonds ≅ 1.92Å. In contrast, Te^{4+} has a stereoactive lone pair and is able to adapt numerous coordination geometries. More often, it has 3 to 4 strongly-bound oxygens on the opposite side of the Te lone pair. The occurrence of Te_mO_n complexes is also possible, leading to rings or chains for instance (*18*).

Ternary (A, Te, O) systems have been studied over several decades, allowing the identification of numerous phases corresponding to the A_2TeO_6 formula, in which tellurium is hexavalent, including the inverse trirutile compounds mentioned in the previous section. Trömel *et al.* (*19*) and Frit *et al.* (*3*) reported that depending on the ionic radius of A^{3+} different structures are stabilized: inverse trirutile, Na_2SiF_6-type or Nd_2WO_6-type structures. Before describing these structures, their main crystallographic

characteristics (space group and lattice parameters) are summarized in Table 1-3, versus the A^{3+} ionic radius.

	Composition	SG (N°)	*a* (Å)	*b* (Å)	*c* (Å)	r_A (Å)	Ref
(iii) Nd_2WO_6-type	La_2TeO_6	$P2_12_12_1$ (19)	5.510	9.441	10.38	1.032	*19*, *20*
	Pr_2TeO_6		5.44	9.329	10.28	0.99	*19*, *20*
	Nd_2TeO_6		5.416	9.298	10.21	0.983	*19–21*
	Sm_2TeO_6		5.36	9.212	10.12	0.958	*19*, *22*
	Eu_2TeO_6		5.339	9.183	10.09	0.947	*19*
	Gd_2TeO_6		5.325	9.160	10.05	0.938	*19*, *23*
	Tb_2TeO_6		5.302	9.138	10.03	0.923	*19*, *20*
	Dy_2TeO_6		5.252	9.056	9.957	0.912	*19*
	Ho_2TeO_6		5.24	9.052	9.935	0.901	*19*, *20*
	Y_2TeO_6		5.325	9.160	10.05	0.900	*19*, *24*
	Er_2TeO_6		5.223	9.006	9.903	0.89	*19*, *20*
	Tm_2TeO_6		5.198	8.979	9.871	0.88	*19*, *20*
	Yb_2TeO_6		5.246	9.036	9.931	0.868	*19*, *20*
(ii) Na_2SiF_6-type	Yb_2TeO_6	*P*321 (150)	8.974	8.974	5.103	0.868	*19*
	Tl_2TeO_6		9.070	9.07	4.984	0.885	*3*
	Lu_2TeO_6		8.945	8.945	5.071	0.861	*20*
	In_2TeO_6		8.883	8.883	4.823	0.800	*25*
	Sc_2TeO_6		8.741	8.741	4.799	0.745	*26*
(i) Inverse trirutile	Fe_2TeO_6	$P4_2/mnm$ (136)	4.601	4.601	9.087	0.645	*11*, *13*, *14*
	Ga_2TeO_6		4.559	4.559	8.970	0.62	*10*
	Cr_2TeO_6		4.546	4.546	9.014	0.615	*11–13*
	Al_2TeO_6		4.445	4.445	8.70	0.535	*10*

Table 1-3 Structures of A_2TeO_6 compounds versus the ionic radius of A^{3+} in VI coordination – taken in ref (27).

(i) For a small ionic radius (0.5 Å < r_A < 0.7 Å), A_2TeO_6 shows an inverse trirutile structure (Ga_2TeO_6-type),

(ii) In the range (0.75 Å < r_A < 0.87 Å), A_2TeO_6 tends to form a honeycomb like Na_2SiF_6-type structure,

(iii) For a large ionic radius (r_A > 0.87Å) an orthorhombic Nd_2WO_6-type structure is observed.

There are two exceptions in this evolution vs. r_A: Yb and Tl-based oxides (in blue and green in Table 1-3), which are at the boundary between Nd_2WO_6 and Na_2SiF_6-type structures. The first one (Yb_2TeO_6) crystallizes within both Nd_2WO_6- and Na_2SiF_6-type structures, while the later (Tl_2TeO_6) exists in the Na_2SiF_6-type structure only. The Nd_2WO_6- and Na_2SiF_6-type structures are drawn in Figure 1-3.

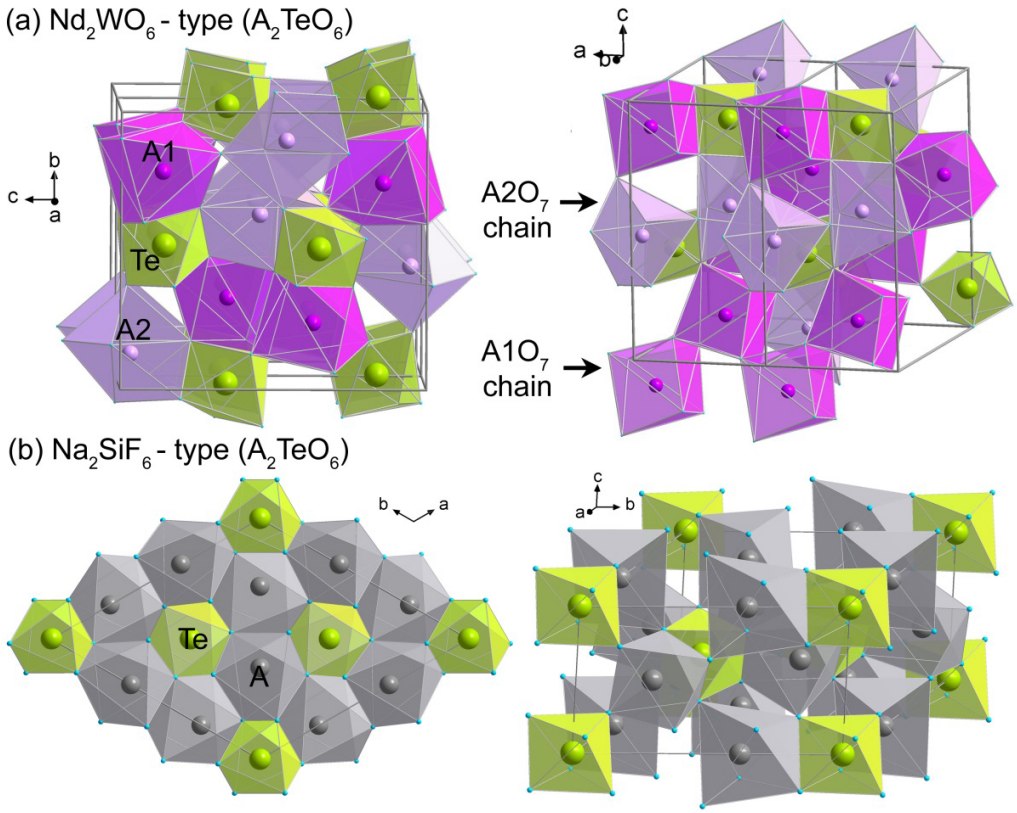


Figure 1-3 Polyhedral presentation of the crystal structures of (a) Nd_2WO_6-type ($P2_12_12_1$) and (b) Na_2SiF_6-type ($P321$).

- The first one is described as TeO_6 octahedra sharing edges and corners with $A1O_7$ and $A2O_7$ polyhedra. There is no direct link in-between the TeO_6 octahedra, which form isolated octahedral units. Both kinds of sevenfold oxygen coordinated AO_7 units form chains along the [100] direction; $A1O_7$ share edges, whereas $A2O_7$ share corners. (Figure 1-3a)
- As shown in Figure 1-3b, the Na_2SiF_6 structure is based on a double-layered hexagonal close-packed (hcp) lattice. Both A^{3+} and Te^{6+} cations are octahedrally coordinated. Each TeO_6 octahedron shares edges with three AO_6 octahedra and corners

with three other AO_6 octahedra which are building layers stacked along the *c*-axis. AO_6 in the z = 1/2 layer shares edges with two TeO_6, while AO_6 in the z = 0 layer shares edges with only one TeO_6 (Figure 1-4a).

In both Nd_2WO_6- and Na_2SiF_6-type structures, the polyhedra around the A cation are strongly distorted, in contrast with regular TeO_6.

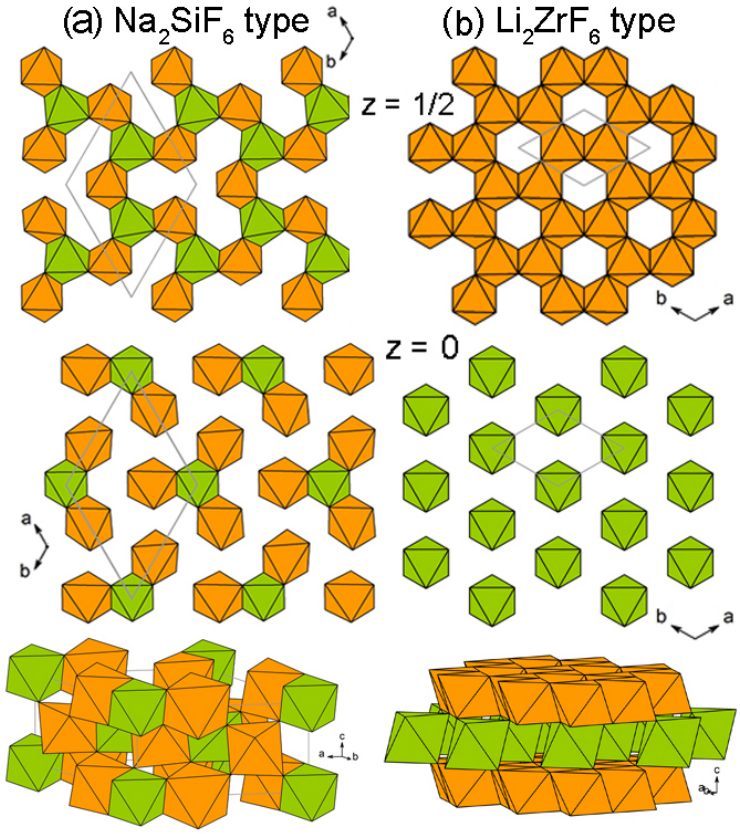


Figure 1-4 Polyhedral presentation of the structures of (a) Na_2SiF_6 and (b) Li_2ZrF_6. In top and middle panels, the two (z = 0 and 1/2) layers are shown separately and their staking is given below. Orange: AO_6 units, green: TeO_6 units.

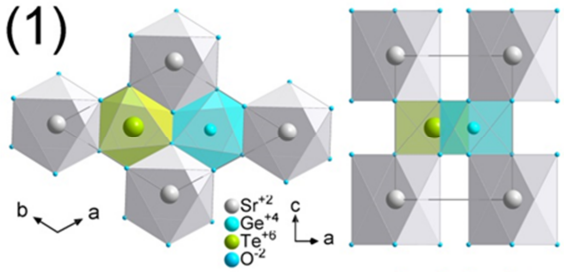
Double-layered hcp structures have also been reported for quaternary compounds $ABTeO_6$, where A and B are trivalent cations or A and B are tetravalent and divalent cations, respectively. In most of the cases, the AO_6 octahedra are significantly larger than the BO_6 and TeO_6 ones. This structure, so-called Li_2ZrF_6-type, presents similarities with the Na_2SiF_6 one and is observed for compounds listed in Table 1-4.

Composition	SG (N°)	a (Å)	b (Å)	c (Å)	Coord.	Cationic ordering	n°	Ref.
$SrGeTeO_6$	*P*312 (149)	5.066	5.066	5.404	O	Yes	1	*28*
$BaGeTeO_6$	*P*312 (149)	5.095	5.095	11.58	P+O	Part.	2	*28*
LaCrTeO6	*P*-3 (147)	5.159	5.159	10.38	O	Yes	3	*29, 30*
$PrCrTeO_6$		5.145	5.145	10.18	O	Yes		*29*
$NdCrTeO_6$		5.14	5.14	10.12	O	Yes		*29*
$SmCrTeO_6$		5.129	5.129	9.993	O	Yes		*29*
$EuCrTeO_6$		5.125	5.125	9.93	O	Yes		*29*
$GdCrTeO_6$		5.122	5.122	9.871	O	Yes		*29*
$TbCrTeO_6$		5.116	5.116	9.812	O	Yes		*29, 30*
$DyCrTeO_6$		5.111	5.111	9.751	O	Yes		*29, 30*
$HoCrTeO_6$		5.107	5.107	9.688	O	Yes		*29, 30*
$YCrTeO_6$		5.105	5.105	9.693	O	Yes		*29, 30*
$ErCrTeO_6$		5.103	5.103	9.647	O	Yes		*29, 30*
$TmCrTeO_6$		5.096	5.096	9.603	O	Yes		*29*
$YbCrTeO_6$		5.093	5.093	9.56	O	Yes		*29*
$BiMnTeO_6$	$P2_1/c$ (14)	5.173	9.060	9.914 β=90.18°	O	Yes	4	*31*
$LaFeTeO_6$	*P*-31*c* (163)	5.205	5.205	10.35	O	Part.	5	*32*
$BiFeTeO_6$	*P*-31*c* (163)	5.212	5.212	9.882	O	Part.		*31*
$BiCrTeO_6$	*P*-31*c* (163)	5.163	5.163	9.919	O	Part.		*31, 33*
$PbMnTeO_6$	*P*-62*m* (189)	5.101	5.101	5.396	P	No	7	*34*
$SrMnTeO_6$	*P*-62*m* (189)	5.143	5.143	5.384	P	No		*35*

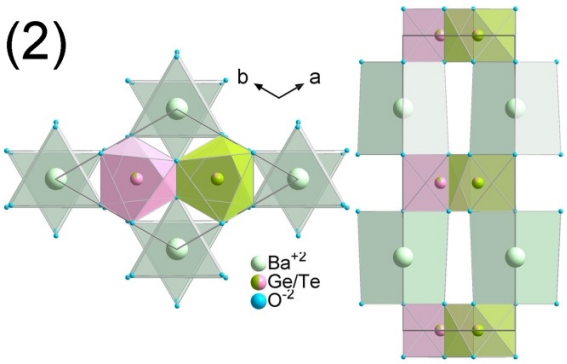
Table 1-4 Structural characteristics of $ABTeO_6$ compounds: space group, lattice parameters, cation coordination (O and P are for octahedron and prism, respectively), cationic ordering (yes, no or partial), n° refers to the labels used in the text and Figure 1-5, and references.

The comparison between Na_2SiF_6 and Li_2ZrF_6-types is made in Figure 1-4. Both structures are based on a double-layered hcp array of oxygen with cations occupying octahedral voids. They differ in the filling modes of these voids. In the Li_2ZrF_6-type, octahedra occupy 2/3 voids within one layer (z = 1/2) forming a honeycomb arrangement by sharing edges, while octahedra occupy 1/3 voids in the second layer (z = 0) and share corners with octahedra belonging to the z = 1/2 layer. The $ABTeO_6$ family with Li_2ZrF_6-type structure is large, as exemplified by the few members gathered in Table 1-4, the corresponding structures are depicted in Figure 1-5.

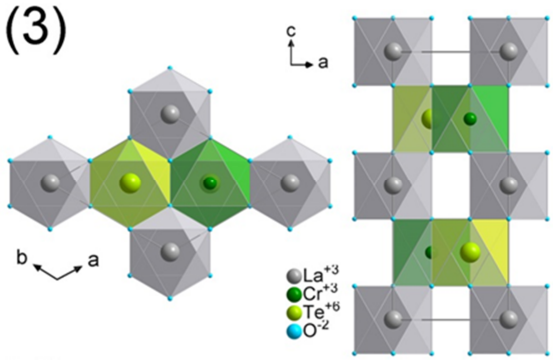
1. One of the simplest structures (label n°1) is $SrGeTeO_6$, which crystallizes in *P*312 and corresponds to a complete order of the cations on the three cationic sites. It can be described as the staking of two types of layers, one containing Ge and Te, in alternation, and the other one only Sr.



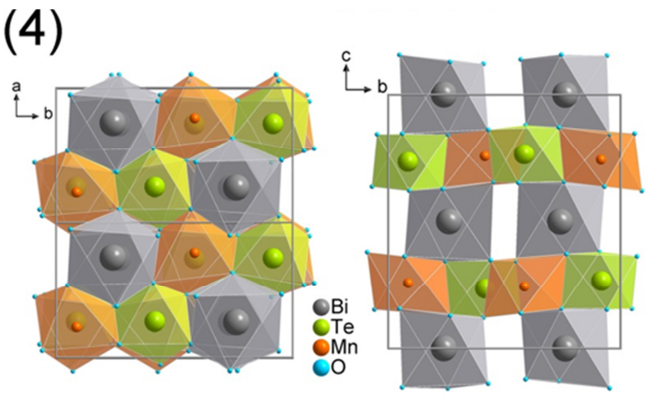
2. The structure (n°2) observed for $BaGeTeO_6$ is close to the previous one but Ba atoms are in a trigonal prismatic coordination, and Ge and Te are randomly distributed over the same crystallographic sites. The structure is refined in the *P*312 space group with a doubling of the *c*-parameter compared to the n°1 model.



3. In the structure (n°3) of $LaCrTeO_6$, all the cations are in octahedral coordination and there is no cationic disorder. The intralayer ordering is such that Cr has only Te as neighbors (and reciprocally) and from one layer to the other there is an alternation between Te and Cr. This structure belongs to the *P*-3 space group with doubled *c*-parameter, like the n°2 structure.



4. The structure of $BiMnTeO_6$ (n°4) is similar to the previous one, with cations in O_6 octahedra and without cation disorder. Nevertheless the structure is monoclinic and refined in the $P2_1/c$ space group, the *c*-parameter is kept and the orientation of the cell in the *ab*-plane is of course different (the *a*-parameter is retained).



5. This structure (n°5), exemplified by $BiCrTeO_6$, is similar to the n°3 one, with close lattice parameters. All cations are in O_6 octahedra but in the honeycomb layer cations are randomly distributed. This structure is refined in *P*-31*c*.

6. The structure type n°6 is the one of $PbSb_2O_6$ or Cr_2UO_6. It is not in Table 1-4 since no tellurium oxide is known to crystallize with this framework. The structure is refined in *P*-31*m* with $a \cong 5.0$Å and $c \cong 4.6$Å. In this case, the cations belonging to the honeycomb layer are statistically distributed and all cations are in octahedral coordination.

7. Structure n°7 is similar to the previous one (n°6), but all cations are in trigonal prismatic coordination. It is what is observed for $SrMnTeO_6$ and this structure is refined in *P*-62*m*.

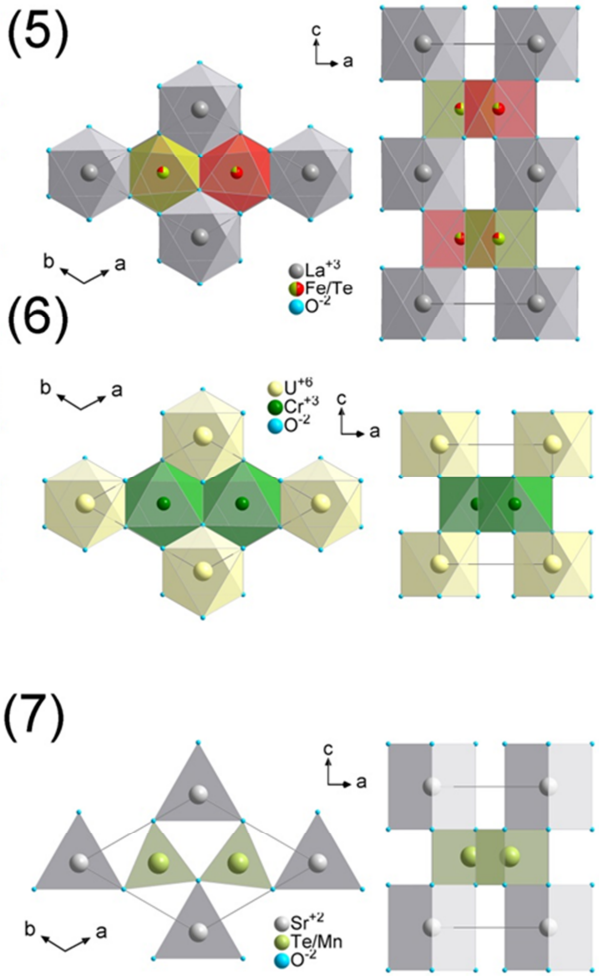


Figure 1-5 Polyhedral representation of known structures in the $ABTeO_6$ family

From this brief description of the different structures belonging to the Li_2ZrF_6-type, it appears clearly that structural determination in these compounds may be challenging, owing to the huge number of possible combinations (*28*).

1.3 *Multiferroic and Magnetoelectric Effects*

This section is not an exhaustive description of multiferroic properties but a brief review of parameters that may be important in the search for new materials, and in the understanding of the relationships between crystal structures and properties.

Multiferroics materials, i.e. which present simultaneously at least two properties among ferromagnetism, ferroelectricity and ferroelasticity- have attracted a huge attention owing to the interesting physics involved to understand the coupling mechanisms, and owing to their possible applications in electronic devices. The schema presented in Figure 1-6a (*36*) is very often used to illustrate the coupling between electric and magnetic, magnetic and strain, strain and electric states. Figure 1-6b (*37*) shows the different class of materials combining these properties.

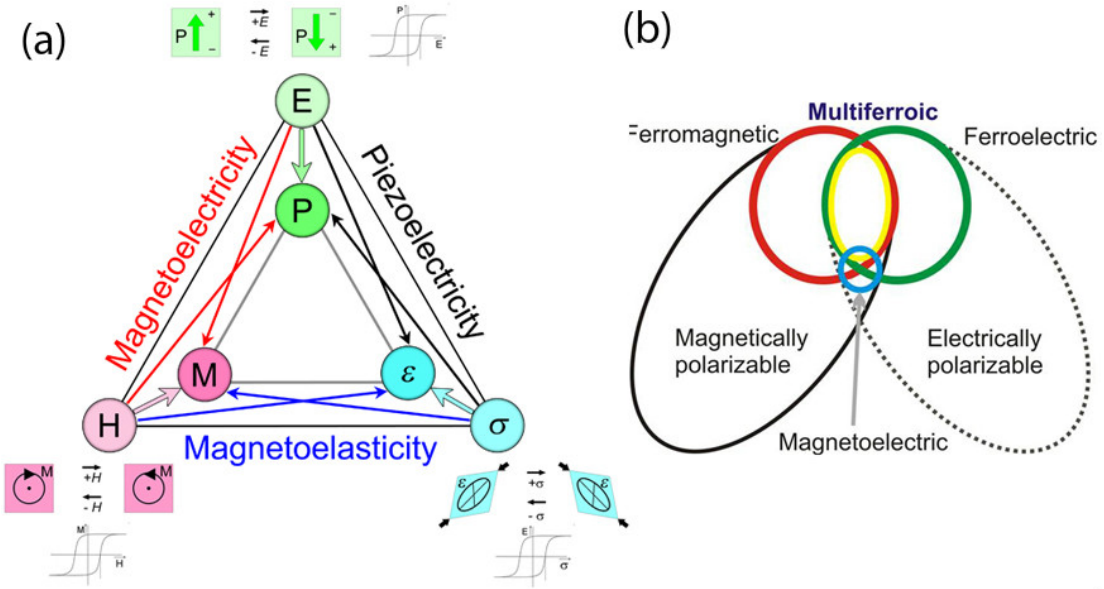


Figure 1-6 (a) Representation of the ferroic orders and their links (36). (b) The relationship between multiferroic and magnetoelectric materials. Ferromagnets (ferroelectrics) form a subset of magnetically (electrically) polarizable materials such as paramagnets and antiferromagnets (paraelectrics and antiferroelectrics). The intersection (yellow circle) represents materials that are multiferroic. Magnetoelectric coupling (blue circle) is an independent phenomenon that can sometimes arise in any of the materials that are both magnetically and electrically polarizable. (37)

The order parameters of ferroelectric, ferromagnetic and ferroelastic materials, i.e., electric polarization P, magnetization M and strain ε (Figure 1-6a), are controlled by an electric field E (green arrow), magnetic field H (pink arrow), and stress σ (light blue arrow), respectively. These order parameters are spontaneously formed and display typical hysteresis in the corresponding $P(E)$, $M(H)$ and $\varepsilon(\sigma)$ curves. To be multiferroic, a compound should present (at least) two ferroic forms which have to be coupled. The coupling between two orders is defined as magnetoelectricity (red arrows for M and P),

piezoelectricity (black arrows for P and ε) and magnetoelasticity (blue arrows between M and ε). For instance, in the case of a magnetoelectric (ME) effect, a magnetic field H may control an electric polarization P (without any spontaneous polarization in $H = 0$) and an electric field E may affect the magnetization M. This ME coupling may be linear (directly between the magnetic and electric polarization order parameters) or non-linear (indirectly via strain). One instance of non-linear ME coupling is a magnetodielectric (magnetocapacitance), in which the dielectric constant is perturbed by the onset of magnetic ordering. (*38*, *39*)

Multiferroicity is used for a compound that is ferroelectric and (anti)ferromagnetic (and corresponds to the yellow area in Figure 1-6b).

Multiferroics are classified in two types (I and II) depending on the mechanism which is at the origin of the spatial inversion symmetry breaking that leads to ferroelectricity (*40*). In type-I multiferroics (proper ferroelectrics), like archetypal $BiFeO_3$, the electric and magnetic dipoles have independent origins and they occur at different temperatures. Consequently their coupling is not very strong, but the spontaneous polarization can be quite large (10 to 100 $\mu C/cm^2$). In type-II multiferroics (improper ferroelectrics), ferroelectricity can be induced by a complex arrangement of magnetic moments. Such "magnetically induced ferroelectrics" may show large ME coupling since the origin of their ferroelectricity is driven by spin ordering; i.e., the inversion symmetry is broken by the ordering of magnetic moments; itself sensitive to an applied magnetic field. However, the polarization is usually much smaller than type-I materials. Type-II ME compounds can further be separated into two groups (*40*):

(1) Ferroelectricity is caused by a particular complex magnetic ordering, sinusoidal spin density wave, cycloidal spiral, proper screw (e.g.: $TbMnO_3$(*41*), $MnWO_4$(*42*), $CaMn_7O_{12}$(*43*), $CuCrO_2$ (*44*))

(2) Ferroelectricity is a consequence of a structural distortion at the onset of magnetic order (e.g., Ca_3CoMnO_6(*45*)), originating from an exchange striction mechanism.

In most magnetic materials the magnetic dipoles are formed by the partial filling of *d* level allowing unpaired electrons to exist with an uncancelled spin component but this

contradicts the requirements for ferroelectricity usually associated to d^0 or d^{10} cation off-centering. It explains the scarceness of such materials. There are only 58 of the 90 magnetic point groups that allow a ME coupling, among these, only 13 point groups are found as corresponding to multiferroics materials (*46*, *47*).

Nevertheless, ME and multiferroic materials have been studied actively and intensively in the past decade, since they could be candidates for the next-generation of magnetic RAM and low-power-consumption spintronic devices in the information-oriented society in this 21st century. It is why the magnitude of the ME coupling and the temperature at which it occurs are two big challenges for researchers. (*37*, *46*)

So far, most experimental research has been focusing on designing new transition metal oxides with optimized physical properties, based on the current understanding of the physics of multiferroics/ME compounds.

1.4 *Problematic of the thesis*

In 1969, Hornreich published a list of "some likely candidates in which magnetoelectric and related effects may be observed" (*48*), based on the analysis of magnetic space group and point group symmetries. In this list, he mentioned the inverse trirutile oxides Fe_2TeO_6, Cr_2WO_6, Cr_2TeO_6 and V_2WO_6. This work was later extended further to inverse trirutile compounds, in a theoretical report about relationships between magnetism and ferroelectricity in this structural type, published by Kurkin *et al*. (*49*). In the inverse trirutile tetragonal unit cell, the nonmagnetic hexavalent ions lie on the 2*a* sites with inversion symmetry, and the magnetic trivalent ions lie on the 4*e* sites with double mirror plane symmetry (*mm*). The magnetic space group of Fe_2TeO_6 (corresponding to a G-type collinear magnetic structure, as shown in Figure 1-2) is $P4_2/m'n'm'$, and its point group is $4/m'm'm'$, which is ME active (*47*, *48*). The ME effect in Fe_2TeO_6 was demonstrated experimentally by Buksphan, who measured magnetic susceptibility as a function of temperature while applying an electric field E (*50*). ME effect was also evidenced recently in Fe_2TeO_6 thin films by X-ray magnetic circular dichroism combined with photoemission electron microscopy (XMCD-PEEM) by Wang *et al*. (*51*). ME and magnetodielectric coupling have also been investigated in

Cr_2WO_6, which has a magnetic point group *m'mm*. A large magneto-dielectric effect and linear ME effects have been reported in Cr_2WO_6 if the sample is cooled down in magnetic and electric fields applied above T_N, consistent with the spin flop usually observed in this class of materials (*52*).

Among the Li_2ZrF_6-type compounds, magnetic susceptibility measurements of $LaFeTeO_6$, $TbCrTeO_6$ and $ErCrTeO_6$ have shown paramagnetic behavior down to low temperature, while $BiMnTeO_6$, $BiCrTeO_6$, $BiFeTeO_6$, $LaCrTeO_6$ and $YCrTeO_6$ are reported as AFM with low T_N (*30–32*). More to the point, recently, $PbMnTeO_6$, the only non-centrosymmetric space group in Table 1-4, was shown to be AFM with a broad magnetic transition at ≅ 20K, and presented as a potential ME material (*34*).

The aim of the thesis was thus to investigate further tellurate oxide materials for (i) a better understanding of the structures-properties relationships in the context of multiferroicity, and (ii) to investigate new possible candidates for multiferroic or ME properties.

In this thesis, we mainly focused on manganese tellurates among the inverse trirutile family for two main reasons. First, the inverse trirutile Mn_2TeO_6 had not been studied in details, and in the only two previous reports (*7*, *53*) available on the subject, no clear description of the crystal and magnetic structures was provided. Second, manganese compounds are known to often exhibit exotic magnetic, orbital or charge ordering phenomena, which could induce a spontaneous electric polarization, and are thus excellent candidates in the search for multiferroicity: amongst tellurates for instance, Mn_3TeO_6 has been reported recently as a type-II multiferroic material with two types of incommensurate spin substructures.

The main part of this work was first devoted to Mn_2TeO_6 (Chapter 3). A few substitutions were also performed, following the $Mn_{2-x}Cr_xTeO_6$ formula (Chapter 4). During the development of the synthesis process, we obtained new polymorphous oxides exhibiting layered honeycomb lattices (Chapter 5).

Chapter 2. Experimental methods

This chapter details the methods of sample preparation and experiments used to determine the crystal and magnetic structures and physical properties of manganese tellurium oxides. The objectives of the experiments are mainly

- to synthesize pure and well crystallized polycrystalline ceramics with controlled compositions
- to perform X-ray diffraction laboratory for all samples
- to perform magnetometry for all single phase samples
- to complete these data by (i) X-ray absorption and electron microscopy and (ii) by synchrotron X-ray and neutron diffraction, to characterize the crystal and magnetic structures as a function of temperature for selected samples
- to measure electrical properties (dielectric constant and polarization), to investigate magnetoelectric coupling as a function of temperature (and magnetic field).

2.1 *Sample Preparation*

In this work, manganese tellurium oxides were synthesized by solid-state reaction. The preparation of well-crystallized samples is challenging because it requires relatively low-temperature sintering to avoid Te evaporation. To improve the quality of materials, we also used the spray drying method, which is well known to increase reactivity and diffusion.

2.1.1 *Solid State Synthesis*

Mn_2TeO_6 was prepared by solid-state reaction, using manganese oxalate ($MnC_2O_4 \cdot 2H_2O$) and commercial telluric acid (H_6TeO_6, Fluka, >99%), as proposed in ref (*7*). For $Mn_{2-x}Cr_xTeO_6$ ($0.01 \leq x \leq 1.5$), commercial chromium oxide (Cr_2O_3, Alfa-Aesar, >99 %) was additionally used.

The precursor $MnC_2O_4 \cdot 2H_2O$ was first synthesized by precipitation of manganese acetate ($Mn(OOCCH_3)_2 \cdot 4H_2O$, Sigma-Aldrich, >99%) by oxalic acid ($H_2C_2O_4 \cdot 2H_2O$, Acros Organics, 99.5%), as reported by Huizing *et al*. (*54*).

All precursors were weighed according to the required Mn(Cr)/Te ratio and then mixed in an agate mortar, before being calcined at 550-600°C in alumina crucibles in air. The powder was then ground again, pressed with a uniaxial press in the shape of bars ($\cong 2 \times 2 \times 12$ mm) or pellets (1 cm diameter) and sintered at 600°C in air or O_2 flow. The bars were then heated again at 700-750°C in same atmospheres. For electrical measurements, dense sintered ceramics were prepared using an isotactic pressing before the last heat treatment. These samples were prepared with the help of Ms. Sophie Dufourd (CRISMAT).

2.1.2 *Spray Drying Method*

This non-conventional process to obtain bulk oxides attracts much attention for several benefits: reducing the sintering temperature, improving the chemical homogeneity and the stoichiometry control, enhancing purity and affecting the microstructure of the materials.

Spray drying is one of the promising methods for precursors synthesis, and it is widely applied in industry, whereas it is less standard at laboratory scale than sol-gel, coprecipitation or hydrothermal synthesis. The advantage of the spray drying method is mainly mass productivity, simplification of the process and reproducibility, as there are fewer parameters to control. The sprayed droplets transform into dry granules with diameters of a few microns. The homogeneous distribution of inorganic precursors in the granules makes them highly reactive and early crystallization usually results in the formation of nanometric crystallites (*55–57*). The spray drying method is used for the synthesis of functional oxides, particularly for polycationic oxides, to make magneto-

resistive compounds (*58*), high-temperature superconductors (*59*), thermoelectric (*60*) or piezoelectric compounds (*61*), electrode materials of lithium-ion battery (*62*). The properties of materials synthesized by spray drying method often show different behaviors to those of materials made by conventional solid state synthesis, mainly because of grain size, cationic distribution and powder morphology.

The spray drying operates in convection mode. The working principle is moisture removal by application of heat to the feed product. Figure 2-1 shows a schematic drawing of spray drying method. First, the feed liquid undergoes atomization. This is a process where there is a breakup of bulk liquid into a large number of droplets by the atomizer. These tiny droplets meet hot air in the drying chamber. This enables rapid evaporation of moisture from the surface of all the droplets in a uniform manner. The formed particles finally separate from the exhaust gas in the cyclone, except the smallest particles which are carried along with the air flow into a safety filter. . The final products are collected into the product container at the bottom of the cyclone.

Mn_xTeO_6 (with x =1.55 - 2.5) were synthesized by heat treatment of powders obtained by the spray drying method prepared at GREENMAT (Université de Liège) by Dr. Bénédicte Vertruyen and Mr. Stéphane Caubergh.

Aqueous, slightly acidic feedstock solutions were prepared from stoichiometric amounts of $Mn(NO_3)_2{\cdot}4H_2O$ and H_6TeO_6. The exact stoichiometry of the reagents was ascertained by inductively coupled plasma optical emission spectroscopy (ICP-OES) and thermogravimetry and differential thermal analysis (TGA-DTA).

The total cation concentration of the feedstock solution was 8.4×10^{-4} mol/g for the manganese and 4.4×10^{-3} mol/g for the tellurium. A semi-pilot-scale apparatus (Niro Mobile Minor, Figure 2-2) equipped with a co-current atomizer (i.e., sprayed solution and drying air flow in the same direction) with a bifluid nozzle was used. The inlet temperature was 200°C with a liquid feed rate of 15 ml/min. The process was carried out in air, using a 1 bar pressure. The outlet temperature during spraying was 123°C. Immediately after spray drying, the precursor powder was calcined at 300°C for 6 h in air. This heat treatment was necessary due to the hygroscopic feature of the powder. The weight of the obtained powder after calcination is ~ 7g. This powder was then

further heated at 500°C for 6 - 24 h in air. It was then ground, pressed with a uni axial press in the shape of bars (≅ 2 × 2 × 12 mm) and sintered at 600 - 740°C in O_2 flow.

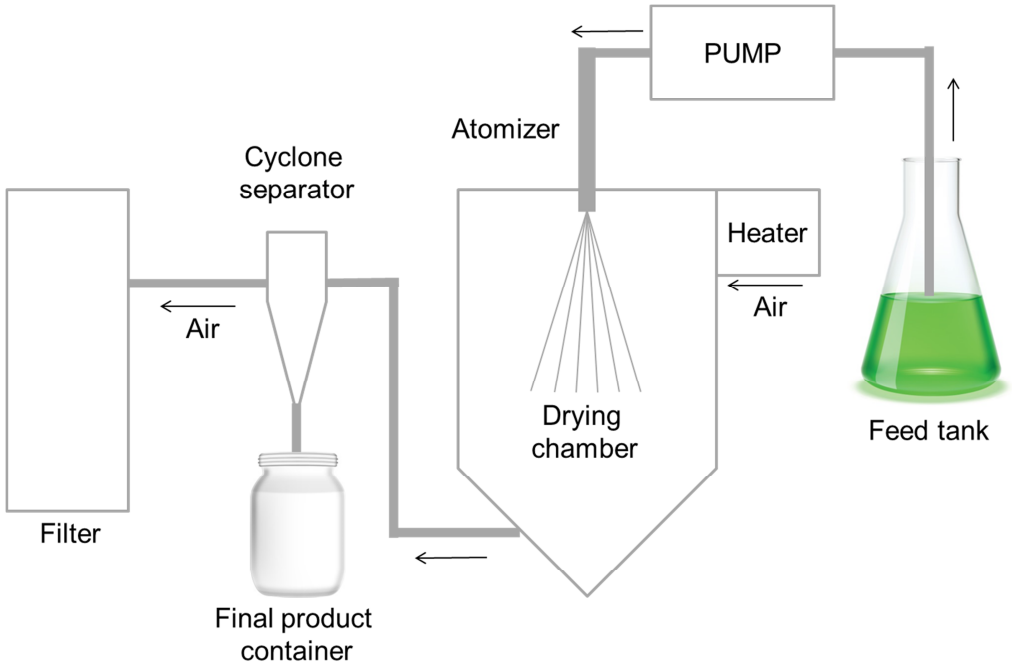


Figure 2-1 Process of spray drying method

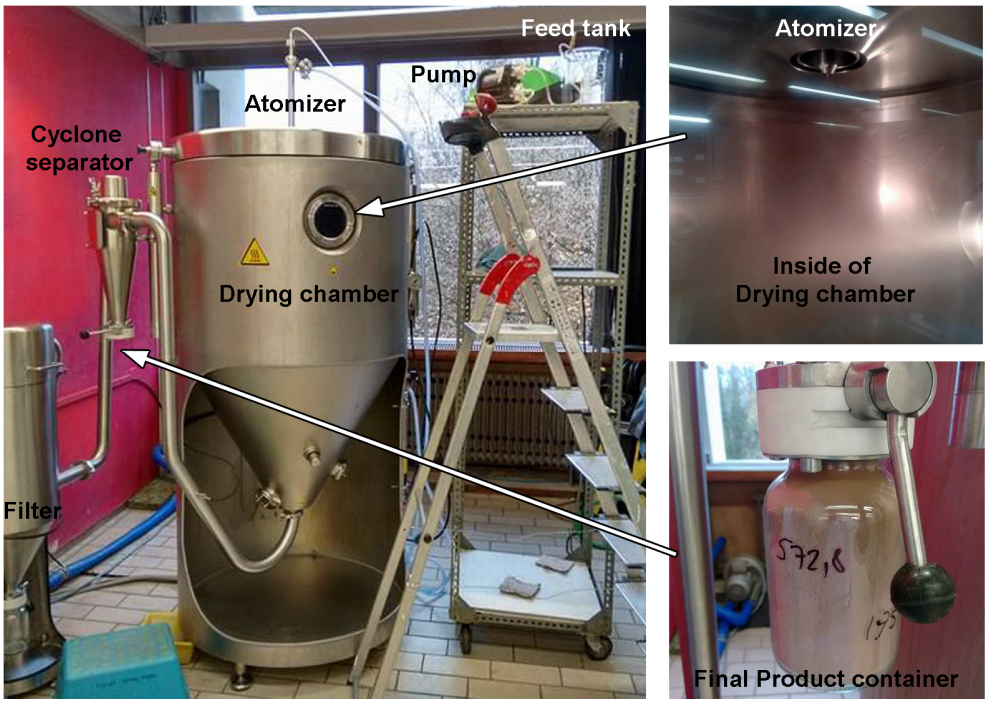


Figure 2-2 Spray drying system at GREENMAT (Université de Liège)

2.1.3 *TGA-DTA*

Thermogravimetry and differential thermal analysis (TGA-DTA) are methods in which the mass of the sample and the temperature difference between the sample and a reference are both monitored over time as the temperature changes at the same time.
TGA-DTA in solid-state chemistry is suitable for studying moisture/volatile contents, thermal stability, purity, transformation/decomposition, etc. (*63*). TGA-DTA was used to check the quality of precursors including the one made with the spray drying method. Furthermore, it was also used to study the phase transformations and decomposition in the manganese tellurates. TGA-DTA measurements were performed by Ms. Sylvie Collin (CRISMAT) using TAG 24 (SETARAM) under air or O_2 flow with 3°C/min heating rate.

2.2 ***Structural Characterizations***

In this work, structural characterizations were performed using X-ray, neutron and electron diffraction, X-ray absorption, scanning and transmission electron microscopy.

2.2.1 *Powder Diffraction*

Diffraction is used to investigate atomic (and spin, in case of neutrons) orderings in a lattice. This technique is based on the Bragg's law:

$$n\lambda = 2d_{hkl}\sin\theta \quad \textit{(Equation 1)}$$

where n is an integer, i.e. the diffraction order, d_{hkl} (Å) is the distance between parallel hkl planes, λ is the wavelength of the incident beam and θ is the Bragg angle. (*64*, *65*) Additionally, diffraction methods can also give useful information about the degree of crystallinity, atomic disorder, grain size, and microstructural stress or strain. In this work, we combine laboratory X-ray, synchrotron, neutron and electron diffraction. In order to compare diffraction patterns obtained from different diffractometers and sources, diffractograms in this work are converted from instrument unit (2θ, T.O.F) into reciprocal space unit Q using following the equations:

(Equation 2) $Q = \frac{4\pi}{\lambda} sin\frac{2\theta}{2}$ for 2θ

(Equation 3) $t(\mu s) = 505.56 L d_{hkl} \sin\theta$ for T.O.F.

where T.O.F (*t*) is measured in microseconds, flight path (*L*) is the known distance in meter the white beam of neutrons travels from source to sample, and θ is from a constant scattering angle 2θ.(*66*)

Laboratory X-ray Powder Diffraction

Laboratory X-ray powder diffraction (XRPD) data were collected by Dr. Stéphanie Gascoin (CRISMAT). An X'PERT Pro MPD (PANalytical) diffractometer (Cu K$\alpha_{1,2}$ radiation; in the θ-θ configuration) and a D8 ADVANCE Vario1 (Bruker, Cu Kα_1 radiation; in the θ-2θ configuration) were used at room temperature (RT). In situ high-temperature XRPD measurements were also carried out using the D8 with an Anton Paar HTK1200N chamber, from RT to 700°C under air or O_2 flow, on a flat alumina sample holder.

Synchrotron Powder Diffraction

Instead of using X-rays produced by X-ray tube in the laboratory, XRPD can be performed using the radiation produced as a by-product of particle acceleration in a synchrotron. A great advantage for powder diffraction is the high intensity and excellent vertical collimation, leading to much-improved resolution compared with laboratory X-ray, usually the synchrotron diffraction can achieve an energy resolution $\Delta E/E \sim 10^{-4}$.

Synchrotron X-ray powder diffraction (SXRPD) experiments were performed using a 2-circle diffractometer and a multi-crystal detector on the CRISTAL beamline at the Soleil synchrotron (Beamline scientist: Erik Elkaïm) (*67*), at RT, with the wavelength λ = 0.7288 Å, using capillary tube (inner diameter (i.d.) 0.5 mm) in rotation. *In situ* high-temperature SXRPD was carried out on the CRISTAL beamline using a blower, from RT to 800°C, with quartz (i.d. 0.7 mm) capillary tube. Low-temperature SXRPD experiment were performed on the BL04-MSPD beamline of the ALBA synchrotron

(Beamline scientist: François Fauth) (*68*) using as detection setup both the high angular resolution (multi-analyzer crystal MAD) and the high intensity mode (position sensitive detector MYTHEN). Data were collected at wavelength λ = 0.4142 Å with sample enclosed in glass capillary (i.d. 0.5mm) spinning within the so-called Dynaflow liquid He flow cryostat (*69*) so to improve powder averaging.

Neutron Powder Diffraction

There is a fundamental difference between the way neutrons and X-ray are scattered by matter. Neutrons are scattered by mainly atomic nuclei while X-rays are scattered by the electron shells. As a result, the scattering factors for neutrons are not proportional to ***Z*** as are those for X-rays, and additionally, there is no scattering-angle dependence. Table 2-1 is a summary of the scattering lengths of neutron and X-ray for elements involved in this work. The neutron scattering amplitude of an oxygen atom is equal to that of tellurium, in contrast with a ratio of about 1: 6.5 for the X-ray scattering amplitudes of the two atoms. Moreover, the contrast of neutron scattering amplitudes among transition metals (Cr and Mn) is significant compared with X-ray. Therefore, neutron diffraction is a useful technique, bringing complementary information from X-rays, for example when one wants to locate light atoms (as oxygen) or differentiate atoms of similar **Z** in a crystal structure like Te/Mn/Cr distribution on cationic site.

Elements involved in this work [Atomic number]	**X-ray scattering length ($\sin\theta$=0), (10^{-12}cm)**	**Neutron scattering length (10^{-12}cm)**
O [8]	2.25	0.58
Cr [24]	6.8	0.352
Mn [25]	7.0	-0.39
Te [52]	14.7	0.58

Table 2-1 Comparison of scattering lengths between X-ray and Neutron (70)

Neutrons are uncharged but do have a magnetic moment. As a result, there is an additional scattering due to the interaction between the neutron magnetic moment and the magnetic moment of the atom. This means that neutron diffraction is invaluable for the investigation of magnetic structures. (*70*, *71*) Not like the scattering of atomic

nuclei, the scattering of magnetic moments comes from the outer electron shell, which has an unpaired electron. As a result, the magnetic scattering has a Q dependence which is even stronger than X-ray, (the magnetic form factor, which depends on the magnetic atom that is considered).

We performed neutron powder diffraction (NPD) on G.4.1 at LLB (Beamline scientist: Dr. Françoise Damay) (*72*), on WISH at ISIS (Beamline scientist: Dr. Pascal Manuel) (*73*), on GEM at ISIS (Beamline scientist: Dr. Ron Smith) (*74*) and on D2B at ILL (Beamline scientist: Dr. Emmanuelle Suard) (*75*). In this work, we performed diffraction from 1.5 to 300K using He cryostat systems with the samples in vanadium cans. For the high-temperature experiment made on the WISH beamline to study in-situ the synthesis, the powder was put in a quartz tube, in which O_2 flowed, and the temperature was increased from 50°C up to 700°C and then decreased back to 50°C. Table 2-2 summarizes these experimental conditions.

Beamline	**Wavelength**	***Q*-range(Å)**	**Temperature**
G41	2.425Å	0.13 - 3.4	1.5 - 298 K
WISH	T.O.F	0.17 - 6.7	1.5 - 285K and 50 - 700°C
GEM	T.O.F	0.25 - 18.9	RT
D2B	1.549 & 2.59Å	0.2 - 5.1	1.5 – RT

Table 2-2 Working condition for the NPD experiments

The thermal two-axis diffractometer D2B is a powder diffractometer designed to achieve high resolution, limited only by powder particle size; moreover a high flux option at 2.59 Å is also available. D2B is well suited for the Rietveld refinement of relatively large structures using a short wavelength (1.549Å).

The cold two-axis diffractometer G4.1 has been designed to study the large cells corresponding to magnetic structures, using a high wavelength that leads to the best instrumental resolution at low Q, where magnetic scattering is expected. G4.1 data does not cover a range of Q that is large enough for structural determination and should be combined with higher resolution data on a thermal diffractometer like D2B.

WISH and GEM are multi-bank high-resolution T.O.F diffractometers, covering a broad *Q*-range. The significant advantage of these diffractometers is that the crystal and magnetic structures can both be studied in a single experiment.

2.2.2 *Symmetry analysis*

A crystalline solid is defined by the periodic arrangement of the atoms which are forming it. Thereby, each periodic arrangement of atoms can be characterized by specific symmetry operations, such as rotations, inversions and mirror planes. The set of all allowed symmetry operations form a mathematical group, called space group (SG). In total they are 230 SG.

The Landau theory (*76*) of symmetry breaking structural phase transitions is based on the postulate that the symmetry break taking place in such transitions is due to the condensation (which should be understood as the change from zero to a nonzero amplitude) of one, or a set of collective degrees of freedom. Accordingly, these degrees of freedom should transform according to one single irreducible representation (Irrep) of the SG of the high symmetry phase G_0. It is called the active Irrep. The amplitudes that become spontaneously non-zero in the low-symmetry phase G form the order parameter $\boldsymbol{Q}$. The symmetry restrictions imposed by Landau theory are generally valid, that is, the existence of a single active Irrep is fulfilled in most cases by group-subgroup phase transitions. Consequently, the fact that the symmetry change in a transition is fully determined by a single active Irrep can be very powerful in the prediction and analysis of the structural properties, and hence the physical properties, of the system.

Structural relationships can be represented in a clear and concise manner using family trees of group-subgroup relations, as exemplified in Figure 2-3 by the ferroelectric transition in $BaTiO_3$. This compound shows three phase transitions (only one of which is shown); the highest symmetry phase G_0 is cubic ($Pm\text{-}3m$) and does not exhibit spontaneous polarization. Decreasing the temperature T < 130°C, the cubic structure is transformed into a tetragonal phase ($P4mm$, subgroup G) associated with a reversible spontaneous polarization which originates from an atomic displacement (*77*, *78*).

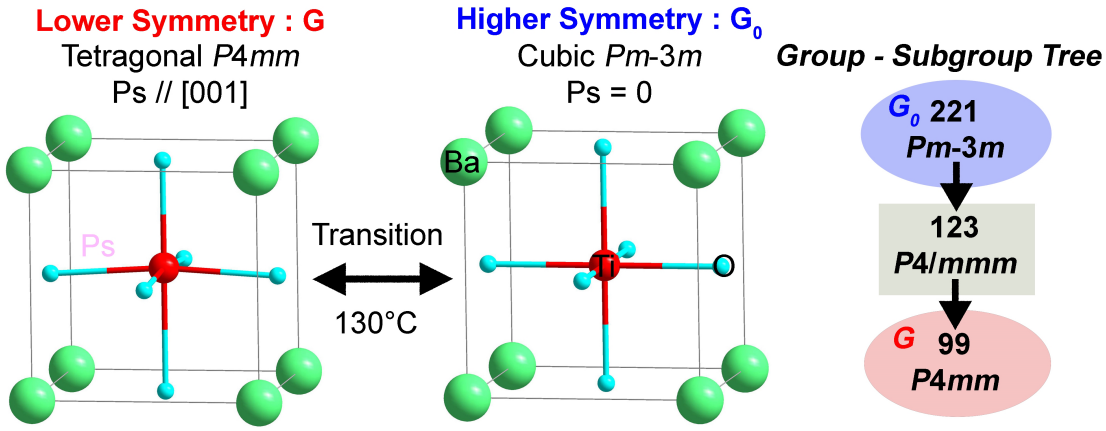


Figure 2-3 (Left) Schema of the phase transition from cubic to tetragonal (in decreasing temperature) generating the spontaneous polarization in $BaTiO_3$. (Right) Group-subgroup relationship between Pm-3m and P4mm.

Order parameters $\boldsymbol{Q}$ depend on external conditions such as temperature, pressure, composition, electric and magnetic field. As illustrated in Figure 2-4, it can describe a simple atomic displacement, a lattice strain, the rotation of a polyhedron, etc. Symmetry-lowering phase transitions sometimes lead to complex structures which can be too complicated to be determined by conventional refinement methods, particularly if powder diffraction data sets only are available.

The symmetry-adapted mode refinement method is a structure refinement approach based on group-subgroup theory to tackle this complexity. It separates the contribution of the different symmetry modes occurring in a structural distortion. The method is based on the calculation of the amplitudes and directions (called thereafter polarization vectors) of the different distortion modes that lead to the low symmetry structure. It is also interesting as it introduces a physical hierarchy among the structural parameters: separating each symmetry mode not only simplifies the refinements by removing non-significant parameters, but also clarifies the physical mechanism which stabilizes a lower symmetry phase (*79–81*). Practical details on this refinement method are described with more details in Section 2.2.3.

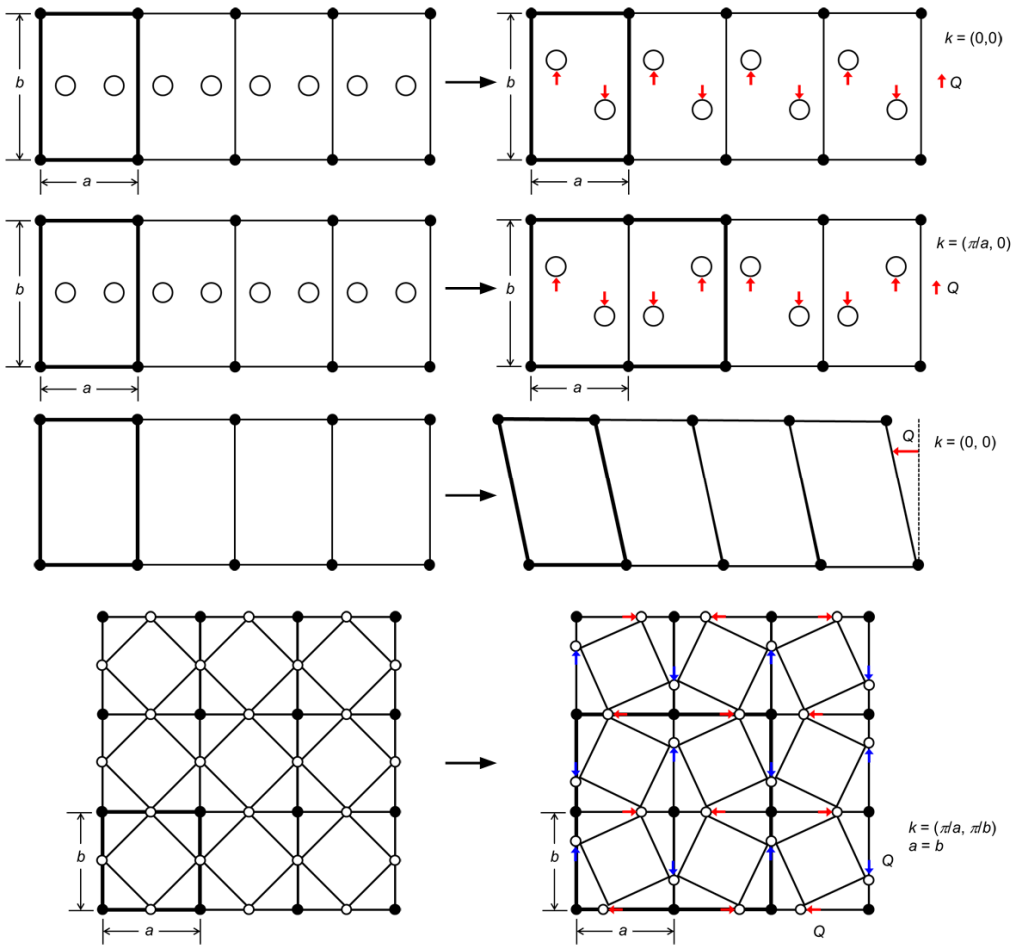


*Figure 2-4 Examples of order parameter **Q** (on 2D lattice); **k** is the propagation vector of high symmetry phase*. (*82*)

In a similar way, symmetry analysis also plays a very important role for magnetic structure determination. For commensurate magnetic structures, the symmetry of magnetic crystals can be described with the aid of black-white SG (so-called Shubnikov groups). They are an extension of the SGs in which the time reversal symmetry operator has been added. In the Hermann-Mauguin symbol, this is expressed by a prime ’. The number of magnetic space groups is large, with 1651 magnetic space groups: 230 monochrome + 230 grey (dia- and para magnetic) + 1191 black-white. (*83–85*) Thus magnetic structure refinement benefits significantly from symmetry analysis. It simplifies the determination of the magnetic structure by enumerating the possible symmetries based on the group-subgroup relationships.

In case of magnetic structure determination, G_0 is the crystal symmetry group of the paramagnetic phase and G describes the magnetic symmetry group. The symmetry breaking is due to the magnetic ordering in the G phase. Within G_0, the symmetry operators which leave $\boldsymbol{k}$ invariant form the so-called little group G_k. If the magnetic phase transition is of the second order and therefore follows Landau theory of symmetry breaking, only one Irrep of G_k will become critical, and the resultant magnetic order can be described by the basis vector of this Irrep. (*86*, *87*) In this work, symmetry analysis were performed using BasIreps (*88*) (from the FullProf Suite), the Bilbao Crystallographic Server (*89*) and ISODISTORT(*90*).

2.2.3 *Structure Refinements*

In the powder diffraction method, the sample to be studied is a fine powder placed in a beam of X-rays or neutrons. Each particle of the powder is a tiny crystal, or assemblage of small crystals, randomly oriented with respect to the incident beam. As a result, there is an overlap of the diffraction peaks which is the drawback of the powder diffraction, but the Rietveld method is an elegant solution to refine the structures because the refinement is undertaken, not using individual structure factors for each reflection, but using the entire diagram. (*71*, *91*) Many programs for Rietveld analysis are available, and one of the most distributed and free ones is the FullProf (*92*) suite package. In this work, crystal and magnetic structure refinements were performed with the FullProf suite of programs, taking into account anisotropic strains and size effects using a spherical harmonics modeling of the Bragg peak broadening (detailed descriptions are in the FullProf manual (*93*)).

As explained before, symmetry analysis for symmetry-mode refinements was carried out using the Bilbao Crystallographic Server (*89*) and its AMPLIMODES routine (*94*) and ISODISTORT server (*90*). The results were directly exported into PCR files, which permit a direct refinement of the amplitude of a basis of symmetry modes, as collective coordinates, instead of individual atomic coordinates.

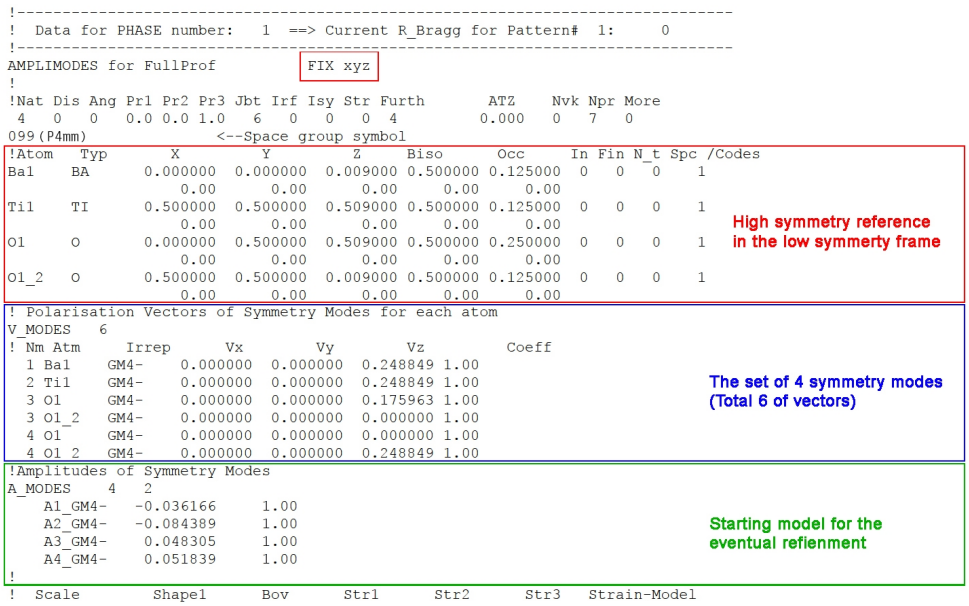


Figure 2-5 Part of the PCR file (for FullProf) exported from AMPLIMODE routine in the Bilbao crystallographic server (Phase transition from cubic to tetragonal in $BaTiO_3$)

Figure 2-5 is an example of PCR file (dealing with the $BaTiO_3$ phase transition illustrated in Figure 2-3) output from AMPLIMODES. In the PCR file, the first lines describe a structure that is considered as a reference of high symmetry, described in the low symmetry frame and is kept fixed. Then the set of symmetry modes defined by the server are listed with their labeling for each atom, the corresponding Irreps, and the vectors of displacements *Vx*, *Vy*, *Vz*. Those come from the symmetry mode analysis and their directions are not refined, only their amplitudes are.

2.2.4 *X-ray Absorption Spectroscopy*

The specificity of the synchrotron radiation is a tunable wavelength, from infra-red to X-ray, which leads to numerous techniques in the synchrotron facilities. Among them, X-ray absorption spectroscopy is a useful tool to complement information obtained from X-ray and neutron diffraction.

X-ray absorption near-edge spectroscopy (XANES) refers to the measurement of the X-ray absorption coefficient as a function of photon energy above the threshold of a

selected absorption edge. Near or below the edge, absorption peaks appear due to excitation of core electrons to some bound states. This pre-edge region contains valuable bonding information such as the energies of virtual orbitals, the electronic configuration, and the site symmetry. The edge position also contains information about the charge on the absorber element.(*95*, *96*) Room-temperature XANES at the Mn K edge (6539 eV) was carried out in the transmission mode on the ODE beamline at the Soleil synchrotron (Figure 2-6) (Beamline scientist: Dr. Lucie Nataf) (*97*). MnO and Mn_2O_3 were used as references for Mn^{2+} and for Mn^{3+}, receptivity.

Sample holders were diamond anvil cells (Figure 2-6) which were filled with a tiny amount of powder (in the 100 μm in diameter and 15 μm in thickness chamber). Raw XANES data were processed using the ATHENA software package (*98*).

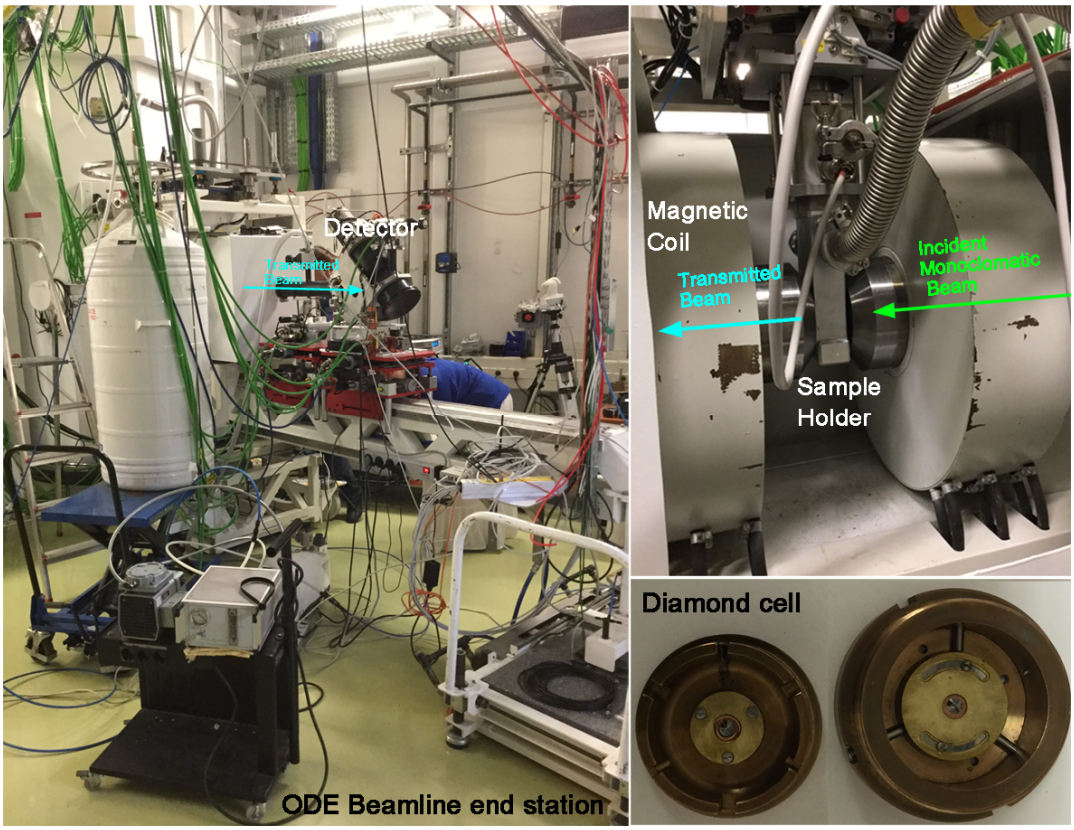


Figure 2-6 ODE Beamline at SOLEIL synchrotron facility, enlargement showing the diamond cell and its sample holder.

2.2.5 *Electron Microscopy*

When the high-energy electron beam is exposed on the sample under high vacuum, as electrons pass through a specimen, they interact with atoms of the solid. Many of the electrons pass through the thin sample without losing energy. A fraction will undergo inelastic scattering and lose energy as they interact with the specimen. This leaves the sample in an excited state. The material can be de-excited by releasing energy typically in the form of visible photons, X-rays, secondary electrons or Auger electrons. Electron microscopy techniques are based on the detection of these scattered or emitted electrons. The features of each technique used in this work are summarized in Table 2-3.

Samples for scanning electron microscopy (SEM) were mounted onto aluminum stubs, fixed with a carbon tape and metallized with a thin layer of sputtered gold to ensure a conductive path from the sample to the stub (and thus to prevent charge accumulation on the sample surface). The surface morphology of the samples was imaged using SEM at GREENMAT (FEI XL30 FEG-ESEM) by Dr. Bénédicte Vertruyen.

Transmission electron microscopy (TEM) and scanning transmission electron microscopy (STEM) experiments were carried out by Dr. Oleg I. Lebedev, Dr. Philippe Boullay, Dr. Sylvie Malo and Dr. Natalia Mordvinova at CRISMAT.

The selected-area electron diffraction (SAED), high-resolution TEM (HRTEM), high angle annular dark field scanning transmission microscopy (HAADF-STEM) and annular bright field STEM (ABF-STEM) were performed at 200 kV using a JEM ARM200F cold FEG probe, image aberration-corrected microscope, equipped with a large angle CENTURIO EDX detector and QUANTUM GIF.

Electron diffraction tomography (EDT) combined with precession electron diffraction (PED) was performed using a JEOL 2010 (200 kV) TEM. For PED, TEM is equipped with a side-mounted Gatan Orius CCD camera and a Nanomegas Digistar precession unit. Precession electron diffraction tomography (PEDT) data sets were collected in a tilt range of about 90° with a precession angle set to 1.2° and a goniometer tilt step below 1°. Lattice parameters and symmetry were deduced from the 3D reconstruction of the reciprocal space using the programs PETS (*99*) and JANA2006 (*100*).

The energy dispersive spectroscopy (EDS) was also carried out using a JEOL 2010. Several dozen crystals were analyzed during EDS to investigate the Mn/Te ratio. Finally, the average of raw data was taken as the result.

Samples for TEM were prepared by grinding materials in an agate mortar in ethanol and then deposited on holey carbon Ni grids. Simulations of the high-resolution TEM images were performed with the JEMS31 software.

Name	Technique	Information	Comment and reference
SEM	Imaging	Roughness of surface	(*101*)
HRTEM	Imaging	Atomic resolution image (diffraction contrast)	The contrast depends on the thickness of the sample and defocuses of the beam. (*101*)
HADDF-STEM	Imaging	Atomic resolution image (**Z**-contrast)	Preference for heavy atoms (*102*)
ABF-STEM	Imaging	Atomic resolution image (**Z**-contrast)	Preference for light atoms (*103*)
SAED-TEM	Diffraction	Reciprocal lattice (2D)	(*101*)
PEDT	Diffraction	Reciprocal lattice (3D)	(*104*)
EDS	Spectroscopy	Elemental analysis, Composition analysis	(*101*)

Table 2-3 Summaries of electron microscopy techniques

2.3 *Physical Properties*

Selected samples are characterized by AC/DC magnetization, dielectric constants and polarization and specific heat measurements as a function of temperature, magnetic field, and electric field. The characterizations reported in this work were done using a Superconducting Quantum Interference Device (SQUID, Quantum Design) magnetometer and Physical Property Measurement System (PPMS, Quantum Design) equipped by commercial or home-made options, in CRISMAT. These measurements were performed with the help of Mr. Fabien Veillon (CRISMAT).

2.3.1 *Magnetic Properties*

When all electrons are paired, materials exhibit diamagnetism. However, some materials show other magnetic behaviors due to the presence of unpaired electrons. Since transition metal can have unpaired 3*d* electrons, their oxides exhibit a large variety of magnetic behaviors.

Unpaired electrons are randomly aligned due to the thermal oscillations; however, they tend to line up under applied external magnetic field. This phenomenon corresponds to paramagnetism. The corresponding magnetic moment M is proportional to the magnitude of the external applied magnetic field H. According to the Brillouin function and for small enough H values, this can be written (*64*):

$$\textit{(Equation 4)}\ M = \chi H,$$

where χ is a constant of proportionality, called magnetic susceptibility.

Most of paramagnetic materials follow the Curie-Weiss law:

$$\textit{(Equation 5)}\ \chi = \frac{\boldsymbol{C}}{(T+\theta_{cw})}\ (T > T_N)$$

where $\boldsymbol{C}$ is the Curie constant, θ_{CW} is the Weiss constant and T is temperature.

An increasing magnetic moment results in an increased susceptibility; the quantitative relation is given by means of the Curie constant:

$$\textit{(Equation 6)}\ \boldsymbol{C} = \frac{N_A^2 \mu^2\, \mu^2{}_B}{3k_B},$$

where μ_B is Bohr magneton, N_A is Avogadro's number, and k is Boltzmann's constant.

Then the effective magnetic moment μ_{eff} is extracted from

$$\textit{(Equation 7)}\ \mu_{eff} = \sqrt{\frac{3k_B \boldsymbol{C} F}{N_A}} = \sqrt{8 \times \boldsymbol{C} \times F}\ (\mu_B)$$

where F is the molar mass (g/mol) and μ_B is Bohr magneton.

A plot of inverse measured magnetic susceptibility $1/\chi_m$ vs. T of a paramagnetic sample is a straight line with slope $1/\boldsymbol{C}$, which crosses the abscissa at T = θ_{CW} (=0, in case of perfect paramagnetism*)*. $\theta_{CW} \neq 0$ values indicate magnetic interactions (which can lead to magnetic ordering at low-tempeature) in the sample, as e.g. ferro- ($\theta_{CW} > 0$) or antiferromagnetic ($\theta_{CW} < 0$) interactions.

Above the magnetic ordering temperature, the magnetic state is paramagnetic due to thermal excitation and follows the Curie-Weiss law. If magnetic moments are ferromagnetically aligned, the transition temperature is called Curie temperature (T_C). If moments are aligned in an antiferromagnetic manner, the transition temperature is called Néel temperature (T_N).

Many antiferromagnetic orders are possible, from simple commensurate ones to incommensurate ones involving for instance spin density waves, cycloidal or helicoidal modulations. Selected simple classifications for collinear spin alignments are summarized in Figure 2-7. Type-A consists in ferromagnetic planes with antiferromagnetic coupling between planes. In type-C, spins are ferromagnetic ordered along a chain with antiferromagnetic coupling in between the chains. In the type-G, the coupling is antiferromagnetic in the three directions. (*105*)

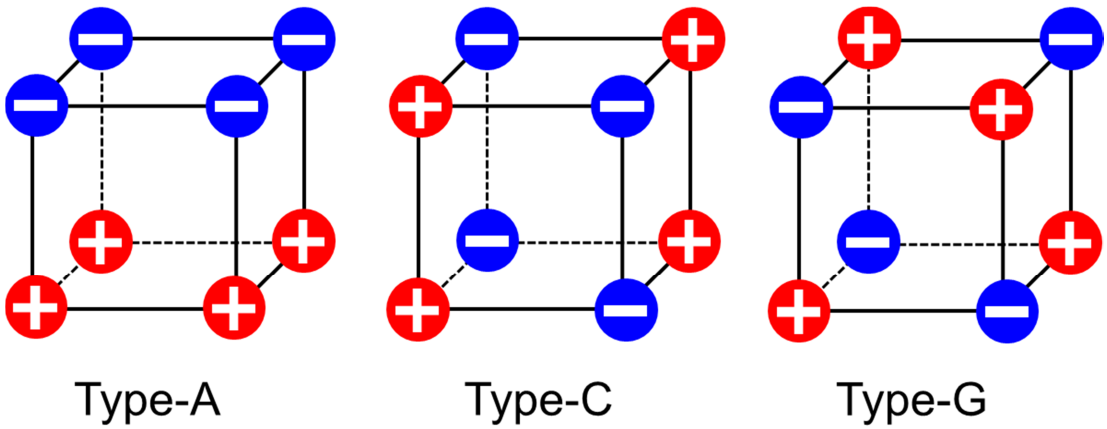


Figure 2-7 Collinear antiferromagnetic structures. The circles are magnetic ions, the relative orientation of the spins is given by + (red) and – (blue) symbols.

Magnetic measurements versus temperature were performed with a 5T SQUID magnetometer in zero-field-cooling warming (*zfcw*) or field-cooling warming (*fcw*) or field-cooling cooling (*fcc*) modes between 5 and 400K under different magnetic fields.

We used two temperature scanning mode; (i) sweep mode without temperature stabilization, (ii) settle mode with temperature stabilization.

Isothermal M versus H curves were also collected using the 5T SQUID magnetometer or the AC measurement system (ACMS) option of a 14T PPMS for magnetic fields ranging from $\mu_0 H = 0$ up to 14 T.

AC magnetic susceptibility curves were obtained by using the 9T PPMS with h_{dc} = 0, h_{ac} = 10 Oe and f = 100 Hz - 10 kHz.

2.3.2 *Dielectric constant and Polarization*

As depicted on Figure 2-8 (Left), when an electric field E_0 is applied to an insulating sample, the charge at the surface (± Q) induces charges producing their own depolarizing field E_1 in the opposite direction: the dielectric material responds with a shift in charge distribution, with the positive charges aligning with the electric field and the negative charges aligning against it. The macroscopic electric field E has the following expression:

$$(Equation\ 8)\ E = E_0 + (-E_1)$$

Here E_1 is opposite to the direction of E_0.

In the case of a thin sample, when the field is applied perpendicular to the surface, the charge distribution can be schematized as a planar capacitor. A parameter to represent the dielectric property is dielectric permittivity ε' which is calculated using the relationship with the capacitance C:

$$(Equation\ 9)\ C = \varepsilon' \varepsilon_0 \frac{S}{d}$$

where ε_0 is permittivity in vacuum, S is electrode area, and d is the distance between electrodes. Overall polarization in dielectric material can be decomposed into three main components; electronic polarization (small displacement of electron cloud while the nucleus moves), ionic polarization (relative displacement of cation and anion) and dipolar polarization (permanent dipoles ferro-like aligned).

The frequency response of the dielectric constant depends on the nature of the charge carriers. Because of the inertia of the molecules and ions, the dipole and ionic contribution are low at high frequencies (Figure 2-8 (Right)), thus we measured at low frequencies (f =5 kHz – 100 kHz) in this work.(*106*, *107*)

Dielectric measurements were carried out with an Agilent 4284 LCR meter by using a home-made sample holder set in the PPMS. It measures the capacitance C and loss tanδ. A platelet of 2 x 2 x 0.5mm was cut from the bars. Silver paste electrodes were

deposited on the largest (2 x 2 mm) parallel surfaces. The capacitance versus temperature was measured between 8 and 300K at different frequencies (f =5 kHz – 100 kHz) at an excitation voltage amplitude of 1 V both on warming and cooling. $C(H)$ curves were registered by varying H between $\mu_0 H$ = 0 and 14 T. Obtained C was converted to ε' using (Equation 9).

Polarization measurements were performed using the same sample set as the dielectric measurement with a Keithley 6517A electrometer, providing an automatic pyroelectric current integration to access the polarization (P). A poling electrical field E_0 of 25 – 400 kV was used upon cooling from a specific temperature and the measurement was performed upon warming.

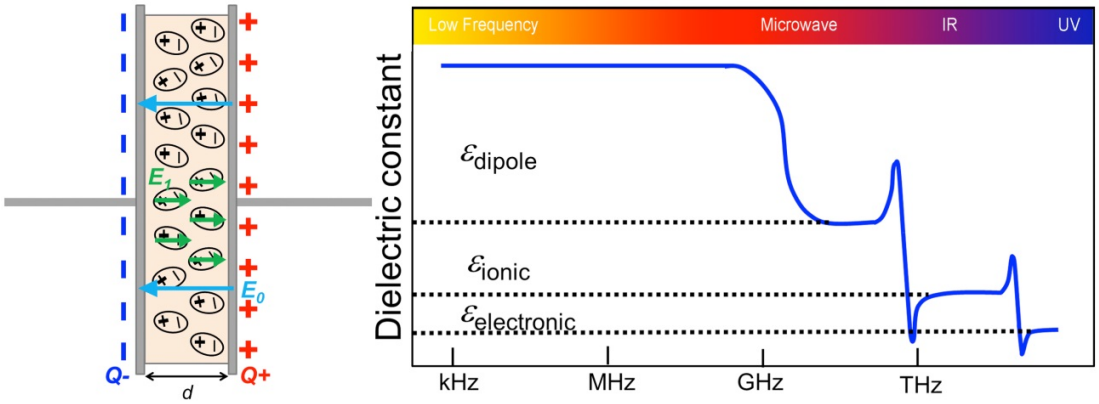


Figure 2-8 (Left) Induced charge on a dielectric placed between the plates of a charged capacitor. (Right) Dependence of the relative dielectric constant on frequency. Contributions of the dipoles, ions and electrons in the total polarization are determined. (107)

2.3.3 *Heat capacity measurement*

The heat capacity (Cp) measurements were carried out by means of the experimental set-up developed by Quantum Design for the PPMS by Dr. Vincent Hardy (CRISMAT). This set-up uses a semi-adiabatic relaxation technique, coupled with a two-τ analysis. Each measurement relies on a temperature pulse (of magnitude ΔT_{pulse}) caused by a transient heating power applied to the platform hosting the sample. The platform temperature is recorded versus time along both stages of the process (heating branch with power on, and cooling branch when the power is shut down); the heat capacity is derived from the analysis of this thermal response. The addenda

corresponding to a thin layer of Apiezon N grease put onto the platform was recorded prior to the sample measurements The used sample had the shape of a thin parallelepiped (16 mg) with a flat bottom face allowing to ensure a good thermal contact to the platform (via the grease).

Two measuring methods were used. In the standard method (hereafter referred to as the QD method), the heat capacity is derived from a global fitting of both the heating and cooling branches. We also used a method developed in the lab that was described in Ref (*108*). It consists of a point-by-point (i.e. time resolved) analysis of each branch of the pulse (within a 1-τ approximation). It is hereafter referred to as the PBP method. Contrary to the QD method, the PBP approach allows to investigate the first-order transitions. If the associated hysteresis remains moderate, it can be directly observed from the independent analysis of the heating and cooling branches. In case of a too wide hysteresis, only the heating branch can be analyzed. An additional advantage of the PBP method is the possibility to reach high resolution in temperature. For the QD method, we used a data spacing of 0.5 K with ΔT_{pulse} = T/100. For the PBP technique, 50 heat pulses were recorded in the range 15-65 K (i.e. starting temperatures spaced by 1 K); we used ΔT_{pulse} = 6 K and kept only for the analysis the central part of each pulse to yield *Cp*(T) segments over ≅ 2 K with a resolution of ≅ 0.05 K; doing so allows to cover the whole T range with an overlapping of ≅ 1 K between successive *Cp*(T) segments. To avoid any history effect, each of these pulses was preceded by a warming up to 100 K followed by a cooling down to 15 K.

Chapter 3. Study of inverse trirutile Mn_2TeO_6

In this chapter, we report the results of investigations in the (Mn,Te,O) system to obtain high-quality inverse trirutile Mn_2TeO_6 samples and their characterizations as a function of temperature.

XRPD and TGA-DTA are used to optimize the synthesis conditions and to follow the different steps in the formation of the inverse trirutile structure. Some samples were then selected for in-depth investigations. Complementary experiments using neutron, synchrotron X-ray and electron diffraction were used to determine crystal and magnetic structures through symmetry analysis and Rietveld refinements. Some samples were also studied by EDX and XANES. Magnetic and dielectric behaviors were characterized using SQUID and PPMS.

3.1 *Synthesis and Structural Characterization above RT*

3.1.1 *Previous results from the literature about Mn_2TeO_6*

In 1971, a single phase was first synthesized by Hund (*53*) starting from manganese sulfate and telluric acid and its crystal structure was reported as an inverse trirutile structure with a tetragonal unit cell. In 1979, Mn_2TeO_6 was reinvestigated by Fruchart et al. (*7*) who used another synthesis process (starting from manganese oxalate and telluric acid) and mentioned two possible structural models at RT: tetragonal and monoclinic. The first one is stable when the sample is prepared in air, while a small

monoclinic distortion appears when it is sintered under low oxygen pressure. The reported synthesis conditions and cell parameters of the obtained phases are summarized in Table 3-1.

Reported by	Synthesis temperature	Synthesis atmosphere	*a* (Å)	*c* (Å)	*β* (°)
Hund (*53*)	600°C	Air	4.608(1)	9.114 (1)	90
Fruchart (*7*)	627°C	Air	4.613	9.082	90
Fruchart (*7*)	727°C	Slight O_2 pressure	4.591	9.125	90.30
Fruchart (*7*)	527°C	40 kb pressure	4.595	9.108	90.51

Table 3-1 Synthesis conditions and cell parameters of Mn_2TeO_6 at RT

The lack of clear description of the monoclinic phase motivated us to revisit this system. Based on these previous reports, we first started with the optimization of the synthesis conditions to obtain single phase and well crystallized Mn_2TeO_6 polycrystalline samples, combining XRPD, TGA-DTA and SEM analyses. It was challenging as the temperature must not exceed 730°C -to avoid Te-losses- a temperature which is a little bit low for the solid state synthesis method.

3.1.2 *Determination of synthesis conditions*

The solid state syntheses were performed in air using manganese oxalate and telluric acid as precursors as previously reported (*7*) and described in Section 2.1. The synthesis temperature was progressively increased so as to obtain a single phase and a good crystallinity. However, above 650°C heat treatments in air lead to the decomposition of Mn_2TeO_6. This thermal behavior was checked by TGA-DTA performed, starting from a mixture of precursors ($MnC_2O_4{\cdot}2H_2O$ + H_6TeO_6), up to 750°C in air, as shown in Figure 3-1a, b.

The TGA curve (Figure 3-1a) shows that the weight starts to decrease around 120°C. This first step corresponds to dehydration in agreement with the DTA curve (Figure 3-1b). It shows two large endothermic peaks in this temperature range; the first peak at ≅ 145°C corresponds to dehydration of 2[$MnC_2O_4{\cdot}2H_2O$] with 9.3 % weight loss (Δm)

(*109*), the second peak at ≅ 160°C corresponds to dehydration of H_6TeO_6 with Δm = 6.7 % (*110*). The total Δm at this stage is about 19 % (at 205°C). Subsequently, decarbonation occurs until 350°C with 23 % of weight loss. The weight decreases then slightly by 1.2 % until 465°C; then a small exothermic peak is observed at 480°C. Afterwards, the weight increases slightly, corresponding to Δm = 1.5 % until 670°C (in agreement with a small and smooth endothermic-like DTA curve). Above 670°C, the weight decrease of 3.6 % and the associated endothermic peak are attributed to a loss of Te and the formation of $Mn_{2.5}TeO_6$, as confirmed by XRPD of the powder recovered after the TGA-DTA experiment.

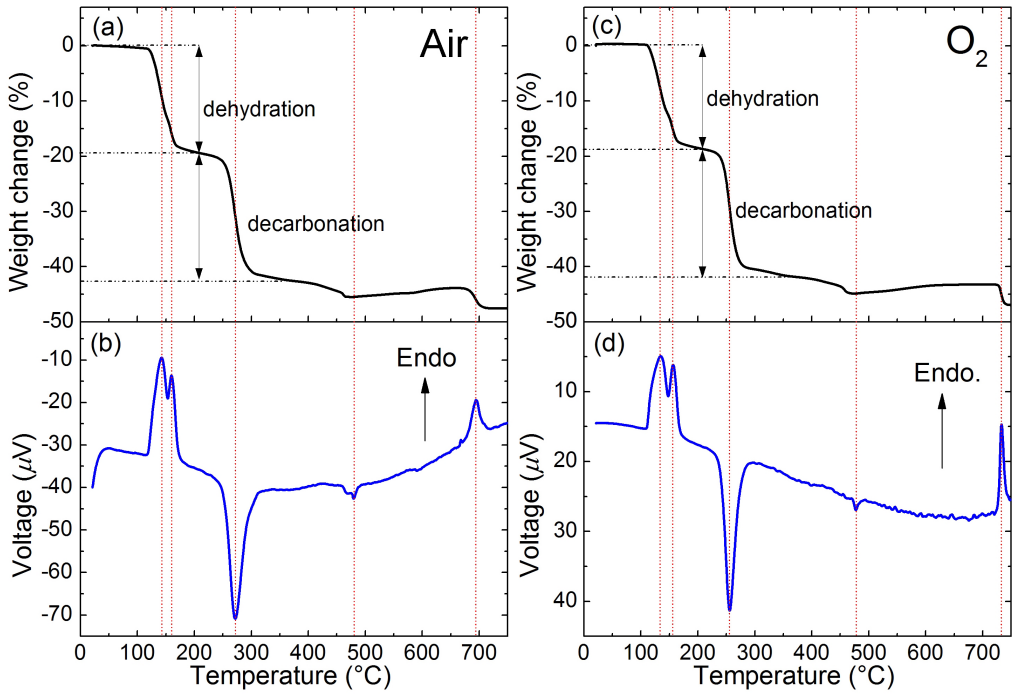


Figure 3-1 Thermogravimetric and differential thermal analysis data in air (TGA(a)-DTA(b)) and in O2 (TGA(c)-DTA(d)) starting from ($MnC_2O_4{\cdot}2H_2O$ + H_6TeO_6) from RT to 750°C. The weight changes corresponding to dehydration and decarbonation are indicated by the black arrows on the TGA curve. Red dot vertical lines corresponding to the DTA peaks are guides to the eyes.

TGA-DTA under O_2 flow (Figure 3-1c, d) exhibits very similar tendency to the results in air until 500°C. Above 500°C, the weight increases slightly (Δm =1.7 %) until 650°C and a plateau is observed up to 720°C. Afterwards, a 3.0 % of weight decrease associated with a sharp endothermic peak corresponds to the decomposition into

$Mn_{2.5}TeO_6$. The decomposition temperature under O_2 flow (720°C) is significantly higher than in air (670°C), in agreement with the previous report of Fruchart et al. (*7*). Therefore, O_2 flow is necessary to reach higher synthesis temperature to obtain a well-crystallized single phase sample of Mn_2TeO_6.

In order to check the phase formation process of inverse trirutile Mn_2TeO_6, the in-situ XRPD measurements were carried out at the laboratory diffractometer. Figure 3-2 is illustrated the in-situ XRPD of the Mn_2TeO_6 synthesis, starting from $2MnC_2O_4{\cdot}2H_2O$ + H_6TeO_6 precursors calcined at 300°C in order to avoid dehydration and decarbonation in the diffractometer (see also Chapter 2), performed under O_2 (similar results were obtained in air, in agreement with the TGA-DTA results of Figure 3-1). The corresponding diagram, shown in Figure 3-3, is only a draft for giving tracks about the synthesis route. These XRPD patterns only allow the identification of the crystallized phases in an amorphous matrix as it is the case for the lower temperature. More often Bragg peaks are broad, in addition in-situ experiments do not lead to a powder statistic and kinetic probably has a strong effect.

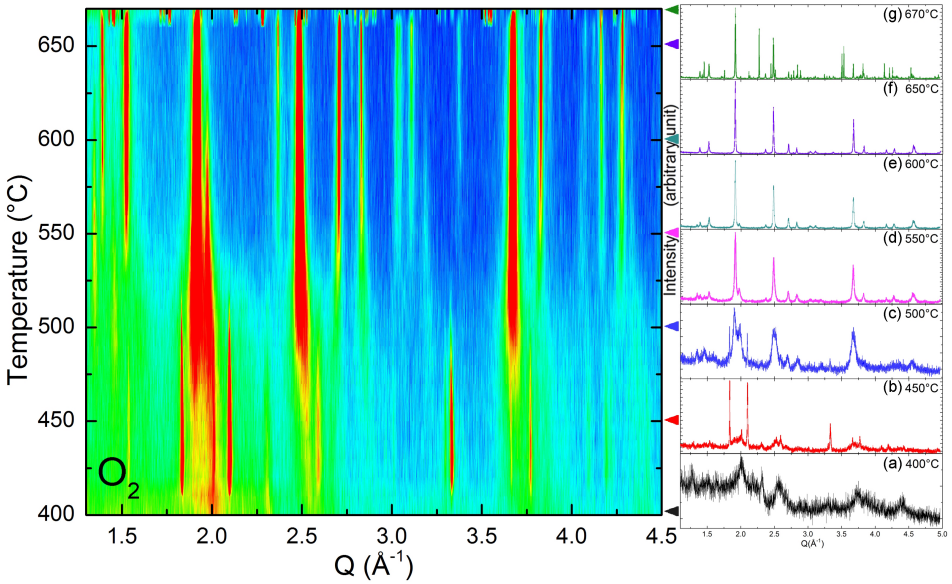


Figure 3-2 In-situ XRPD patterns of the Mn, Te, O system as a function of temperature in O_2, from 400 to 670°C. Selected diffraction patterns are presented on the right side.

The first XRPD pattern recorded at 300°C (not shown in Figure 3-2) shows a poorly crystallized multiphasic state, containing at least Mn_5O_8 (SG: *C*2/*m* with *a* = 10.3 Å, *b*

= 5.72 Å, c = 4.85 Å and β = 109° (*111*)), and Mn_2O_3 (SG: *Ia*-3 with a = 9.43 Å (*112*)). No significant change is observed up to 350°C. Above 400°C (Figure 3-2a), a new phase appears, which can be indexed in a trigonal Na_2SiF_6-type structure (SG: *P*321 with a = 8.9 Å, c = 4.7 Å, γ = 120°). This is the same structure as reported for the A_2TeO_6 series with A = Sc (*26*), Tl (*3*), In (*25*), mentioned in Chapter 1. Above 440°C (Figure 3-2b), the Bragg peaks corresponding to the expected "inverse trirutile" structure start to appear; at this stage, only three large Bragg peaks are observed, so that it is not possible to distinguish between an ordered inverse trirutile and a disordered rutile diffraction pattern.

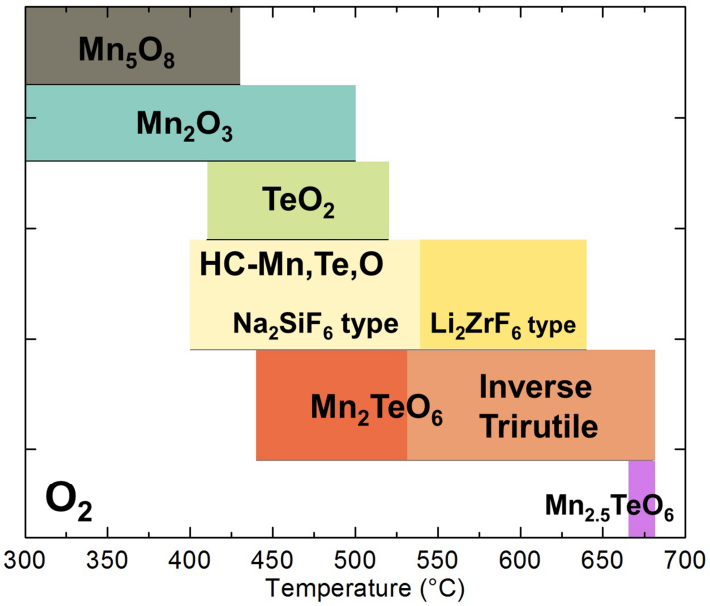


Figure 3-3 Phases involved during the synthesis of the inverse trirutile (versus temperature), extracted from the in-situ XRPD patterns presented in Figure 3-2, the reported temperature range for each phase is only approximate.

Above 420°C (Figure 3-2b), several well defined peaks corresponding to TeO_2 (SG: $P4_12_12$ with a = 4.81 Å, c = 7.62 Å (*113*)) are observed up to 510°C. Both "inverse trirutile" and Na_2SiF_6-type structures progressively form between 470°C and 520°C. The "inverse trirutile" phase clearly crystallises above 530°C (Figure 3-2c, d) and can be easily indexed as tetragonal inverse trirutile Mn_2TeO_6 (SG: $P4_2/mnm$ with a = 4.6 Å, c = 9.06 Å). Simultaneously, at 540°C (Figure 3-2d, e), the peaks characteristic of the Na_2SiF_6-type structure disappear, and the observed Bragg peaks could be indexed with

the inverse trirutile Mn_2TeO_6 structure and one of the trigonal Li_2ZrF_6-type structures (e.g. SG: *P*-31*m*, *a* = 5.0 Å, *c* = 4.6 Å, γ= 120° & Chapter 1). Up to 640°C (Figure 3-2d, e), Bragg peaks corresponding to the inverse trirutile become sharper and larger, while the ones of the Li_2ZrF_6-type structure progressively disappear. This suggests a transformation from the Li_2ZrF_6-type structure to the inverse trirutile Mn_2TeO_6. Single phase inverse trirutile Mn_2TeO_6 is observed above 650°C (Figure 3-2f), before decomposition into $Mn_{2.5}TeO_6$ above 670°C (Figure 3-2g).

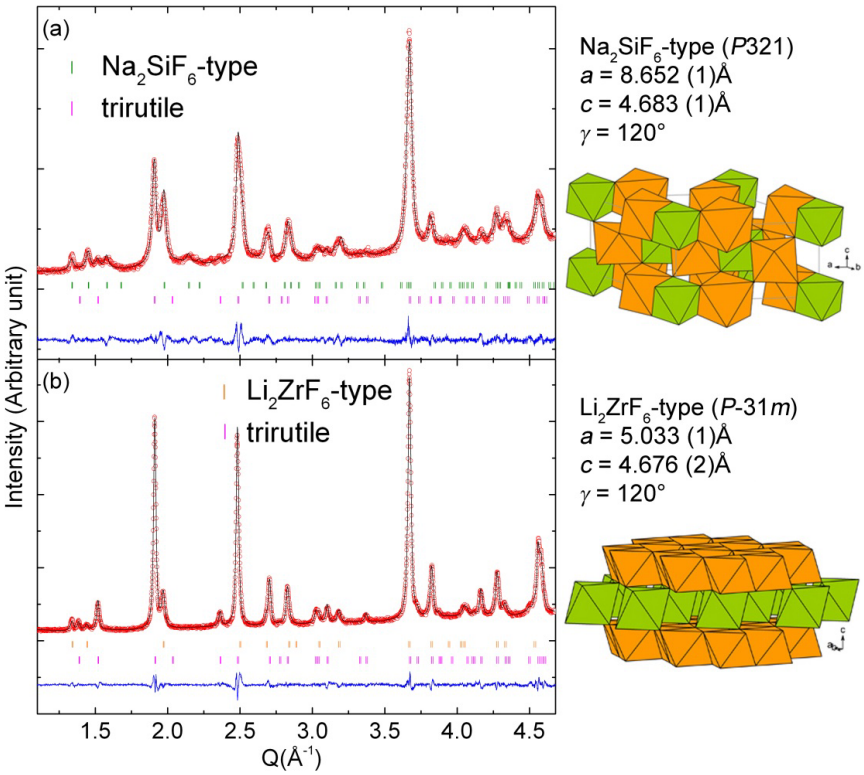


Figure 3-4 Le Bail fits of XRPD patterns recorded during in-situ synthesis of Mn_2TeO_6, at 510°C (a) and 550°C (b) in air, showing the coexistence of tetragonal inverse trirutile Mn_2TeO_6 with (a) the Na_2SiF_6-type structure and (b) the Li_2ZrF_6-type structure. Corresponding cell parameters and crystal structures are summarized on the right side.

The Le Bail fits of the XRPD patterns recorded at 510°C and 550°C (in air), corresponding to the coexistence of inverse trirutile Mn_2TeO_6 with, respectively, the Na_2SiF_6-type phase and the Li_2ZrF_6-type phase, are shown in Figure 3-2. As can be seen in Figure 3-2a, the diffraction pattern of the Na_2SiF_6-type phase shows rather poor crystallinity at 510°C, with broad Bragg peaks and a large background, so that the

existence of this Na_2SiF_6-type structure is actually questionable. On the other hand, the Li_2ZrF_6-type phase is clearly identifiable at 550°C on Figure 3-2b. More details about these two new phases will be given in Chapter 5.

In conclusion, the inverse trirutile Mn_2TeO_6 synthesis temperature must be chosen carefully in order to avoid both low temperature intermediate phase and high temperature decomposed phase. In the following, for all samples, the last synthesis step was between at 600 to a maximal temperature of 710°C in O_2 flow to avoid these impurities.

The effect of the synthesis temperature on the morphology of the samples was followed by SEM images taken on a batch of bars, heated at different temperatures (between 600 and 700°C) and durations of the plateau (up to 2 weeks).

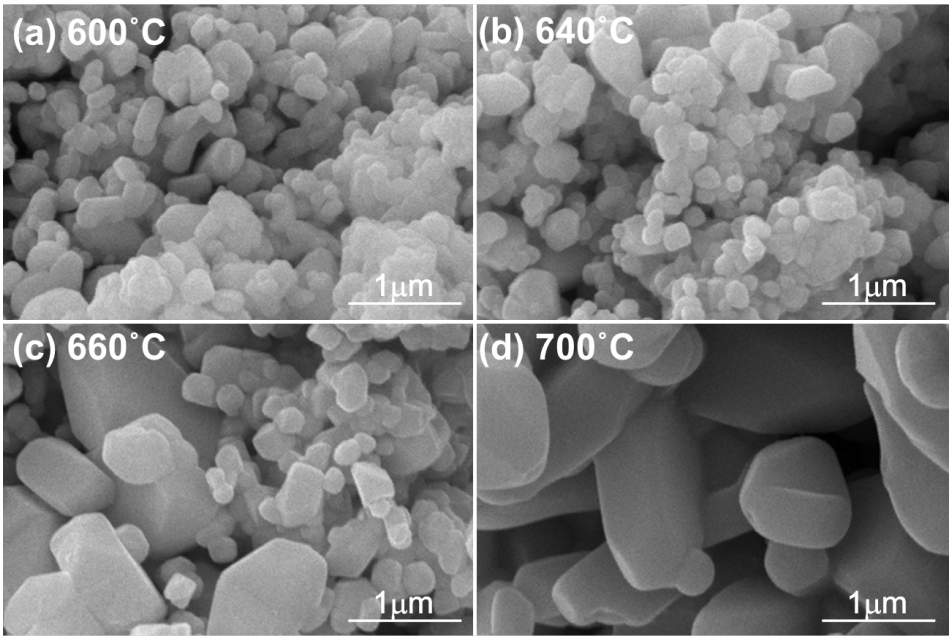


Figure 3-5 SEM micrographs of Mn_2TeO_6 at different steps of the synthesis process.

The bars (made from a mixture of precursors calcined at 600°C for 12h in air) were introduced in the furnace all at once and were heated at 600°C for 24 h under O_2 flow. The temperature was decreased to take out a bar from the furnace and the temperature was then increased to a higher value. For each temperature step, one bar was taken out of the furnace for SEM observations. Comparing samples sintered at 600°C (Figure 3-

5a) and at 640°C (Figure 3-5b), no significant change is observed in the shape and size of grains; in contrast, samples heated above 660°C (Figure 3-5c, d) show larger grains.

At this point, it is clear that the preparation of Mn_2TeO_6 is rather difficult, due to the necessity to keep a rather low synthesis temperature for solid-state reaction. Consequently several ways were followed simultaneously to progress: (i) A careful systematic analysis (combining structural and magnetic characterizations) was performed on samples prepared in air and/or O_2, varying the temperature and the duration of the plateau at the synthesis temperature; this part of the work is reported in the next part of this chapter (Section 3.1.3). (ii) In-situ and ex-situ measurements, by XRPD and TGA-TDA, were combined to follow the synthesis from the early steps, i.e., from RT to 750°C and then down to RT; this study allowed us to evidence intermediate phases that we tried then to stabilize as "pure" compounds. To reach this goal, it was necessary (iii) to use new precursors that were prepared by the spray-dry method. This last part is reported later in Chapter 5.

3.1.3 *Preliminary Structural Study*

From the series of samples prepared varying the synthesis conditions, starting from $MnC_2O_4 \cdot 2H_2O$ and H_6TeO_6 as explained before, three types of Mn_2TeO_6 samples were selected for a more detailed study, labeled S1 to S3 (Table 3-2).

Label	Temperature	Duration	Atmosphere
S1	600°C	24h	Air
S2	700°C	24h	O_2
S3	710°C	One week	O_2

Table 3-2 Synthesis conditions of the 3 Mn_2TeO_6 samples (S1-S3) characterized in this study.

The samples were characterized by laboratory XRPD at RT for quality check, the patterns are characteristic of the inverse trirutile Mn_2TeO_6. The main Bragg peaks may be indexed using the reported monoclinic cell parameters (See Table 3-1). However, many peaks remain non indexed, none of them belonging to any reported Mn or Te-

based oxides. The main difference between the three XRPD patterns is the width of the Bragg peaks. This is highlighted in Figure 3-6 with the comparison of the RT diffraction patterns using a synchrotron beamline (SXRPD performed on BL04, ALBA).

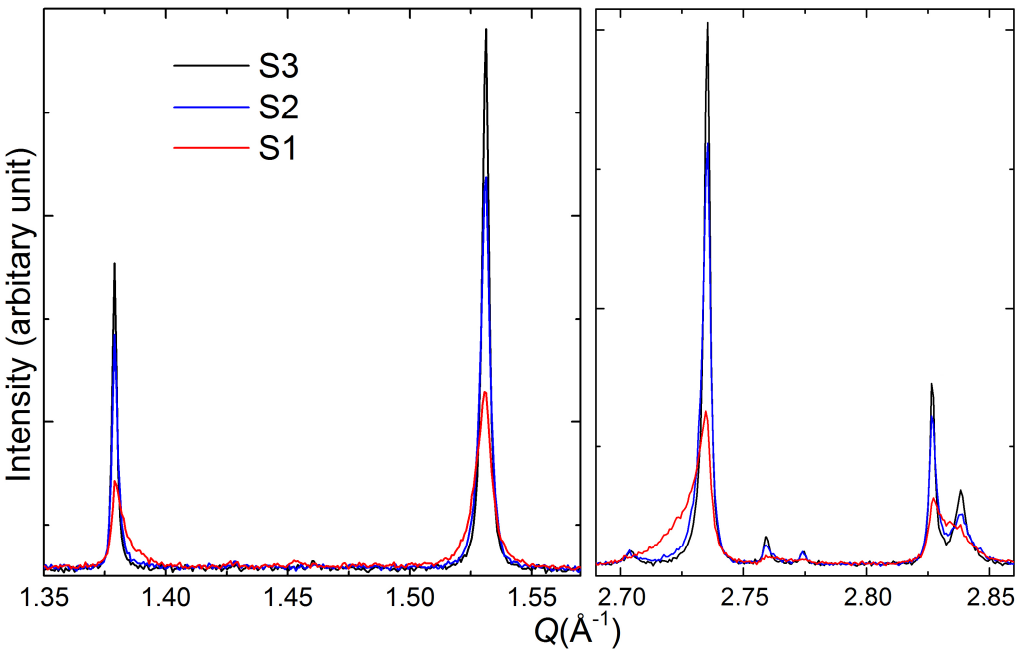


Figure 3-6 SXRPD patterns (in selected Q-ranges) of the three Mn_2TeO_6 samples

Asymmetric broadening is particularly strong for the S1 pattern. Playing again with the preparation conditions, it appears that this broadening is rather difficult to control, it may be reduced but it always persists. This asymmetry induces intensity on the low or high angle side of the peaks depending on their Q position (see Bragg peaks $Q \cong 1.37$ and $\cong 2.72$ in Figure 3-6). The corresponding sample microstructures observed by SEM are illustrated in Figure 3-7; the size of the grains increases from S1 to S2 and then to S3. This size effect above does not explain the observed broadening on XRPD patterns. To better understand the evolution from S1 to S3, a crystal structure study of Mn_2TeO_6 was performed using laboratory X-ray diffraction versus temperature (>RT).

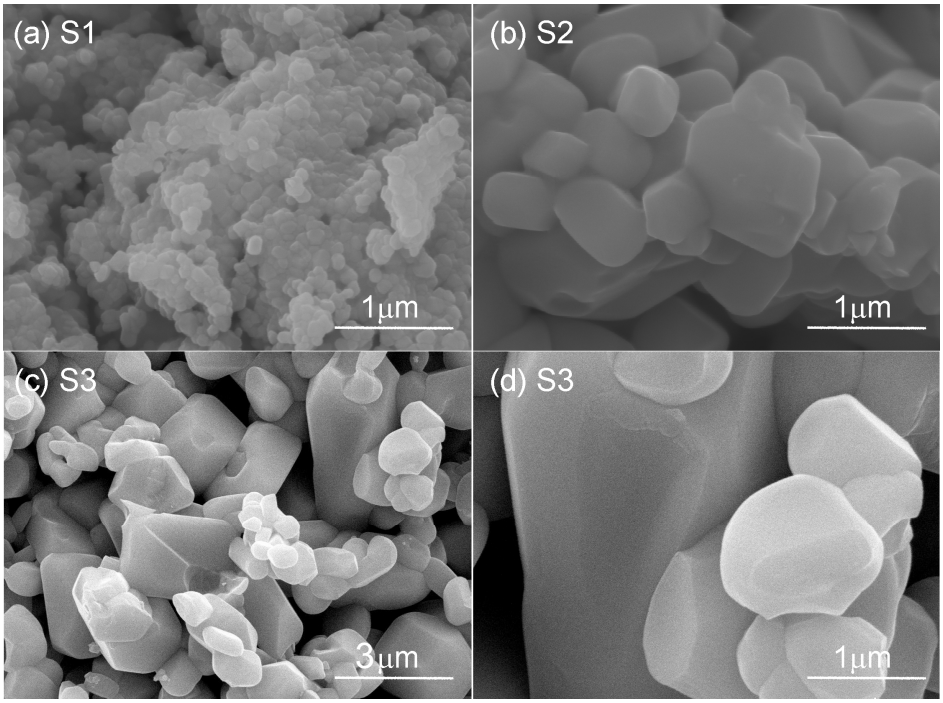


Figure 3-7 SEM micrographs of the three Mn_2TeO_6 samples (a) S1, (b) S2 and (c, d) S3

3.1.4 *XRPD vs. T*

The temperature dependence of the XRPD was carried out, from 640 to 25°C in O_2, using the S2 powder, on a D8 diffractometer (see Section 2.2). At 640°C, the pattern can be indexed using a tetragonal unit cell: $P4_2/mnm$ with a = 4.6390 (1) Å, c = 9.0685 (1) Å, in agreement with those previously reported (Table 3-1). This SG and cell parameters also correspond to the well-known inverse trirutile compounds described for Cr_2TeO_6 and Fe_2TeO_6 (*14*, *114*).

The structure, shown in Figure 3-8, can be regarded as a supercell of the rutile one with a tripling of the *c*-parameter, resulting from the 2:1 ordering of Mn and Te species. Both Mn^{3+} and Te^{6+} cations are in an octahedral environment, the octahedra sharing edges along *c* and corners in the *ab*-plane. The structure was thus refined using the Rietveld method (Figure 3-9). The diffractograms recorded between 640 and 450°C can be indexed in this tetragonal structure, which will be referred to as high temperature tetragonal (HTT) in the following. Below 400°C, and down to RT, a splitting of a few Bragg peaks is observed, in addition to the appearance of several small peaks, signature of a phase transition.

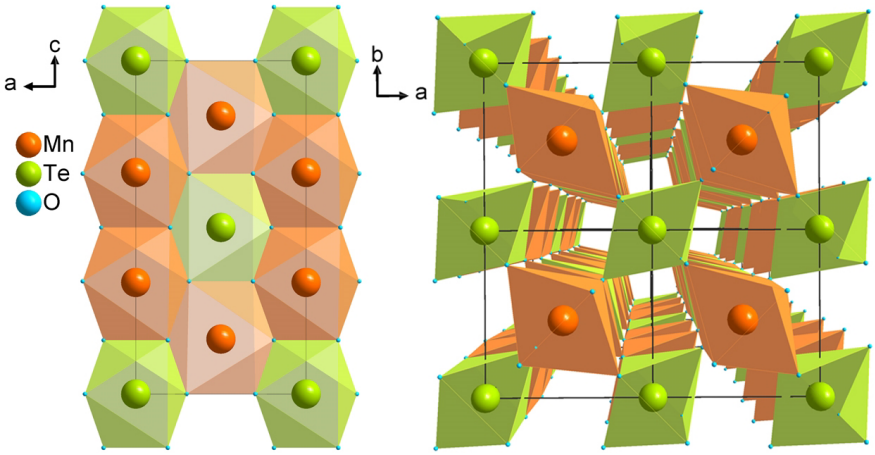


Figure 3-8 Crystal structure of the tetragonal ($P4_2/mnm$) inverse trirutile Mn_2TeO_6 projected (left) along [010] and (right) along [001].

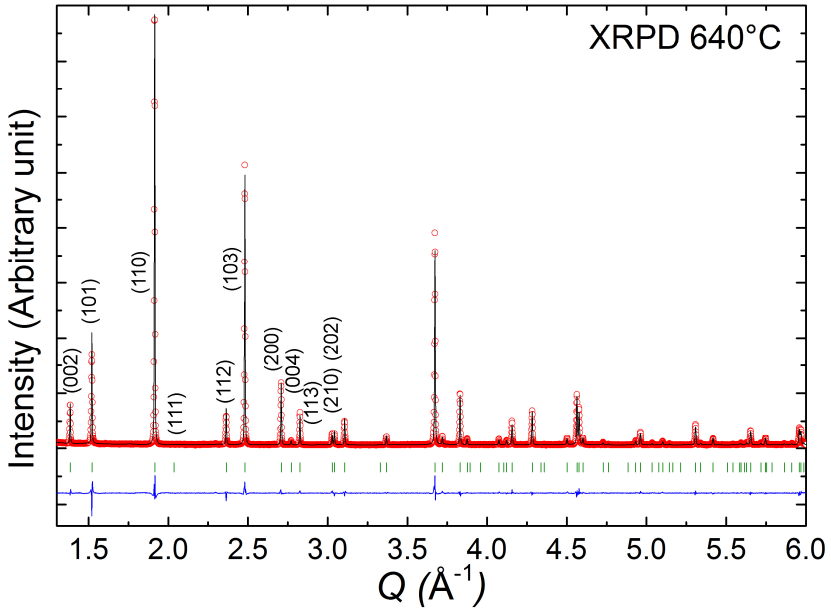


Figure 3-9 Rietveld refinement of the Mn_2TeO_6 structure from XRPD data recorded at 640°C using $P4_2/mnm$: experimental data (open red circles); calculated pattern (black line); allowed Bragg reflections (green vertical marks). The difference between the experimental and calculated profiles is displayed at the bottom of the graph as a blue line. In following sections, unless otherwise mentioned, Rietveld refinements of powder diffraction patterns will be described in this manner.

To go further in the understanding of this phase transition around 400°C, high resolution NPD was carried out. This experiment was motivated by two goals; to determine the RT structure including the oxygen positions and also to know the Mn and Te distribution on the cationic lattice (thanks to the strongest Mn/Te contrast compared with X-ray).

3.1.5 *NPD vs. T*

This experiment (performed on WISH, ISIS) differs slightly from the previous X-ray one as the S1 sample, instead of S2 was used. The S1 powder sample was loaded into a quartz tube, in which O_2 was flowing, and put in the neutron beam. The temperature was varied from RT to 700°C and then back to RT, which corresponds to a transformation of S1 into S2 (Table 3-2). The recorded patterns show clearly that the transformation induced by this thermal cycling is not reversible: the patterns recorded at RT for the sample at the beginning (S1) and at the end of the experiment (S2) are different, as expected from the SXRPD results of Figure 3-6. The evolution of the patterns is presented in Figure 3-10. In agreement with the XRPD, at the highest temperature (700°C), the diffractograms are well fitted using $P4_2/mnm$ (i.e., HTT) with a = 4.6421 (1) Å, c = 9.0750 (2) Å, as shown in Figure 3-11. The corresponding crystallographic parameters and agreement factors are summarized in Table 3-3.

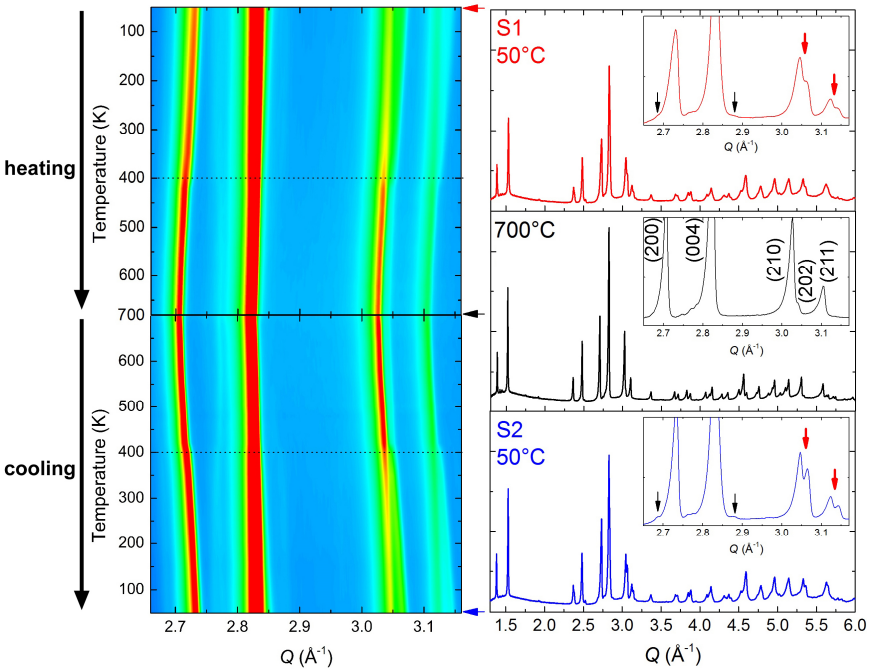


Figure 3-10 (left) Temperature evolution of the NPD patterns of Mn_2TeO_6, in the 2.65–3.17 $Å^{-1}$ selected Q range (from 50 to 700°C and then back to 50°C). The horizontal black dotted lines indicate the structural transition at 400°C during both the heating and cooling processes. (right) NPD data of Mn_2TeO_6 at 700 and 50°C (S1 and S2). The insets indicate additional small peaks (thin black arrows) and the splitting of peaks (thick red arrows) in the 50°C patterns. Indexation given in the 700°C pattern is based on the tetragonal unit cell.

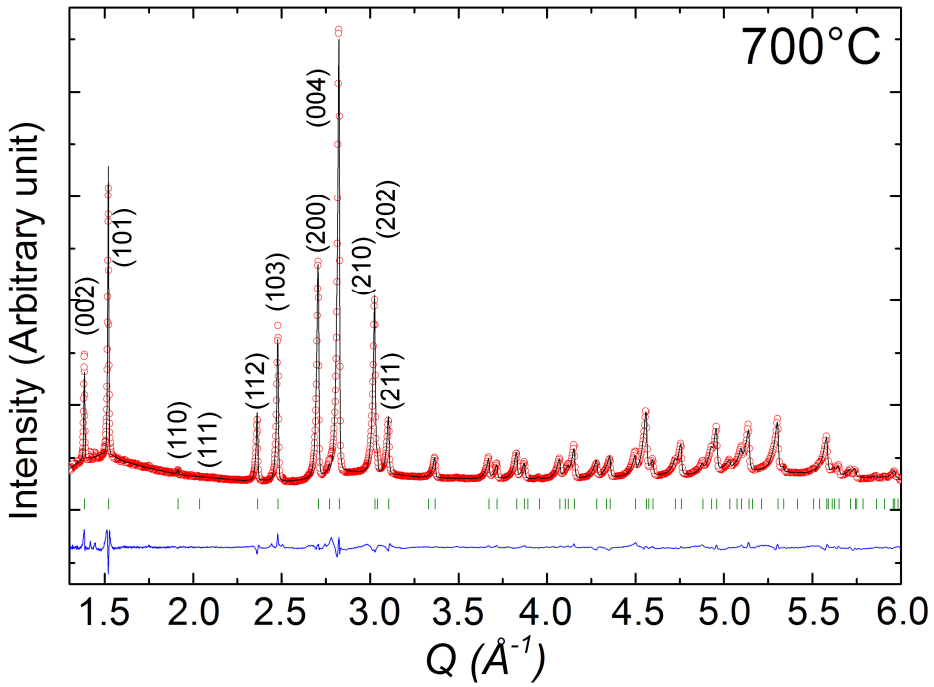


Figure 3-11 NPD pattern of Mn_2TeO_6 at 700°C, Rietveld refinement performed in $P4_2/mnm$.

Crystallographic parameters		Selected inter-atomic distances (Å)	
a_{HTT} (Å)	4.6421 (1)	Mn-O_I (x 2)	2.000 (2)
c_{HTT} (Å)	9.0750 (2)	Mn-O_{II} (x 2)*	2.045 (1)
z_{Mn}	0.3350 (3)	Mn-O_{II} (x 2)	2.003 (3)
x_{OI}	0.2981 (3)	<*d*> (Mn-O)	2.016(2)
x_{OII}	0.3115 (2)	Δ (MnO_6) (x10^{-4})	1.0
z_{OII}	0.3385 (2)	Te-O_I (x 2)*	1.957 (1)
B_{Mn} (Å^2)	3.00 (7)	Te-O_{II} (x 4)	1.918 (2)
B_{Te} (Å^2)	3.43 (7)	<*d*> (Te-O)	1.932(2)
B_{OI} (Å^2)	3.03 (7)	Δ (TeO_6) (x10^{-4})	0.9
B_{OII} (Å^2)	1.56 (11)		
χ^2	3.21	Mn-Mn	3.001 (2)
R_{Bragg} (%)	3.07	Mn-Te	3.034 (1)

Te atoms are in the Wyckoff position (WP) (*2a*: 000), Mn in (*4e*: 00*z*), O_I in (*4f*: *xx*0), and O_{II} in (*8j*: *xxz*). The refined *x* and *z* parameters and isotropic thermal factors (*B*) are given for the different ions. The distortion parameter Δ is calculated for each octahedron as $\Delta = (1/6)\sum_{n=1,6}\{(d_n - \langle d\rangle)/\langle d\rangle\}^2$, with $\langle d\rangle$ being the average cation-oxygen distance. *Corresponding to the longest apical distance in each octahedron.

Table 3-3 Crystallographic parameters and corresponding interatomic distances in Mn_2TeO_6 ($P4_2/mnm$) at 700°C, from Rietveld refinement of NPD data.

The diffraction patterns recorded between 700 and 420°C can be indexed in HTT, and below 400°C, the phase transition is confirmed, with the splitting of several peaks and additional small peaks (red and black arrows, respectively in the insets of Figure 3-10 (Right)). This transition is observed at the same temperature in both heating and cooling modes within the experimental resolution.

The determination of the RT structure was then performed, taking into account the observed peak splitting and additional small extra peaks on XRPD and NPD patterns and the crystallographic rules to lower the symmetry (from tetragonal to orthorhombic or monoclinic). X-ray synchrotron data (S2) were also used, especially to minimize the peak overlapping and to be able to take into account the small extra peaks in the Rietveld refinements. In addition, electron diffraction was also performed to obtain information at the local scale, and we will first report on these observations.

3.1.6 *Precession electron diffraction tomography*

PEDT were carried out on both S1 and S2 samples. The reconstructed patterns (Figure 3-12) confirm the existence of extra reflections (pointed by green arrows) compared to the HTT form (red dot lines). The new cell can be indexed with the following parameters $a = c_{HTT} \cong 9.1$ Å, $b = 2\sqrt{2} \times a_{HTT} \cong 13.0$ Å and $c = \sqrt{2} \times a_{HTT} \cong 6.5$ Å.
The diffracted dots observed on Figure 3-12b correspond to the general indexation $0kl$. On this plane, the limiting condition for observing the dots is $0kl$, $k + l = 2h$, which implies that the diffracted dots such as 010, 030, 001, 021, 012… are systematically absent, whereas the ones indexed 020, 040, 011, 013, 002, 022... are systematically present. For the (010)* plane (Figure 3-12c), the diffracted dots such as 001, 003… are systematically absent in contrast to the ones indexed 002, 004… which are systematically present. For the $h1l$ plane (Figure 3-12d), there is no systematic extinction. Considering these conditions limiting the reflections: $h0l$, $l = 2n$; $0k0$, $k = 2n$; $00l$, $l = 2n$, the centrosymmetric monoclinic $P2_1/c$ could be a possibility for the RT structure of Mn_2TeO_6, which will be labeled thereafter RTM (for room-temperature monoclinic).

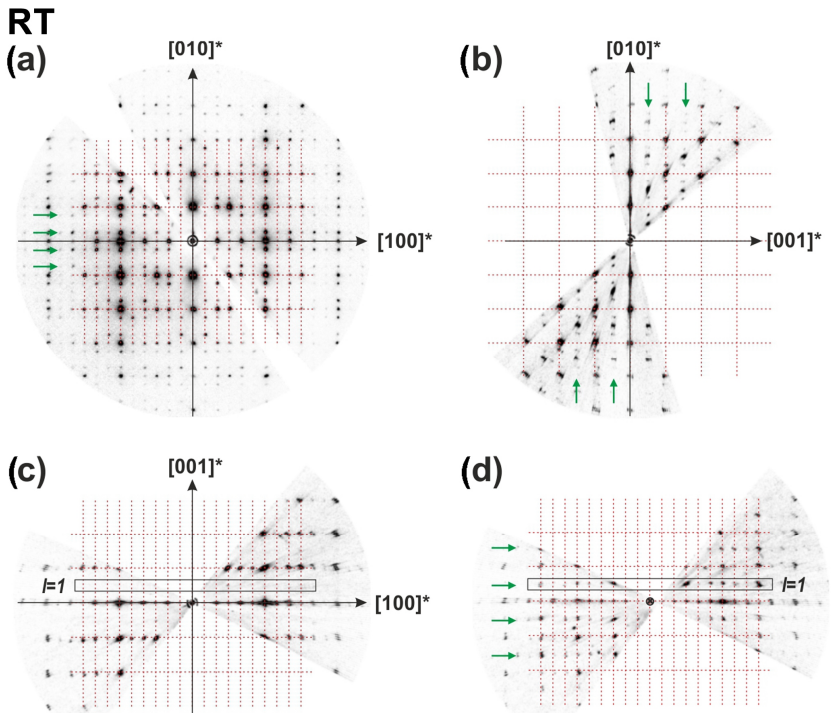


Figure 3-12 (a) [hk0], (b) [0kl], (c) [h0l], and (d) [h1l] reciprocal space sections reconstructed from the PEDT data obtained at RT on a S2 crystalline. Rows of extra reflections (green arrows) show the existence of a superstructure with respect to the HTT (highlighted by a red dashed grid). These extra reflections can be accounted for by considering lattice parameters a ≅ 9.1 Å, b ≅ 13.0 Å, and c ≅ 6.5 Å.

The unit cells of the HTT and RTM phases are depicted in Figure 3-13. c_{HTT} corresponds to a_{RTM}. a_{HTT} is transformed in b_{RTM} and c_{RTM} by taking $\sqrt{2}$ of a_{HTT}, and in addition, b_{RTM} is doubled. These cell parameter variations lead to a change in the number of atoms per unit cell $Z_{HTT} = 2$ to $Z_{RTM} = 8$; i.e., the cell volume V_{RTM} is four times bigger than V_{HTT}.

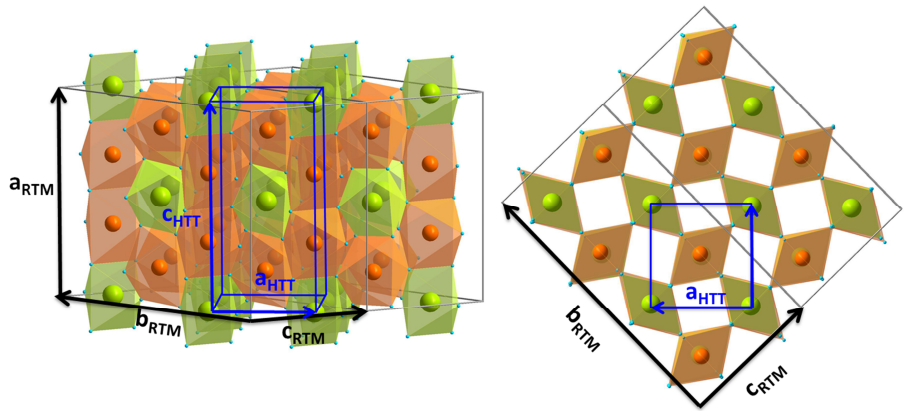


Figure 3-13 Comparison between the HTT (blue) and RTM (black) unit cells of Mn_2TeO_6.

3.1.7 *Structure refinement using SXRPD data and AMPLIMODES*

The RT-SXRPD pattern of Mn_2TeO_6 is shown in Figure 3-14. The peaks due to the cell doubling along *b* are identifiable, as illustrated in the inset of Figure 3-14. As explained before, on the basis of the PEDT study, it is necessary to build a large cell of monoclinic symmetry ($P2_1/c$ with $a \cong 9.1$ Å, $b \cong 13.0$ Å, and $c \cong 6.5$ Å, $\beta \cong 90°$), which contains 6 cations and 12 oxygen atoms, all on general Wyckoff positions, leading to 54 (*x y z*) atomic positional parameters to be refined. The refinement of the structure using SXRPD data presents a challenge due to the small intensity of the peaks induced by the doubling of the *b*-parameter and the large number of (*x y z*) structural parameters compared with the HTT structure ($P4_2/mnm$ with $a \cong 4.6$ Å and $c \cong 9.0$ Å).

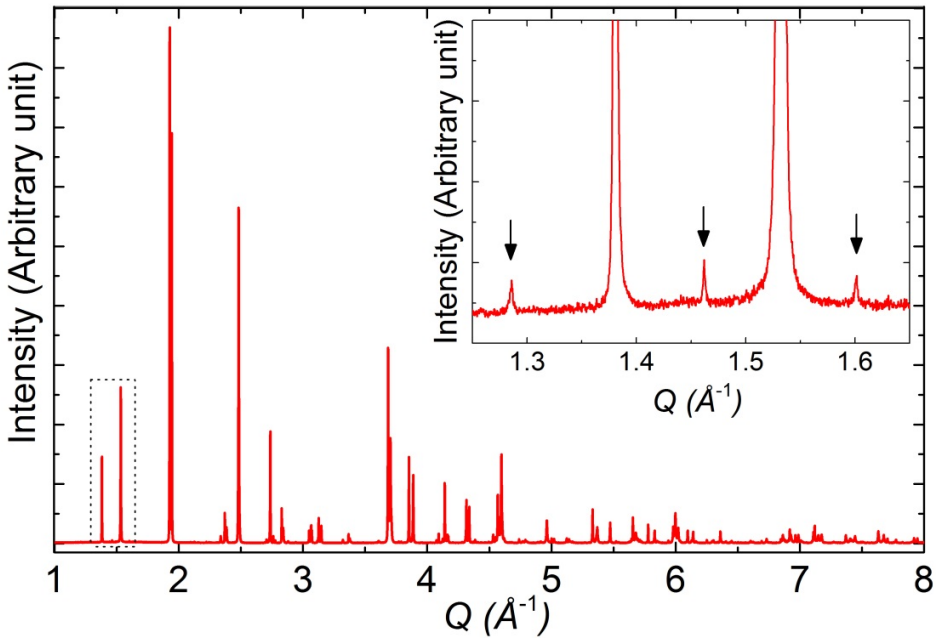


Figure 3-14 SXRPD data (CRISTAL, SOLEIL) of Mn_2TeO_6 at RT. The inset shows an enlarged view of extra peaks induced by the doubling of the b parameter (with respect to the HTT form).

As shown in Table 3-4 and Figure 3-15, there are 6 Irreps of the $P4_2/mnm$ space group in addition to the isostructural mode Γ_1^+, that can be used to achieve the $P2_1/c$ distortion: Γ_4^+, Γ_5^+, Σ_2, Σ_3, $M_1^-M_4^-$, and M_5^- . The RTM $P2_1/c$ structure of Mn_2TeO_6 can be derived therefore from a linear combination of a maximum of 7 Irreps (24 modes) of $P4_2/mnm$. The mode distribution on each atom is given in Table 3-5.

k-vector	Irrep	Direction	Isotropy Subgroup	N° of modes
(0 0 0)	Γ_1^+	(a)	$P4_2/mnm$ (n°136)	4
(0 0 0)	Γ_4^+	(a)	$Cmmm$ (n°65)	4
(0 0 0)	Γ_5^+	(a, a)	$C2/m$ (n°6)	6
(¼ ¼ 0)	Σ_2	(a, 0, 0, a)	$Pbam$ (n°55)	13
(¼ ¼ 0)	Σ_3	(a, 0, 0, -a)	$Pbcm$ (n°57)	16
(½ ½ 0)	$M_1^- M_4^-$	(a, b)	$Pban$ (n°50)	2
(½ ½ 0)	M_5^-	(a, a)	$Pmma$ (n°51)	9

Table 3-4 Summary of the mode decomposition showing the different distortion components and isotropy subgroups.

Atom	WP	Irreps (Number of modes)
O2	8*j*	$\Gamma_1^+(2)\ \Gamma_4^+(2)\ \Gamma_5^+(3)\ \Sigma_2(5)\ \Sigma_3(7)\ M_1^-M_4^-(2)\ M_5^-(3)$
O1	4*f*	$\Gamma_1^+(1)\ \Gamma_4^+(1)\ \Gamma_5^+(1)\ \Sigma_2(4)\ \Sigma_3(3)\ M_5^-(2)$
Mn	4*e*	$\Gamma_1^+(1)\ \Gamma_4^+(1)\ \Gamma_5^+(2)\ \Sigma_2(2)\ \Sigma_3(4)\ M_5^-(2)$
Te	2*a*	$\Sigma_2(2)\ \Sigma_3(2)\ M_5^-(2)$

Table 3-5 Summary of the basis modes involved in the distortion of Mn_2TeO_6, distributed per type of WP in $P4_2/mnm$. The numbers in parentheses indicate the number of modes for each Irrep.

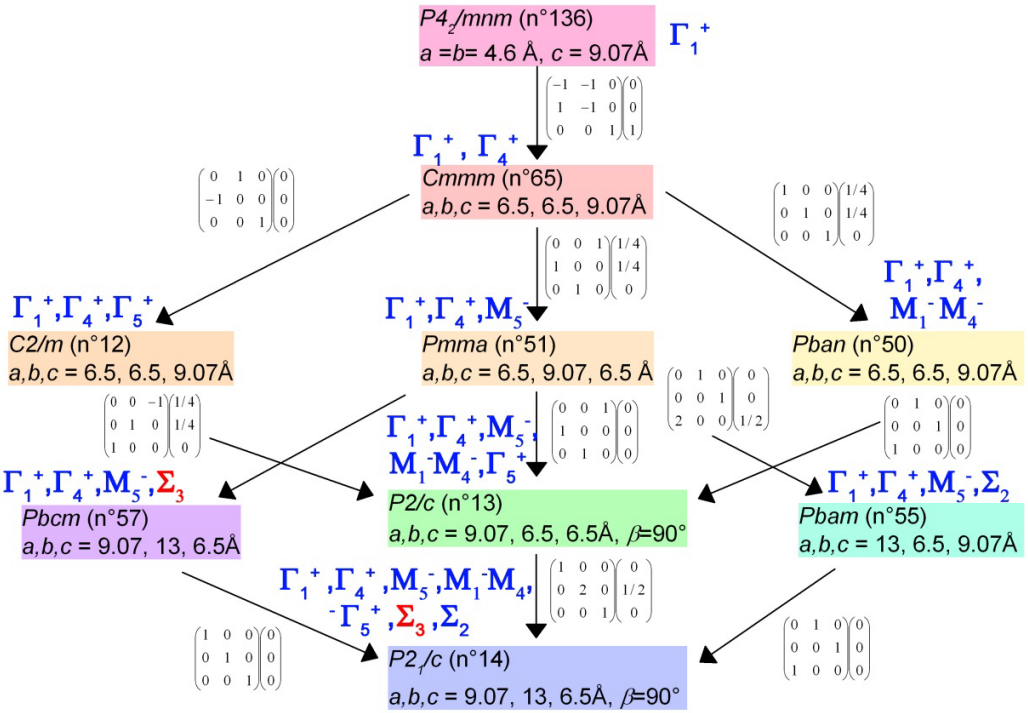


Figure 3-15 Symmetry relations for the transformation from $P4_2/mnm$ to $P2_1/c$ via five possible subgroup paths. The irrep labels (blue) indicate the active irrep components of each subgroup. Σ_3 is highlighted in red. Numbers in brackets denote SG numbers according to the international tables for crystallography. Corresponding cell parameters and transformation matrixes, which relate the coordinate system of the subgroup to that of the super-group, are also given.

Rietveld refinements based on symmetry-adapted modes (constructed with AMPLIMODES) were then undertaken. The high symmetry reference structure used was naturally the $P4_2/mnm$ structure (determined at 420°C, see later), described in the low symmetry frame, and onto which were added the different displacement modes derived from the symmetry analysis, to reproduce the distortion. This procedure is actually a natural way to classify and quantify the distortions involved, and allows differentiating primary and secondary distortive modes based on their symmetries and amplitudes (Section 2.2.2). As shown in Figure 3-15, a single Irrep distortion is not sufficient to explain the full symmetry breaking of the transformation from $P4_2/mnm$ to $P2_1/c$. Nevertheless, during the symmetry mode amplitude refinements, it became clear that one mode was persistently preponderant: the Σ_3 mode, whose 16 atomic displacements correspond to a symmetry breaking to the *Pbcm* isotropy subgroup, induced by the doubling of the cell along *b*. Indeed, as shown in Figure 3-16, the Rietveld calculations in which only the Σ_3 mode has been refined (with a spherical harmonic description of anisotropic strains) lead to satisfactory profile (see in particular the superstructure peaks in the inset) and to good agreement factors.

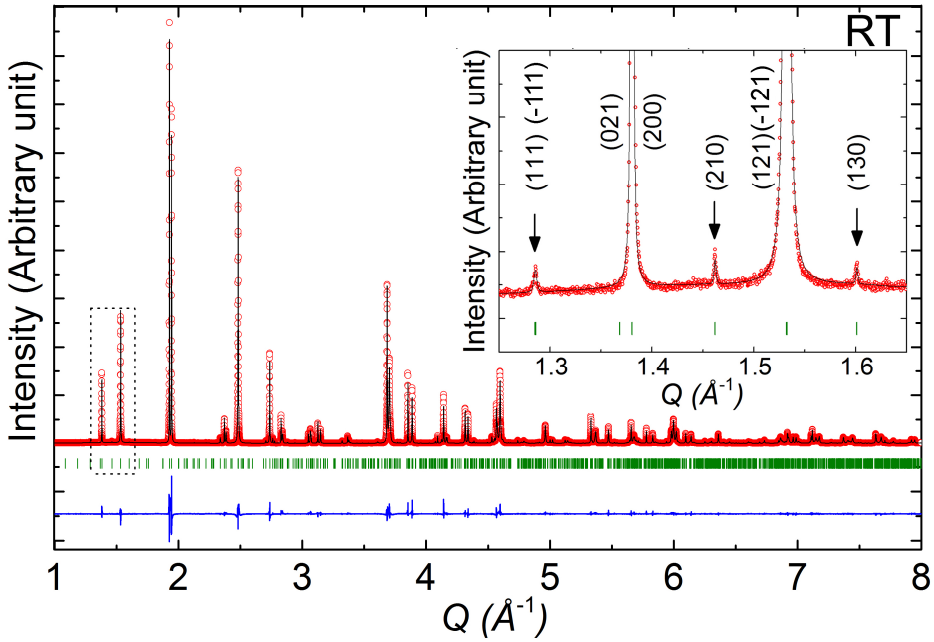


Figure 3-16 Rietveld refinement of the SXRPD data of Mn_2TeO_6 at RT. The inset shows an enlarged view of peaks indexed in $P2_1/c$ with a = 9.103 Å, b = 13.046 Å, c = 6.466 Å, β = 90.03°.

Table 3-6 shows the normalized polarization vectors for the Σ_3 mode, in terms of the *x*, *y* and *z* components of the basis modes. As mentioned earlier, the mode amplitudes are calculated with respect to the reference $P4_2/mnm$ structure at 420°C.

Atom	δ_x	δ_y	δ_z
Mn1	-0.0131(2)	-0.0007(2)	0.0000
Mn2	0.0043(2)	0.0057(2)	0.0000
Mn3	0.0043(2)	-0.0057(2)	0.0000
Mn4	-0.0131(2)	0.0007(2)	0.0000
Te1	-0.0087(2)	0.0000	0.0000
Te2	0.0080(2)	0.0000	0.0000
O1	-0.0056(12)	0.0000	0.0000
O2	-0.0071(12)	0.0000	0.0000
O3	0.0182(7)	0.0000	0.0000
O4	0.0182(7)	0.0000	0.0000
O5	-0.0170(7)	0.0086(6)	0.0000
O6	-0.0015(7)	-0.0124(6)	0.0000
O7	0.0039(5)	0.0023(4)	0.0020(11)
O8	0.0039(5)	0.0023(4)	-0.0020(11)
O9	0.0039(5)	-0.0023(4)	-0.0020(11)
O10	0.0039(5)	-0.0023(4)	0.0020(11)
O11	-0.0170(7)	-0.0086(6)	0.0000
O12	-0.0015(7)	0.0124(6)	0.0000

Table 3-6 Normalized polarization vectors for the Σ_3 distortion components of Mn_2TeO_6, expressed as displacements in relative units for the asymmetric cell of the structure (Normalization unit: 1 Å)

A representation of the polarization vectors corresponding to this Σ_3 mode is also shown in Figure 3-17, using the setting of the RTM structure. Displacements are observed along *a* for the six cationic sites, and a significant *b* component is only seen for Mn2 and Mn3 sites. There is no displacement along *c*. In each –TeMnMnTe- row (that is, with the same *y* value), all of the cations move in the same direction along *a*; two rows with opposite *y* coordinates (*y* and -*y*) move in the opposite direction. A complementary drawing including the displacements of oxygen atoms around the Te and Mn sites is given in Figure 3-18.

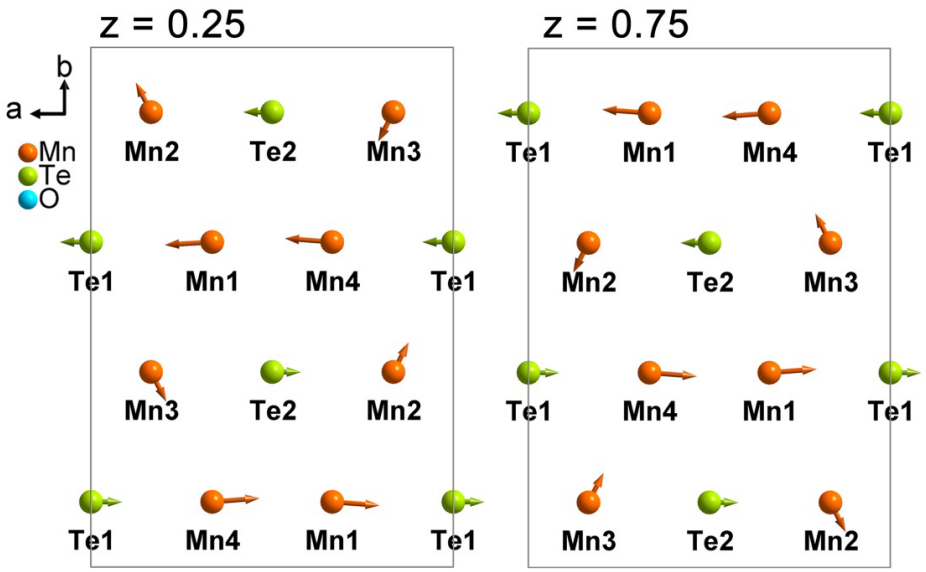


Figure 3-17 Description of the Σ_3 distortion components of Mn_2TeO_6 through the polarization vectors of the Mn and Te cations, projected along [001]. The atomic displacements correspond to the direction of the arrows, and their relative length is proportional to the mode amplitude.

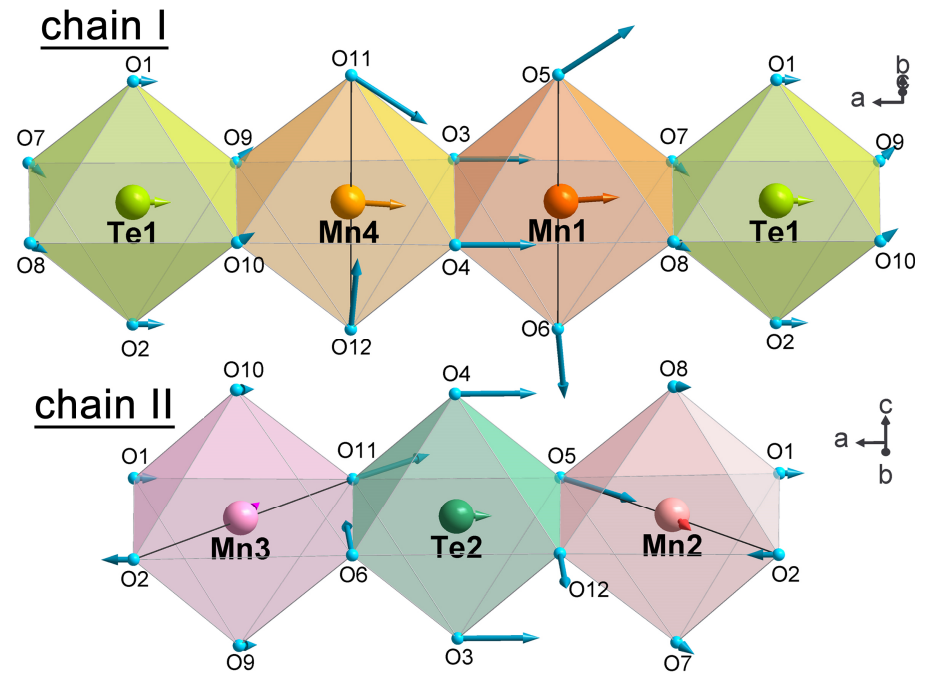


Figure 3-18 Description of the Σ_3 distortion components (polarization vectors) of all atoms in Mn_2TeO_6, using projections chosen to single out each octahedra chain separately for clarity.

The atomic positions and thermal displacement factors are given in Table 3-7. These parameters were obtained from the single-mode (Σ_3) refinement. The thermal displacement parameters reported in this table are constrained to be equal for atoms of

the same species to decrease the number of free parameters (note that refining them separately did not significantly improve the agreement factors). Refining cationic occupancies converged systematically to a composition in excellent agreement with the expected one. It was also further substantiated by EDX analysis, which revealed a ratio Mn/Te = 2.03 (0.15), by averaging the composition of 40 grains.

Type	*x*	*y*	*z*	B_{iso} (Å^2)
Mn1	0.3206(2)	0.1243(2)	0.2500	0.309 (11)
Mn2	0.8390(2)	0.8810(2)	0.2500	0.309 (11)
Mn3	0.1700(2)	0.8690(2)	0.2500	0.309 (11)
Mn4	0.6516(2)	0.1257(2)	0.2500	0.309 (11)
Te1	-0.0092(2)	0.1250	0.2500	0.349 (5)
Te2	0.5085(2)	0.8750	0.2500	0.349 (5)
O1	-0.0059(12)	0.2736	0.2500	0.115 (26)
O2	-0.0076(12)	0.9764	0.2500	0.115 (26)
O3	0.5193(7)	0.8750	0.5472	0.115 (26)
O4	0.5193(7)	0.8750	0.9528	0.115 (26)
O5	0.3210(8)	0.2895(6)	0.2500	0.115 (26)
O6	0.3375(7)	0.9565(6)	0.2500	0.115 (26)
O7	0.8433(5)	0.8774(4)	0.5628(11)	0.115 (26)
O8	0.8433(5)	0.8774(4)	0.9372(11)	0.115 (26)
O9	0.1651(5)	0.8726(4)	0.5586(11)	0.115 (26)
O10	0.1651(5)	0.8726(4)	0.9414(11)	0.115 (26)
O11	0.6428(8)	0.2712(6)	0.2500	0.115 (26)
O12	0.6593(8)	0.9828(6)	0.2500	0.115 (26)

Table 3-7 Atomic coordinates and thermal displacement parameters (from SXRPD data) of Mn_2TeO_6 at RT. SG: $P2_1/c$, a = 9.1030(1) Å, b = 13.0463(1) Å, c = 6.4659(1) Å, β = 90.0331(4) °. Agreement factors: R_{Bragg} = 3.29 %, χ^2 = 8.45.

The corresponding structure, illustrated in Figure 3-19, shows that Mn_2TeO_6 retains an inverse trirutile structure, albeit distorted, with Mn/Te chains of edge-sharing octahedra running along *a* (Figure 3-19b, c). There are two types of chains of edge-sharing octahedra, either consisting of -Mn1Mn4Te1Mn1- (chain I) or -Te2Mn3Mn2Te2- (chain II), which are connected through oxygen atoms (Figure 3-19b). In contrast with the parent $P4_2/mnm$ structure, these chains are puckered, particularly the second one (Figure 3-19c). This is connected with different distortions of the octahedra: $Mn1O_6$

and $Mn3O_6$ are elongated but $Mn2O_6$ and $Mn4O_6$ are compressed, and $Te1O_6$ and $Te2O_6$ are nearly regular (Figure 3-18 and Figure 3-19d). The waving of both chains mainly originates from oxygen displacements and appears larger for chain II, although the more distorted octahedra are observed in chain I around Mn1. In each chain, there is a pair of one elongated and one compressed MnO_6 octahedron, sandwiched between two TeO_6 octahedra. The unique axes of the octahedra are along *b* for Mn1 and Mn4 and in the *ab*-plane for Mn2 and Mn3, thus forming a herringbone-like pattern, as shown in Figure 3-19b.

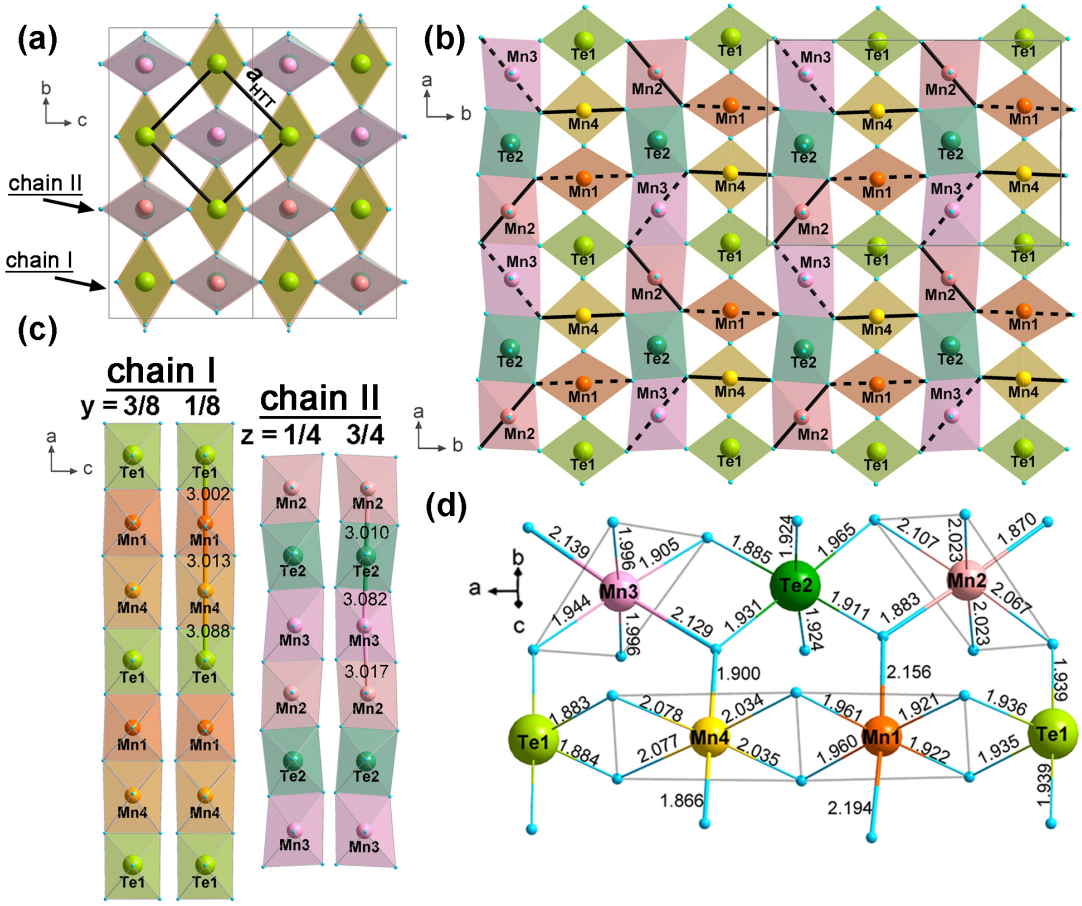


Figure 3-19 Representation of the $P2_1/c$ distorted inverse trirutile structure of Mn_2TeO_6 at RT projected (a) along [100], (b) along [001] and (c) along [010] and [001]. The parent HTT cell is shown in (a) as a black line. In (b) both types of chains are represented, and the full/dotted black lines highlight the compressed/elongated Mn–O distances of the MnO_6 octahedra. For clarity, only one type of chain is shown in each projection in (c). (d) Mn–O and Te–O interatomic distances (Å) are given for each of in the six octahedra building Mn_2TeO_6.

This also leads to slight differences in the cation-cation distances along the chains (Table 3-8): although the Mn-Mn distances are similar (3.013 and 3.017 Å), in each chain there is a long and a short Mn-Te distance (3.088 vs 3.002 Å and 3.080 vs 3.010 Å in chains I and II, respectively).

Cation	**O**	**Distance**	**<*d*>**	**Δ*d*** 10^{-4}	**Cation**	**O**	**Distance**	**<*d*>**	**Δ*d*** 10^{-4}
Mn1	O3	1.960(5)	2.019(6)	30.9	Mn3	O1	1.944(9)	2.018(8)	18.9
	O4	1.961(5)				O2	2.139(8)		
	O5	2.156(8)				O6	1.905(8)		
	O6	2.194(8)				O9	1.996(7)		
	O7	1.922(6)				O10	1.996(7)		
	O8	1.921(6)				O11	2.129(8)		
Mn2	O1	2.067(8)	1.996(7)	19.7	Mn4	O3	2.035(5)	1.998(6)	17.6
	O2	1.870(8)				O4	2.034(5)		
	O5	1.883(8)				O9	2.077(6)		
	O7	2.023(7)				O10	2.078(6)		
	O8	2.023(7)				O11	1.900(8)		
	O12	2.107(8)				O12	1.866(8)		
Te1	O1	1.939(1)	1.919(4)	1.8	Te2	O3	1.924(1)	1.923(5)	1.5
	O2	1.939(1)				O4	1.924(1)		
	O7	1.935(6)				O5	1.911(8)		
	O8	1.936(6)				O6	1.885(8)		
	O9	1.884(6)				O11	1.931(8)		
	O10	1.883(6)				O12	1.965(8)		
Mn1-Mn4			3.013 (2)		Mn1-Te1			3.002 (2)	
Mn3-Mn2			3.017(3)		Mn4-Te1			3.088(2)	
					Mn2-Te2			3.010 (2)	
					Mn3-Te2			3.082(2)	

Table 3-8 Selected inter-atomic distances (in Å) in Mn_2TeO_6 ($P2_1/c$) at RT

3.1.8 *RT-TEM study: SAED and images*

The structural model proposed above is confirmed by microscopy studies combining SAED patterns and HRTEM images as shown in Figure 3-20. Indeed, the [001] SAED pattern exhibits extra spots, in comparison with the HTT unit cell; all patterns are thus indexed using the large RTM cell. Moreover, the regular contrast of the HRTEM images shows that the sample is well crystallized and free of extended defects in large areas.

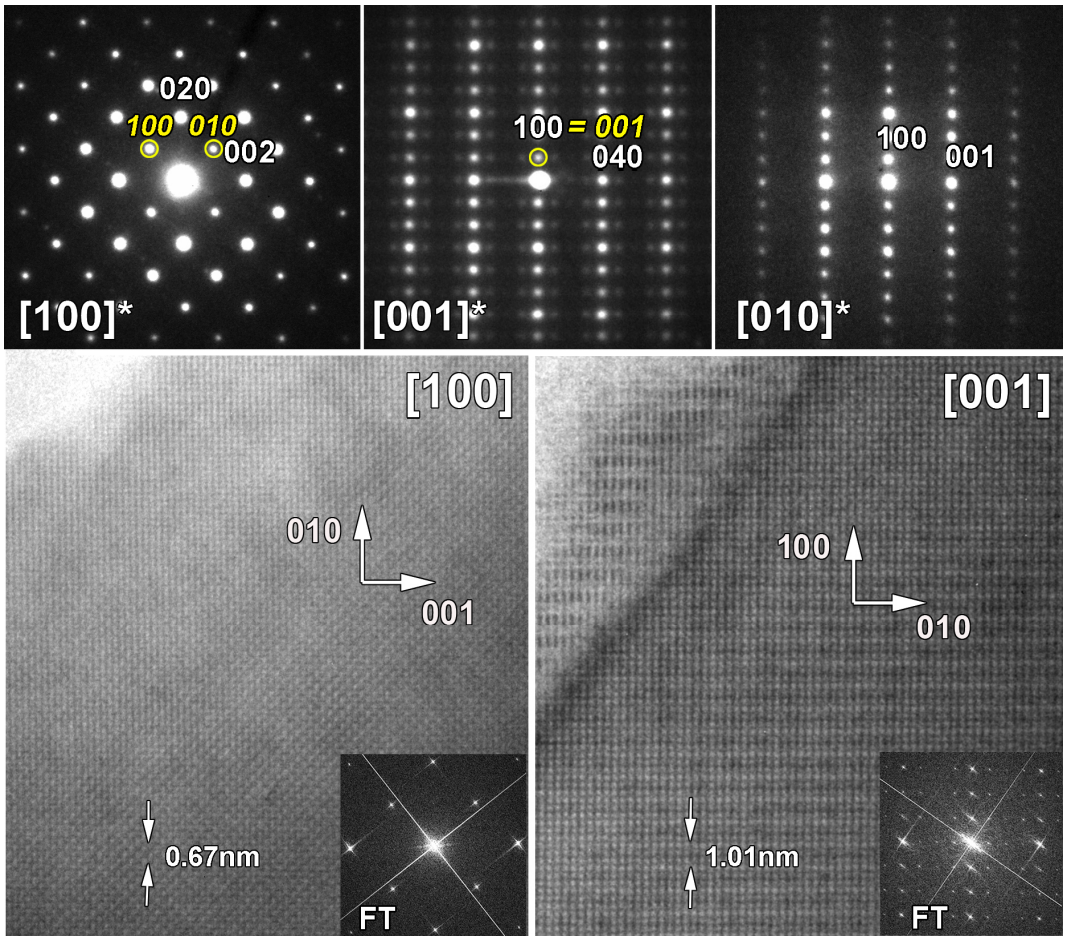


Figure 3-20 SAED patterns along the main zone axes [100], [001], and [010] and corresponding [100] and [001] HRTEM images and associated FT patterns. The indexation corresponds to the RTM (white) and HTT (italic yellow) structures.

This is also in agreement with the [010] HAADF-STEM and [100] HAADF-STEM images (Figure 3-21a, b) and corresponding FT patterns, in which the positions of Te (***Z*** = 52) and Mn (***Z*** = 25) appear as very bright and less bright dots, respectively.

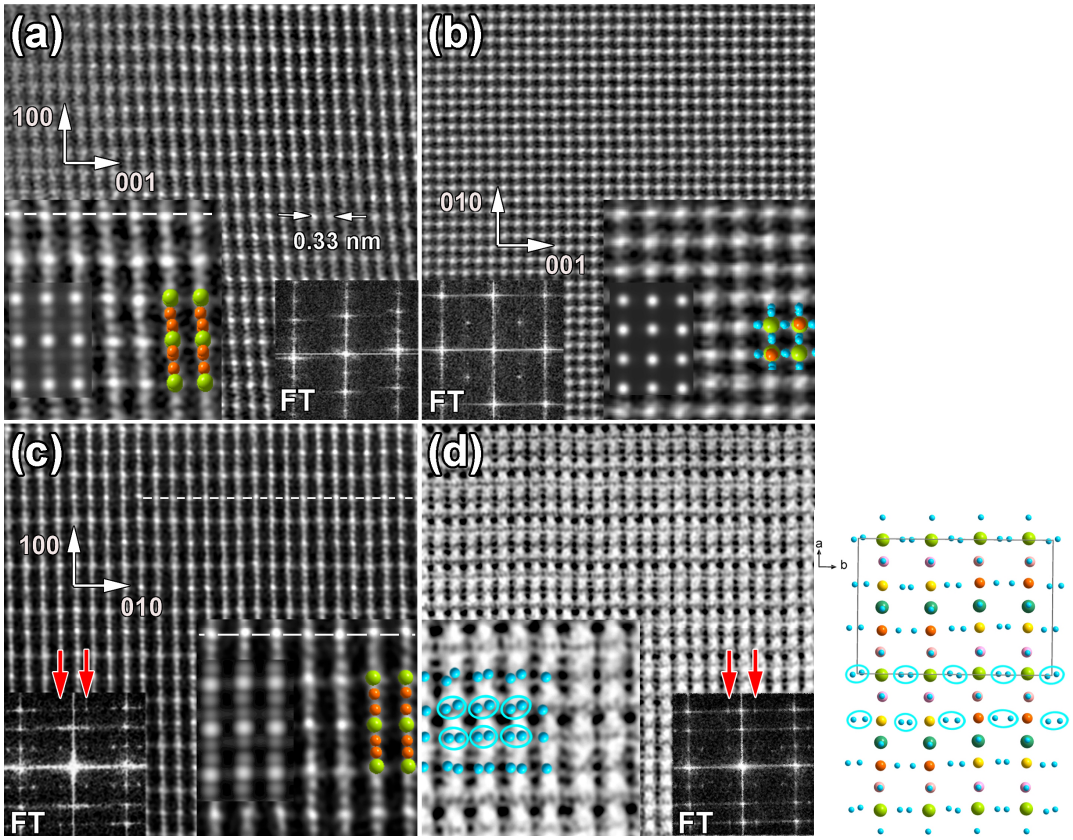


Figure 3-21 (Left) High-resolution HAADF-STEM images and corresponding FT pattern of main zone axes along (a) [010], (b) [100] and (c) [001]. On the enlarged images, color-coded atoms are overlapped (Mn, Te, and O in orange, green and blue, respectively), and simulated patterns are given in the inset. (d) [001] ABF-STEM image acquired simultaneously with HAADF-STEM image given in (c) and its FT pattern. For simplicity, only O atoms are shown in the enlarged image. (Right) Projection along [001] of the RTM of Mn_2TeO_6, deduced from the SXRPD refinement results, highlighting the atomic oxygen arrangement along b (blue ellipses) (for comparison with (d)).

No additional features -such as unindexed spots or modulations- are observed along these zone axes. The large b_{RTM} parameter ($\cong 2\sqrt{2}a_{HTT}$) is clearly confirmed by the [001] HAADF-STEM and ABF-STEM images (Figure 3-21c, d), with the presence of the spots highlighted by the arrows in the corresponding FT pattern. In agreement with the RTM structure determined by SXRPD data, the cations and oxygen atoms are no longer aligned along [010] (in comparison with the HTT phase), as shown in HAADF-STEM (Figure 3-21c) and ABF-STEM images (Figure 3-21d). Occasionally, the position of oxygen atoms deviates from the refined structure over several periods. This is highlighted by blue ellipses in Figure 3-21d, whose relative orientations along the *b*-axis differ from those calculated from the X-ray structural model (blue ellipses in

Figure 3-21, right). Such level of disorder in oxygen positions might be linked with possible occupancy variations within cation columns, inducing a tilt of octahedra, or by oxygen vacancies. In any case, this deviation is small and at short distance, explaining why it cannot be refined from X-ray or neutron data meaningfully.

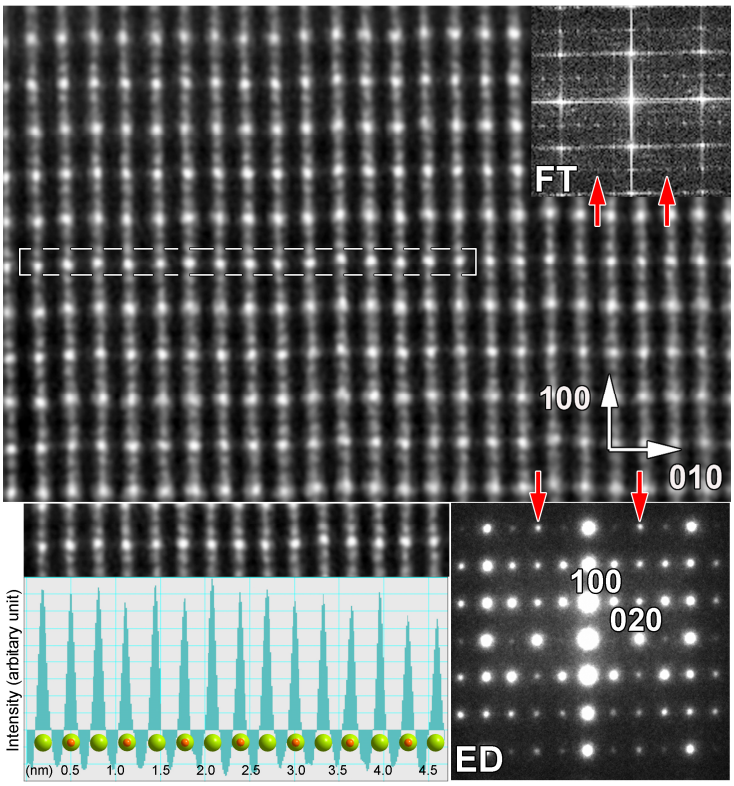


Figure 3-22 [001] HADDF-STEM image highlighting the area corresponding to the 020 spots in the FT and ED patterns (red arrow). The intensity plot profile along the Te row of the selected area (white rectangle) is also given in insert.

Nevertheless, the uncertainly about the cationic distribution is supported by another phenomenon evidenced in the ED pattern and in the corresponding HAADF-STEM image presented in Figure 3-22. Surprisingly strong 020 diffraction spots are observed in this [001] ED pattern, in contrast with the [001] ED pattern of Figure 3-20. Corresponding FT patterns taken from HAADF- STEM images also show that the intensity of the 020 diffraction spots varies from one crystal to another and that often both types of [001] ED patterns (Figure 3-20 and Figure 3-22) coexist in the same crystallite. This is associated with a variation in the intensity of the brightness of Te columns along the [010] direction, as revealed by a close inspection of the HAADF-

STEM images. The corresponding intensity profile (plotted in Figure 3-22) suggests a chemical disordering within Te columns, incorporating Mn or vacancies: the bright dots correspond to 100% Te columns, while less bright dots correspond to mixed Te/Mn columns. This is further confirmed by structure factor calculations, which show that the intensity of the 020 spot is directly linked to Te amount, full Te occupancy corresponding to zero intensity of the 020 spot.

Such a distribution of Mn in Te columns might also be correlated with the existence of dislocations. These are rather unusual in bulk oxides, and they are associated with antiphase boundaries (APBs) as illustrated in the HAADF-STEM image viewed along [001] (Figure 3-23). The APB appears as bright Te layers shifted with respect to each other by one-third along the [100] direction (region A), as schematized in the lower part of Figure 3-23. Such APBs originate from dislocations, which consist of the splitting of one Te plane in two, between which extra Te/Mn planes are inserted.

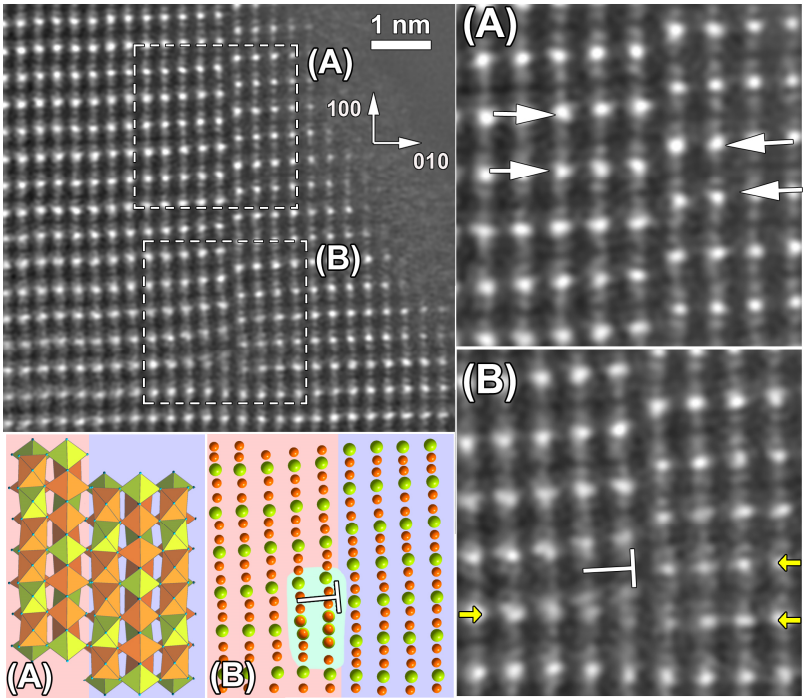


Figure 3-23 [001] HAADF-STEM image of an area with two types of defects. The (A) and (B) regions are enlarged (right panels), and corresponding structural models are proposed in the bottom left panel.

The corresponding model is also drawn in Figure 3-23 (region B). In view of these local defects, the RT crystal structure of Mn_2TeO_6 deduced from the SXRPD data is undoubtedly somewhat idealized, as it does not take into account local scale disorder, which probably explains the anisotropic broadening of the Bragg peaks mentioned at the start of this chapter (Figure 3-6).

3.1.9 *Tetragonal to monoclinic transition: from 700°C to RT*

As pointed out above, the phase transition from HTT to RTM was studied by XRPD and NPD. Both sets of data are in good agreement and the evolution of the refined lattice parameters as a function of temperature (extracted from NPD data) is shown in Figure 3-24.

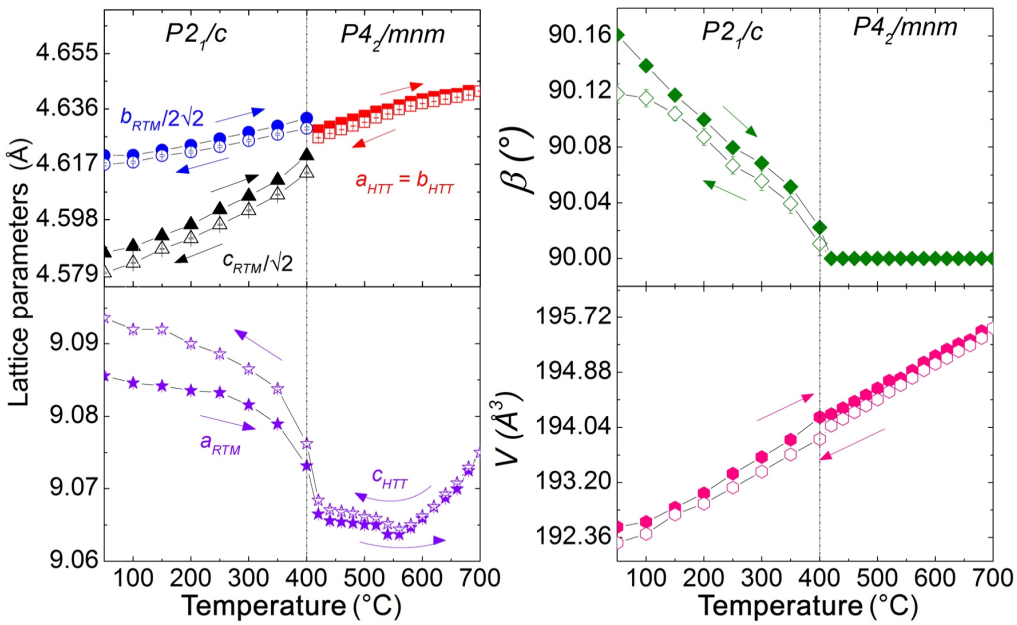


Figure 3-24 Temperature evolution between RT and 700°C of the lattice parameters and cell volume of Mn_2TeO_6, from NPD data upon heating (full symbols) and cooling (open symbols).

The a_{HTT} cell parameter decreases with decreasing temperature, and its splitting in b_{RTM} and c_{RTM} is clearly observed below 400°C. The difference between b and c increases with decreasing temperature, along with the monoclinic angle. The cell parameters evolution follow the same trend whether the NPD patterns were recorded while heating

or cooling, but the cell volume and monoclinic distortion extracted in the cooling process are slightly smaller than in the heating one, which might be due to a better cation ordering once the sample reached the highest temperature (S1 transformation in S2). Moreover, no weight change is observed during this transformation by TGA-DTA study.

In the HTT form, the temperature evolution of c_{HTT} is not monotonous (in contrast with the a_{HTT} vs T evolution): from 700 to 550°C the usual decrease due to thermal contraction is observed, but below 550°C c_{HTT} starts to increase slightly, before increasing more sharply around 400°C, when the structural transition occurs. This could suggest that preliminar atomic movements, premises of the structural transition, could start as high as 550°C. The negative thermal expansion of c_{HTT} below 400°C is balanced by the decrease of the two others cell parameters, leading to a continuous decrease of the cell volume. A possible origine for this negative thermal expansion of the c_{HTT} parameter below 550°C (i.e. above the structural transition) will be discussed later.

Concerning the trivalent state of manganese, Figure 3-25 shows the Mn K-edge XANES spectra for two Mn_2TeO_6 samples (S3 and S1) at RT. The white-line peaks of Mn_2TeO_6 are located at approximately 6560 eV. This energy is close to the main peaks of Mn_2O_3, which is used as reference for Mn^{3+}, showing thus unequivocally that manganese is in a trivalent state. XANES revealed also that the manganese oxidation state does not vary within our synthesis conditions, since there is no significant difference in the edge position between S1 and S3.

The manganese oxidation state was also confirmed by the μ_{eff} value extracted from the $1/\chi(T)$ curve in the paramagnetic domain (see Figure 3-26 in the next section). Finally, oxygen stoichiometry was established by combining the hexavalent state of tellurium evidenced by nuclear forward scattering (*115*), EDX analysis and NPD, thus confirming the expected Mn_2TeO_6 stoichiometry.

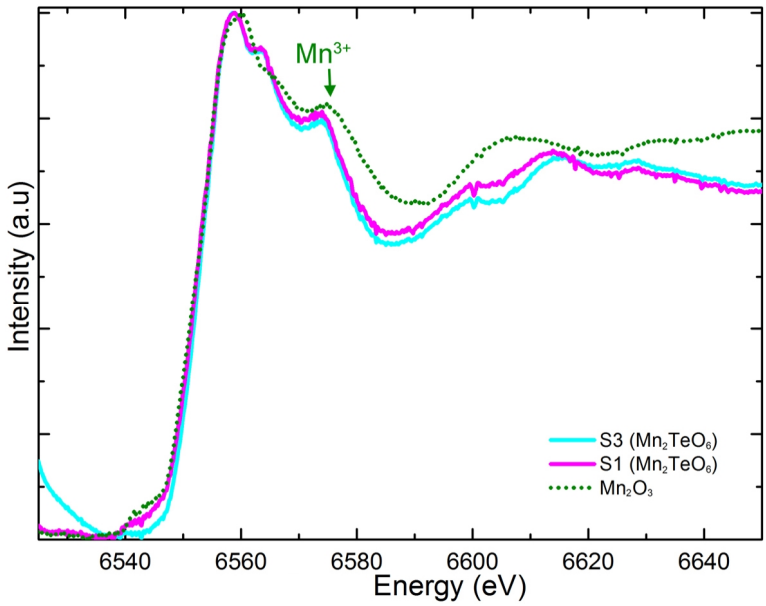


Figure 3-25 Mn K-edge XANES spectra of Mn_2TeO_6 (S3 and S1) and Mn_2O_3 as a reference sample for Mn^{3+} at RT. The highest absorbance of each spectrum was normalized to unity.

3.2 *Low-temperature structures and properties*

The low-temperature (LT) behavior of Mn_2TeO_6 was first investigated as a function of temperature, in the 5 - 300K range, by using magnetic susceptibility, specific heat and dielectric measurements. Moreover, these results were combined with SXRPD and NPD studies to study the crystal structures and the magnetic ones in the NPD case. Like for the previous section, several selected Mn_2TeO_6 samples were used leading to a coherent set of data. Further physical properties were then examined as a function of magnetic field. At the end of this section, some changes observed in the low-temperature behaviors of different samples will be presented.

3.2.1 *Previous reports*

A low-temperature study of Mn_2TeO_6 has been first reported by Fruchart et al. (*7*), with a magnetic transition temperature T_N at 25.5K. They performed a NPD experiment at 2K on a tetragonal form of Mn_2TeO_6 ($a = b = 4.613$Å, $c = 9.082$Å), and concluded on a non-collinear magnetic structure with $\boldsymbol{k}$ = (0 0 1/2), in which the manganese magnetic moments are confined in the *ab*-plane, lying either along [110] or [-110]. It is illustrated on Figure 3-41a.

3.2.2 *Preliminary physical characterizations*

Magnetic susceptibility vs. T

The temperature dependence of the magnetic susceptibility χ(T) recorded in 100 Oe upon warming is shown in Figure 3-26 (left axis). Two transitions can be determined, taken at the two maxima, at temperature ≅ 63 K and ≅ 29 K, that is close to the T_N = 25.5K previously reported for Mn_2TeO_6 (*7*).

The inverse of the susceptibility curves (Figure 3-26, right axis) shows a large linear domain allowing a Curie-Weiss fitting that leads to μ_{eff} = 4.96 μ_B/Mn and θ_{CW} = -38.0 K. This μ_{eff} value is close to the theoretical one of 4.89 μ_B for Mn^{3+}, confirming thus the trivalent state of manganese in Mn_2TeO_6. The negative θ_{CW} value indicates predominant antiferromagnetic interactions. The zero field-cooling warming (*zfcw*) and field-cooling warming (*fcw*) curves in 100 Oe are nearly superimposed, confirming the strong antiferromagnetic character of Mn_2TeO_6.

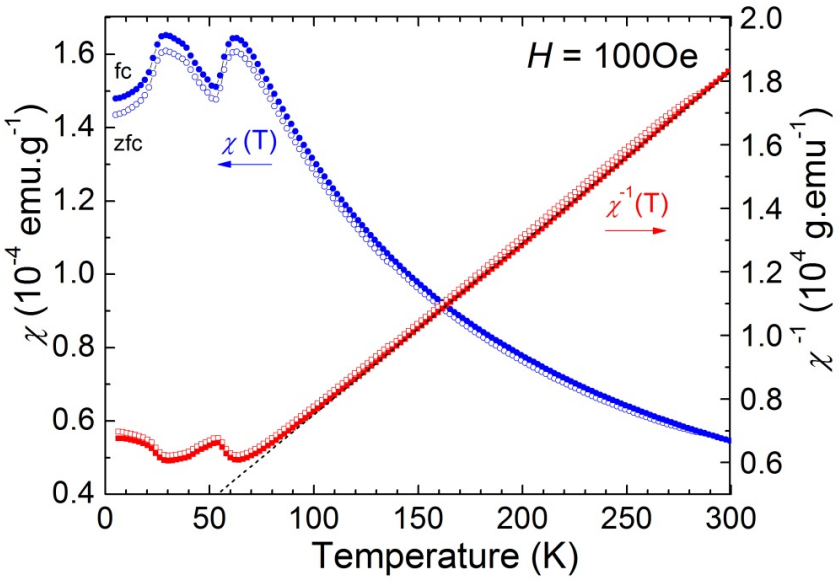


Figure 3-26 Zero field-cooling warming (zfcw) and field-cooling warming (fcw) χ(T) curves (left axis) of Mn_2TeO_6 (S2 sample) and χ^{-1}(T) (right axis) in 100 Oe. The dotted black line show the linear fit to a Curie-Weiss regime.

On the other hand, the comparison of the *fc* susceptibility curves collected upon cooling (*fcc*) and warming (*fcw*) shows the existence of a large temperature hysteresis (2-*fcc*

and 3-*fcw* in Figure 3-27a). For a more precise determination of the transition temperatures, the $\Delta\chi/\Delta T$ curves vs. T (right axis of Figure 3-27a) are used and these temperatures will be used in the following. Depending on the measurement conditions, the first transition is shifted by about 10K, from $T_1 \cong 53$ K (warming) down to $\cong 43$ K (cooling). This 10 K difference remains unchanged if measurements are performed in larger $\mu_0 H$ values (up to 5T), as both characteristic temperatures keep the same values (Figure 3-27b). This strongly suggests that the hysteresis is not of magnetic origin but rather results from a first-order structural transition. Moreover, as no spin dynamics effect can be detected in the ac-χ'(T) measurements recorded at different frequencies (Figure 3-27c) the hypothesis of a structural transition around T_1 is supported.

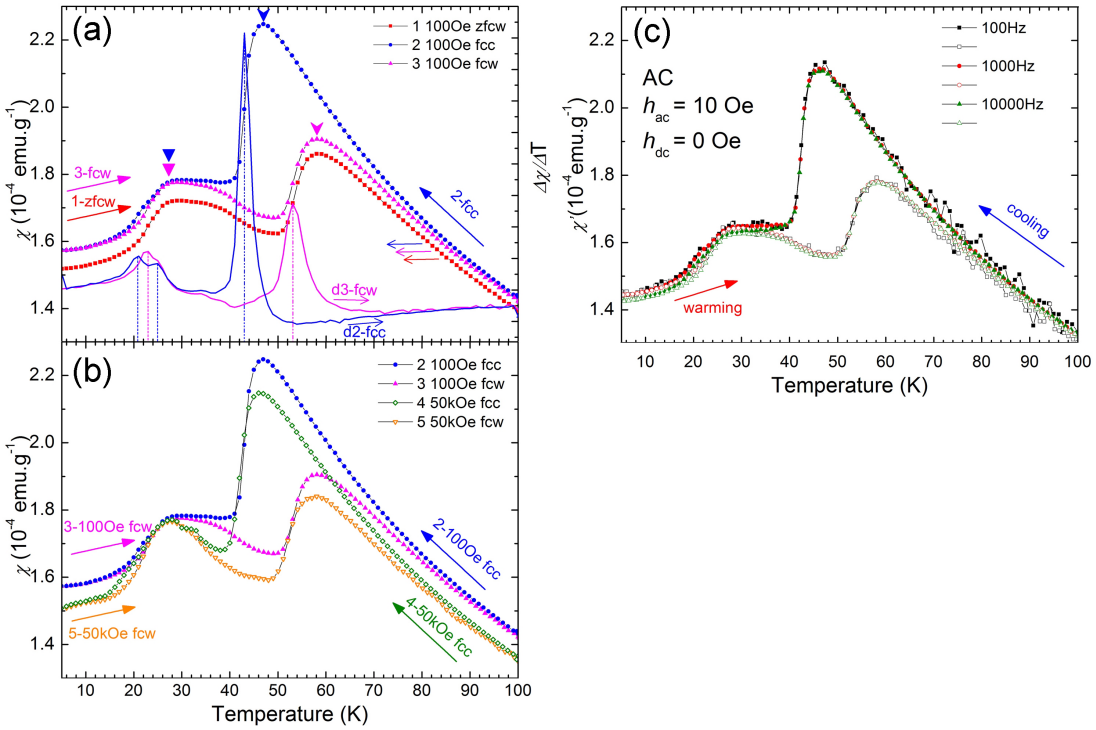


Figure 3-27 (a) χ(T) curves (of S2 sample) recorded upon warming and cooling (1-zfcw, 2-fcc, and 3-fcw modes) in 100 Oe (left axis) and corresponding Δχ/ΔT vs. T curves (right axis);(b) In addition to 2- and 3-curves of panel of (a), χ(T) curves recorded in 5T in 4-fcc and 5-fcw modes; (c) Ac susceptibility χ'(T) upon warming and cooling in h_{ac} = 10 Oe at different frequencies in the 100 – 10k Hz range.

A possible spin-lattice coupling is not to exclude at this stage, however, as it is possible that a magnetic transition could also be taking place around T_1. To differentiate

between them in the following, T_N will be used for a magnetic transition and T_S for a structural one.

A very small hysteresis around 20K also exists in 100 Oe (Figure 3-27a) that, in contrast, is reinforced by application of 5T (Figure 3-27b). The values of the susceptibility are slightly lower in 5 T than in 100 Oe except at the lower temperatures for which they reach the same magnitude.

For the low-temperature transition, the $\Delta\chi/\Delta T$ curves show one peak at ≅ 23K on the *fcw* branch, which splits into two at ≅ 25 and ≅ 21K on *fcc* one. A transition around 35K is also a possibility; it seems to be magnetic field-sensitive, as it is suppressed under high magnetic field (Figure 3-27b).

Dielectric constant vs. T

The temperature dependence of the dielectric constant ε' (Figure 3-28) shows an anomaly around T_1 (≅ 53K upon warming and ≅ 43K on cooling), in the same temperature range as the χ(T) ones (Figure 3-27).

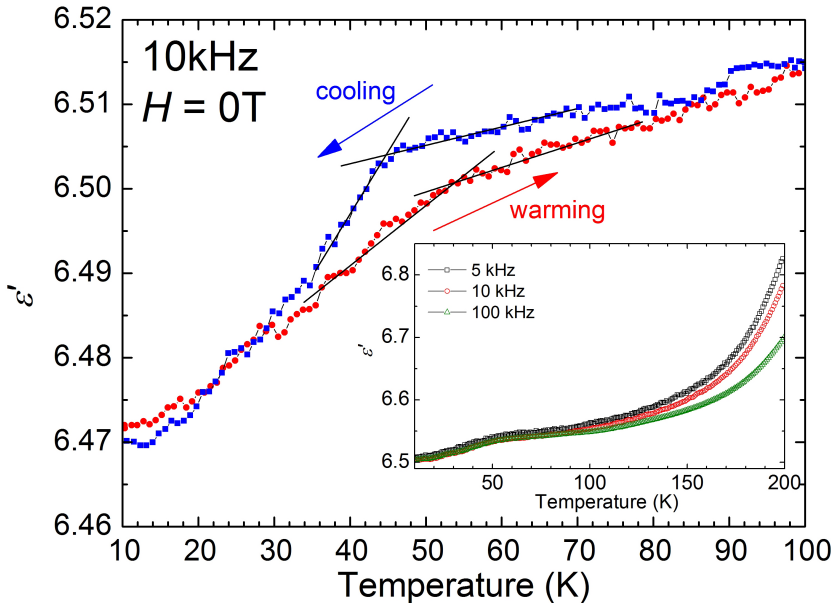


Figure 3-28 T dependence of the dielectric constant (ε') at 10k Hz upon warming and cooling between 100 and 10K, and in inset, from 10 to 200K upon warming measured at different frequencies from 5k to 100k Hz.

The absence of frequency dependence of ε'(T) outlines the fact that the electric charges, like spins, do not exhibit dynamical features, ruling out dipolar glass behavior. Pyroelectric measurements did not reveal any measurable electrical polarization below T_1.

Specific heat vs. T

To go further in the understanding of these magnetic and dielectric features, specific heat (*Cp*) measurements were carried out and are illustrated in Figure 3-29, using S2 sample. Two measuring methods were used here, QD method and PBP method (red and black line in Figure 3-29, respectively.). Detail of these methods is described in Section 2.3.3. An even more complex picture emerges from those measurements, as at least 6 transitions are observed, marked by the red and black triangles in Figure 3-29.

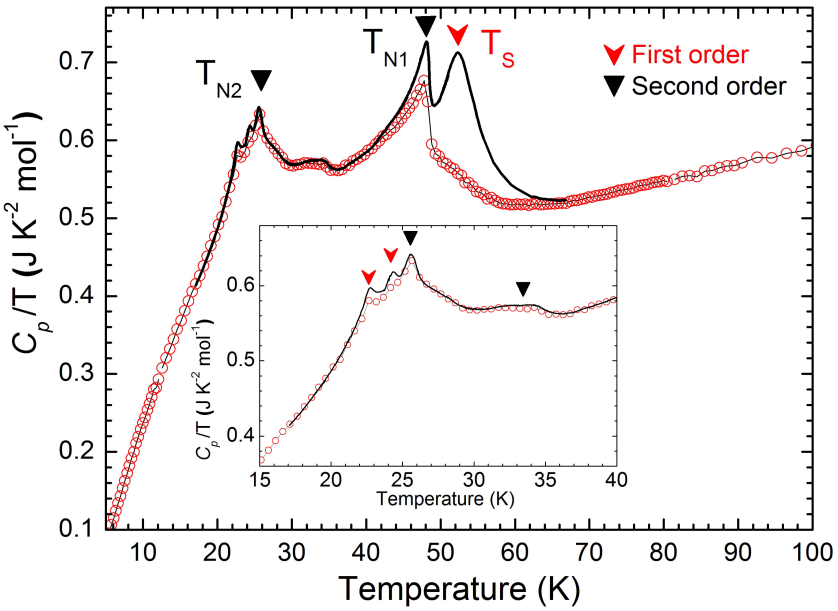


Figure 3-29 Cp(T) curves of the Mn_2TeO_6 (S2 sample) shows at least 6 transitions including T_s, T_{N1} and T_{N2}. First and second order transitions are indicated by red and black triangles, respectively.

For three of them (black triangles), one observes the same signature for the two measuring techniques (same shape and position in temperature), showing that one is dealing with second-order transitions (no latent heat, no hysteresis). In contrast, the

other three transitions (red triangles) exhibit a significant difference between the two techniques, which points to a first-order nature. The most pronounced first-order character is found for the transition at T_S, which is quite broad; since it is also strongly hysterical (see Figure 3-27) the transition cannot be observed on the cooling branch of the *Cp* data collected by the PBP method. This is perfectly in line with the previous susceptibility results and shows in particular the existence of two neighbouring transitions, at 53K and 48K, which could not be distinguished from one another on the susceptibility curves. Two additional transitions are also seen below 25K. *Cp* being sensitive to transitions of either structural and/or magnetic origin, these results have to be combined with LT-SXRPD and NPD experiments.

3.2.3 *LT-SXRPD study*

A SXPRD study in the 295 - 10K range was performed on the BL04-MSPD beamline at the ALBA synchrotron (using S3 sample). Experimental conditions, sample environment (N_2 gas blowing or cryostat), warming or cooling mode, temperature stabilizing or sweeping mode (rate: 1K/min) were varied to obtain data with increasing and decreasing temperature, so as to correlate with previous measurements (and taking into account the optimization of the allocated beamtime).

Structure evolution: 295 – 200K

Figure 3-30 shows the comparison of two SXRPD patterns recorded upon cooling from 295 to 205K using the N_2 gas blower. All the diffraction patterns recorded in this temperature range can be indexed using the RTM phase and the symmetry adapted mode refinement with a spherical harmonics description of anisotropic strains.

At 295K, the refined structure is in agreement with the one mentioned in Table 3-7, confirming that the primary Σ_3 mode remains the largest mode and that other modes stay negligible from 295 down to 205 K. The evolution of the cell parameters will be presented later with the evolution at lower temperature. Indeed below 200K, important changes start to be observed in the diffraction patterns.

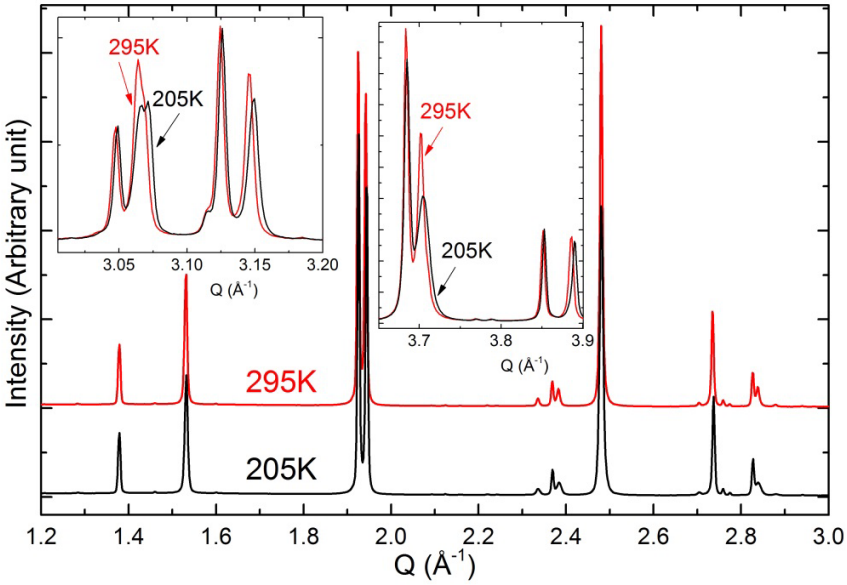


Figure 3-30 SXRPD data of Mn_2TeO_6 (S3 sample) at 295 and 205K in the 1.2 – 3.0 Å^{-1} Q range and in insets selected Bragg peaks at higher-Q ranges.

Structure evolution: 200 – 10K

Figure 3-32 show the evolution of the SXRPD patterns recorded upon warming, between 10 and 200K, using a cryostat. There is no significant difference between the diffraction patterns at 205K recorded upon cooling (Figure 3-30) and the one recorded at 200K upon warming (Figure 3-32).

As shown in Figure 3-31 illustrating diffraction results in increasing or decreasing temperature (sweeping mode), a structural transition appears clearly (highlighted by white lines with the T_s label on the plots), which is reversible but with a strong temperature hysteresis. According to these results, T_S is determined to be ≅ 37 K in cooling mode, while it is ≅ 50 K in warming mode. This is excellent agreement with the temperatures determined from magnetic susceptibility and dielectric constant curves (Figure 3-27 and Figure 3-28). The structural transition is evidenced by a splitting of several Bragg peaks, and the appearance of new small peaks. In fact, as seen in Figure 3-32-left, this structural transition is not sharp but occurs over a very wide temperature range: the low temperature phase (labelled LT in the following, and indicated by green arrows on Figure 3-32), coexists with the RTM phase from 100K down to 40K (this temperature range is symbolized by the grey dashed area of Figure 3-32). Above 100K, only the RTM phase is observed, and below 40K, only the LT one. These observations

confirm the previous hypothesis of a structural transition and bring the additional and important precision that a biphasic domain is observed over 40 - 100K.

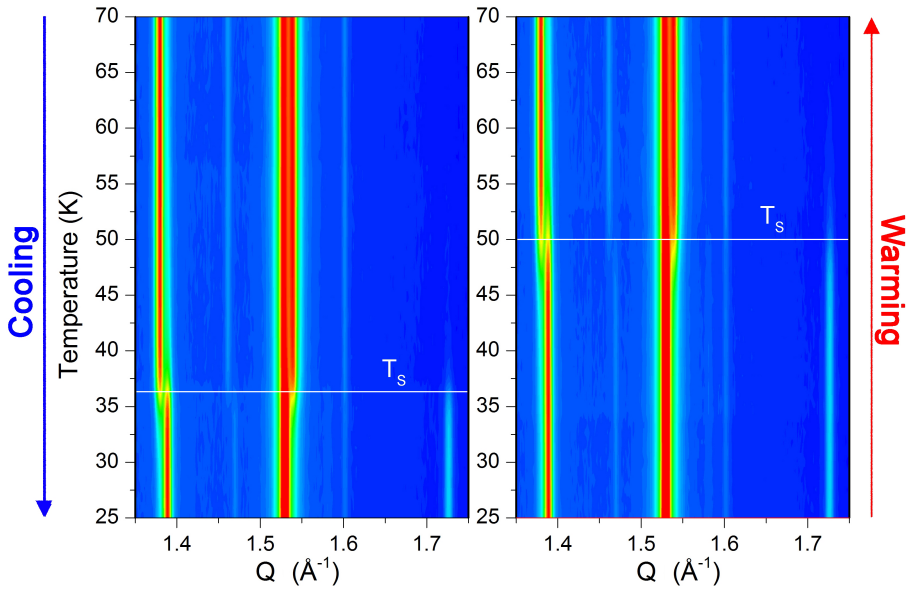


Figure 3-31 Temperature evolution of the SXRPD data of Mn_2TeO_6 (S3 sample) recorded from 70 to 25K (cooling) and from 25 to 70K (warming) in temperature sweeping mode.

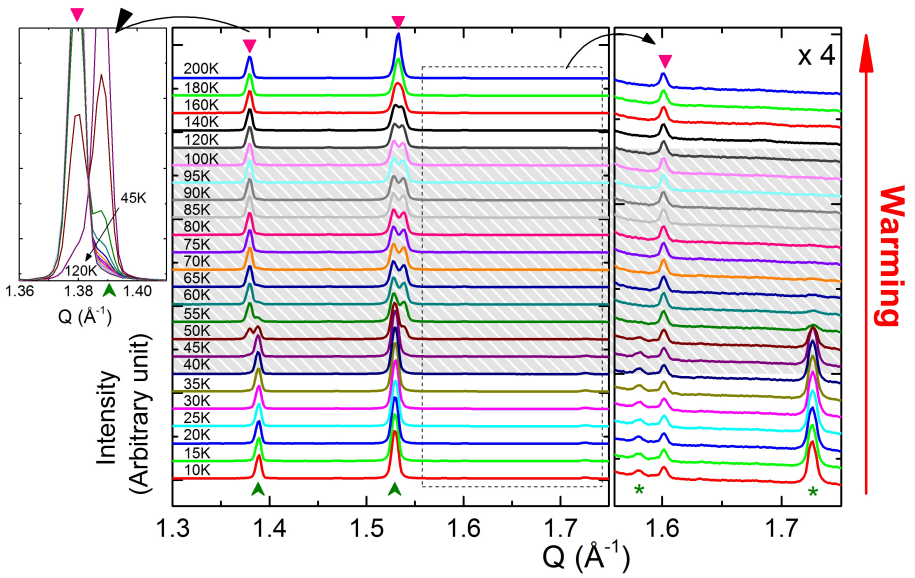


Figure 3-32 Temperature evolution of the SXRPD data of Mn_2TeO_6 (S3 sample) from 10 to 200K. The temperature range covered by dashed area (100 – 40K) corresponds to the coexistence of two phases. Pink arrows (on the top of figure) point out selected Bragg peaks belonging to RTM phase, while green arrows (on the bottom of figure) are for the LT phase. Two enlarged Q ranges are shown: on the right to highlight new small peaks compared with the RTM phase (indicated by green stars) and on the left to visualize the LT-RTM phase transition.

Rietveld refinements of the structures below 200K were performed in the same conditions as before, refining only the Σ_3 mode and keeping a spherical harmonic description of the strains. The quality of these refinements gradually deteriorates with decreasing T, owing to (i) the larger strains resulting from the increasing monoclinic distortion of the RTM crystal structure and (ii) the coexistence of the RTM and LT phases between 100 and 40K. As a consequence, only the results of the refinements performed above 120 K are described in what follows.

The results of Rietveld refinement performed using the 120K data are shown in Figure 3-33. As already stated, the diffraction pattern at 120 K shows only the RTM phase, and is similar to the one obtained at RT (Figure 3-30). The displacement mode with the largest amplitude is still Σ_3, and its amplitude is similar to the RT value. The amplitudes of all the other modes remain close to zero, like at RTM.

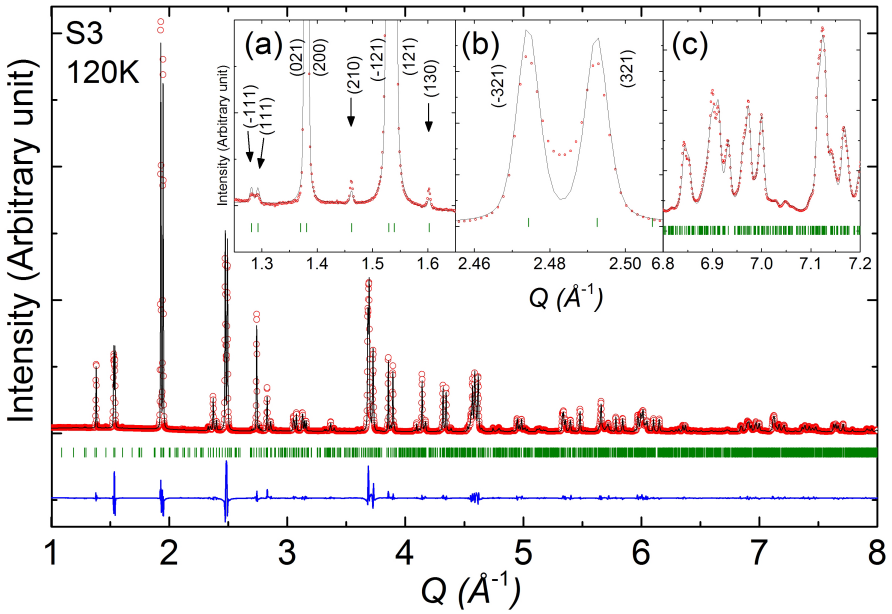


Figure 3-33 Rietveld refinement of the SXRPD data of Mn_2TeO_6 (S3 sample) at 120K in $P2_1/c$ with a = 9.101 Å, b = 13.035 Å, c = 6.453 Å and β = 90.64°. The insets show chosen Q ranges to highlight (a) small peaks corresponding to the doubling along b (compared with the HTT phase), (b) Bragg peaks characteristic of the monoclinic distortion, (c) the quality of the fit at high angles.

Nevertheless, these results are only qualitative, as the refinement agreement factors are significantly higher at 120K than at RT, $\{R_{Bragg} = 3.05, \chi^2 = 250\}$ to compare with $\{R_{Bragg} = 2.66, \chi^2 = 50.7\}$, respectively. The fit of the experimental data is not perfect

for some Bragg peaks (as shown in insets (b) and (c) of Figure 3-33), probably because strains are not handled perfectly in the refinement. These results show nevertheless that the herringbone pattern of distorted octahedra in the RTM phase is preserved down to 120 K, and probably in the whole temperature range of its existence. The evolution of cell parameter vs T is discussed further below.

The next step is the determination of the LT phase. Two diffractograms recorded at 295K and 10K are plotted in Figure 3-34 for comparison; the RTM and LT phases present obvious similitudes, suggesting close crystal structures, i.e., a monoclinic inverse trirutile framework, but with slightly different cell parameters. Nonetheless, as mentioned before in the description of Figure 3-32, new extra peaks (green wedge triangles on the inset of Figure 3-34) are observed, in addition to the ones attributed to the *b*-doubling (pink triangles on the inset of Figure 3-34) by analogy with the RTM phase. In the next section, we report our attempts to investigate this LT structure further.

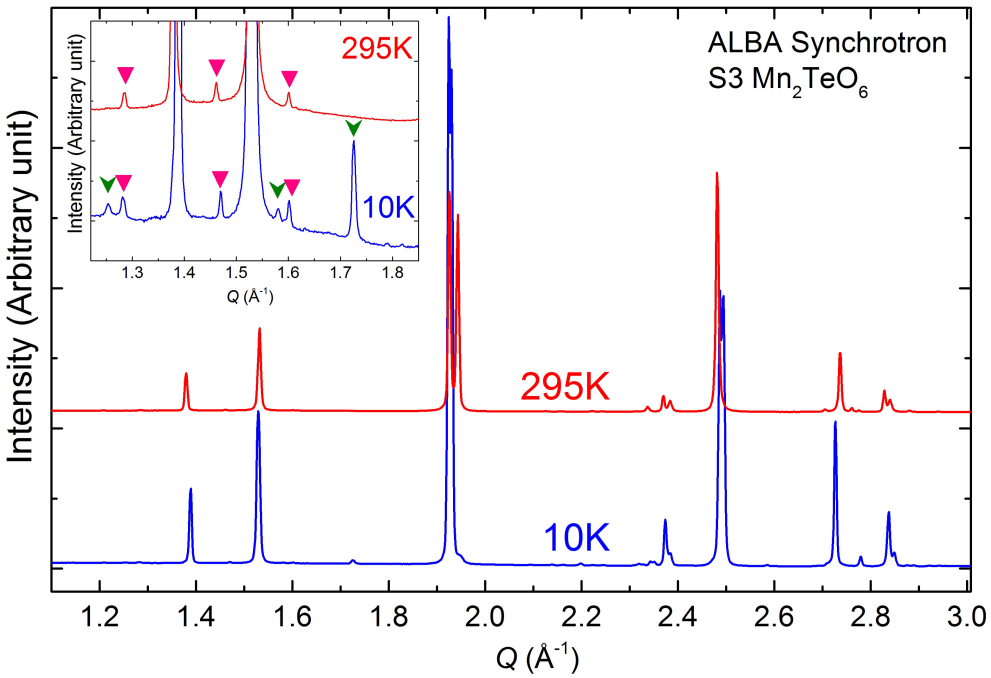


Figure 3-34 SXRPD data of Mn_2TeO_6 (S3 sample) recorded at 295K (red) and 10K (blue). The inset shows a Q-range chosen to highlight the small "satellite" peaks existing at RT (pink triangles) and only at LT (green wedge triangles).

Le Bail analysis

As a starting point, Le Bail fittings of the patterns outside the range of phase coexistence (T < 45 K) were performed. Keeping the $P2_1/c$ SG and cell metrics of the RTM phase, the main Bragg peaks can be indexed readily with $a \cong 9.03$ Å, $b \cong 13.05$ Å and $c \cong 6.50$ Å, with $\beta \cong 90.23°$ at 10 K. Therefore this LT phase is named low-temperature monoclinic (LTM) subsequently. Accordingly, the evolution of the cell parameters with temperature was studied and the results are reported in Figure 3-35 in the 10 to 300K range.

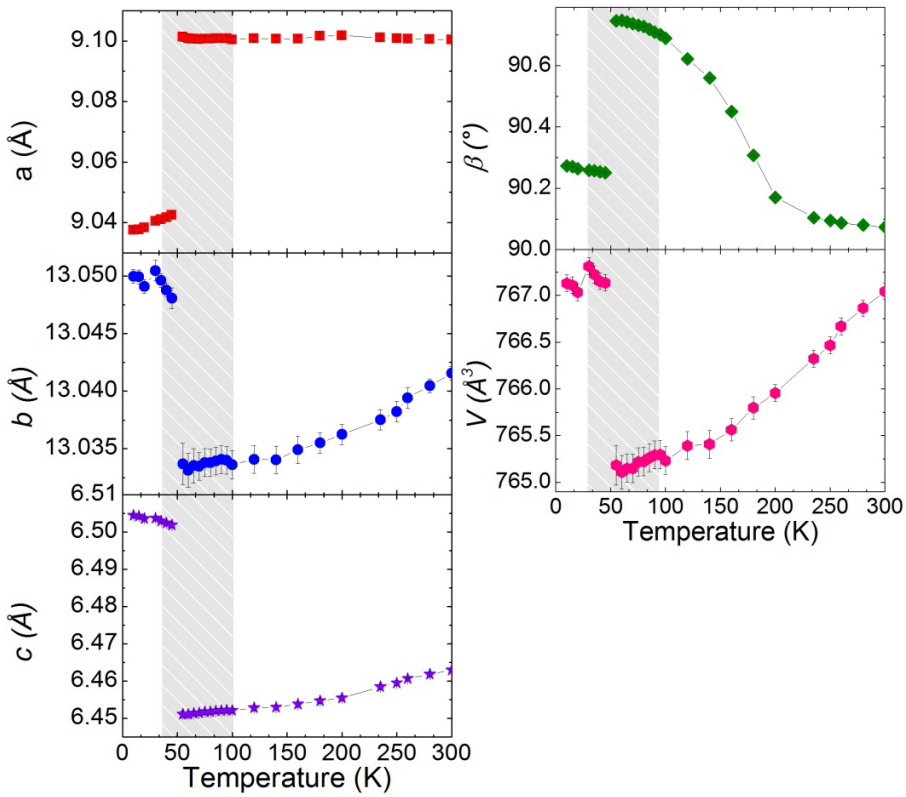


Figure 3-35 Temperature evolution of lattice parameters and cell volume of Mn_2TeO_6, from SXRPD data (Le Bail fit). Between 295 and 205K the parameters are extracted from data (Figure 3-30) recorded upon cooling, while between 200 and 10K they are obtained upon warming (Figure 3-32). The grey area indicates the temperature range where the two phases (RTM and LTM) coexist.

In the biphasic area, only the characteristics of the main phase are reported. Decreasing the temperature from RT, the volume of the RTM phase decreases progressively down to the transition temperature, below which a sudden volume increase is observed (LTM

phase), leading to a volume of the LTM below 40K close to that of the RTM one at 300K. This is also seen on the cell parameters, in opposite ways: there is a decrease of *a*, an increase of *b* and *c*, while the monoclinic angle is strongly reduced (Figure 3-35).

Regrettably, as explained before (see inset of Figure 3-34), the Le Bail fitting performed with these cell metrics is not fully adequate, as a few small extra peaks remain unaccounted for. No solution based on one propagation vector in one direction was found to index all the extra peaks, despite numerous trials. On the other hand, many solutions using several commensurate or incommensurate modulations along at least two cell directions were found. It is thus impossible to determine uniquely and unequivocally the propagation vectors at the origin of the observed extra reflections and thus to go in more details in the description of the low temperature crystal structure of Mn_2TeO_6. As an example, one solution with propagation vector $\boldsymbol{k}$ = (1/2 0 1/4) indexes all the reflections observed in the LTM phase, as shown in Figure 3-36; the corresponding cell is so large, and so many calculated Bragg peaks have no intensity, that it is not possible to ascertain the validity of this solution.

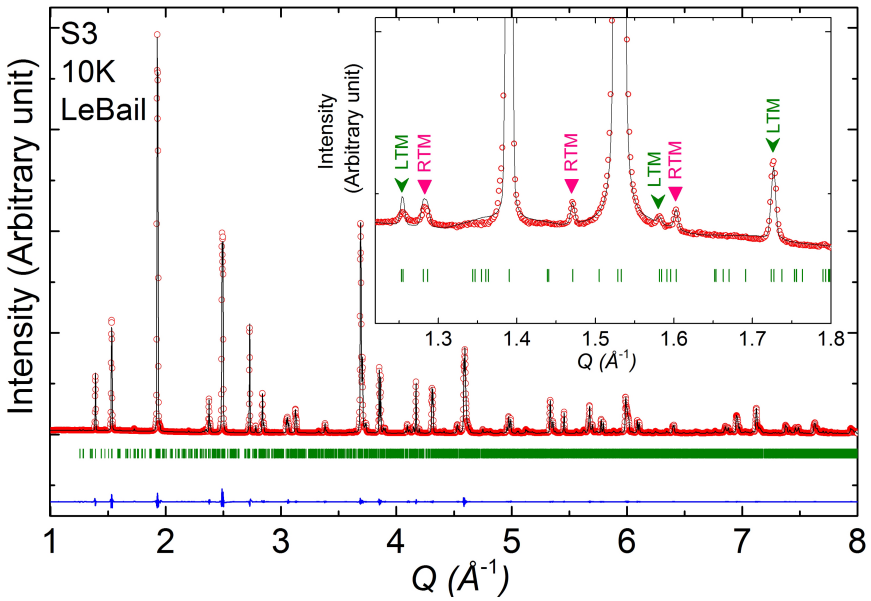


Figure 3-36 Le Bail fit of the SXRPD data of Mn_2TeO_6 at 10K. The inset shows a Q-range chosen to show the small peaks (pink arrows: RTM-like b doubling, green arrows: LTM), indexed in the monoclinic structure ($P2_1/c$, a = 9.0386 (1) Å, b = 13.0498 (1) Å, c = 6.5048 (1) Å, β = 90.285 (1) °) with $\boldsymbol{k}$ *= (1/2 0 1/4).*

These attempts show in any case additional modulations with respect to the RTM cell, leading to a large complex structure necessarily involving new distortion modes. The example of the model based on a (1/2 0 1/4) superstructure gives ≅ 18 x 13 x 26 $Å^3$ structure which contains 144 atoms (32Mn, 16Te and 96 oxygen) in general Wyckoff positions, i.e., 432 structural parameters to refine. It is thus unrealistic at the current stage to determine such a structure using only powder diffraction data, as single crystal or low temperature electron diffraction are now mandatory to go further.

Nevertheless the structural character of the T_S transition being now established and an approach sub cell determined. NPD experiments were carried out to investigate which of the five transitions (including T_S in case of a magneto-elastic transition) on the *Cp* curves correspond to magnetic orderings. Further structural information was also expected, due to higher sensibility to oxygen and to higher Mn/Te contrast compared with X-ray.

3.2.4 *LT-NPD study*

Neutron diffraction experiments were carried out on the WISH T.O.F diffractometer (ISIS) and on G4.1 (LLB), from 1.5 to 300K upon warming. The results shown in this section are not an exhaustive report of our whole investigation: as all experiments were in good agreement, only the most representative results are presented.

Crystal structure study

Figure 3-37 shows the results of the NPD study from 1.5 to 250K recorded upon warming on WISH. There is a good agreement between the neutron (S2 sample) and synchrotron X-ray (S3 sample) diffraction patterns, with the two phases coexisting in the [100 - 52K] temperature range and a structural transition at Ts ≅ 60K.

Below 50K, the crystal structure corresponds to that of the LTM phase. In addition to the crystal structure Bragg peaks, Bragg reflections due to long-range magnetic ordering appear at T_{N1} ≅ 46 K and change in position and intensity at T_{N2} ≅ 24 K, but

they are in excellent agreement with the previous results (Figure 3-29). The determination of the structural transition temperatures is less accurate on diffraction data, as the temperature step between two recorded patterns is much larger than between two points on a *Cp*(T) or χ(T) curve.

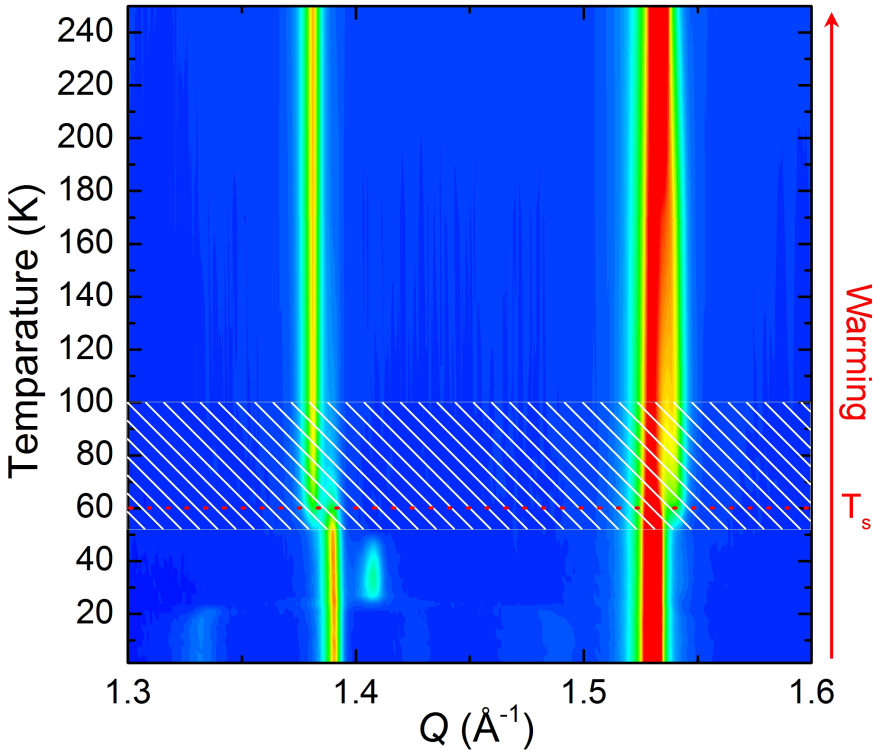


Figure 3-37 Temperature evolution of the NPD patterns of Mn_2TeO_6 (S2 sample), in a selected Q range, from 1.5 to 250 K upon warming (WISH@ISIS). The dashed area corresponds to the two-phase temperature range. The horizontal red dot line indicates Ts.

It is difficult to use the RTM model to refine the structure (even above 120K) using these NPD data, since the superstructure peaks caused by the *b*-doubling (visible on XRPD) are too weak to be visible. The same is also true for the extra peaks of the LTM phase. Nevertheless, the evolution of the cell parameters can be studied (not reported here) and is in good agreement with Figure 3-35.

Magnetism and magnetic structure study

Figure 3-38 presents the evolution with temperature of the NPD data upon warming recorded using G4.1. These diffractograms are in agreement with the previous

observations on WISH of new Bragg peaks of magnetic origin, as emphasized in Figure 3-38b. Two magnetic transitions are confirmed at ≅ 46 K and ≅ 25 K upon warming, in good agreement with at T_{N1} ≅ 48 K and T_{N2} ≅ 25 K obtained from *Cp*(T) (Figure 3-29) and χ(T) curves (Figure 3-26). There is no obvious sign of short-range ordering above T_{N1}. It is also clear that the first magnetic transition occurs only at the end of existence of the biphasic domain (with decreasing temperature), which imply a strong link between the structural and magnetic transitions.

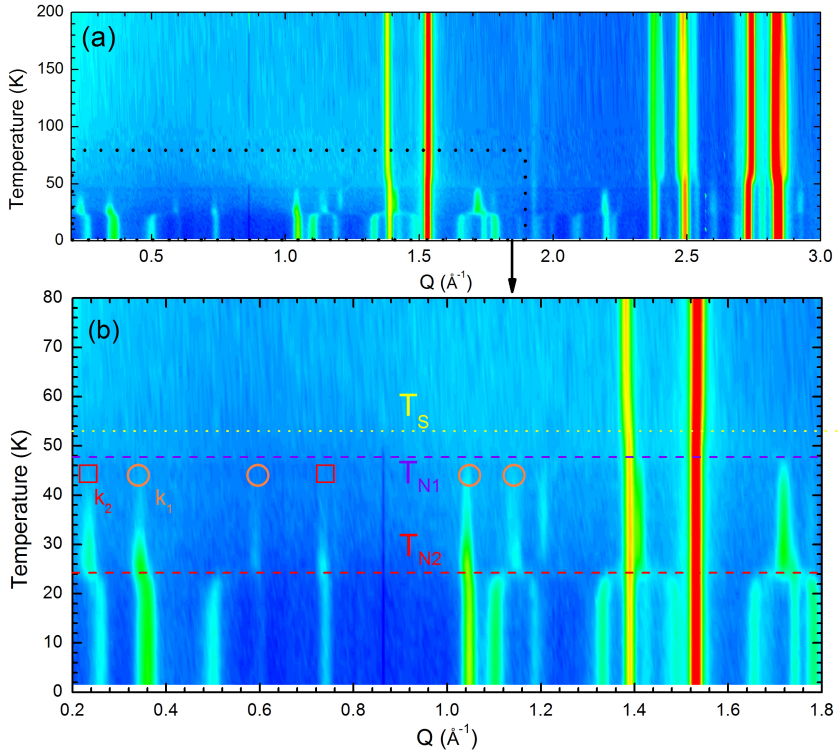


Figure 3-38 Temperature evolution of the NPD patterns (G4.1) of Mn_2TeO_6 (S2 sample) (a) between 1.5 K and 200 K, in the 0.2 - 3 Å^{-1} range (b) between 1.5 and 80 K, in the 0.2-1.8 Å^{-1} range. T_S is marked in yellow, T_{N1} in purple and T_{N2} in red. Main magnetic Bragg peaks and their corresponding propagation vectors are also shown (circles and squares for $\mathbf{k_1}$ *and* $\mathbf{k_2}$ *respectively).*

Without the details of the "exact" LT structure including its true cell parameters, the determination of magnetic propagation vectors is rather problematic. As a first approximation, we tried to index the observed magnetic peaks using the average unit cell parameters of the LTM determined previously from the SXRPD study ($P2_1/c$, a ≅ 9.039 Å, b ≅ 13.05 Å, c ≅ 6.505 Å, β ≅ 90.29°). This approach allows one to index the

magnetic Bragg peaks between T_{N1} and T_{N2} with two commensurate propagation vectors, namely $\boldsymbol{k_1}$ = (1/2 0 0) and $\boldsymbol{k_2}$ = (0 1/2 0), which correspond respectively to a doubling along *a* and *b* of LTM. Figure 3-39 shows the result of the Le Bail fitting of the NPD pattern recorded on WISH at 27K, i.e. below T_{N1} and just before T_{N2}, with the indexation of the main magnetic peaks using $\boldsymbol{k_1}$ and $\boldsymbol{k_2}$.

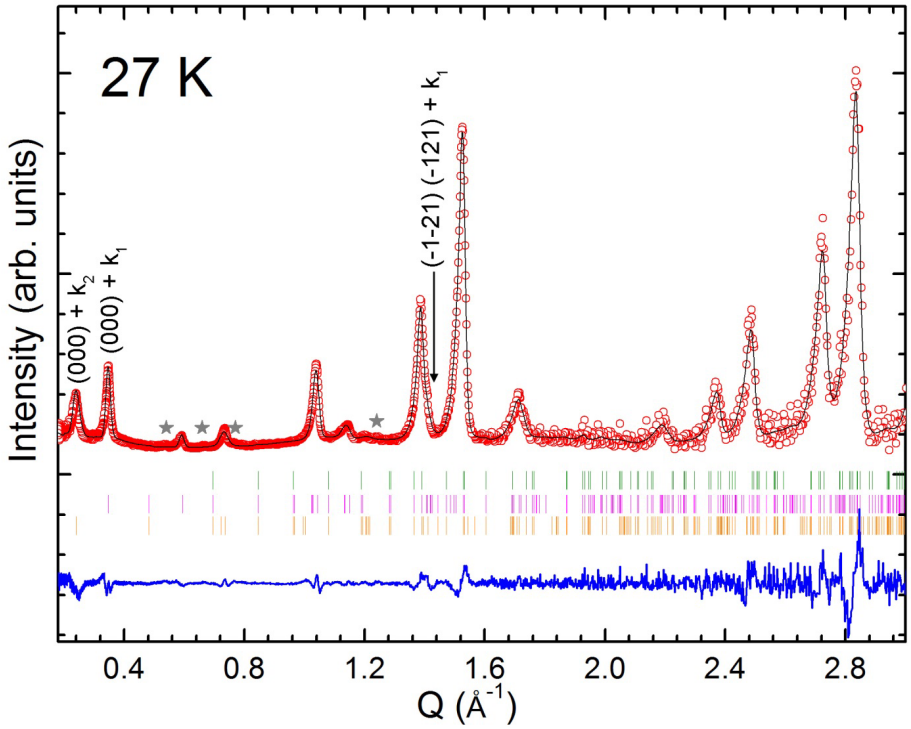


Figure 3-39 Le Bail fitting of the LT crystal structure of Mn_2TeO_6 at 27 K (WISH): $P2_1/c$ with a = 9.0354 (2) Å, b = 13.0478 (3) Å, c = 6.5039 (1) Å, β = 90.2302 (2) ° and the magnetic peaks indexed with $\boldsymbol{k_1}$ = (1/2 0 0) and $\boldsymbol{k_2}$ = (0 1/2 0). Weak additional magnetic peaks are outlined by grey stars.

These propagation vectors $\boldsymbol{k_1}$ and/or $\boldsymbol{k_2}$ do not index successfully, either partially or wholly, the extra peaks observed on the SXRPD patterns. This means that the true crystal structure does not correspond to a mere doubling along *a* and *b* of the LTM metrics used so far.

Both $\boldsymbol{k_1}$ and $\boldsymbol{k_2}$ magnetic peaks appear at the same temperature (T_{N1}) and shift concomitantly to incommensurate positions at T_{N2}, strongly suggesting that $\boldsymbol{k_1}$ and $\boldsymbol{k_2}$ do not belong to two different phases or to decoupled sublattices (Figure 3-38b), but

describe a single complex magnetic ordering. No simple solution (that is involving only one incommensurate component) was found to describe the incommensurability of $\boldsymbol{k_1}$. For $\boldsymbol{k_2}$, a possible indexation is $(0, 1/2+\delta, 0)$ with $\delta \sim 0.05$ at 1.5 K.

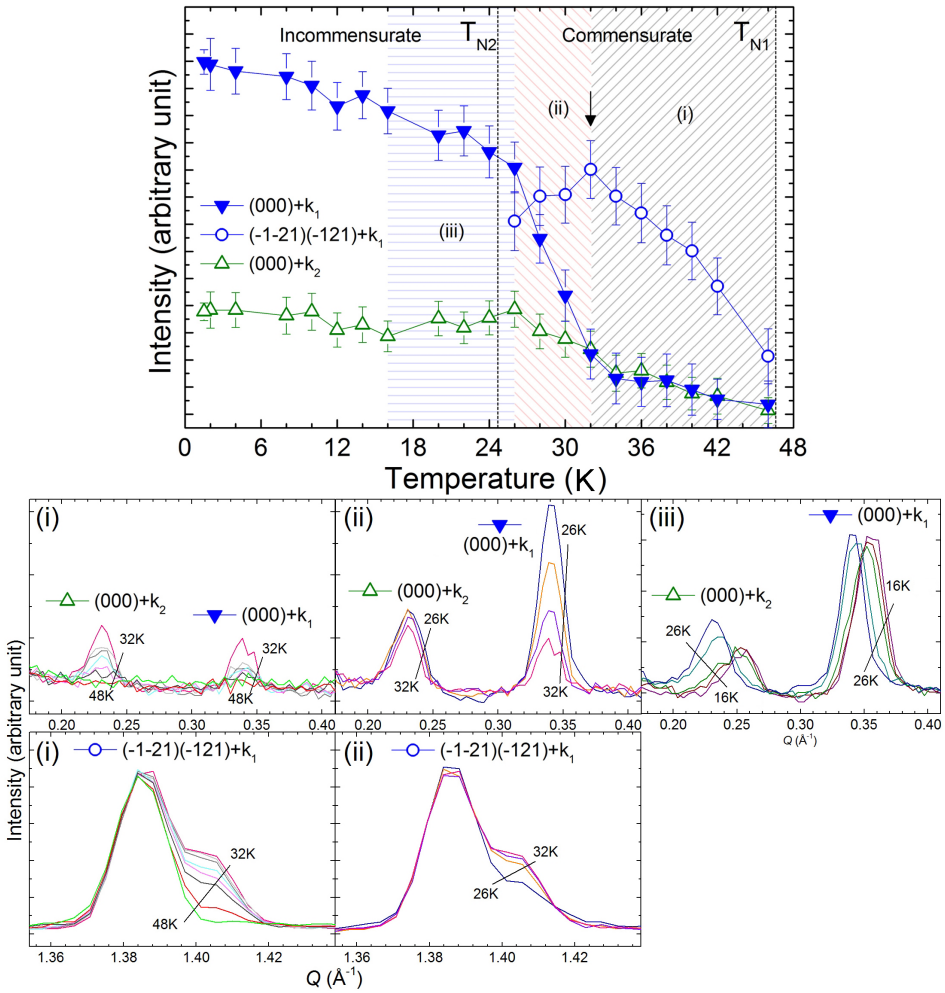


Figure 3-40 Upper panel: Temperature evolution (below T_{N1}) of the integrated intensities of a few magnetic Bragg peaks (G4.1 data, see indexation on Figure 3-39 with the 27K pattern). The vertical arrow shows the maximum of intensity for the (-1 -2 1) (-1 2 1) + $\boldsymbol{k_1}$ Bragg peak. Lower panel: NPD patterns in selected T - range and Q - range used to build the plot above.

Nevertheless more information can be gathered from the neutron diffraction data. Magnetic Bragg peaks indexed with $\boldsymbol{k_1}$ are more intense and sharp than the ones indexed with $\boldsymbol{k_2}$ (see Figure 3-39 and Figure 3-40). In addition, the temperature evolution of the intensity of chosen magnetic peaks, (0 0 0)+$\boldsymbol{k_1}$, (-1 -2 1) (-1 2 1)+$\boldsymbol{k_1}$ and (0 0 0)+$\boldsymbol{k_2}$ shows that magnetic intensity of the (-1 -2 1) (-1 2 1)+$\boldsymbol{k_1}$ peaks actually

goes through a maximum around 33 K (arrow on Figure 3-40), concomitantly with an increase of the magnetic intensities on (0 0 0)+$\boldsymbol{k_1}$ and (0 0 0)+$\boldsymbol{k_2}$. This could be linked with the very broad second order transition which can be discerned between 34 K and 30 K on the *Cp* curve (Figure 3-29) and with the weak transition feature observed on χ(T) at ≅ 35K, which seems to be magnetic field sensitive (Figure 3-27b), and could arguably be ascribed to a spin reorientation before the incommensurate ordering. There is no clear sign of subsequent magnetic transitions below 25 K on the NPD data so that the origin of the two additional transitions on the *Cp*(T) curve remains an open question. It should also be added here that, on the high-resolution NPD data recorded at WISH, weak broad magnetic peaks can be seen (grey stars on Figure 3-39), which are not indexed by either $\boldsymbol{k_1}$ or $\boldsymbol{k_2}$ in the commensurate or in the incommensurate phase, suggesting an even more complex magnetic arrangement, possibly involving short-range correlations.

At this stage it is obviously elusive to propose a detailed magnetic ordering model for Mn_2TeO_6. It is interesting nonetheless to compare the present results with those reported by Fruchart et al. (*7*) for a tetragonal polymorph. The magnetic ordering proposed for tetragonal Mn_2TeO_6 can be described by a doubling of the cell along the 4-fold axis (equivalent to $\boldsymbol{k_1}$ in this work) and corresponds to a collinear magnetic structure with an alternation along *c* of ferromagnetic and antiferromagnetic pairs. Because these pairs should be symmetrically equivalent, the change of the coupling sign did not seem physical to Fruchart, who instead, proposed a non collinear magnetic structure with the same magnetic structure factors. This non collinear magnetic structure has orthogonal spins lying in the *ab*-plane; spins inside a pair of MnO_6 are always orthogonal, and spins belonging to adjacent corner-sharing octahedra are antiparallel (illustration in Figure 3-41a). This model is actually not in agreement anymore with symmetry analysis (performed for Mn, lying on the (*4e*) Wyckoff site of $P4_2/mnm$, with $\boldsymbol{k}$ = (0 0 1/2) – more details can be found in Section 4.4). Possible models can also lead to a non collinear magnetic structure with orthogonal spins, but with antiparallel spins inside the edge-sharing MnO_6 pairs, and parallel spins in corner sharing MnO_6 pairs between the bilayers separated by TeO_6 (see Figure 3-41b). They

do not have the same calculated structure factors as Fruchart's model, but actually match his data reasonably well. Consequently we will consider in the discussion the magnetic ordering allowed by symmetry analysis, which is, moreover, more consistent with the AFM coupling in pairs of edge sharing octahedra observed in other inverse trirutile structures (*15*, *116*). This model is obviously far too simple to describe the magnetic structure of monoclinic Mn_2TeO_6 as (i) it does not taken into consideration the LTM supercell, (ii) it does not take into account the magnetic modulation along *b* ($\boldsymbol{k_2}$) and (iii) it does not describe spin reorientation.

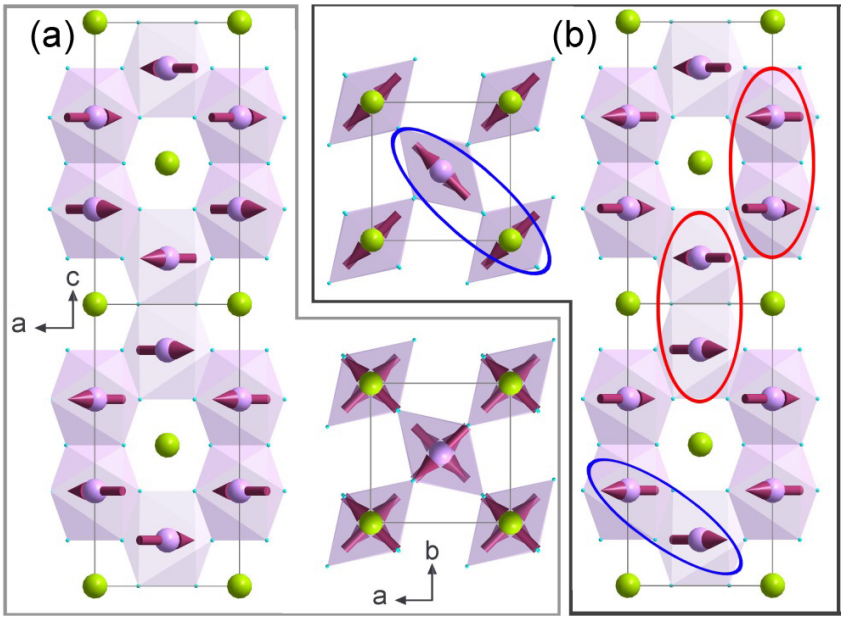


Figure 3-41: Views along b and c-axis of the magnetic model for the tetragonal Mn_2TeO_6; as proposed by Fruchart (7) in (a) and derived from the Γ_3 representation in (b) The red ellipses show the magnetic bi-unit made of two edge-sharing octahedra, while the blue ellipse show corner sharing octahedra.

Based on these considerations, the magnetic ordering of distorted trirutile Mn_2TeO_6 should be seen as a complex modulation of the more simple one expected in the case of a tetragonal structure, retaining the most important features, like, the orthogonal orientation of the Mn moments in the "basal" plane (i.e. the plane perpendicular to the Te-Mn-Mn-Te chains), and the antiparallel coupling within each bi-unit made of two edge-sharing octahedra. To this simple picture should be added a modulation of either the amplitude and/or the orientation of the moments, likely following the complex pattern of octahedral distortions that is presumed in the low temperature crystal

structure. In both cases, the temperature dependence of the magnetic ordering is complex, spin reorientations or ordering of disordered components are expected, following the cascade of transitions identified on the *Cp*(T) curve.

3.2.5 *Effect of applied magnetic field*

Magnetization vs. H

M(*H*) curves were collected at several temperatures below 60K as shown in Figure 3-42. The curves collected at 5 and 10K are similar: they first show a linear domain, with similar slopes; then (for > 4.5T) the slopes increase corresponding to a smooth metamagnetic transition; followed by another linear *M*(*H*) dependence for $\mu_0 H > 13$ T with a steeper slope than in the first domain. To summarize, the *M*(*H*) curve have a flattened S-shape.

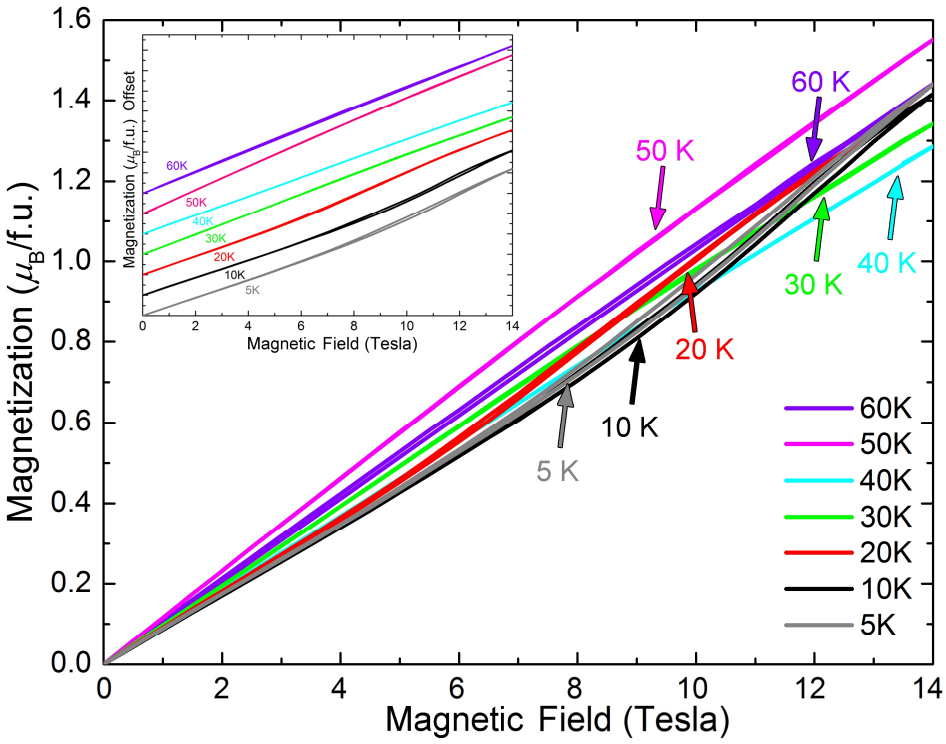


Figure 3-42 Magnetic field dependence of magnetization of Mn_2TeO_6 recorded at 5, 10, 20, 30, 40, 50 and 60K. A small hysteresis is seen in the M(H) curve at 5 and 10K.

For higher temperatures (30, 40, 50 and 60K) no such transition is observed, indicating that the metamagnetic transition exists only for the LT magnetic state (see inset of

Figure 3-42), and suggesting that it is related to the AFM state below T_{N2}. This is confirmed by the 20K curve which exhibits an intermediate behavior. Moreover the fact that the magnetization values recorded at 14T are smaller at 30 and 40K means that the application of a magnetic field does not transform the LT state (< T_{N2}) in the other one (T_{N2} < T < T_{N1}). All these results suggest that the more stable antiferromagnetic state is observed around 40K.

Dielectric constant vs. H

Figure 3-43 shows the dielectric constant as a function of magnetic field at 10K and the magneto-dielectric (MDE) effect (calculated as $[\varepsilon'_H-\varepsilon'_0/\varepsilon'_0]$ x 100 (%) , where ε'_H and ε'_0 are dielectric constants measured with and without magnetic field, respectively).

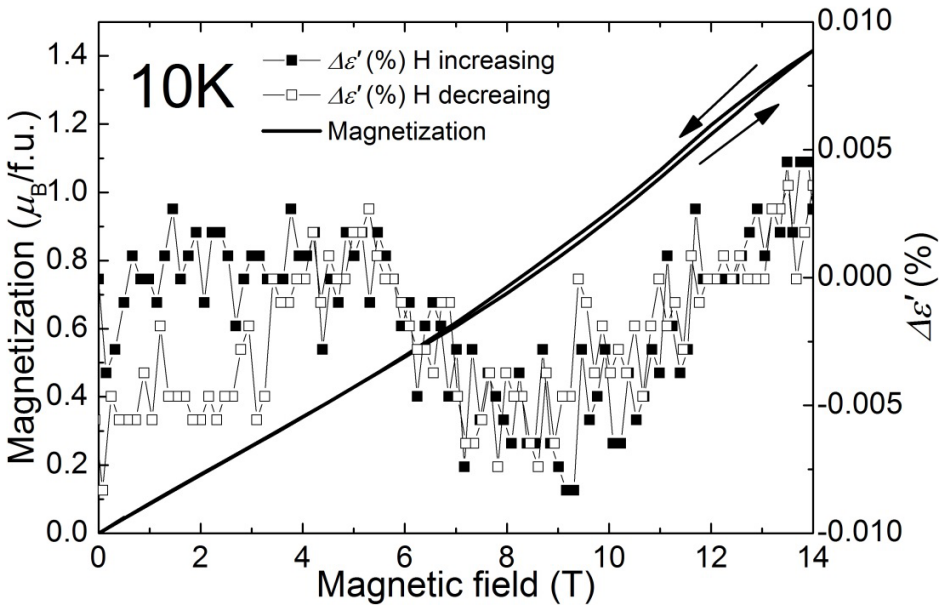


Figure 3-43 Magnetic field dependence of dielectric constant measured in Mn_2TeO_6 recorded at f =100 kHz at 10K. M(H) curve (10K) is also shown for comparison.

It shows that some degree of coupling exists between spins and charges, as the MDE effect at 10K shows a minimum at 9 T which corresponds to about half of the metamagnetic transition completion. This negative MDE regime starts for $\mu_0 H$ > 5 T – 6 T, $\mu_0 H$ value below which the $M(H)$ curve at the same T is linear.

3.2.6 *Structural and magnetic behavior of different Mn_2TeO_6 samples*

As already mentioned, numerous samples were prepared during this thesis, changing the conditions to improve the sample quality or to check the effect of parameters such as temperature, atmosphere etc. A large number of samples were thus characterized and the comparison of the results brings interesting information, described in what follows.

Magnetic measurements of Mn_2TeO_6 were done on a series of samples annealed in different conditions. In the experimental section, details were given for the synthesis of samples labelled S1 (600°C in air) and S2 (700°C in O_2 flow). The effect of synthesis conditions upon the χ(T) curves is shown in Figure 3-44. Increasing temperature, whatever the samples, the magnetic signal increases slightly up to a characteristic temperature at ≅ 27K (taken at the maximal of intensity), corresponding to T_{N2} in the previous sections. The S1-type samples exhibit only this transition. For the S2-like compounds, increasing temperature again, a second bump is observed on the χ(T) curves allowing a second temperature transition to be determined that, in contrast with the first one, varies slightly from sample to sample in the range ≅ 65 - 60K. It is rather difficult to control precisely this transition temperature by annealing.

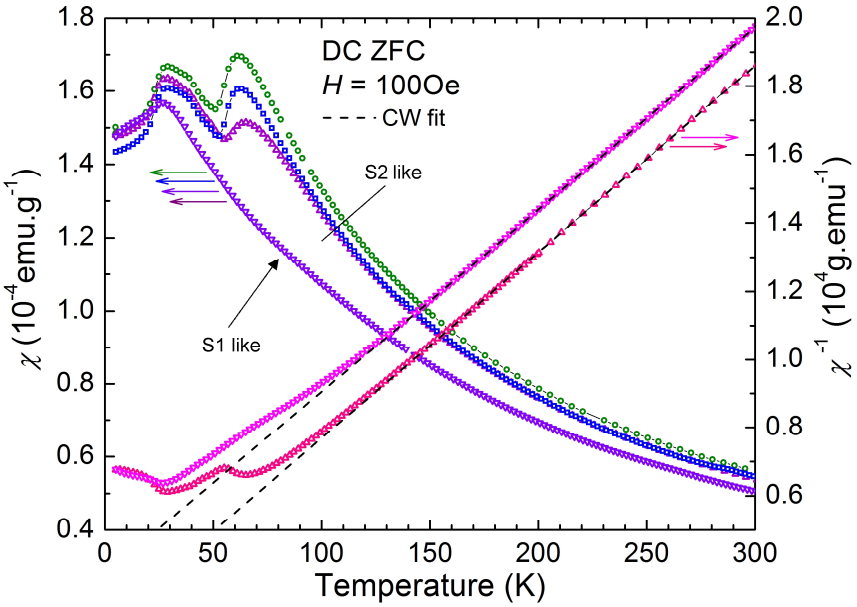


Figure 3-44 Temperature dependence of the zfc (left axis) susceptibility and (right axis) inverse susceptibility curves of S1 sample (inverse triangle) and S2 like samples (triangle, square and circle) of Mn_2TeO_6 recorded under 100 Oe.

The inverse of the susceptibility curves of all samples show a large linear domain whose Curie-Weiss fitting leads to a similar μ_{eff} value (≅ 5.0 μ_B/Mn). This confirms the trivalent state of manganese, in agreement with RT-XANES results (Figure 3-25), in all the samples. Some differences appear on the χ^{-1} (T) curves; for S1, the curve departs from the Curie-Weiss law at a temperature which is much higher than T_{N2} ≅ 27K, and this divergence temperature (≅ 110K) is close to the one observed for S2 like sample. These observations suggest that there are antiferromagnetic interactions in this temperature range, as premises of the transition observed at T_{N1} for S2. The low-temperature behaviors of two S1 and S2 samples were also compared using neutron diffraction data recorded on WISH upon warming (Figure 3-45). This comparison should be taken with caution because (i) the patterns are not recorded at the same temperatures in both sets and (ii) the peak broadening is different for both samples (Figure 3-6).But, both samples show a structural phase transition from RTM to LTM accompanied by similar large biphasic area (vs T) and two magnetic transitions at ≅ 48K and ≅ 27K. The magnetic transition at T_{N1} that was not clear in the magnetic susceptibility curve of the S1 sample (Figure 3-44) is obvious on the neutron diffraction patterns.

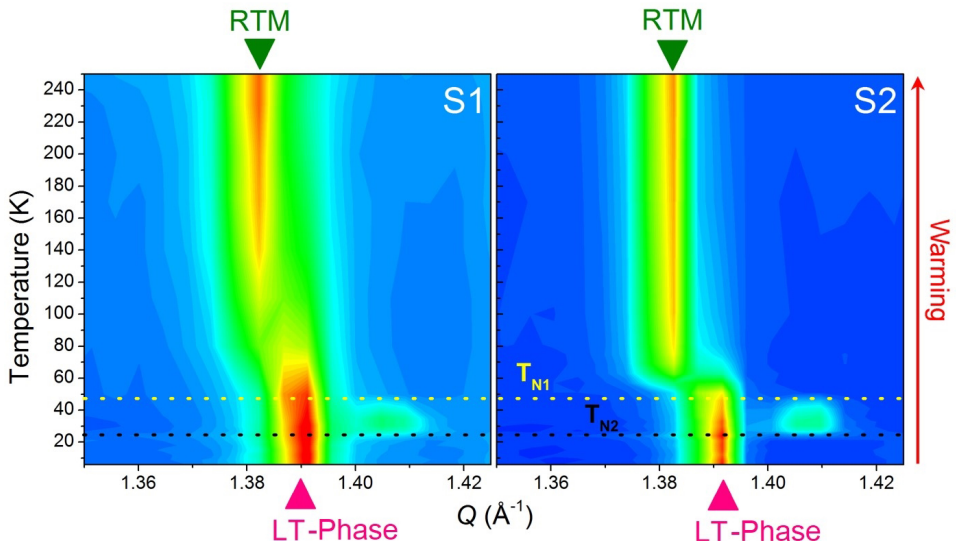


Figure 3-45 Temperature evolution (from 6 to 250K) of the NPD patterns (selected Bragg peaks) of Mn_2TeO_6 (Left: S1, Right: S2 sample) recorded upon warming. Green triangles (top of figure) and pink triangles (bottom of figure) point out Bragg peaks belonging to RTM and LT phase, respectively. The horizontal yellow and black dotted lines indicate the T_{N1} and T_{N2} magnetic transition, respectively.

3.3 *Discussion*

It is difficult to review our results because the observed structural and magnetic phenomena are complex and rather unusual, and also because some small differences are observed from sample to sample. Moreover we cannot determine clearly the low temperature structure of Mn_2TeO_6, which hinders solving the magnetic one and interpreting fully the observed results. Nevertheless, we combine in the following all the information gathered previously to obtain as unified and complete a picture as can be.

Figure 3-46 gathers the structural results presented in the previous sections, allowing one to overview the Mn_2TeO_6 structure evolution from 973K (700°C) down to 2K. The high temperature part (right) corresponds to neutron diffraction data recorded for the S2 sample in cooling mode and complete Rietveld refinements (HTT and RTM phases). The low temperature graph (left) corresponds to SXRPD data recorded on S3 while warming; Rietveld calculations were performed using RTM and equivalent LTM models, but refining only the cell parameters and scale factors. In the biphasic area, the phases are reported when the corresponding amount is 5% at least. For easy comparison the cell parameters are reported using the monoclinic setting, which means that the Te-Mn-Mn-Te chains are oriented along the *a*-axis.

In the 2-973K temperature range, all Mn_2TeO_6 samples present at least two structural phase transitions (HTT to RTM ≅ 673K (400°C) and RTM to LTM ≅ 100K whose average sub-cell only is known). As is usually observed, decreasing the temperature from 973K, the cell volume decreases. There is no impact on the volume at the tetragonal to monoclinic transition, but there is a sudden increase of the volume (≅ +0.3%) corresponding to the RTM to LTM structural transition.

The cell parameters evolution with temperature is more complex. A small monoclinic distortion appears at 673K and increases slowly as the sample is cooled down; a sharper increase of the β-angle is seen below 200K, to reach 90.75° (+0.78%) at its maximum in the RTM phase. In contrast, in the LTM phase it is only 90.30° at 50K (-0.57% refers to RTM phase at same T). At the high temperature transition at 673K, the *c* parameter decreases slightly, then decreases progressively in the RTM phase, to increase again in

the LTM phase (+ 0.78%). The *b*-parameter shows a small (positive) jump at both transitions. Along the Te-Mn-Mn-Te chains, the *a*-parameter stops decreasing at 823K (550°C), before increasing again below 673K. This increase takes place progressively and the parameter does not vary down to 50K in the RTM phase, it is however strongly shortened in the LTM phase (-0.62 %).

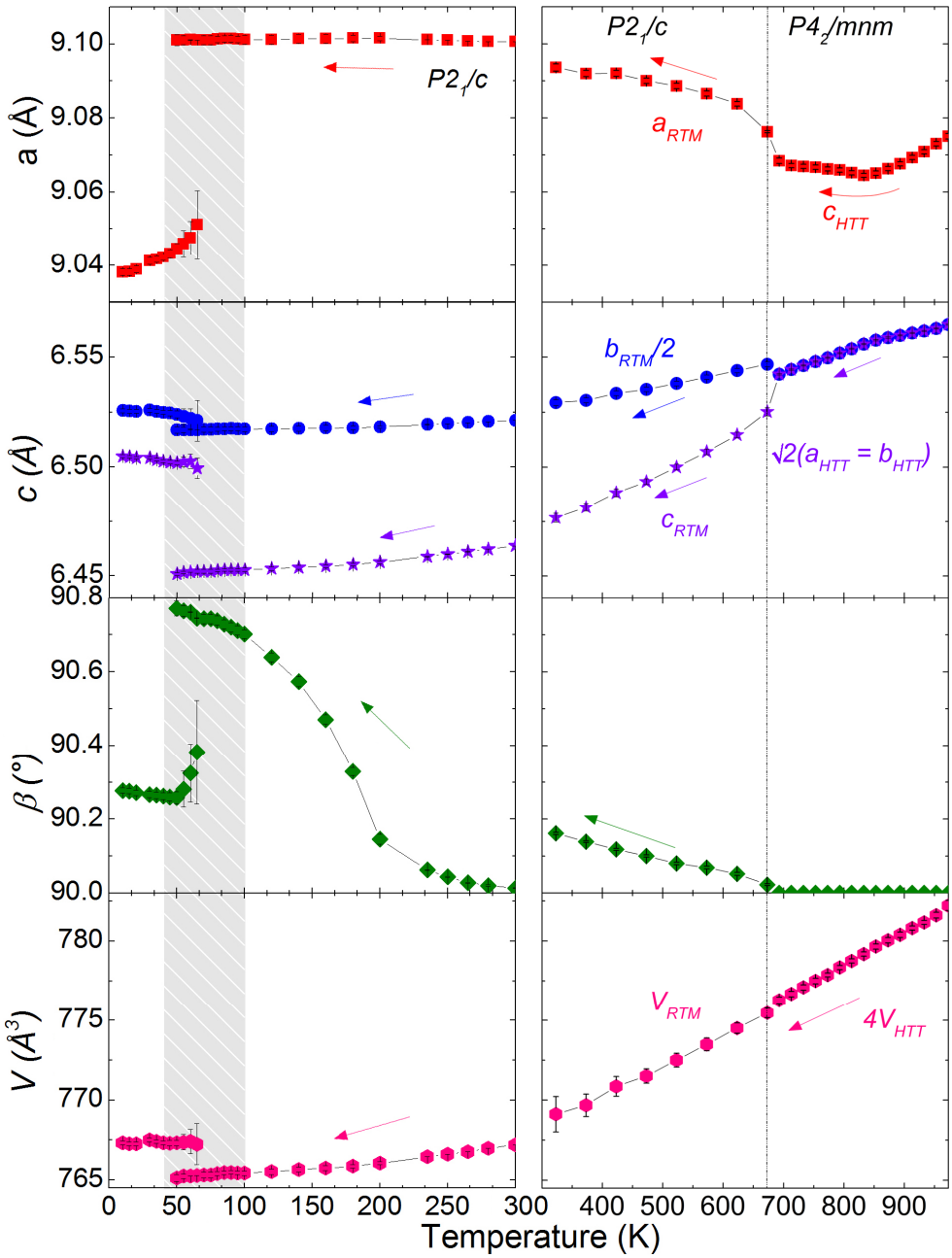


Figure 3-46 Evolution of the cell parameters of Mn_2TeO_6 between 973 and 1.5K.

The high temperature transition is smooth and broad, compared with the low temperature one that is very sharp but associated with a biphasic domain. The evolution of the ratio of the RTM and LTM phases in this biphasic domain is illustrated on Figure 3-47-down. The cooling/warming hysteresis is once more observed, the biphasic domain being larger in warming, in good agreement with the magnetic properties (Figure 3-47-up). The temperature for which both phases coexist in the same amount (50%-50%) corresponds roughly to T_s determined from the *Cp*(T) and χ(T) curves.

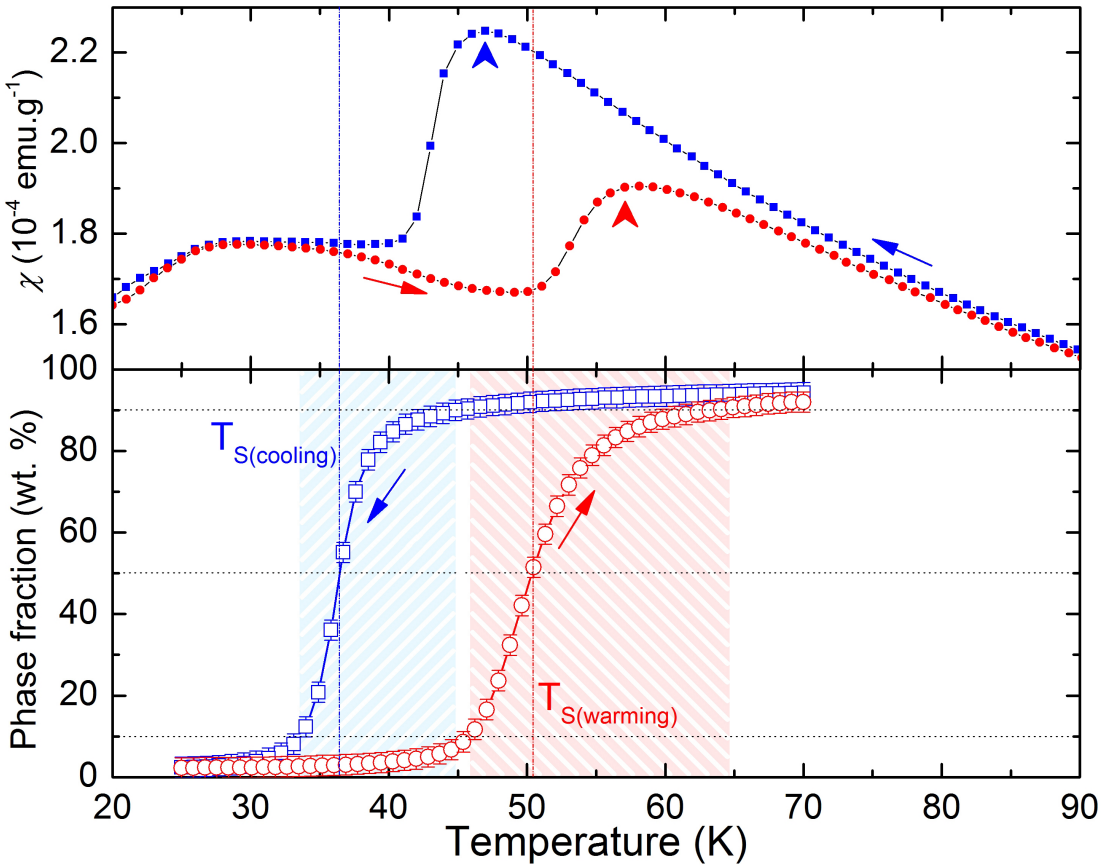


Figure 3-47 Transformation of the RTM to LTM phase versus temperature in warming and cooling; the biphasic areas in red (warming) and blue (cooling) are determined using a 10% threshold (lower panel) and corresponding χ(T) curves (upper panel).

It is well known that orbital degrees of freedom are an important ingredient of the physics of manganites with Jahn-Teller active Mn^{3+} cations in octahedral coordination. For instance, cooperative Jahn-Teller (JT) distortions take place in manganese perovskites $LaMnO_3$ and $TlMnO_3$ up to 750K, and in $PbMn_7O_{12}$ ordered quadruple

manganites up to 294 K, inducing complex crystal and magnetic structures (*43*, *117*, *118*). The inverse trirutile compound shows some similarities with the well-known mixed valence $Pr_{0.5}Ca_{0.5}MnO_3$, for which a structural transition, associated with charge ordering appears at higher temperature than the antiferromagnetic one. Moreover for this manganite, the χ(T) curve evidences more clearly the structural transition than the magnetic one (*119*). In this context, in Mn_2TeO_6, although no charge ordering is expected, orbital ordering (OO) should be discussed.

The JT effect is relatively straightforward to explain with crystal-field theory. The crystal-field characteristics of the octahedral symmetry splits the electronic configuration of Mn^{3+} ($3d^4$) to triplet t^3_{2g} (3 spins in t_{2g}), and doublet e^1_g (1 spin in e_g) and the Hund's-rule coupling dictates a ferromagnetic coupling for the t^3_{2g} and e^1_g electrons, the so-called high spin configuration. As shown in Figure 3-48, the JT distortion gives rise to the displacements of Mn-coordinated oxygen, resulting in a low-energy e^1_g level that removes the orbital degeneracy (*63*, *120–122*). In case of a d^4 high-spin configuration, both configurations (compressed and elongated) can lower the energy of the system. It is not easy to predict how octahedra will distort because of the JT effect, but generally, in oxide compounds, the d^4 high-spin configuration tends to be stabilized by inducing an elongation of the octahedron rather than a compression (*63*).

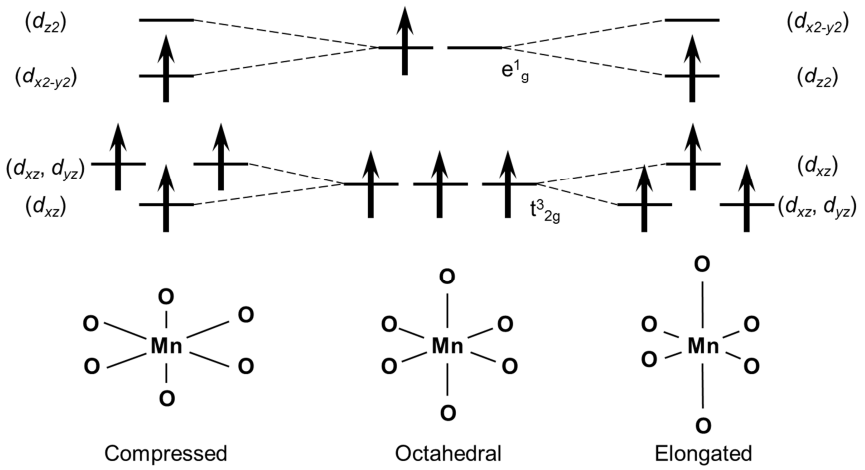


Figure 3-48 The two Jahn-Teller distortions of the manganese (III) octahedron (high-spin configuration), (left) compressed and (right) elongated. Both distortions lower the energies of one electron in the eg level. (*63*)

One useful factor to quantify the relative distortion of MnO_6 across the transitions is the distortion parameter Δd, which corresponds to the deviation of Mn-O distances with respect to the average ⟨Mn-O⟩ value. The Δd values given in Table 3-3 and Table 3-8 show that the distortion of the MnO_6 octahedra increases on going from the HTT (Δd = 1.0 x 10^{-4}) to RTM (Δd = 17.6 – 30.9 x 10^{-4}). This evolution is comparable with the one observed in $LaMnO_3$: Δd increases from Δd_{HT} = 0.9x 10^{-4} to Δd_{LT} = 33.1 x 10^{-4} through the OO transition (*118*).

In the HTT phase, the two apical bonds lying in *ab*-plane are always slightly longer than the four equatorial bonds in both Mn and Te octahedra, which is a well-known tendency in rutile oxide (*123*). More precisely, if in the HTT phase MnO_6 octahedra are a little elongated, in the RTM phase the Σ_3 mode displacements of the oxygen atoms lead to strongly elongated $Mn1O_6$ and $Mn3O_6$ octahedra, while surprisingly the $Mn2O_6$ and $Mn4O_6$ octahedra are compressed (Figure 3-19d). The coexistence of both elongated and compressed octahedra probably originates from the sequence of two Mn atoms sandwiched between Te species in each chain (itself a consequence of Mn/Te order), which is supposed to limit the freedom to distort of the Mn octahedra. Indeed, within a chain, all octahedra are connected by edges, and the TeO_6 units are known to be rather rigid (*18*) with shorter and regular bonds, in contrast with the more flexible MnO_6 units. Moreover, the two types of Te-Mn-Mn-Te chains have to adapt their distortions to each other because of their corner sharing.

Figure 3-49 illustrates this behavior: it schematizes the transformation from the HTT to the RTM structure assuming that TeO_6 are rigid octahedra. If $Mn1O_6$ become elongated because of the JT effect (step I), then $Mn4O_6$ octahedra is compressed to adjust oxygen positions along the *a*-axis (step II) without perturbation of the Te1 environment. It means that for each pair of manganese octahedra, one will be elongated and the other one will be compressed. Consequently $Te2O_6$ octahedra tilt, to adjust to the distortion of Mn1 and Mn4 octahedra (step III). In parallel, the second type of chains goes through the same type of deformation, and there is a distortion of the Mn2 and Mn3 octahedra in the *ab*-plane (IV, V). Then, sturdy TeO_6 octahedra prevent the usual elongated distortion of MnO_6 octahedra to extend through the whole chain, and lead to the stabilization of compressed MnO_6 octahedra, and building the herringbone orbital

ordering pattern that is observed in the RTM structure. Examples of compressed octahedra are rare, and as far as we know, have been reported only in $CaMn_7O_{12}$ for Mn^{3+}, first by Bochu et al (*124*). They actually report that only $KCuF_3$ and $KCrF_3$ are known to have apically compressed octahedra, making this finding even more surprising. This finding lead recently to a revisiting of the $CaMn_7O_{12}$ crystal structure (*43*), in which it was shown that actually there is an additional structural modulation in this compound, that leads to an incommensurate rotation of the long bond in the *xy*-plane, and which means that the compressed octahedra is only so in the averaged (un-modulated) structure. In Mn_2TeO_6, the existence of a compressed Mn^{3+} octahedron is therefore a new finding.

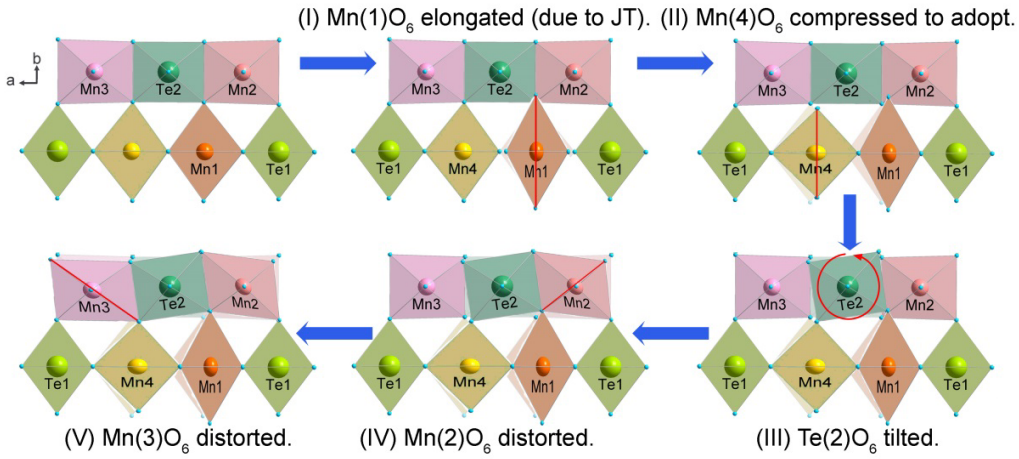


Figure 3-49 Sketches explaining the transition from HTT to RTM, by decomposing the distortions. The sequence follows the blue arrows. The red lines indicate the change at each step (elongation, compression, rotation…).

The second transition from RTM to LTM cannot be described down to such details. Even studying the evolution of the octahedral distortions in the RTM structure from RT down to ≅ 120K is far from straightforward, as the refinements become more difficult and Bragg peak intensities unreliable owing to enhanced strain effects (Figure 3-33). One hypothesis is that the increase of β (Figure 3-46) i.e., the monoclinic distortion could be viewed as a progressive shift of the two types of Te-Mn-Mn-Te chains (Figure 3-50). This sliding can be accommodated by distortions or tilts of the Mn environments only up to a point, after which the structural phase transition to the LT-phase is observed. The fact that the average cell volume of the LT-phase is larger than in the

RTM phase at the same temperature (in the biphasic domain); could be due to a release of the MnO_6 compression. In the LT-phase, there would be therefore a new orbital ordering pattern, involving the standard apically elongated octahedra only, and which would also allow spin ordering in the *bc*-plane. Within such a scenario, the orbital ordering in the RTM phase could be seen as unstable or even built on a "frustrated" JT deformation of compressed MnO_6 octahedra. The JT effect would be again the driving force behind the RTM-LTM structural transition, towards a more stable orbital ordering with z^2 orbitals confined in the *bc*-plane.

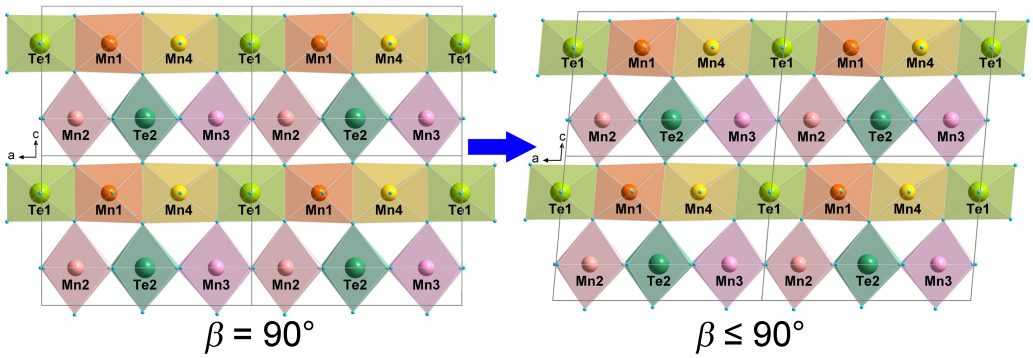


Figure 3-50 (010) projection of RTM structure (β ≅ 90°) and simulated structure model with shorter c-axis and bigger β angle (β ≤ 95°).

Trirutile structures with JT active cations have been studied in the literature, but never with Mn^{3+}, only with divalent Cu^{2+} and Cr^{2+}: $CrTa_2O_6$ (*125*, *126*), $CuTa_2O_6$ (*127*), $CuSb_2O_6$ (*128*, *129*), reported as monoclinic ($P2_1/c$ or $P2_1/n$) at RT. Recently a study has been published on a new 1D Heisenberg magnet, $CuTa_2O_6$ (*130*). Its diffraction study as a function of temperature has evidenced a phase transition at 503K from HTT ($P4_2/mnm$) to RTM ($P2_1/c$) similarly to Mn_2TeO_6. But the monoclinic cell is not doubled along *b*. This difference may be related to the fact that there is no edge-sharing octahedra of JT active cations, as the sequence along the chain is - $A^{2+}B^{5+}B^{5+}A^{2+}B^{5+}B^{5+}A^{2+}$, where A^{2+} is the JT active cation. This would support our scenario, in which the key feature of Mn_2TeO_6 is its pairs of trivalent manganese, which are the origin of both the observed structural transitions.

It is rather difficult to compare rutiles and (inverse)trirutiles as they incorporate a nonmagnetic cation in the chains, nevertheless a parallel can be done. Dimerization of

cations is often argued in rutiles, owing to the overlapping of *d* electrons of the cations in edge-sharing octahedra, for example, NdO_2, MoO_2, $V_{1-x}W_xO_2$ (*131*, *132*). The archetypal compound is VO_2, which exhibits a tetragonal to monoclinic transition associated with a metal to insulator one: a striking feature of this monoclinic phase is the presence of cation-cation pairs along the chains, V-V distances are alternatively 2.65 and 3.12 Å instead of 2.78 Å in the tetragonal phase, just above the transition temperature (*131–134*). Mn_2TeO_6 is naturally dimerized, because of the Te-Mn-Mn ordering along the chains. In its tetragonal phase, Mn-Mn distances are shorter than the Mn-Te ones (see Table 3-3 for instance), and decreasing temperature, In the RTM phase, they slightly increase, in agreement with the increase of the *a*-parameter (along the chains). The largest change in the interatomic distances is observed in the Mn-Te distances, which become alternatively shorter and longer in each chain. Even if it is not possible to quantify precisely the evolution of the Mn-Mn distances in the LTM phase, it is arguable that the strong decrease of the *a*-parameter (along the chain) could correspond to an antiferromagnetic Mn-Mn pairing effect (with spins perpendicular to the chain axis) linked with magneto-striction, as is often encountered in manganese oxides (*135*, *136*).

Negative thermal expansion (NTE) is also worth discussing in Mn_2TeO_6. Thermal expansion is a fundamental property of solids, i.e. the cell parameters increase with increasing temperature; however, although rare, in some compounds the opposite can be observed. The mechanisms involved to explain NTE are classified into three categories, (i) flexible network, (ii) atomic radius contraction and (iii) magnetovolume effect (*137*, *138*). NTE has been reported on $CaMn_7O_{12}$ for which one lattice parameter has a local maximum (50K) and a local minimum (250K), while the unit cell volume continually decreases with decreasing temperature. In this case, there is a charge modulation transition around 250K, which could be correlated with this NTE (*139*), before the magnetic ordering transition at 49K. In Mn_2TeO_6, we observe two NTE behaviours with decreasing temperature: (I) in the HTT phase, the parameter c_{HTT} has a local minimum at 823K before increasing more clearly at the HTT to RTM transition, (II) a larger NTE, visible in the *V* (T) curve at the RTM to LTM transition, corresponding to a large increase of c_{RTM} (Figure 3-46).

The reason of the anomaly at 823K on c_{HTT} could be linked with the structural transition just a few degrees below, and could correspond to a non cooperative JT effect. At the transition, there is an increase of the average Mn–O distances because of their local JT distortion (*137*).

The most plausible explanation is a magnetovolume effect for the NTE appearing at the RTM to LTM transition. Since Mn_2TeO_6 shows a magnetic transition just after the structural transition from RTM to LTM is completed, and as the magnetic moments are highly likely aligned in the *bc*-plane, it could explain the increase of lattice parameters *b* and *c*. This also reinforces the hyposithesis of a magneto-elastic coupling, the relationship between magnetism and structure is illustrated in Figure 3-51.

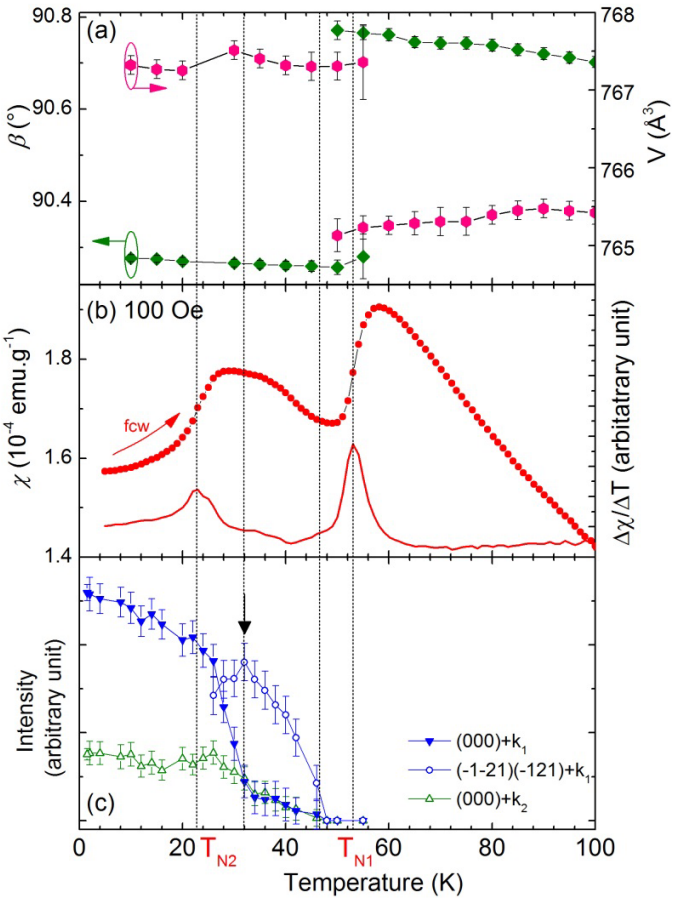


Figure 3-51 Relationships between structural parameters V and β (a), magnetic properties illustrated by χ(T) and Δχ/ΔT(T) curves (b) and the temperature evolution of the intensity of chosen magnetic Bragg peaks (c) from 1.5 to 100K

Moreover, as described in Figure 3-46, *a*-parameter (along rigid edge-sharing chain) shrinks while *b*, *c*-parameter expands, thus volume of cell is net NTE. This tendency could be comparative with anisotropic NTE material silicates, which originated in flexible 2D sheet structure thus expansion occurs in 2D within the sheets and these sheets pulled closed together in the direction perpendicular to the sheets (*138*).

In order to evaluate the magnitude of the NTE effect, the coefficient of linear thermal expansion α is calculated with the following equation:

$$\textit{(Equation 10)}\quad \alpha = \frac{1}{L_0}\frac{dL}{dT}$$

where L and L_0 are the lengths at temperature T and at reference temperature T_0 (*137*, *138*). For example, a typical "normal" thermal expansion compound has α_V = +16.6 ppm/K (Cu) or α_V = +2.45 ppm/K (Si). The calculated α for cell volume of Mn_2TeO_6 between each temperature and 10K is summarized in Figure 3-52.

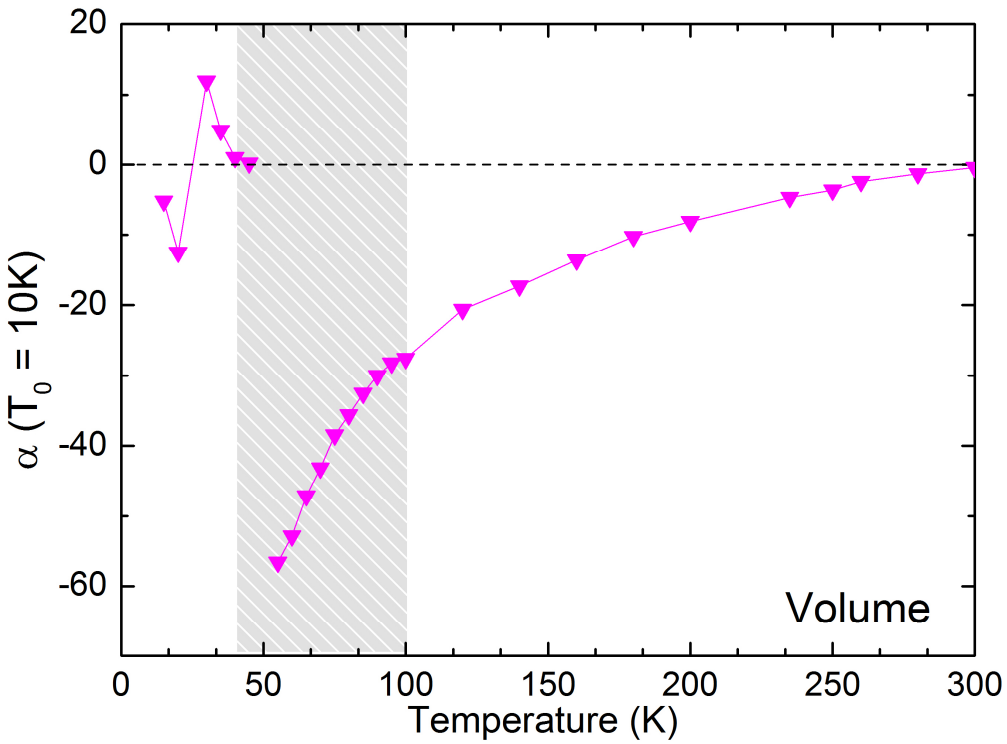


Figure 3-52 Coefficients of the linear thermal expansion α (ppm/K) for the cell volume. Parameters at each temperature (V, T) are used to calculate α_V using 10K parameters as the reference (V_0, T_0). The dashed area indicates the temperature range where the two phases coexist.

For RT, calculated coefficient is α_V = -0.38 ppm/K; this is comparable with reported NTE materials, like ReO_3: α_V = -0.5 ppm/K (*137*). It is interesting to remark that there is almost no volume different between RT and 10K.
In Mn_2TeO_6, the α for volume calculated at 120K is α_V = -20.6 ppm/K. In the 50K to 100K temperature range, α_V of Mn_2TeO_6 is much greater than one of the best NTE oxide ZrW_2O_8 with α_V = -9.1 ppm/K (*137*). Consequently, these interesting NTE effects could lead to the use of Mn_2TeO_6 as thermal-expansion controlled material for applications (*137*, *138*).

Although the presence of the JT active Mn^{3+} cation is fundamental in the behavior of Mn_2TeO_6, other parameters are probably necessary to explain its full complexity. Amongst them, cationic ordering in trirutiles has always been an issue, as exemplified by $FeNb_2O_6$ and $FeSb_2O_6$, for which a rutile structure with random cationic distribution has been reported (*140*, *141*), or by the trirutile tapiolite $(Fe,Mn)(Nb,Ta)_2O_6$, in which metal ions are considered ordered (*142*). In the tapiolite case, different cationic distributions are proposed, however, covering a continuum from perfect order to total disorder. For instance, a single-crystal study of $FeNb_2O_6$ (*143*) describes a structure which is intermediate between disordered rutile and ordered trirutile, while in a natural tapiolite sample the coexistence of both phases is observed (*144*). Such issues led researchers to describe the structure of $FeTa_2O_6$ as modulated, that is, a basic structure plus an occupancy/displacive wave (*4*), to take into account partial cationic ordering. There is no such extensive literature about cationic disorder in the inverse trirutile, but tellurates are known to adopt cation distributions ranging from fully ordered to disordered (*28*). A similar cation distribution may easily occur in our Mn_2TeO_6 because both cations have close ionic radii: Mn^{3+} (HS: 0.64 Å) and Te^{6+} (0.56 Å). If the cationic distribution is at play in the investigated Mn_2TeO_6 samples, it should have an effect on the O sub-lattice, with also displacements or deficiency. Nevertheless our X-ray and neutron diffraction experiments suggest that such disorders would be limited to the standard deviations (<5%) or are at too short range to be visible on these data. Such inhomogeneities at the local scale could explain the differences observed among the series of samples. The diffraction study (SXPRD: Figure 3-6, NPD: Figure 3-45) shows

that the Bragg peaks of S1 (corresponding to the lower temperature synthesis) present a strong asymmetric broadening compared with S2 and S3 samples. This broadening can be discussed as originating from several contributions, (i) the quality of the crystallization (possible traces of an amorphous matrix and distribution of cell parameters), (ii) a grain size effect (confirmed by SEM image (Figure 3-7)), (iii) a local cation distribution and local disordering (evidenced by TEM images in Figure 3-21-Figure 3-23). The refined structural parameters being slightly different, as mentioned before, the main difference between S1 and S2 deals with higher atomic displacement parameters for all atoms (except Mn3, from refinements results not shown). As explained earlier in the NPD study, the structural evolution from RT to 973K is not totally reversible, the cell volume and monoclinic distortion of S1 are bigger than for S2. All these parameters lead to the hypothesis that the degree of ordering is increasing from S1 to S3. Surprisingly, this does not seem to affect strongly the RTM to LTM transition and the magnetic ordering temperatures T_1 and T_2 (Figure 3-45), although the effect on the $\chi(T)$ curves (Figure 3-44) is obvious, with the T_1 transition being almost invisible on the S1 sample. It would be interesting in this context to study, on a S1 sample, the effect of cation disorder on the widths and temperatures of the various transitions observed by *Cp*, as well as on the LTM superstructure peaks.

As a final remark, this disorder (distribution of cations on the sites, distortion of the polyhedra, small deviation from the theoretical Mn_2TeO_6 composition) could probably explain the discrepancies with the report of Fruchart et al. (*7*), who mentioned several monoclinic forms of Mn_2TeO_6 that are different from the present one. Indeed, many parameters seem to be involved -that may be correlated or in competition- and small differences in the synthesis process may induce structural differences difficult to control, but which could impact the orbital ordering. This underlines the necessity to carry on future work on extremely well characterized samples, using an extended combination of techniques similar to the approach presented here.

3.4 *Conclusion and perspective*

In situ neutron powder diffraction shows that Mn_2TeO_6 exhibits the standard tetragonal inverse trirutile structure between 973 (700°C) and 673K (400°C). Below 673K, a structural phase transition occurs toward a distorted form, which is observed down to RT. This complex crystal structure can be described as a superstructure of the high temperature phase, involving a doubling along the *b*-axis and a monoclinic distortion. Strongly distorted MnO_6 octahedra are evidenced, which are arranged following a unusual herringbone pattern of elongated and compressed apical bonds. The existence of residual disorder, seen as oxygen displacement modulations and dislocations on TEM images, could have its origin in local Mn/Te substitutions, a known issue in trirutile compounds. Below RT, an additional first order structural transition, strongly hysteretic, and leading to a biphasic domain spanning almost 50 K is observed. It corresponds to a transition to another monoclinic phase of larger volume, involving a complex superstructure that remains to be determined. Beside this structural transition, which is complete below 40K, four additional transitions are seen, at least two of them being undoubtedly of magnetic origin. Although here again, the magnetic ordering remained unsolved, a tentative description of the magnetic structure is given, based on the antiferromagnetic coupling of Mn spins within edge sharing pairs of MnO_6 octahedra. This extremely complex behavior is interpreted as the result of the existence of Jahn-Teller active Mn^{3+} pairs sandwiched in rigid units of TeO_6: it is proposed that, at the first transition from tetragonal to monoclinic, the cooperative orbital ordering that sets in is rather unstable, owing to the presence of (most uncommon) compressed octahedra. This unstable configuration could then be released at the second (first-order) transition, into a more energetically favorable one, which results into a new, and even more intricate, orbital ordering pattern, in which all octahedra are apically elongated. This scenario needs to be confirmed by single crystal diffraction experiments below 40K.

Chapter 4. Study of Cr-substitution effect in Mn_2TeO_6

In this chapter, we report on the effect of Cr-substitution on the structural and magnetic properties of $Cr_xMn_{2-x}TeO_6$. This study was motivated by the fact that RT structures and magnetic properties are different for Mn_2TeO_6 and Cr_2TeO_6 and the impact of substitution was expected to bring new information that could confirm or not our conclusions on Mn_2TeO_6.

$Cr_xMn_{2-x}TeO_6$ (x = 0, 0.01, 0.025, 0.05, 0.075, 0.1, 0.15, 0.2, 0.5, 1, 1.5, 2) samples were prepared by solid-state reaction. Laboratory XRPD was used to check the quality of the samples, and magnetic properties were investigated using SQUID and PPMS apparatuses. $Cr_{0.2}Mn_{1.8}TeO_6$ was also studied using SXRPD and NPD, in order to investigate in further details its crystal and magnetic structures.

4.1 *Synthesis and Preliminary Structural Characterizations*

4.1.1 *Sample preparation*

$Cr_xMn_{2-x}TeO_6$ samples were prepared by solid-state reaction, based on the synthesis procedure of Mn_2TeO_6 (*7*, *145*), using manganese oxalate ($MnC_2O_4 \cdot 2H_2O$), commercial telluric acid (H_6TeO_6), and chromium oxide (Cr_2O_3). These precursors were weighted to obtain the desired stoichiometry (x = 0, 0.01, 0.025, 0.05, 0.075, 0.1, 0.15, 0.2, 0.5, 1, 1.5 and 2), then mixed in an agate mortar, before being calcined in alumina crucibles at 550°C for 12 h in air. Powders were then ground again, pressed with an uniaxial press

in the shape of bars (≅ 2 x 2 x 12 mm) and sintered at 600°C for 24 h in air, before another sintering at 700°C for a time varying from 24 to 72 h under O_2 flow. A more detailed description of the synthesis process can also be found in Section 2.1.1. Synthesis of Cr_2TeO_6 was done using the conventional solid-state reaction, starting from Cr_2O_3 and TeO_2. Precursors were weighted in the Cr: Te = 2:1.1 ratio, then mixed in an agate mortar. Pressed bars were sintered at 750°C for 48h in air.

4.1.2 *Laboratory XRPD analysis*

XRPD patterns of selected $Cr_xMn_{2-x}TeO_6$ samples are shown in Figure 4-1, from $x = 0$ (Mn_2TeO_6) to $x = 2$ (Cr_2TeO_6). The $x = 1$ and 1.5 samples contain a small amount of Cr_2O_3 as impurity (≅ 4% and ≅ 12%, respectively), but the rest of $Cr_xMn_{2-x}TeO_6$ series was found to be single phase.

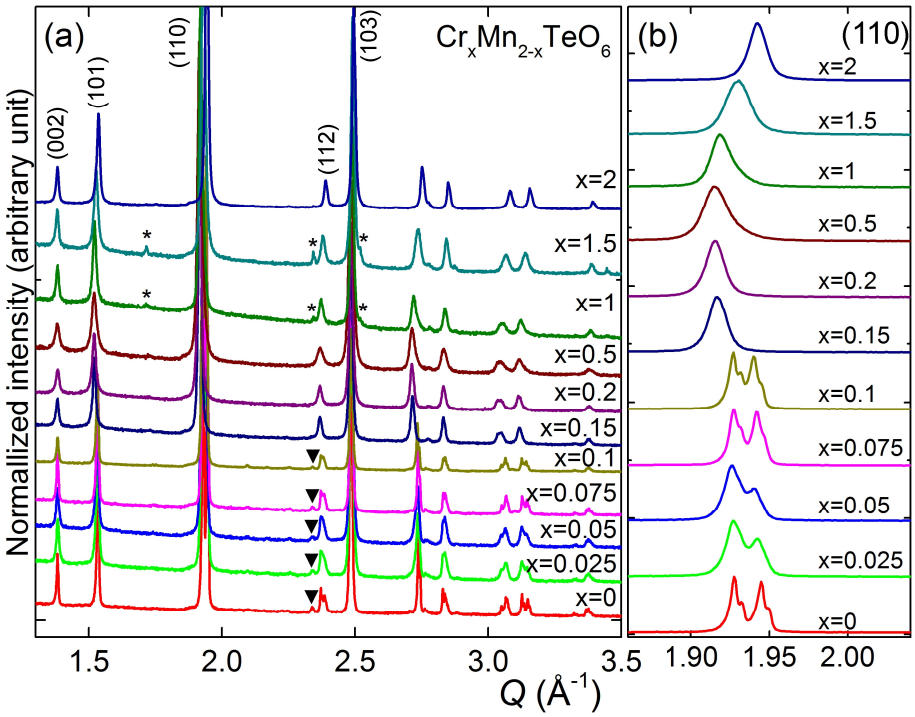


Figure 4-1 (a) Selected room-temperature XRPD patterns in the $Cr_xMn_{2-x}TeO_6$ series, from x = 0 to x = 2. A minor amount of Cr_2O_3 is observed in the x =1 and 1.5 samples (shown with black stars). The main peak indicating the doubling of the unit cell along b (in the RTM setting) is indicated by a triangle. Indexations using the tetragonal unit cell are given. (b) Enlargement of (110) Bragg peak around Q = 1.95 Å^{-1}.

As detailed in Section 3.1, Mn_2TeO_6 crystallizes in a distorted inverse trirutile structure at RT. On the other hand, Cr_2TeO_6 crystallizes in the inverse trirutile tetragonal cell (*116*), as observed for Mn_2TeO_6 at high temperature. From $x = 2$ to $x = 0$, a clear peak splitting is observed in the diffraction patterns as shown with the enlargement of Figure 4-1. In addition small extra reflections (the main one being indicated by a triangle in Figure 4-1a) are also observed for Mn_2TeO_6 owing to the monoclinic symmetry and doubling along *b*. This effect of the substitution on the patterns from $x = 2$ to 0 present similarities with the effect of temperature from 700°C to RT for Mn_2TeO_6.

For low substitution levels ($0.01 \leq x \leq 0.1$), the $Cr_xMn_{2-x}TeO_6$ compounds have a similar structure to Mn_2TeO_6 at RT. Similarly to Mn_2TeO_6, accurate crystal structure refinements are not possible with these laboratory-XRPD data only because of the weak intensities of the superstructure Bragg peaks. Moreover, as is also clearly seen in Figure 4-1b (comparing for instance $x = 0$ to 0.1), the Bragg peak broadening differs strongly from sample to sample. As already discussed the peak broadening is probably due to grain size and cation distribution effects. As Cr_2TeO_6 can be prepared starting from its oxide (Cr_2O_3), in contrast with Mn_2TeO_6, which requires manganese oxalate, the $Cr_xMn_{2-x}TeO_6$ series was prepared using mixtures of $MnC_2O_4{\cdot}2H_2O$ and Cr_2O_3 (as chromium oxalate is not easy to stabilize). The reactivity of precursors is probably different, a fact that could affect the cation distribution in the trirutile compounds.

For $x = 0.15$ and above, the structure changes sharply to the inverse trirutile tetragonal unit cell, with space group $P4_2/mnm$ and $a \cong 4.6$ Å, $c \cong 9.0$ Å, like for Cr_2TeO_6 (*13*, *16*, *116*).

Figure 4-2 shows the cell parameters and cell volume evolution of $Cr_xMn_{2-x}TeO_6$ as a function of Cr level (x) extracted from the Le Bail fitting of the XRPD data. The fits were performed using the monoclinic unit cell ($P2_1/c$ with $a \cong 9.1$ Å, $b \cong 13.0$ Å, $c \cong 6.5$ Å and $\beta \cong 90°$) for $0 \leq x \leq 0.1$, and using the tetragonal unit cell ($P4_2/mnm$ with $a \cong 4.6$ Å and $c \cong 9.0$ Å) for $0.15 \leq x \leq 2$. For $x \leq 0.1$ samples, because of the larger cell with a lower symmetry, compared to the structure of the $x > 0.1$ samples, the fit is less accurate than for higher Cr substitutions. For $x \geq 0.15$, the *a*-parameter and cell volume decrease almost linearly as a function of the Cr content in agreement with the smaller ionic radii of Cr^{3+} (0.615Å in 6-fold coordination) with respect to that of Mn^{3+} (0.65Å)

(*27*). On the other hand, the *c*- (a_M-) parameter seems to stay rather constant with *x*. Even if the accuracy is not very good, it seems that the volume is nearly constant for *x* < 0.15 due to different *x*-dependences of the cell parameters (*a*, *b*, *c* and *β*).

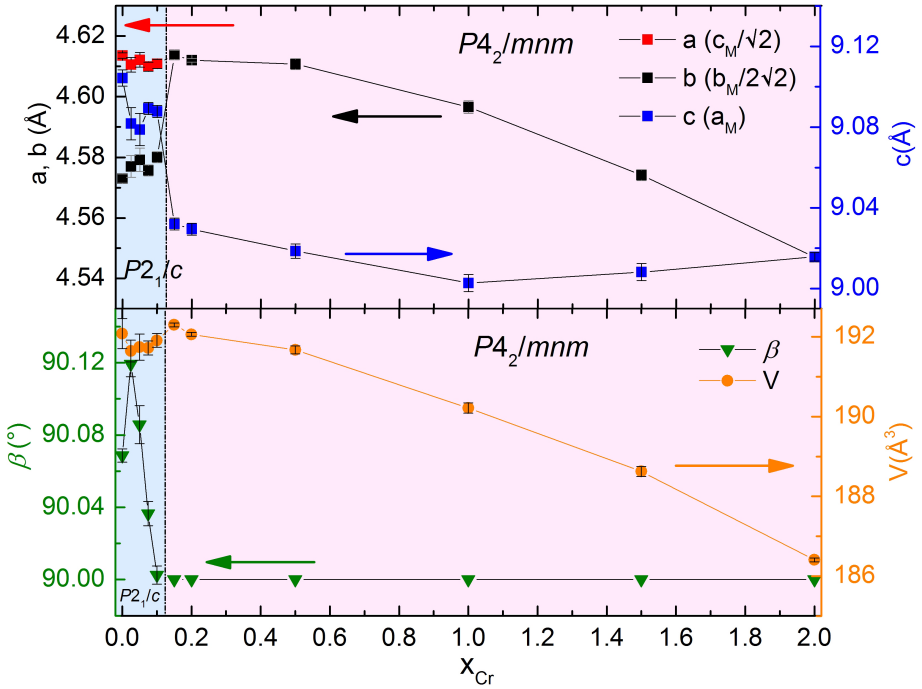


Figure 4-2 Variation of lattice parameters and cell volume of $Cr_xMn_{2-x}TeO_6$ as a function of the Cr-content x, obtained from the Le Bail fitting of laboratory XRPD data.

As discussed in Section 3.1, the room temperature crystal structure of Mn_2TeO_6 is a distorted superstructure of the inverse trirutile cell. This is thought to originate from a cooperative Mn^{3+} JT effect, which leads to a complex network of elongated and compressed MnO_6 octahedra surrounded by more regular TeO_6 units. In the $Cr_xMn_{2-x}TeO_6$ system, a substitution with a level $x \geq 0.15$ stabilizes the tetragonal inverse trirutile structure, which means that 7.5% of Cr-substitution destroys the JT induced ordering pattern at RT. Most likely, this is because the introduction of disorder, in the form of a random distribution of undistorted CrO_6 octahedra (since the *3d* electronic state of Cr^{3+} is not a JT active cation) in the MnO_6 octahedra intricate network prevents any long-range cooperative phenomenon.

To investigate this hypothesis further, a more detailed crystal structure study was carried out on the $x = 0.2$ sample. The results are presented in Section4.4.

4.2 *Comparison of the χ(T)curves of Mn_2TeO_6 and Cr_2TeO_6*

The magnetic susceptibility curves of the end members Mn_2TeO_6 and Cr_2TeO_6 (shown in Figure 4-3) are rather different. The magnetic properties of the former are extensively commented in Section 3.2. The curve of the latter shows a broad susceptibility maximum at $T_N \cong 90K$, followed by an upturn at low temperature, probably due to paramagnetic impurities, in excellent agreement with previous reports (*11*, *13*, *15*, *146*), see also in Section 1.1). The origin of this broad maximum is attributed to low dimensionality, probably 2D, following Yamaguchi et al. (*13*), or because of quasi-isolated (Cr_2O_{10}) bi-units (*147*, *148*), although this needs to be confirmed by either a proper modeling of the susceptibility data, or by performing inelastic neutron scattering just above T_N. In Cr_2TeO_6, a *zfc/fc* effect is observed below T_{N1}, which is not seen in Mn_2TeO_6 (not so significantly).

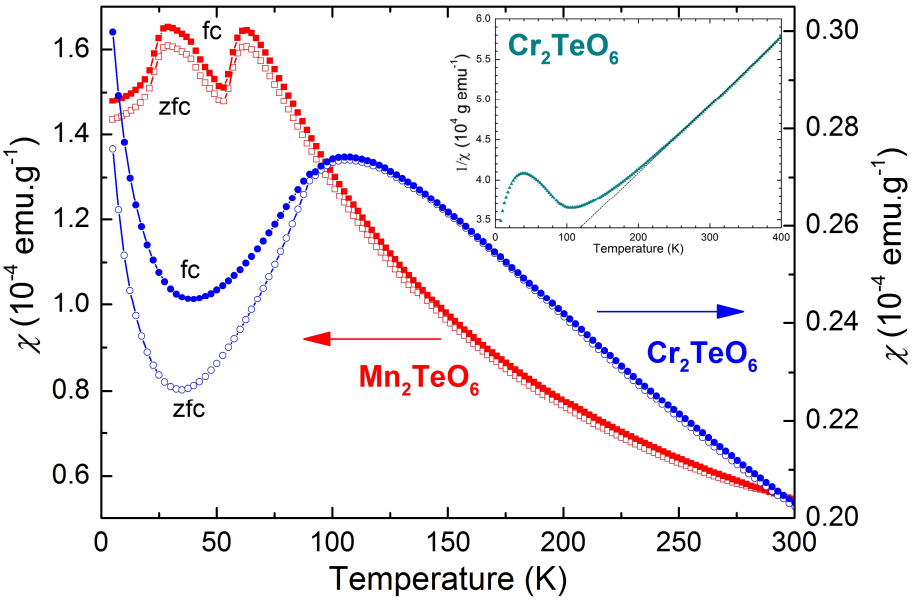


Figure 4-3 Magnetic susceptibility vs. temperature curves (zfc and fc) for (left axis) Mn_2TeO_6 in 100Oe and (right axis) Cr_2TeO_6 in 3000Oe. The inset shows the corresponding $\chi^{-1}(T)$ curve of Cr_2TeO_6. The black dot line is for the Curie-Weiss fitting.

The inverse magnetic susceptibility vs temperature (inset of Figure 4-3) shows a linear regime above 220K. A linear fit of the data with a Curie-Weiss law yields paramagnetic moments of 3.98 μ_B per Cr^{3+}. This is in good agreement with the expected value for Cr^{3+} (d^3: $\mu_{eff} = 3.8\ \mu_B$). The Curie-Weiss temperature also obtained from the fit is θ_{CW} =

-275.9 K. This value of θ_{CW} is controversial issue as Drillon *et al*. (*148*) found it as θ_{CW} = -150K while Yamaguchi et al. (*13*) mentioned that it is not possible to fit a paramagnetic range with a Curie-Weiss law. These discrepancies could be also due to the paramagnetic impurities. This negative value indicates predominant AFM interactions, as in Mn_2TeO_6 and implies that antiferromagnetic exchange in Cr_2TeO_6 is much stronger than in Mn_2TeO_6. Defining the frustration parameter $f = |\theta_{CW}/T_N|$, it can be underlined that there is no frustration effect in this compound ($f = 2.8$).

4.3 *Neutron diffraction study of Cr_2TeO_6*

Figure 4-4 shows the NPD patterns of Cr_2TeO_6 recorded upon warming from 1.6 to 289K on G4.1 (LLB). The RT structure is studied by Rietveld refinement using XRPD data and is characteristic of the well-known tetragonal inverse trirutile structure in agreement with previous reports (*13*, *16*, *116*). The corresponding structural parameters and agreement factors are summarized in Table 4-1. No structural transition is evidenced in this temperature range. Below 105K (Figure 4-4-left), we do not observe any magnetic Bragg reflections that correspond to 3D long-range ordering, rather we observe diffuse scattering (Figure 4-4-right) at $Q \cong 1.55 Å^{-1}$, which indicates short-range correlations before the magnetic transition, although it could also be of inelastic origin. Below 90K, magnetic Bragg peaks start growing on top of nuclear peaks. Thus T_N in Cr_2TeO_6 is defined at 90K.

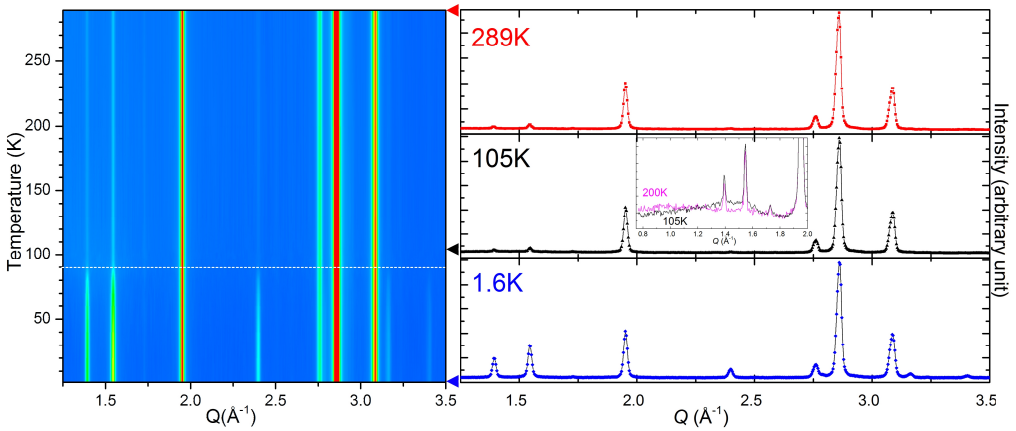


Figure 4-4 (left) Temperature evolution of the NPD (G4.1@LLB) patterns of Cr_2TeO_6, in the 1.25–3.5 $Å^{-1}$ selected Q range (from 1.6 to 289 K). The horizontal white dot line indicates the magnetic transition at 90K. (right) NPD data of Cr_2TeO_6 at 289, 105 and 1.6K, the inset on the pattern at 105K emphases the diffuse scattering signal observed at this temperature.

Crystallographic parameters		Selected inter-atomic distances (Å)	
a_{HTT} (Å)	4.5474 (1)	Cr-O_I (x 2)	1.948 (2)
c_{HTT} (Å)	9.0166 (1)	Cr-O_{II} (x 2)*	1.9845 (2)
V (Å^3)	186.45 (1)	Cr-O_{II} (x 2)	1.949 (2)
z_{Cr}	0.3354 (1)	<d> (Cr-O)	1.961 (3)
x_{OI}	0.3037 (7)	$\Delta(CrO_6)10^{-4}$	0.75
x_{OII}	0.3086 (4)		
z_{OII}	0.3322 (4)	Te-O_I (x 2)*	1.953 (3)
B_{Cr} (Å^2)	1.62 (2)	Te-O_{II} (x 4)	1.951 (3)
B_{Te} (Å^2)	1.84 (2)	<d> (Te-O)	1.931 (4)
B_{OI} (Å^2)	1.90 (5)	Δ (TeO_6) (x10^{-4})	0.005
B_{OII} (Å^2)	1.90 (5)		
χ^2	6.66	Cr-Cr	2.968 (2)
R_{Bragg} (%)	4.84	Cr-Te	3.024 (1)

Te atoms are in the WP, (2a: 000), Cr in (4*e*: 00*z*), O_I in (4*f*: *xx*0), and O_{II} in (8*j*: *xxz*).
*Corresponding to the longest apical distance in each octahedron.

Table 4-1 Crystallographic parameters and corresponding interatomic distances in Cr_2TeO_6 ($P4_2/mnm$), obtained from Rietveld refinements of XRPD data at 300K.

Magnetic structure refinement was performed using a pattern recorded at 1.6K (Figure 4-4-left and Figure 4-5) and all observed magnetic reflections can be indexed using $\boldsymbol{k}$ = (0 0 0). Symmetry analysis performed using BasIreps (*88*) on the $P4_2/mnm$ space group, for chromium in the (4e) Wyckoff site (0 0 *z*) and $\boldsymbol{k}$ = (0 0 0), shows a constraint on the moment direction, which can be either along *c* or in the *ab*-plane. Symmetry analysis indicates that there are six Irreps, four Irreps of dimension 1 (Γ_2, Γ_3, Γ_6, Γ_7) and two Irreps of dimension 2 (Γ_9, Γ_{10}), which are summarized in Table 4-2 (the labelling of Cr atoms refers to Figure 4-6a). In the global magnetic representation, $\Gamma_{mag} = 1\Gamma_2 \oplus 1\Gamma_3 \oplus 1\Gamma_6 \oplus 1\Gamma_7 \oplus 2\Gamma_9 \oplus 2\Gamma_{10}$. In $\Gamma_2, \Gamma_3, \Gamma_6, \Gamma_7$, all moments are aligned along the *c*-axis. In Γ_7, moments are in FM configuration. In Γ_2 and Γ_6, moments are antiparallel within bi-units of edge-sharing octahedra. In Γ_9, Γ_{10}, moments lay in the *ab*-plane; if one basis vector only is considered, a collinear magnetic structure is obtained, with moments either aligned along *a* or *b*; moments in the bi-units (Cr1-Cr4 or Cr2-Cr3) are either parallel (Γ_{10}) or antiparallel (Γ_9). For both Irreps, ψ_1 (ψ_3) leads to an antiparallel spin configuration in corner-sharing octahedra (Cr1-Cr2 or Cr3-Cr4), while ψ_2 (ψ_4) leads to a parallel one. If two basis vectors are chosen, perpendicular or non-collinear magnetic structures can be obtained.

		Cr1 (0, 0, 0.33) *(x, y, z)*	Cr2 (0.5, 0.5, 0.17) *(-x+1/2, y+1/2, -z+1/2)*	Cr3 (0.5, 0.5, 0.83) *(y+1/2,- x+1/2, z+1/2)*	Cr4 (0, 0, 0.67) *(y, x,- z+1)*
Γ_2	ψ_1	0 0 1	0 0 -1	0 0 1	0 0 -1
Γ_3	ψ_1	0 0 1	0 0 -1	0 0 -1	0 0 1
Γ_6	ψ_1	0 0 1	0 0 1	0 0 -1	0 0 -1
Γ_7	ψ_1	0 0 1	0 0 1	0 0 1	0 0 1
Γ_9	ψ_1	1 0 0	-1 0 0	1 0 0	-1 0 0
	ψ_2	0 1 0	0 1 0	0 -1 0	0 -1 0
	ψ_3	0 -1 0	0 1 0	0 -1 0	0 1 0
	ψ_4	-1 0 0	-1 0 0	1 0 0	1 0 0
Γ_{10}	ψ_1	1 0 0	-1 0 0	-1 0 0	1 0 0
	ψ_2	0 1 0	0 1 0	0 1 0	0 1 0
	ψ_3	0 1 0	0 -1 0	0 -1 0	0 1 0
	ψ_4	1 0 0	1 0 0	1 0 0	1 0 0

Table 4-2 Basis functions for axial vectors bound to the Wyckoff site 4e, within the irreducible representations of the propagation vector group for $\mathbf{k}$ *= (0 0 0) in* $P4_2/mnm$.

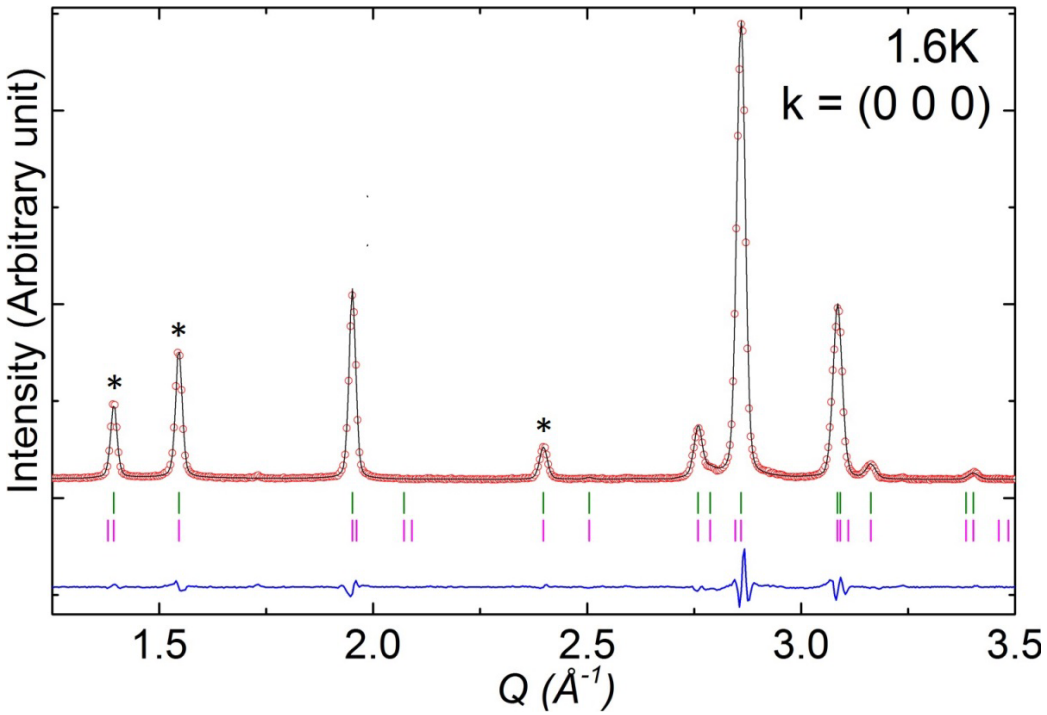


Figure 4-5 Rietveld refinement of the NPD data of Cr_2TeO_6 *at 1.6K within the* $P4_2/mnm$ *space group and* $\mathbf{k}$ *= (0 0 0). Stars indicate main magnetic peaks.*

Testing the different magnetic models allowed by symmetry, only one collinear model, belonging to Γ_9 with ψ_1 (ψ_3) shows good agreement with the experimental data. The final fit of the Rietveld refinement and obtained model are shown in Figure 4-5 and

Figure 4-6, respectively. The magnetic structure of Cr_2TeO_6 has a collinear spin configuration, i.e., it has components only along *x (or y)* with a value $m_{x(y)} = 2.34(3)\ \mu_B$. The Cr^{3+} spins are ferromagnetically aligned within each basal (*ab*)-plane and anti-ferromagnetically coupled within pairs of edge- (red ellipse in Figure 4-6) and corner- (blue ellipse) sharing octahedra. The model provides a good refinement (Figure 4-5, $R_{Bragg\ \text{magnetic}} = 2.30$) and is identified as *Pn'nm* (Shubnikov group: 58.395) and magnetic point group *m'mm* which has a ME tensor (*47*) so could potentially show a magnetoelectric effect. This result is in excellent agreement with the previous reported magnetic structure of Cr_2TeO_6 (*116*).

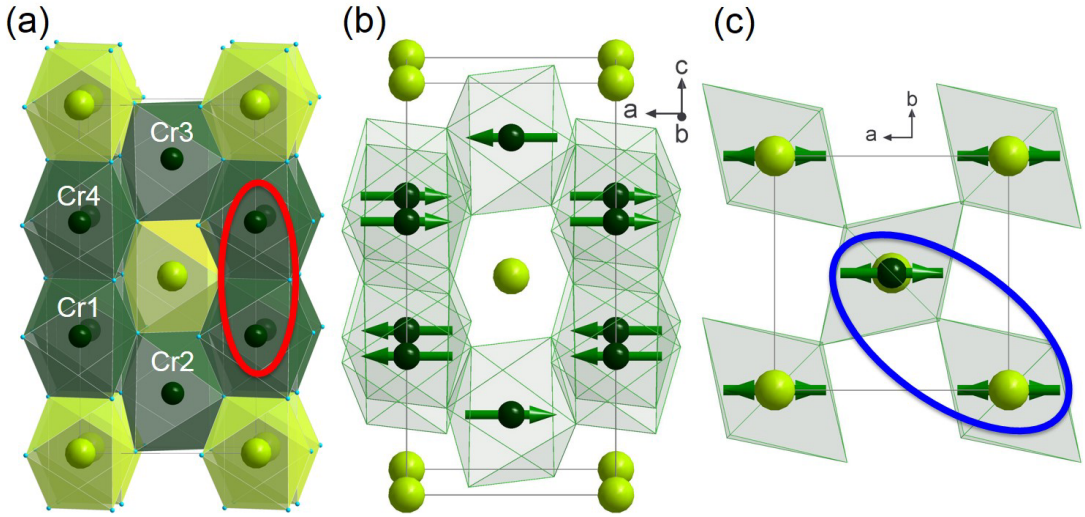


Figure 4-6 (a) Structure of Cr_2TeO_6 with the labels corresponding to the four (symmetrically equivalent) Cr-sites. The red ellipse shows the magnetic bi-unit made of two edge-sharing octahedra, while the blue ellipse shows corner sharing octahedra. Magnetic structure of Cr_2TeO_6 (Γ_9 with ψ_1) projected along (b) [010] and (c) [001]

These results correspond to the description of the magnetic interactions argued by Zhu et al. in Cr_2TeO_6 (*8*, *15*). The AFM coupling in the edge-sharing octahedra pairs is dominated by direct AFM exchange, as the super-exchange via O is weak, due to a Cr1(2)-O-Cr4(3) angle (≅ 98°) close to 90°. The AFM coupling between Cr^{3+} in corner-sharing octahedra is considered to be mediated by super-exchange interactions (as the Cr1(3)-O-Cr2(4) angle is ≅ 130°).

4.4 $Cr_{0.2}Mn_{1.8}TeO_6$

4.4.1 *Preliminary magnetic characterization*

The χ(T) curves of $Cr_{0.2}Mn_{1.8}TeO_6$ recorded in 100Oe upon warming are shown in the Figure 4-7-left axis. They show a transition at ≅ 40K and below this temperature the *zfc* and *fc* curves are not superimposed. The *zfc* one shows a maximum at T_{peak} ≅ 22K. The difference in between both curves could be the signature of a spin-glass or cluster glass-like behavior. In order to get a better understanding of the magnetically ordered state, we have made *ac*-χ'(T) measurement on this sample at low fields using different frequencies. Inset of Figure 4-7 shows the *ac*-χ'(T), which exhibits a peak similar to that of dc-*zfc* magnetization. The real components of ac susceptibility show a weak dependence of frequency, the T_{peak} slightly increases on increasing the measuring frequency. This peak position shift is a common feature of spin-glass and cluster-glass systems (*149*, *150*).

The inverse of the susceptibility curves (Figure 4-7-right axis) shows a large linear domain allowing a Curie-Weiss fitting that leads μ_{eff} = 4.96 μ_B/(Mn, Cr) and θ_{CW} = -115.7 K. This μ_{eff} value is close to the theoretical one of 4.89 μ_B for Mn^{3+} and to the one extracted for Mn_2TeO_6 (Section 3.2.2/Figure 3-26). The theoretical μ_{eff} value for Cr^{3+} being 3.89 μ_B, the expected effect of the substitution is a small decrease but it is not observed (within the accuracy of the fitting). The negative θ_{CW} value indicates predominant antiferromagnetic interactions. To go further in the understanding of the magnetic behavior of $Cr_{0.2}Mn_{1.8}TeO_6$, NPD (G4.1@LLB) was carried from 2 to 300K. This study was combined with XRPD at temperature > RT and the structural results are first described.

The shape of these curves is different from those of Mn_2TeO_6 and Cr_2TeO_6, and the values of the magnetization at low temperature are higher than for the parent compounds. This point will be discussed later.

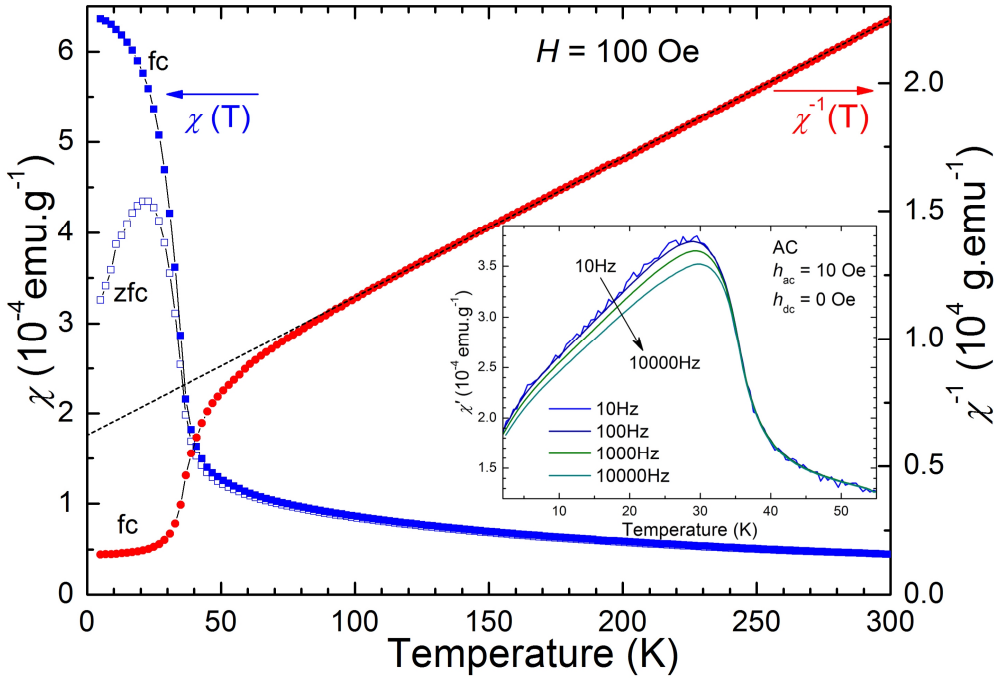


Figure 4-7 Magnetic susceptibility vs. T curves (left axis) (zfc and fc) for $Cr_{0.2}Mn_{1.8}TeO_6$ and $\chi^{-1}(T)$ (right axis) in 100 Oe. The black dotted line is the Curie-Weiss fitting. The inset shows the ac susceptibility $\chi'(T)$ in h_{ac} = 10Oe at different frequencies in the 10 - 10kHz range.

4.4.2 *T evolution of the crystal structure of $Cr_{0.2}Mn_{1.8}TeO_6$*

According to the preliminary XRPD study (Figure 4-1), $Cr_{0.2}Mn_{1.8}TeO_6$ crystallizes at RT in the inverse trirutile tetragonal structure ($P4_2/mnm$, a = 4.613 (1) Å, c = 9.030 (1) Å), similarly with Cr_2TeO_6 (Section 4.3) or with the HTT form of Mn_2TeO_6 (see Section 3.1).

Figure 4-8 shows the results of the high-temperature (473K (200°C) and 873K (600°C)) XRPD diffraction study performed in air using the D8 diffractometer of the laboratory. Unlike Mn_2TeO_6 (which exhibits a phase transition at 673K (400°C)), in $Cr_{0.2}Mn_{1.8}TeO_6$ there is no structural transition up to 873K. At 873K, the cell parameters are a = 4.6345 (1) Å, c = 9.0484 (1) Å. No supercell is observed which could correspond to a Cr:Mn order, their distribution occurs thus randomly on the same crystallographic site. This structure is illustrated in Figure 4-9. As mentioned earlier in Chapter 3, this structure can be seen as a stacking along c of three rutile type cells, resulting from the ordering of Mn/Cr and Te species in a 2:1 ratio. Both Mn/Cr and Te sites are in octahedral environments, sharing edges along c and corners in the ab-plane.

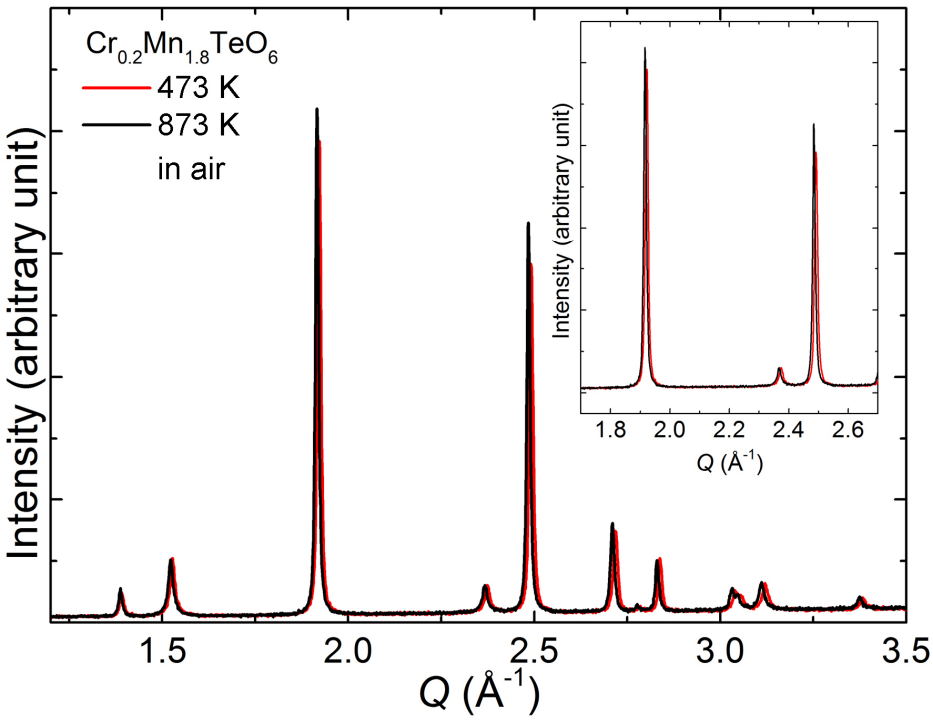


Figure 4-8 *Laboratory XRPD patterns of $Cr_{0.2}Mn_{1.8}TeO_6$ at 473K (red line) and 873K (black line) in air.*

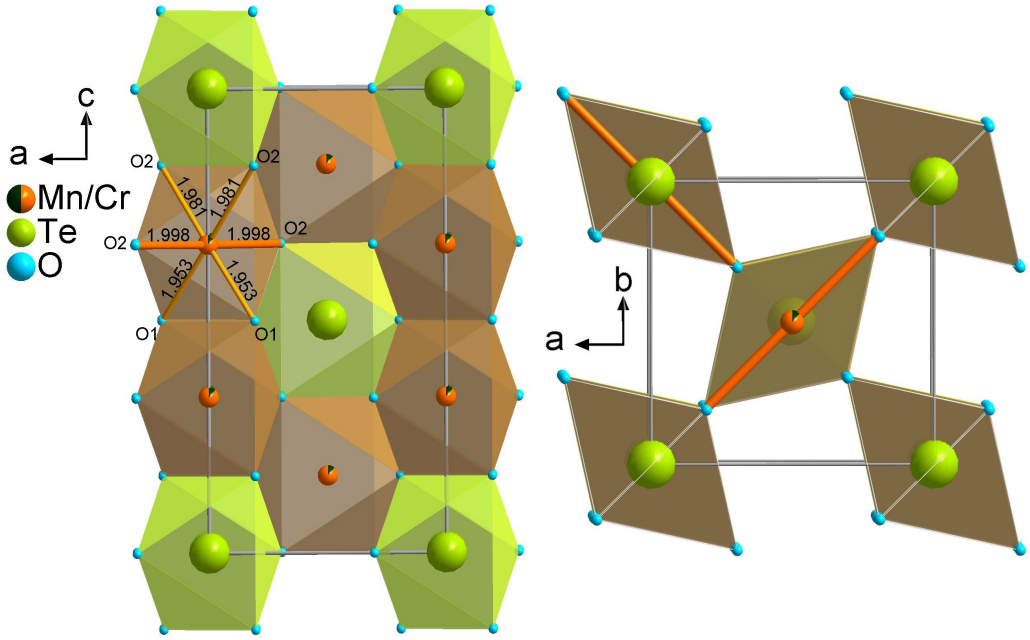


Figure 4-9 *Two views of the crystal structure of the tetragonal ($P4_2/mnm$) inverse trirutile structure of $Cr_{0.2}Mn_{1.8}TeO_6$, showing the 2:1 cationic ordering of Mn/Cr (orange/dark green) and Te (green) species. O species are light blue. (Cr/Mn)-O distances corresponding to RT structure are given and the longest apical bond along <110> direction is highlighted in thick orange line.*

SXRPD and NPD measurements were also performed at low temperature, at 10 and 300K, and from 2 to 300K, respectively. In this whole temperature range, the diffractograms are still characteristic of the inverse trirutile tetragonal unit cell. Figure 4-10 shows the results of Rietveld refinements of SXRPD data recorded at 300 and 10K, and corresponding parameters and agreement factors are gathered in Table 4-3. Several impurity phases are observed on the synchrotron data; the main one can be indexed as Mn_2O_3 (< 2%, for which the T_N = 90K (*151*)), whose the main peak is pointed out by an orange star on Figure 4-10. The refinements are not flawless, as reflected by the large χ^2 values (3 or 4 times larger compared to other samples characterized in same conditions); this might be due to the impurity phases as well as to a broadening of the Bragg peaks. The peak profile is difficult to model; arguably it contains different phases with very close cell parameters. This also supports an inhomogeneous cation distribution in the inverse trirutile samples.

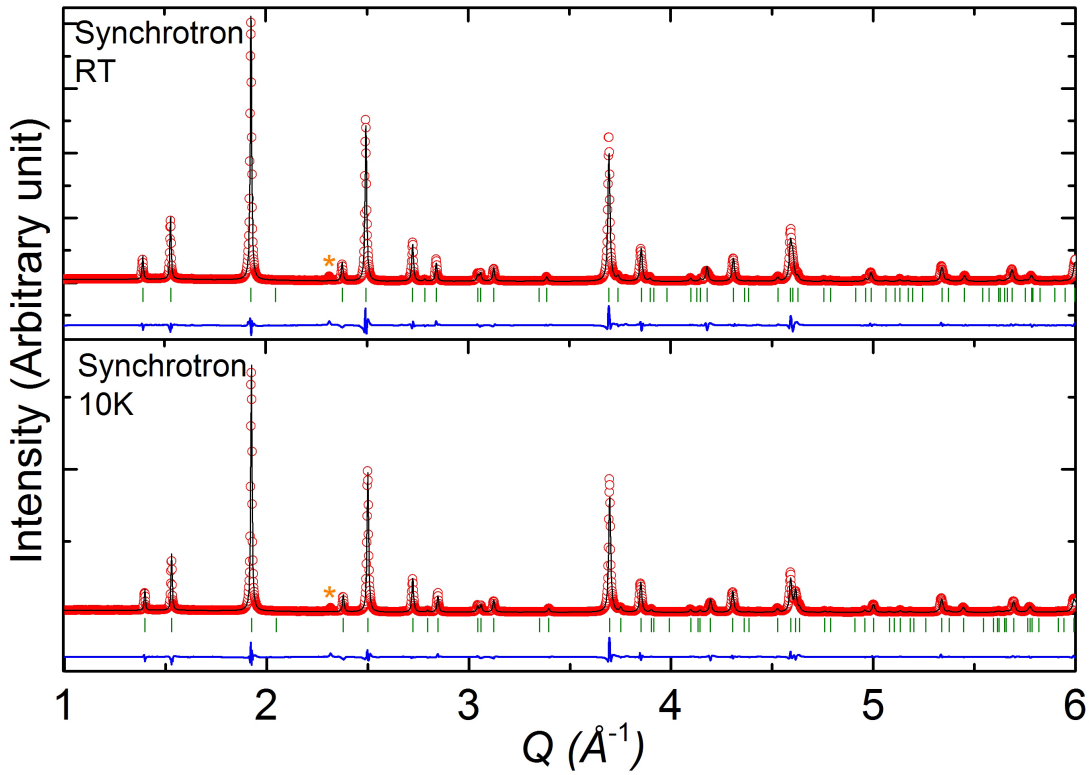


Figure 4-10 Rietveld refinement of the SXRPD data of $Cr_{0.2}Mn_{1.8}TeO_6$ at 300 and 10K ($P4_2/mnm$ space group). Orange stars indicate the main peak of Mn_2O_3.

Crystallographic parameters			Selected inter-atomic distances (Å)		
	300K	**10K**		**300K**	**10K**
a_{HTT} (Å)	4.6100 (1)	4.6154 (1)	Mn/Cr-O_I (x 2)	1.953 (2)	1.949 (2)
c_{HTT} (Å)	9.0184 (1)	8.9871 (1)	Mn/Cr-O_{II} (x 2)	1.998 (2)	2.006 (2)
V (Å^3)	191.662 (2)	191.442 (2)	Mn/Cr-O_{II} (x 2)	1.981 (4)	1.977 (3)
$z_{Mn/Cr}$	0.3359 (1)	0.3359 (1)	<d> (Mn/Cr-O)	1.977 (3)	1.977 (2)
x_{OI}	0.3047 (7)	0.3048 (6)	Δ(Mn/CrO_6)10^{-4}	0.88	1.39
x_{OII}	0.3065 (5)	0.3073 (4)			
z_{OII}	0.3335 (4)	0.3339 (4)	Te-O_I (x 2)	1.987 (3)	1.989 (3)
$B_{Mn/Cr}$(Å^2)	0.32 (2)	0.22 (1)	Te-O_{II} (x 4)	1.961 (3)	1.953 (3)
B_{Te} (Å^2)	0.74 (1)	0.68 (1)	<d> (Te-O)	1.970 (4)	1.965 (3)
B_{OI} (Å^2)	0.12 (11)	0.13 (10)	Δ (TeO_6) (x10^{-4})	0.387	0.746
B_{OII} (Å^2)	0.73 (7)	0.71 (7)			
χ^2	159	124	Mn/Cr-Mn/Cr	2.961 (2)	2.950 (2)
R_{Bragg} (%)	2.79	2.50	Mn/Cr-Te	3.029 (1)	3.019 (1)

Te atoms are in the WP (2*a*: 000), Cr/Mn in (4*e*: 00*z*), O_I in (4*f*: *xx*0), and O_{II} in (8*j*: *xxz*)
*Corresponding to the longest apical distance in each octahedron.
Table 4-3 Crystallographic parameters and corresponding interatomic distances in $Cr_{0.2}Mn_{1.8}TeO_6$ ($P4_2/mnm$), obtained from Rietveld refinements of SXRPD (BL04 at ALBA) data at 300 and 10 K.

As mentioned in the description of Figure 4-1, the effect of Cr substitution in $Cr_xMn_{2-x}TeO_6$ is to decrease the cell parameters, because of the smaller ionic radius of Cr^{3+} with respect to Mn^{3+}. Accordingly, at RT, the average (Mn/Cr)-O distance is shortened with increasing Cr-content: from 2.008Å in Mn_2TeO_6 to 1.977Å in $Cr_{0.2}Mn_{1.8}TeO_6$ (and 1.961Å in Cr_2TeO_6). The average Te-O distance (1.970Å) is on the other hand longer in $Cr_{0.2}Mn_{1.8}TeO_6$ than in both end members: Mn_2TeO_6 (1.921Å) and Cr_2TeO_6 (1.931Å). This could suggest that cation disordering between trivalent and hexavalent sites are larger in the substituted sample than in non-substituted samples. As mentioned in Section 3.1, MnO_6 octahedra in Mn_2TeO_6 are strongly distorted, with Δd in the range 17.6 - 30.9 x 10^{-4}. In contrast, as expected, in the tetragonal $Cr_{0.2}Mn_{1.8}TeO_6$, the (Mn/Cr) O_6 octahedra are much more regular, with an average $\Delta d \cong 0.623 \times 10^{-4}$ (0.75 x 10^{-4} for Cr_2TeO_6). Furthermore, TeO_6 octahedra remain relatively regular, from $\Delta d \cong$ 1.65 x 10^{-4} for $x = 0$ to 0.359 x 10^{-4} for $x = 0.2$ ($\Delta d \cong 0.005 \times 10^{-4}$ for $x = 2$). Common feature for two tetragonal phases is, as already mentioned for HTT Mn_2TeO_6, the two

apical bonds lying in *ab*-plane are always longer than the four equatorial bonds, which is highlighted in Figure 4-9.

In $Cr_{0.2}Mn_{1.8}TeO_6$, decreasing the temperature from 300 to 10K, the unit cell expands along the *a*-axis, but contracts along the *c*-axis (Table 4-3 and Figure 4-11), corresponding to a decrease of the Mn-Mn interatomic distance in the edge-sharing octahedra units. Along the *a*-axis, this anisotropic NTE might occur because of the increase of the Mn-O_{II} distance that is in the *ab*-plane, that is also the apical one of the octahedral, from 1.998 at 300 K to 2.006Å at 10 K, similarly to what was observed in the HTT phase of Mn_2TeO_6 (Table 3-3 and Figure 3-24). Consequently, octahedral distortion of both (Mn/Cr) O_6 and TeO_6 units slightly increases with decreasing temperature.

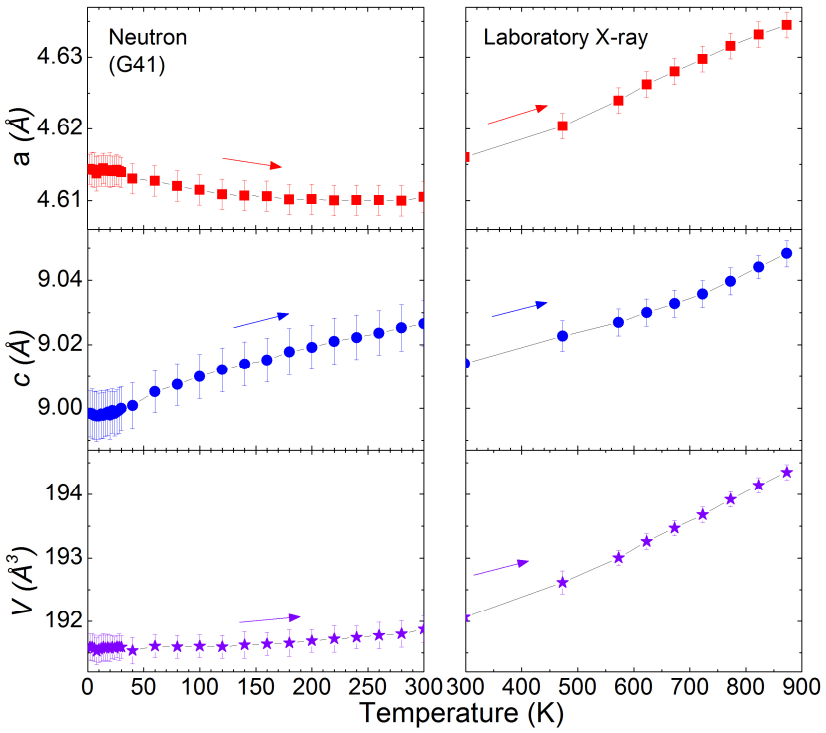


Figure 4-11 Temperature evolution of the lattice parameters and cell volume of $Cr_{0.2}Mn_{1.8}TeO_6$ obtained from Le Bail fitting of laboratory XRPD data recorded in air (right, from 300 to 873K) and NPD (G4.1@LLB) data (left, 2K to 300K) upon warming. Characterized samples and measurement conditions are not same, explaining the discrepancy at 300K between the two plots.

The complete evolution of the cell parameters (obtained from Le Bail fitting of X-ray and neutron diffraction data) of $Cr_{0.2}Mn_{1.8}TeO_6$ as a function of temperature between

2K and 900K is plotted in Figure 4-11. The cell volume V decreases with decreasing temperature, but the slope of the V (T) curve is rather flat below 200K. It is due to an opposite evolution of the cell parameters: c decreases as a mainly increases but exhibits a slight minimum between 220 and 280K. There is also a small change in the temperature dependence around 40K associated with magnetic transition observed on χ(T) (Figure 4-7). It confirms the NTE effect deduced from the refinements of the 300 and 10K structures.

4.4.3 *Neutron diffraction study*

Magnetic Bragg peaks appear clearly on the diffractograms below ≅ 23K, but they are weak and extremely broad, even down to 2K (Figure 4-12), characteristic of short-range magnetic ordering. Interestingly, they appear at the same Q positions as those of the $\boldsymbol{k}_1$ = (1/2 0 0) commensurate magnetic phase of monoclinic Mn_2TeO_6, as seen in Section 3.2 (pink arrows in Figure 4-12). Accordingly, the magnetic peaks of $Cr_{0.2}Mn_{1.8}TeO_6$ can be indexed with the commensurate propagation vector $\boldsymbol{k}$ = (0 0 1/2) (Figure 4-13), which corresponds to a doubling of the unit cell along its 4-fold axis.

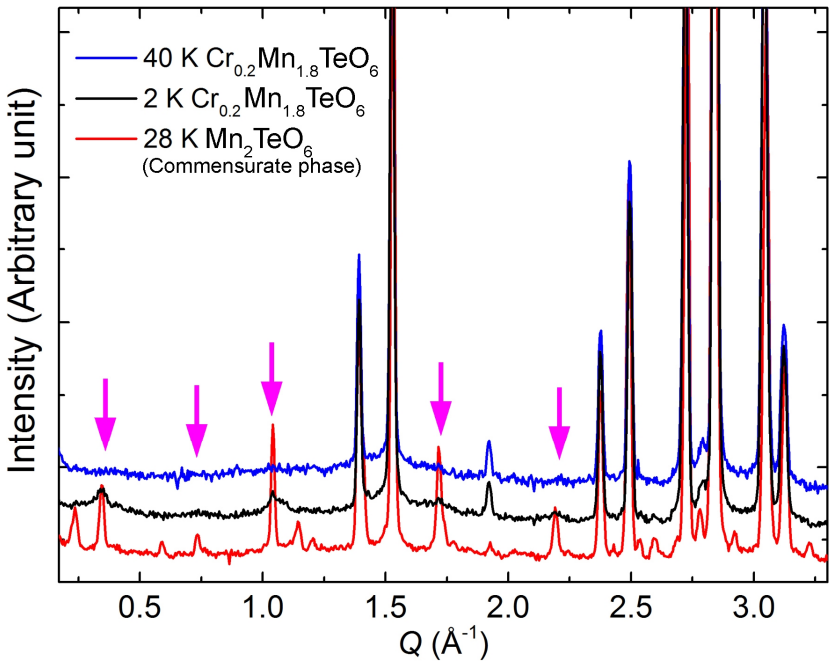


Figure 4-12 Neutron diffraction patterns of $Cr_{0.2}Mn_{1.8}TeO_6$ at 40 and 2K and of Mn_2TeO_6 at 28K, for which the main $\boldsymbol{k}_1$ magnetic reflections are indicated by pink arrows.

The results of the symmetry analysis performed using BasIreps (*88*), for space group $P4_2/mnm$, the propagation vector $\boldsymbol{k}$ = (0 0 1/2) and the Wyckoff site 4*e* (0 0 *z*) are summarized in the following. There are three irreducible representations of dimension 2; each contained twice in the global magnetic representation, $\Gamma_{mag}=2\Gamma_1\oplus2\Gamma_3\oplus2\Gamma_4$, so there are therefore 4 basis vectors per representation, summarized in Table 4-4. The labels of Mn are given in the same manner as for Cr_2TeO_6 (Figure 4-6a).

In Γ_1, all moments are aligned along *c*. Moments are constrained to be parallel (or antiparallel) within Mn1-Mn2 or Mn3-Mn4 pairs of corner-sharing octahedra. The moments belonging to those pairs are not constrained together by symmetry.

In Γ_3 and Γ_4, moments are aligned in the *ab*-plane. If one basis vector only is considered, a collinear magnetic structure is obtained, with moment either aligned along *a* or *b*; moments in pairs of Mn1-Mn2 are either parallel or antiparallel, moments in pairs of Mn3-Mn4 are also parallel or antiparallel, and the moments belonging to different pairs are perpendicular.

		Mn1 (0, 0, 0.33) *(x, y, z)*	Mn2 (0.5, 0.5, 0.17) *(-x+1/2, y+1/2, -z+1/2)*	Mn3 (0.5, 0.5, 0.83) *(y+1/2, –x+1/2, z+1/2)*	Mn4 (0, 1, -0.33) *(y, x+1, -z)*
Γ_1	ψ_1	0 0 1	0 0 -1	0 0 0	0 0 0
	ψ_2	0 0 0	0 0 0	0 0 1	0 0 -1
	ψ_3	0 0 0	0 0 0	0 0 -1	0 0 -1
	ψ_4	0 0 1	0 0 1	0 0 0	0 0 0
Γ_3	ψ_1	1 0 0	-1 0 0	0 1 0	0 1 0
	ψ_2	0 1 0	0 1 0	-1 0 0	1 0 0
	ψ_3	0 1 0	0 -1 0	1 0 0	1 0 0
	ψ_4	1 0 0	1 0 0	0 -1 0	0 1 0
Γ_4	ψ_1	1 0 0	-1 0 0	0 -1 0	0 -1 0
	ψ_2	0 1 0	0 1 0	1 0 0	-1 0 0
	ψ_3	0 -1 0	0 1 0	1 0 0	1 0 0
	ψ_4	-1 0 0	-1 0 0	0 -1 0	0 1 0

Table 4-4 Basis functions for axial vectors bound to the Wyckoff site (4e), within the irreducible representations of the propagation vector group for $\boldsymbol{k}$ *= (0 0 1/2) in* $P4_2/mnm$.

If two basis vectors are chosen, and the Fourier coefficients in front of the basis vectors are the same, perpendicular, or non-collinear magnetic structures can be obtained, depending on the chosen combination of basis vectors.

Testing the different magnetic models allowed by symmetry, it quickly appeared that only the magnetic structures belonging to Γ_3 or Γ_4 (that is, with magnetic moments in the *ab*-plane) could lead to a satisfying refinement of the data. Among those, two main non-collinear magnetic models, which cannot be distinguished from each other with powder diffraction, show good agreement with the experimental data (Figure 4-13). Those models are illustrated in Figure 4-14 and correspond to Γ_3 with ψ_3-ψ_4 (or ψ_1-ψ_2) (model I) and to Γ_4 with ψ_3+ψ_4 (or ψ_1+ψ_2) (model II). In each bi-unit of (Mn/Cr)O_6 edge-sharing octahedra, magnetic moments are aligned antiferromagnetically. Moments in (Mn/Cr)O_6 octahedra sharing one corner are perpendicular (an additional degeneracy is that both 90° and -90° rotations are possible) (Figure 4-14).

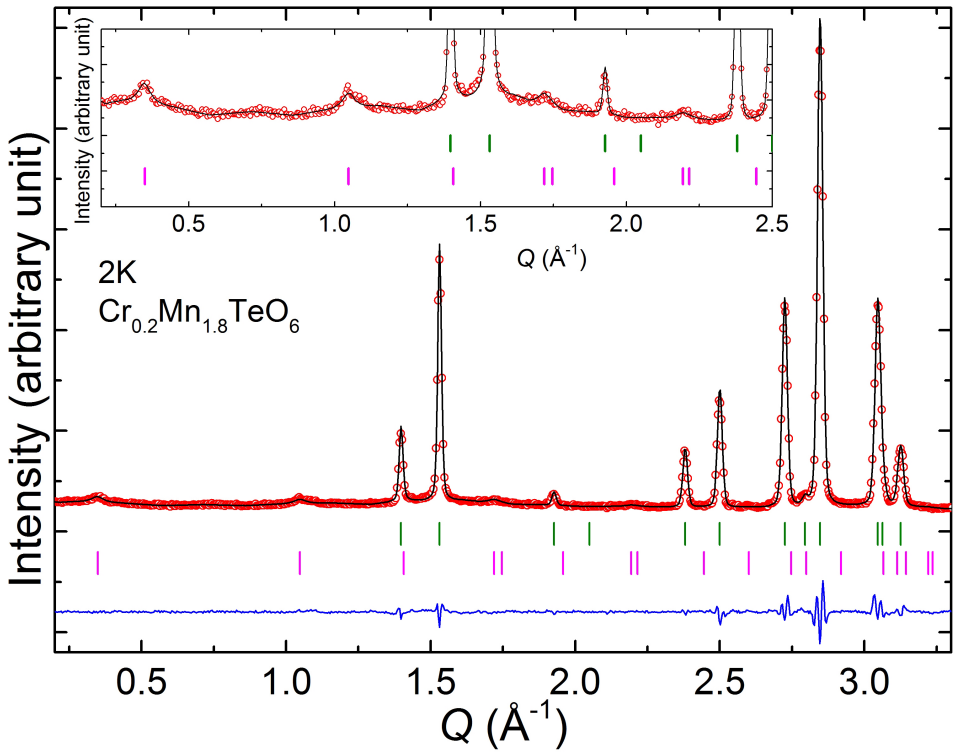


*Figure 4-13 Refinement of the NPD data of $Cr_{0.2}Mn_{1.8}TeO_6$ at 2 K (G4.1@LLB). Magnetic peaks indexation is shown for propagation vector **k** = (0 0 1/2) with $P4_2/mnm$ space group. The inset shows an enlargement of the magnetic Bragg peaks profiles. This refinement corresponds to model I; model II gives identical magnetic structure factors.*

The main difference between both models, which give identical structure factors in a powder diffractogram, as illustrated in Figure 4-14, is the orientation of the moment with respect to the apical bond of the $(Mn/Cr)O_6$ octahedron. In model I, moments are perpendicular to this apical bond (while still in *ab*-plane), while in model II, the moments are parallel to the longest axis of the octahedra (Figure 4-14c). In both models, according to the refinements, the moments are actually not exactly along the <110> directions, a slight tilting (tilting angle ≅ 8.3° (9)) of the moments with respect to the apical axis is necessary to obtain the best fitting with experimental data ($R_{Bragg\ magnetic}$ = 5.49). The value of the ordered moment at 2K is ≅ 4.0(1.0) μ_B, which would agree with a mixture of Cr^{3+} (S = 3/2) and Mn^{3+} (S = 2) species. The broadening of the magnetic peaks was satisfactorily modelled using a particle-size-type Lorentzian term, from which, using the simple Scherrer formula, a magnetic domain size of 58.4 (1) Å can be calculated (corresponding to around ten unit cells).

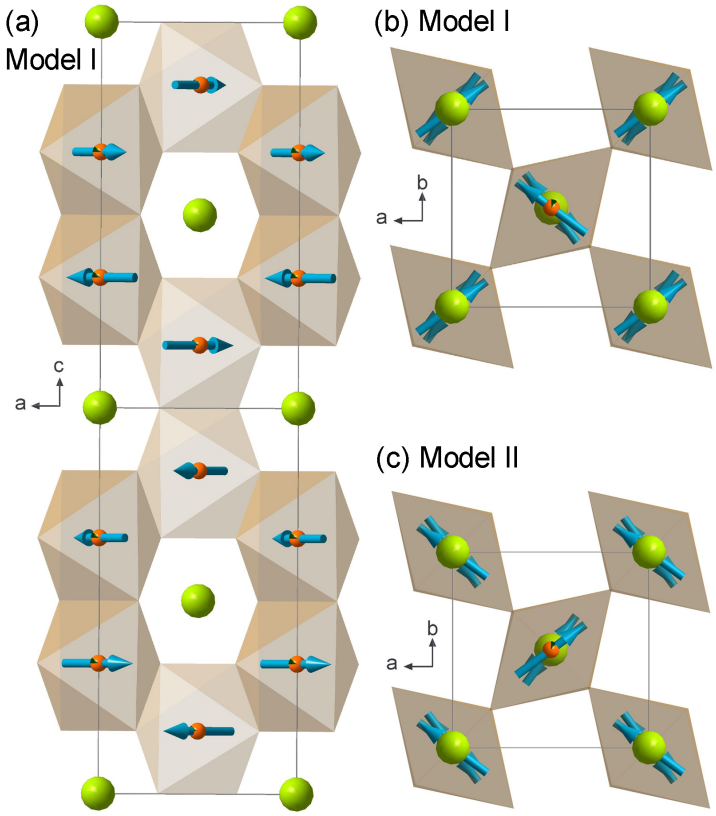


Figure 4-14 Models of magnetic structures for $Cr_{0.2}Mn_{1.8}TeO_6$ projected along (a) [010] and (b) [001].

As it has already been discussed in Section 3.2, model II seems to be more likely with regards to the known behavior of Mn moments in a distorted octahedron (*152*, *153*). It is interesting to emphasize that in $Cr_{0.2}Mn_{1.8}TeO_6$ one is quite close to the case of tetragonal Mn_2TeO_6 studied by Fruchart *et al.*(*7*). It substantiates, therefore, the fact that in tetragonal Mn_2TeO_6, antiferromagnetic pairs and strong magnetic uniaxial anisotropy of Mn^{3+} are the key parameters of the magnetic ground state. The existence of the $\boldsymbol{k_2}$ propagation vector in monoclinic Mn_2TeO_6 could be therefore a direct consequence of the unresolved complex pattern of distorted MnO_6 octahedra which, by modifying axial bond orientations and lengths, would modulate simultaneously Mn^{3+} magnetic moments. In the $x = 0.2$ compound, there is no sign of another propagation vector; as the magnetic peaks are fairly weak, however, it remains possible that the magnetic structure could be more complicated than in model II. Possible hint of this is the fact that moments are not aligned exactly along <110>, which could be due to local departure from the average octahedral distortion and orientation. This could also be a consequence of the Cr substitution, affecting the in-plane orientation of the moment, as in Cr_2TeO_6 moments are aligned along *a* (or *b*).

It is of interest here to compare the magnetic orderings in Cr_2TeO_6 (Figure 4-6) and $Cr_{0.2}Mn_{1.8}TeO_6$ (Figure 4-14). In both, AFM pairs are observed. The main difference is that in $x = 2$, moments are collinear, and corner-sharing octahedra units are aligned AFM. In $x = 0.2$, because of the stronger axial magnetic anisotropy, moments in corner-sharing octahedra are almost perpendicular. It would be interesting to carry on a neutron investigation of this system, to see at which substitution level one goes from a $\boldsymbol{k}$ = (0 0 1/2) structure to the $\boldsymbol{k}$ = (0 0 0) structure of Cr_2TeO_6, and/or if a different intermediate magnetic structure is stabilized.

4.5 *Properties along the $Cr_xMn_{2-x}TeO_6$ series and discussion*

As explained before, for small x values, the structure at room temperature is monoclinic like Mn_2TeO_6 and it remains tetragonal for $x \geq 0.15$, like Cr_2TeO_6. To draw a complete phase diagram it is necessary to characterize all the samples vs. temperature, to check if a tetragonal to monoclinic transition occurs and at which temperature. For $x \leq 0.15$ this structural transition temperature is higher than room temperature; for $x = 0.2$ there is no transition, the sample being tetragonal over the whole T range, which is likely to be the case too for $x > 0.2$. It would be interesting to know how varies the temperature of the HTT to RTM transition vs. x in the [0 - 0.2] x-range and to check whether there is a regular evolution, or if there is a threshold effect.

The magnetic behavior of Mn_2TeO_6 was deeply commented in the Chapter 3, with differences from one sample to the other depending mainly on the synthesis conditions. As could be expected, discrepancy issues are also encountered for the low x levels ($x < 0.15$). For this low x range, it is supposed that the monoclinic distortion is preserved, and that the same magnetic ground state as Mn_2TeO_6, with the existence of two transitions on the χ(T) curves, is preserved too. It seems that, in addition, substitution systematically induces differences in the *zfc*/*fc* branches of the χ(T) curves, as often observed in substituted systems (*154–156*), and the appearance of a small FM component. This is exemplified for $x = 0.025$ on Figure 4-15 and Figure 4-16. A clear ferromagnetic component appears below 45K in 0.01T, with a *zfc* - *fc* divergence around 37K (Figure 4-15). It is in agreement with a hysteresis in the $M(H)$ curves of Figure 4-16 at 5K and 35 K. This ferromagnetic component disappears at high magnetic field ($H \geq 1$T) (Figure 4-15), a feature that remains to be investigated further to be properly understood. Note that several transitions can be observed on the χ(T) curve in 1T at ≅ 85K, ≅ 55K, and ≅ 27K.

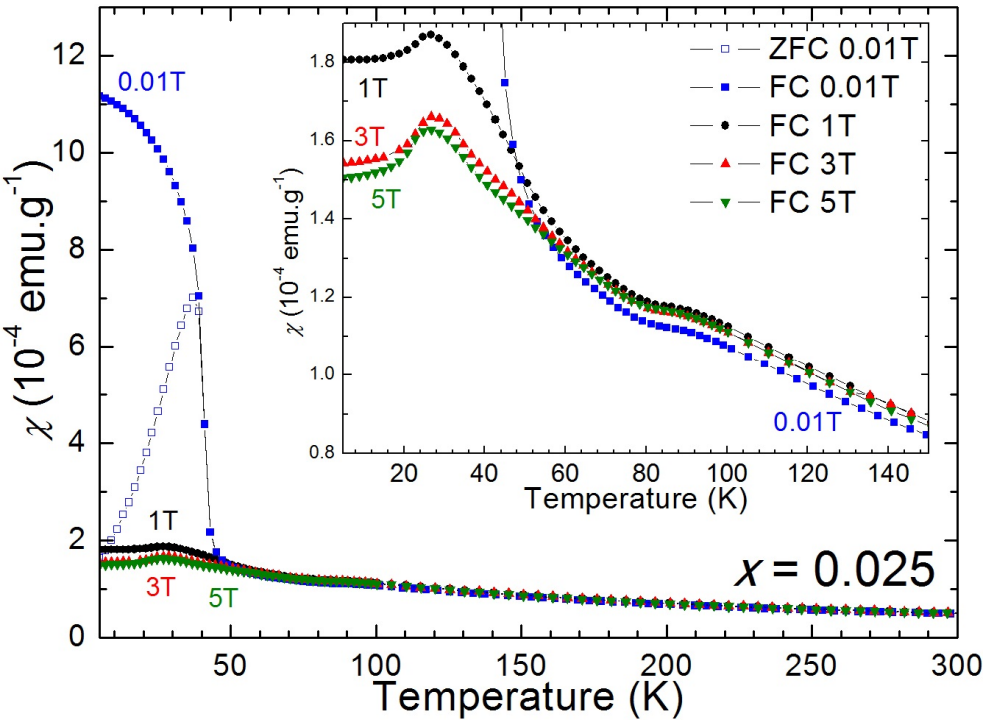


Figure 4-15 *Temperature dependence of the magnetization curves (zfc, fc) of $Cr_{0.025}Mn_{1.975}TeO_6$ in an applied field of 0.01, 1, 3 and 5T.*

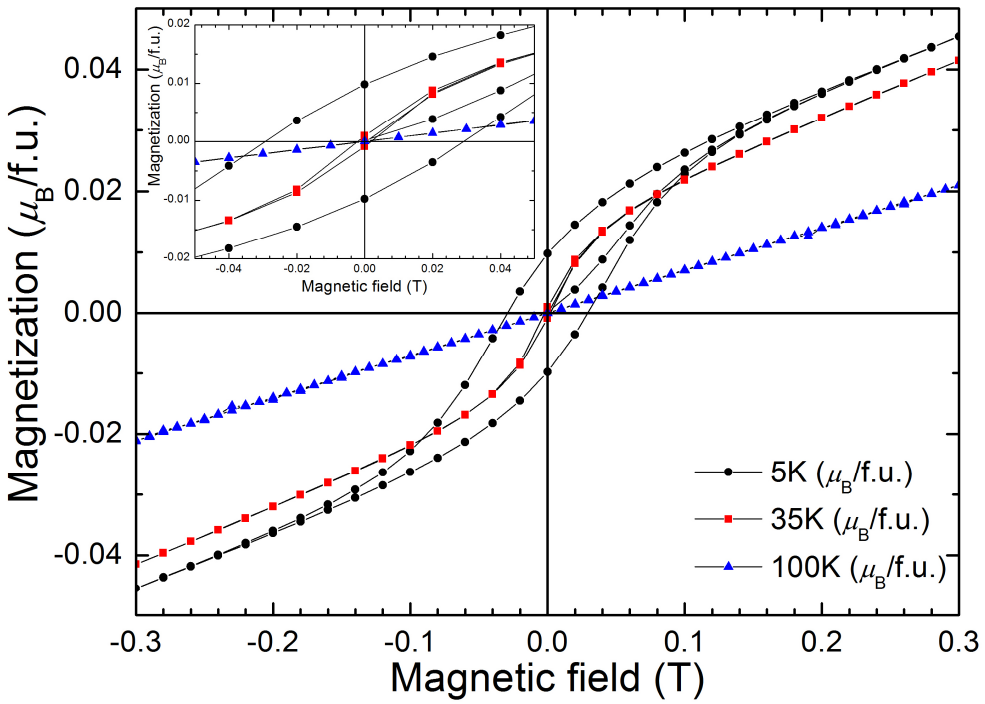


Figure 4-16 *Magnetic field dependence of the magnetization of $Cr_{0.025}Mn_{1.975}TeO_6$ recorded at 5, 35, and 100K. Hysteresis features are seen in the MH curve at 5 and 35K. The inset shows the enlargement of the selected range.*

It is clear that a careful investigation, involving complementary techniques, and in particular specific heat and neutron diffraction experiments, as for Mn_2TeO_6, is necessary to draw reliable conclusions; consequently the analysis of these data is not pushed further here. In particular, the monophasic character of the samples is crucial, as several transitions appear in the χ(T) curves, and because some small extra peaks were observed on the SXRPD patterns, identified as $(Cr,Mn)_2O_3$ or $(Cr,Mn)_3O_4$, which are magnetic. Nevertheless this $0 < x < 0.2$ range deserves more attention in future explorations, because it is well known that interesting behaviors often emerge at the boundary between two phases in a phase diagram (like a possible FM component when the AFM structures of the parents compounds become unstable).

On the other hand, for Cr_2TeO_6, there is no problem of inconsistencies or reproducibility. Accordingly, for higher Cr substitutions, when a tetragonal structure is observed, only one T_N is observed, which increases almost linearly from ≅ 20K (x = 0.2) to ≅ 90K (x = 2). A tentative phase diagram is presented in Figure 4-17, showing the x dependence of μ_{eff}, θ_{CW}, and T_N.

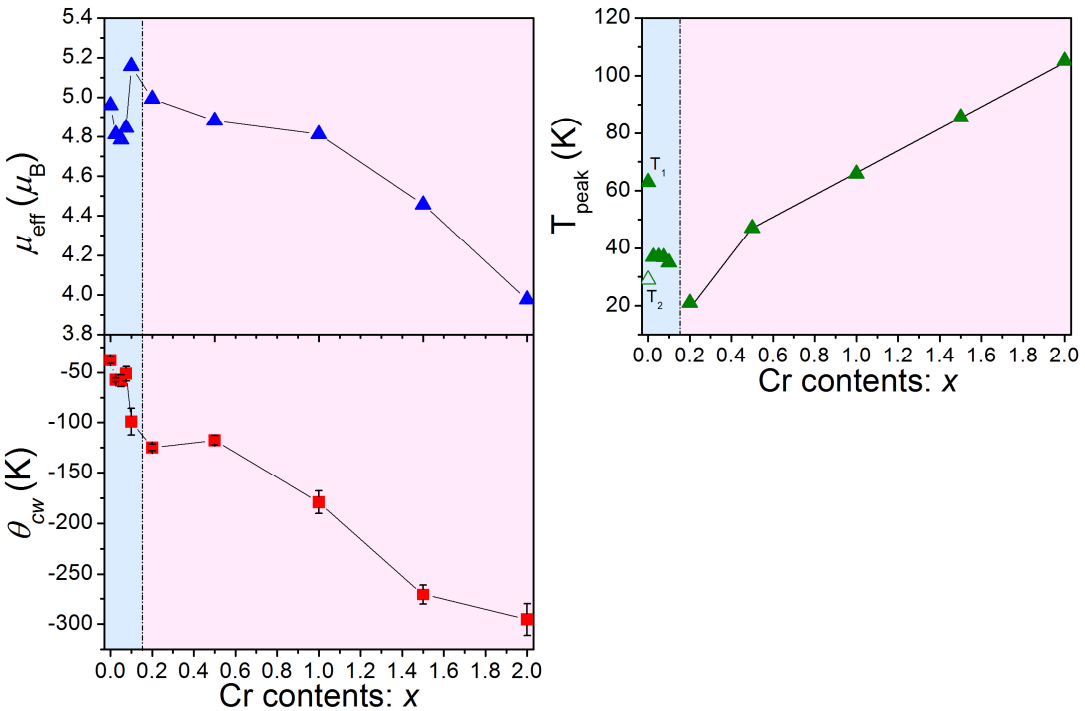


Figure 4-17 Extracted μ_{eff}, θ_{cw} and transition temperatures (T_{peak}) as a function of x in the $Cr_xMn_{2-x}TeO_6$. T_N, T_{peak} and T_{peak2} are shown when compounds show two peaks on susceptibility curve.

From the study of the magnetic properties of $Cr_xMn_{2-x}TeO_6$, it is possible to distinguish at least two different regimes:

- a low Cr substitution level ($x < 0.15$), in which the monoclinic structure distortion is preserved, and which presumably preserves the same magnetic ground state as Mn_2TeO_6, with the existence of several transition temperatures. Discussion is impaired by magnetic impurity issues and the need of a thorough experimental work akin to the one employed to study Mn_2TeO_6.

- for higher Cr substitution, a single tetragonal structure is observed, with only one T_N, which increases almost linearly with x, from $\cong$ 20K ($x = 0.2$) to $\cong$ 90K ($x = 2$). The magnetic ordering of the $x = 0.2$ sample has the same characteristics as tetragonal Mn_2TeO_6 (*7*), with $\boldsymbol{k}$ = (0 0 1/2), and antiferromagnetic bi-units of edge-sharing octahedra, but with only short-range ordering. The x boundary with the $\boldsymbol{k}$ = (0 0 0) magnetic ordering of Cr_2TeO_6 is not known yet and would require a dedicated neutron diffraction investigation.

Chapter 5. Conclusion & Perspectives

This work has shed light on the inverse trirutile system, especially on the Mn_2TeO_6 member, and expands the knowledge of this series of compounds, opening doors for future research on e.g., honeycomb tellurates or new types of orbital ordering, and building motivation to investigate substituted systems.

First was the work done on the optimization of synthesis conditions, in order to obtain monophasic samples of Mn_2TeO_6. High-temperature in situ X-ray and neutron powder diffraction experiments revealed a structural evolution of Mn_2TeO_6 at high-temperature. For temperature 400°C< T ≤ 700°C, Mn_2TeO_6 is crystallized in the standard tetragonal inverse trirutile structure, like Cr_2TeO_6 or Fe_2TeO_6, with SG $P4_2/mnm$ (a = 4.642 Å, c = 9.075 Å at 700°C). Cooling from high-temperature results in a structural transition at 400°C from the tetragonal unit cell to a lower symmetry room-temperature (RT) phase.

An extensive study, combining synchrotron, neutron, electron diffraction (including electron diffraction tomography), TEM imaging, EDX, and XANES, was carried out to determine this RT structure phase precisely. Electron diffraction of Mn_2TeO_6 at RT shows superstructure spots, owing to a doubling along *b*-axis of the cell. Thanks to the high flux and resolution of synchrotron XRPD, Rietveld refinement of this enlarged structure was possible. Symmetry analysis allowed one to identify the primary order parameter behind the structural transition, and to better understand the role of the distortions. The RT phase was finally identified as a monoclinically distorted inverse

trirutile structure with SG $P2_1/c$ (a = 9.103 Å, b = 13.046 Å, c = 6.466 Å, β = 90.03 Å at RT). The MnO_6 octahedral network of this structure is complex and to our knowledge unprecedented, as it is built from two types of distorted chains, consisting in one elongated and one compressed MnO_6 octahedron sandwiched by regular TeO_6. This complex distortion pattern is thought to originate from the combination of cooperative Jahn-Teller effects of Mn^{3+}, leading to orbital ordering, and a rigid structural framework. The electron microscopy study also showed examples of local disorder in this system, with modulation in oxygen positions, existence of dislocation, and departure from perfect cation distribution.

Decreasing the temperature further, a second phase transition (first order) is observed, from the RT monoclinic to a low-temperature phase, accompanied with a large biphasic domain between 45 and 100K (upon warming). This low-temperature structure is actually related to the RT monoclinic phase, retaining a monoclinic distortion and the doubling along the *b*-axis, but with slightly different cell parameters, and most importantly, new superstructure peaks. Solving this LT structure was unfortunately out of reach, as we were not able to determine its supercell metrics. Single crystal experiments or low-temperature electron diffraction are necessary for future work, in particular to better understand the origin of the structural transition, and the possibility of a new orbital ordering.

In parallel, magnetic properties of Mn_2TeO_6 were examined by magnetization measurement and neutron powder diffraction, and confirmed at least two magnetic transitions at $T_1 \cong 46$K and $T_2 \cong 24$K (upon warming). The magnetic structure determination was impaired as the low-temperature crystal structure was not known. Using the average low temperature cell, however, it was possible to index the main magnetic Bragg peaks using two commensurate propagation vectors between T_1 and T_2, and at least two incommensurate propagation vectors derived from commensurate ones below T_2. Combining our results with those of a previous report on a tetragonal sample of Mn_2TeO_6, a rough magnetic ordering model based on an antiferromagnetic coupling of Mn spins (spins are in the *bc*-plane) in edge-sharing pairs of octahedra was proposed. Nevertheless, to go further in the determination of the real magnetic structure of Mn_2TeO_6, single crystal neutron diffraction is now mandatory.

The study of the series of Cr-substituted Mn_2TeO_6, i.e. $Mn_{2-x}Cr_xTeO_6$ (x = 0 - 2), has revealed a strong substitution effect on the crystal structure and magnetic properties. Contrary to Mn_2TeO_6, $Mn_{2-x}Cr_xTeO_6$ compounds with more than 7.5% ($x \geq 0.15$) of Cr are found tetragonal with SG $P4_2/mnm$ ($a \cong 4.6$ Å, $c \cong 9.0$ Å) at room temperature. Moreover there is no structural transition observed in the examined temperature range (for $Cr_{0.2}Mn_{1.8}TeO_6$ sample from 10K to 620°C). This Cr-substitution effect strongly supports the scenario that the complex structure and unusual pattern of MnO_6 distortions evidenced in Mn_2TeO_6 result from a cooperative Jahn-Teller effect.

The neutron diffractogram of $Cr_{0.2}Mn_{1.8}TeO_6$ at low temperature exhibits weak and broad additional peaks of magnetic origin. This short-range magnetic ordering with $\boldsymbol{k}$ = (0 0 1/2) propagation vector takes place below ≅ 22K and involves, like in Mn_2TeO_6, antiferromagnetically coupled spins within each bi-unit of $(Mn/Cr)O_6$ edge-sharing octahedra. This magnetic structure substantiates therefore the main characteristics of the magnetic ordering proposed for Mn_2TeO_6, which can be pictured as a modulation (probably following the complex LT orbital ordering pattern) of the magnetic ordering of the tetragonal phase. The comparison between the magnetic structures of $Cr_{0.2}Mn_{1.8}TeO_6$ and Cr_2TeO_6 is also interesting. Both have AFM bi-units, but while the former one is non-collinear ($\boldsymbol{k}$ = (0 0 1/2)), the latter one shows collinear magnetic ordering ($\boldsymbol{k}$ = (0 0 0)). Further investigations using neutron diffraction would be very valuable, to know at which substitution level the magnetic structure changes and if is correlated with magnetic easy axis anisotropy.

The initial aim of this work was to propose new possible candidates for ME or multiferroic materials; to this end, electrical measurements were performed on inverse trirutile Mn_2TeO_6 to characterize the antiferromagnetic and potential (magneto) electrical polarization contributions. Although complex crystal structures and exotic orbital orderings do have a known potential to show ME or multiferroic properties, no clear ME or multiferroic effect was identified in Mn_2TeO_6 despite numerous experimental attempts. Nevertheless, the weak magnetodielectric coupling has been observed in Mn_2TeO_6 at the structural transition from RTM to LT phase is encouraging. Polarization studies deserve to be pursued therefore, in particular taking care of the quality of the sintering, as the samples have to be prepared at low temperature. For

future work, Cr-substituted sample should also be investigated carefully, especially for the Cr composition range where they are isostructural to known ME compounds like Fe_2TeO_6 or Cr_2WO_6.

While working on the development and optimization of the solid state synthesis process of inverse trirutile Mn_2TeO_6, we discovered a new manganese tellurates phase, as an intermediate state (appearing at lower temperature, up to 620°C) before obtaining the pure inverse trirutile phase (see Chapter 3/Figure 3-1 and Figure 3-2). It was unfortunately impossible to stabilize this new intermediate compound as a single phase using the same synthesis method as inverse trirutile. The challenge was therefore to obtain at low temperature (< 600°C) a monophasic compound, with proper crystallinity. To this end, a spray-dry method was used (see details in Chapter 2), as it is simple and reproducible, and provides homogeneous nanosize powders.

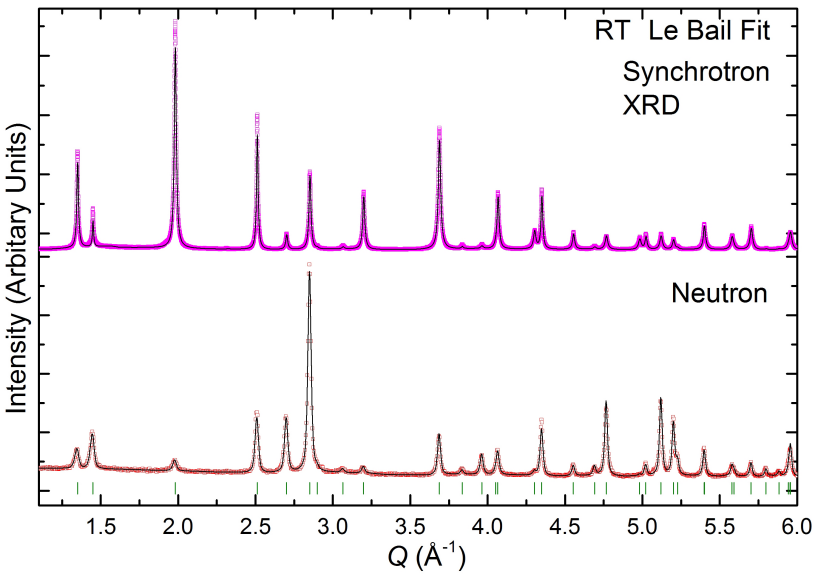


Figure 5-1 Le Bail fitting of the SXRPD (CRISTAL@Soleil) and NPD (D2B@ILL) data of HC-MTO phase recorded at RT. Both patterns are indexed in a trigonal structure (SG: P-31m with $a \cong 5.00$Å, $c \cong 4.65$Å and $\gamma = 120°$)

The precursor powders prepared from spray drying (starting from *x* $Mn(NO_3)_2$ + 1 H_6TeO_6) were calcined at 300°C for 6h in air. This powder was then further heated at 500°C for 24h in air. The obtained powder was pressed in the shape of bars then sintered at 600°C for 72h in O_2 flow. Optimizing the Mn/Te ratio, sintering

temperature, time, and atmosphere, we were able to obtain a single phase of Li_2ZrF_6-type Mn,Te,O system (called HC-MTO in the following, HC is for honeycomb) (Figure 5-1). After optimization of Mn/Te ratio, further heat treatment (700°C) could lead the transformation from HC-MTO to single inverse trirutile Mn_2TeO_6 phase (Figure 5-2). The Le Bail fits (Figure 5-1) of the SXRPD and NPD patterns at RT show good agreement with a single phase characterized by SG *P*-31*m* with a = 5.004 (1) Å and c =4.652 (1) Å, γ = 120°, which is one of the simplest structures in Li_2ZrF_6-type structure family. This structure is known for $PbSb_2O_6$ or Cr_2UO_6 (details are given in Section 2.1). There has been always some controversy surrounding the correct crystallographic description of compounds in the Li_2ZrF_6-type family, owing to the huge number of possible combination among SG, cell parameters, coordination numbers, cationic ordering (*28*), as presented in Section 1.2/Table 1-4.

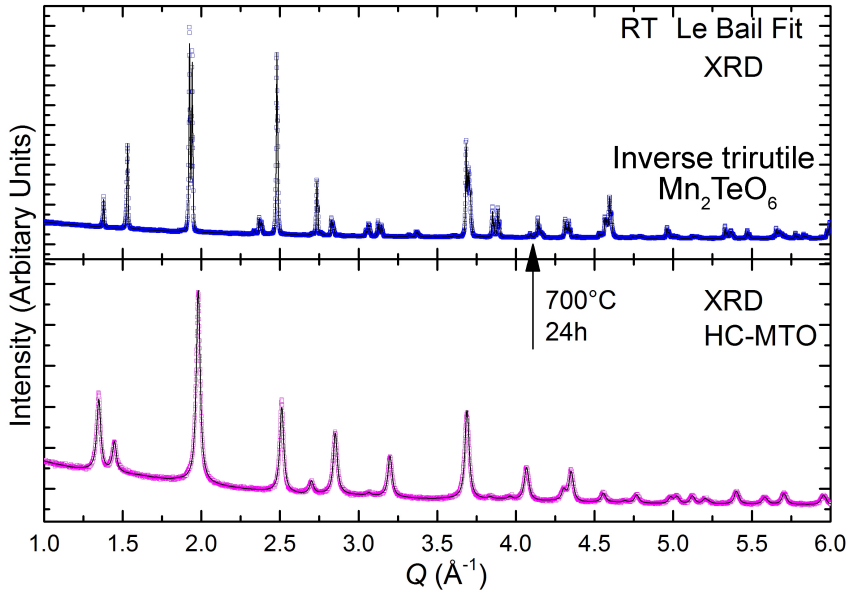


Figure 5-2 Le Bail fits of the XRPD patterns of the HC-MTO phase and the inverse trirutile Mn_2TeO_6 recorded at RT. The HC-MTO pattern is indexed in the trigonal structure (SG: P-31m with $a \cong 5.00$Å, $c \cong 4.65$Å and $\gamma = 120°$), while the inverse trirutile Mn_2TeO_6 pattern is indexed in the RTM structure (SG: $P2_1/c$ with $a \cong 9.10$Å, $b \cong 13.05$Å, $c \cong 6.47$Å and $\beta \cong 90.07°$)

In our case, full Rietveld refinements based on a Li_2ZrF_6-type structure was unsuccessful so far. The details of the true composition and crystal structure remain still unknown, as structural determination is rendered difficult by (i) broad Bragg peaks, and (ii) a nanocrystalline state preventing accurate electron diffraction analysis. Future

investigations of the crystal and magnetic structures and of the physical properties of HC-MTO are necessary but are beyond the scope of this thesis. These preliminary results nonetheless exemplify the potential of the spray dry technique for stabilizing new phases, and also as a different route to synthesize the inverse trirutile Mn_2TeO_6.

The MnTeO polymorphism that was evidenced in these results is an interesting -and promising for future research- aspect of the system, and led us to consider the structural transformations and relationships between the Na_2SiF_6-type, Li_2ZrF_6-type and inverse trirutile type structures. The idea is actually not new and was first studied by Galy et al (*157*), who suggested that a simple cation rearrangement was enough to interconvert those three structures. Figure 5-3 shows a polyhedral representation of these structures, to explain this transformation mechanism.

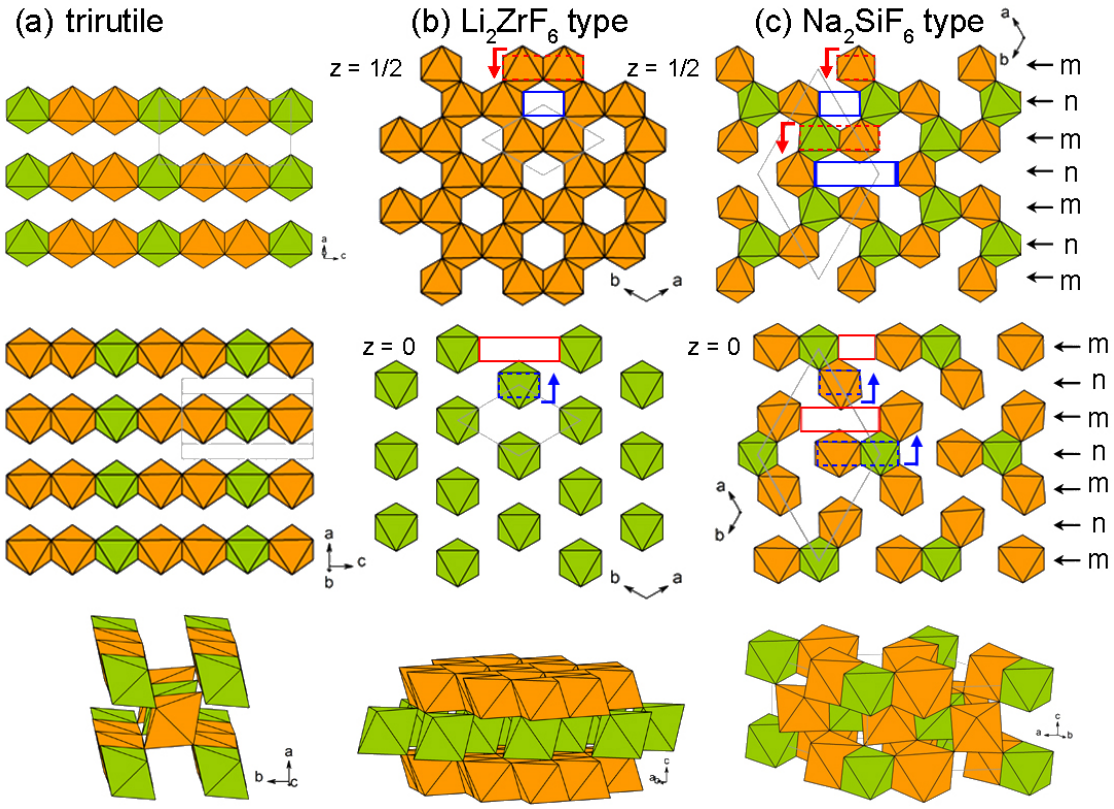


Figure 5-3 Drawing of the structures (lower panel) and showing each time only one octahedral layer (higher and middle panels) (a) inverse trirutile ($P4_2/mnm$), (b) honeycomb with P-31m and (c) honeycomb with P321 from (157). In (b) and (c), red and blue arrows show cation shifts layer to layer ($z = 0 \leftrightarrow z = 1/2$) to highlight the relationship between structures. Cations move from dot rectangles to solid rectangles.

The Li_2ZrF_6-type structure can transform into the trirutile one when half of the cations are shifted by 1/2 along the *c*-axis (Figure 5-3b, see rectangles and arrows). Figure 5-3c shows the Na_2SiF_6-type structure projected along the *c*-axis, to explain the transformation from the Na_2SiF_6-type structure to the trirutile structure. If the cations at $z = 1/2$ in the *m*-plane shift to $z = 0$, and those at $z = 0$ in the *n*-plane shift to $z = 1/2$, the trirutile structure is obtained. According to Galy, "this involves that half the cations pass through octahedral faces along half the *c*-axis, while the anion lattice remains intact". If the Mn and Te atoms keep their relative order during the transformation, the Na_2SiF_6 structure type may, in the reverse way, be derived directly from the trirutile type. These considerations could be the key to the understanding of the structure of HC-MTO, and how it is related to the Li_2ZrF_6-type structure, and eventually to the inverse trirutile Mn_2TeO_6 one. It could also help one picturing why it is not possible to stabilize HC-MTO by standard solid state chemistry, and how the spray dry technique facilitates the process.

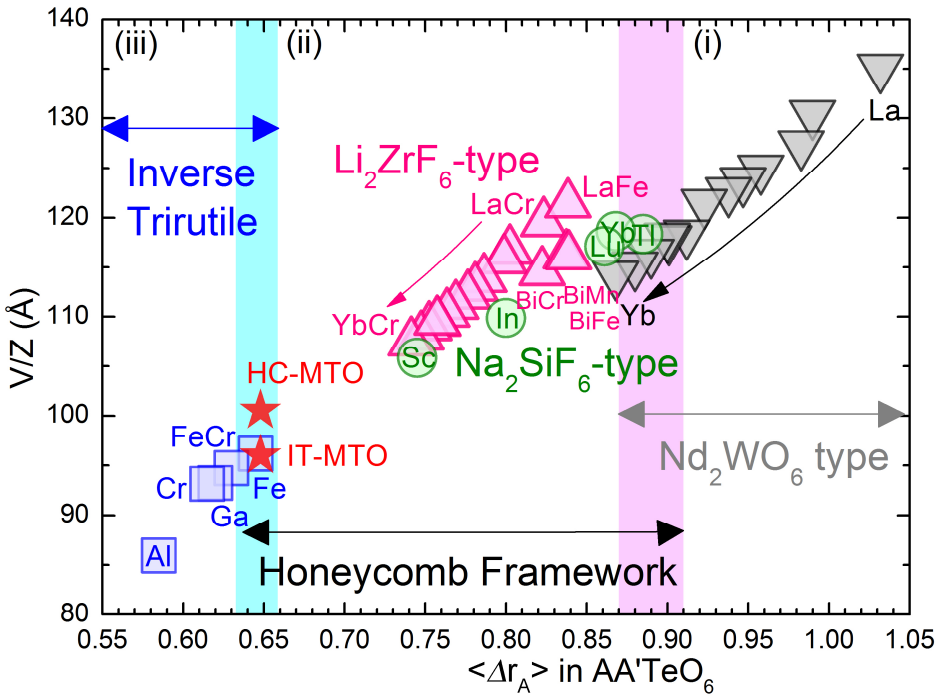


Figure 5-4 Relationships between the ionic radius of A^{3+} ($<r_A>$:average ionic radius of A and A' in VI coordination (27)) and the reduced cell volume V/Z in $AA'TeO_6$ compounds. Grey triangles, pink triangles, green circles, and blue squares are for Nd_2WO_6 (i), Li_2ZrF_6, Na_2SiF_6 (ii) and inverse trirutile–types (iii), respectively. Some corresponding A^{3+} cations are indicated. The areas at the borderline between two regimes are highlighted by a colored background.

As a final conclusion to this work, we would like to replace this study of Mn_2TeO_6 in the more general context of A_2TeO_6 compounds. As already mentioned in Chapter 1, Trömel et al. (*19*) and Frit et al. (*3*) have reported that tellurium oxides with the general formula A_2TeO_6 adopt different crystal structures, depending on the ionic radius of A^{3+}. The normalized *V*/*Z* volume versus the ionic radius of A (A') $^{3+}$ ions is shown in Figure 5-4. Three regions can be outlined: (i) large A cations (r_A > 0.87Å), which exhibit the Nd_2WO_6-type structure ($P2_12_12_1$ with $a \cong 5.5$ Å, $b \cong 9.4$ Å, $c \cong 10$ Å), (iii) small A cations (0.5 Å < r_A < 0.7 Å), with the inverse trirutile structure, and (ii) intermediate A ionic radii, for which a honeycomb like structure (Na_2SiF_6-type or Li_2ZrF_6-type) is observed (*3*, *19*). Exceptions are Yb (r_A = 0.868 Å), and Tl (r_A = 0.885Å), whose ionic radii are at the "i/ii" boundary between the Nd_2WO_6- and Na_2SiF_6-type structures. While Tl_2TeO_6 exists only in the Na_2SiF_6-type structure (*3*), Yb_2TeO_6 is reported with both Nd_2WO_6-type and Na_2SiF_6-type structure. Another obvious boundary is "ii/iii", between the honeycomb structures (Li_2ZrF_6 type + Na_2SiF_6 type) and the inverse trirutile structure, where indeed Mn_2TeO_6 is placed. Likewise to Yb_2TeO_6, the present graph therefore supports the idea of polymorphism in Mn_2TeO_6, between the inverse trirutile, Li_2ZrF_6-type and even possibly a Na_2SiF_6-type. It will be challenging to determine the synthesis conditions necessary to stabilize each of these phases, and fascinating to study their structural and physical properties, especially with regards to the JT effect that was evidenced in inverse trirutle Mn_2TeO_6, and how it will adapt to new structural frameworks. In addition, the discovery of a new honeycomb structure is an excellent starting point to design new multiferroic materials because it belongs to a large family that is not so far deeply investigated. These compounds exhibit features favorable to ME coupling, such as (i) spin frustration (due to the honeycomb framework) and/or (ii) non-centrosymmetric space groups for some of them (e.g., *P*312 for $PbMnTeO_6$ (*34*)).

Finally, Figure 5-5 is overall summary of the possible crystal structure relationship diagram among trirutile, inverse trirutile, Li_2ZrF_6 and Na_2SiF_6 families. This work contributes not only in the detail investigation of inverse trirutile Mn_2TeO_6 system (green half circle) but also opens new road map to expand A_2TeO_6 compounds to these honeycomb frameworks.

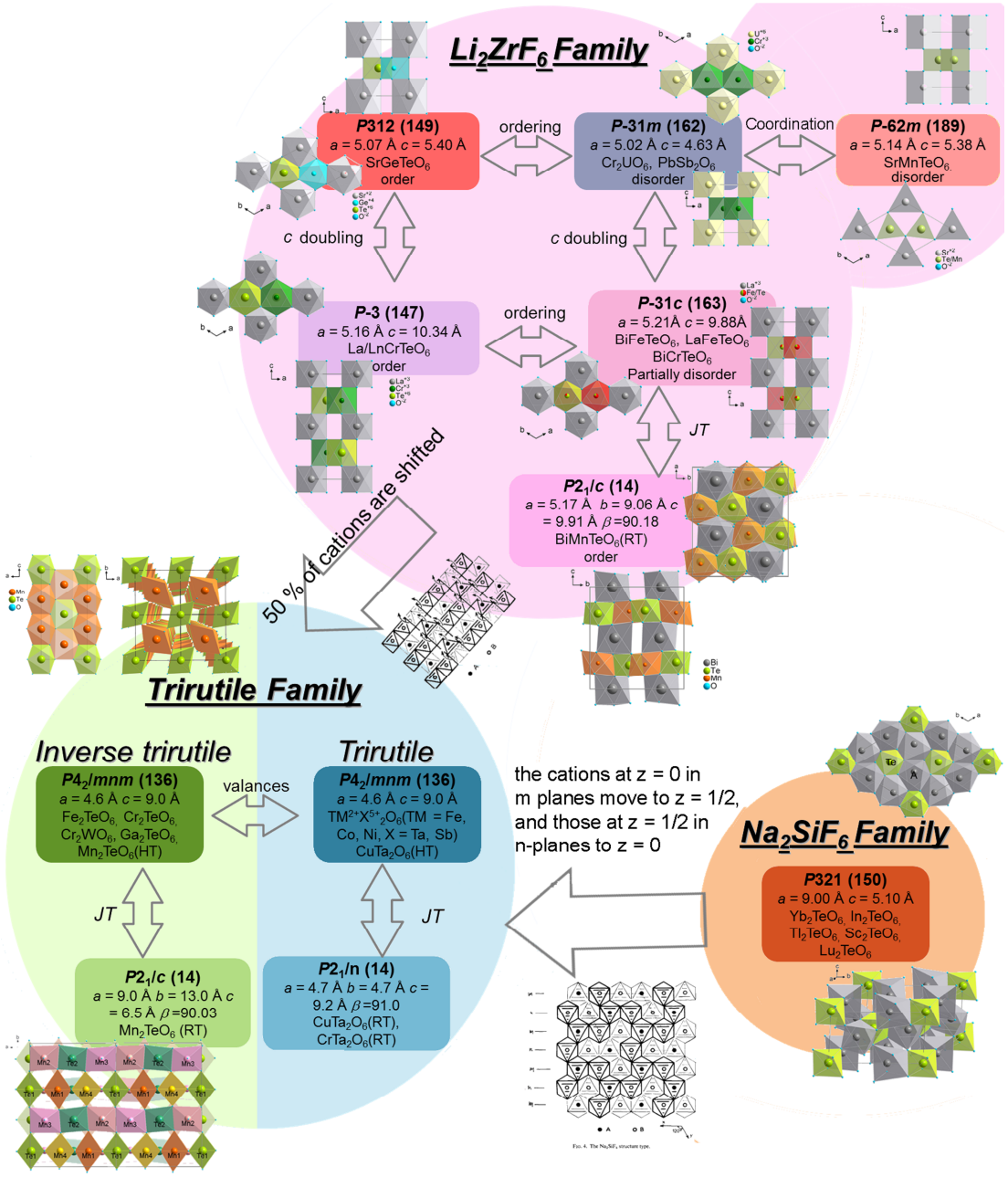


Figure 5-5 Relationship between structure of diagram of $AA'TeO_6$ compounds, among trirutile, Li_2ZrF_6 and Na_2SiF_6 families.

Bibliography

1. L. Vegard, *Philos. Mag. Ser. 6.* **32**, 65–96 (1916).
2. Goldschmidt. V. M., *Skr. Nor. Vid.-Akad, Matern.* **1**, 17–19 (1926).
3. B. Frit, R. Pressigout, D. Mercurio, *Mater. Res. Bull.* **10**, 1305–1312 (1975).
4. S. Hansen, A. Landa-Cánovas, K. Ståhl, J. Nilsson, *Acta Crystallogr. Sect. A.* **51**, 514–519 (1995).
5. G. Bayer, *J. Am. Ceram. Soc.* **43**, 495–496 (1960).
6. G. Bayer, *Ber. Deutsch. Keram. Ges.* **39**, 535 (1962).
7. D. Fruchart, M. C. Montmory, E. F. Bertaut, J. C. Bernier, *J. Phys.* **41**, 141–147 (1980).
8. M. Zhu *et al.*, *Phys. Rev. B.* **92**, 4–9 (2015).
9. Y. Y. Jiao *et al.*, *Phys. Rev. B.* **97**, 1–11 (2018).
10. N. Berand, K. J. Range, *J. Alloys Compd.* **205**, L3–L5 (1994).
11. W. Kunnmann, S. La Placa, L. M. Corliss, J. M. Hastings, E. Banks, *J. Phys. Chem. Solids.* **29**, 1359–1364 (1968).
12. N. S. Saleh, *J. Phys. C, Solid State Phys.* **17**, 3087–3090 (1984).
13. M. Yamaguchi, M. Ishikawa, *J. Phys. Soc. Japan.* **63**, 1666–1669 (1994).
14. M. C. Montmory, M. Belakhovsky, R. Chevalier, R. Newnham, *Solid State Commun.* **6**, 317–321 (1968).
15. M. Zhu *et al.*, *Phys. Rev. Lett.* **113**, 1–5 (2014).
16. M. C. Montmory, R. Newnham, *Solid State Commun.* **6**, 323–326 (1968).
17. M. C. Montmory, E. . F. Bertaut, P. Mollard, *Solid State Commun.* **4**, 249–253

(1966).

18. A. G. Christy, S. J. Mills, A. R. Kampf, *Mineral. Mag.* **80**, 415–545 (2016).
19. M. Trömel, F. W. Hützler, H. G. Burckhardt, C. Platte, E. Münch, *Z. Anorg. Allg. Chem.* **551**, 95–100 (1987).
20. E. Bâati, A. Kabadou, J. A. Alonso, *Arab. J. Chem.* **6** (2016).
21. S. F. Meier, T. Schleid, *Zeitschrift Fur Krist. NCS.* **219**, 359–360 (2004).
22. J. Llanos, R. Castillo, D. Barrionuevo, D. Espinoza, S. Conejeros, *J. Alloys Compd.* **485**, 565–568 (2009).
23. S. F. Meier, T. Schleid, *J. Solid State Chem.* **171**, 408–411 (2003).
24. P. Höss, T. Schleid, *Acta Crystallogr. Sect. E.* **E63**, i133–i135 (2007).
25. M. J. Redman, W. P. Binnie, M. W. J, *J. Less-Common Met.* **23**, 313–315 (1971).
26. P. Höss, S. Thomas, *Z. Anorg. Allg. Chem.* **633**, 1391–1396 (2007).
27. R. D. Shannon, *Acta Crystallogr. Sect. A.* **A32**, 751–767 (1976).
28. P. M. Woodward, A. W. Sleight, L.-S. Du, C. P. Grey, *J. Solid State Chem.* **147**, 99–116 (1999).
29. H. M. Kasper, *Mater. Res. Bull.* **4**, 33–38 (1969).
30. G. Narsinga Rao, R. Sankar, I. Panneer Muthuselvam, F. C. Chou, *J. Magn. Magn. Mater.* **370**, 13–17 (2014).
31. S. W. Kim *et al.*, *Inorg. Chem.* **55**, 10229–10237 (2016).
32. R. Phatak *et al.*, *Mater. Res. Bull.* **45**, 1978–1983 (2010).
33. B. G. Vats, R. Phatak, K. Krishnan, S. Kannan, *Mater. Res. Bull.* **48**, 3117–3121 (2013).
34. S. W. Kim *et al.*, *Inorg. Chem.* **55**, 1333–13S38 (2016).
35. L. Wulff, H. Mueller-Buschbaum, *Naturforsch., B Chem. Sci.* **53**, 283–286 (1998).
36. N. A.Spaldin, M. Fiebig, *Science (80-.).* **309**, 391–392 (2005).
37. W. Eerenstein, N. D. Mathur, J. F. Scott, *Nature.* **442**, 759–765 (2006).
38. M. Fiebig, T. Lottermoser, D. Meier, M. Trassin, *Nat. Rev. Mater.* **1**, 1–14 (2016).
39. G. Catalan, *Appl. Phys. Lett.* **88**, 102902-1–3 (2006).

40. D. Khomskii, *Am. Phys. Soc.* **2** (2009).
41. T. Kimura *et al.*, *Nature*. **426**, 55–58 (2003).
42. B. Kundys, C. Simon, C. Martin, *Physical*. **17**, 172402 (2008).
43. N. J. Perks, R. D. Johnson, C. Martin, L. C. Chapon, P. G. Radaelli, *Nat. Commun.* **3**, 1277 (2012).
44. M. Poienar, F. Damay, C. Martin, J. Robert, S. Petit, *Phys. Rev. B - Condens. Matter Mater. Phys.* **81**, 1–8 (2010).
45. S. D. Kaushik *et al.*, *J. Appl. Phys.* **108**, 84106 (2010).
46. N. A. Hill, *J. Phys. Chem. B.* **104**, 6694–6709 (2000).
47. R. E. Newnham, *Properties of materials* (2005).
48. R. M. Hornreich, *Solid State Commun.* **7**, 1081–1085 (1969).
49. M. I. Kurkin, N. B. Orlova, *Phys. Met. Metallogr.* **115**, 1093–1111 (2014).
50. S. Buksphan, E. Fischer, R. M. Hornreich, *Solid State Commun.* **10**, 657–662 (1972).
51. J. Wang *et al.*, *J. Phys. Condens. Matter.* **26**, 055012 (2014).
52. Y. Fang *et al.*, *Appl. Phys. Lett.* **104**, 1–5 (2014).
53. F. Hund, *Naturwissenschaften*. **58**, 323 (1971).
54. A. Huizing, H. A. M. van Hal, W. Kwestroo, C. Langereis, P. C. van Loosdregt, *Mater. Res. Bull.* **12**, 605–611 (1977).
55. K Masters, *Spray Drying Handbook* (Longman Scientific and Technical, New York, 1991).
56. B. Rivas-Murias *et al.*, *J. Phys. Chem. Solids.* **72**, 158–163 (2011).
57. D. Segal, *J. Mater. Chem.* **7**, 1297–1305 (1997).
58. B. Vertruyen, A. Rulmont, R. Cloots, *J. Mater. Sci.* **40**, 117–122 (2005).
59. D. Depla, R. Mouton, S. Hoste, *J. Eur. Ceram. Soc.* **17**, 153–159 (1997).
60. T. Motohashi, Y. Nonaka, K. Sakai, M. Karppinen, H. Yamauchi, *J. Appl. Phys.* **103**, 033705 (2008).
61. F. Bezzi *et al.*, *J. Eur. Ceram. Soc.* **25**, 3323–3334 (2005).
62. A. Ito, D. Li, Y. Lee, K. Kobayakawa, Y. Sato, *J. Power Sources*. **185**, 1429–1433 (2008).
63. P. Atkins, T. Overton, J. Rourke, M. Weller, F. Armstrong, *Inorganic chemistry*

(Oxford University Press, Oxford, 2006).

64. C. Kittel, *Introduction to Solid State Physics* (Wiley, 2005).
65. B. D. Cullity, *Elements of X-ray diffraction* (Addison-Wesley Publishing company inc, 1978).
66. B. T. M. Willis, *Zeitschrift für Krist.* **209**, 385–389 (1994).
67. CRISTAL beamline (SOLEIL), (available at https://www.synchrotron-soleil.fr/en/beamlines/cristal).
68. F. Fauth, I. Peral, C. Popescu, M. Knapp, *Powder Diffr.* **28**, S360–S370 (2013).
69. P. J. E. M. Van Der Linden *et al.*, *Rev. Sci. Instrum.* **87** (2016).
70. G. E. Bacon, *Neutron diffraction* (Clarendon Press, 1975).
71. W. Massa, R. O. Gould, *Crystal Structure Determination* (Springer Berlin Heidelberg, 2010).
72. Powder diffraction, LLB, (available at http://www-llb.cea.fr/en/Phocea/Vie_des_labos/Ast/ast_sstechnique.php?id_ast=1612).
73. L. C. Chapon *et al.*, *Neutron News.* **22**, 22–25 (2011).
74. W. G. Williams, R. M. Ibberson, P. Day, J. E. Enderby, *Phys. B.* **241–243**, 234–236 (1998).
75. High-resolution two-axis diffractometer, D2B, ILL, (available at https://www.ill.eu/users/instruments/instruments-list/d2b/description/instrument-layout/).
76. L. D. Landau, E. M. Lifshitz, *Statistical Physics* (Pergamon press, 1969).
77. M. E. Lines, A. M. Glass, *Principles and Applications of Ferroelectrics and Related Materials* (Oxford University Press, 1977).
78. R. E. Cohen, *Nature.* **358**, 136–138 (1992).
79. J. L. Mañes, M. J. Tello, J. M. Pérez-Mato, *Phys. Rev. B.* **26**, 250–268 (1982).
80. J. M. Pérez-Mato, F. Gaztelua, G. Madariaga, M. J. Tello, *J. Phys. C.* **19**, 1923–1935 (1986).
81. H. T. Stokes, D. M. Hatch, *Isotropy subgroups of the 230 crystallographic space groups* (World Scientific Publishing Co. Pte. Ltd, 1988).
82. 中村 輝太郎, 強誘電体と構造相転移 (裳華房, 1988).
83. N. V Belov, *Kristallografiya.* **2**, 315–325 (1957).

84. R. L. E. Schwarzenberger, *Bull. London Math. Soc.* **16**, 216–229 (1984).
85. A. L. Mackay, *Acta Cryst.* **10**, 543–548 (1957).
86. J. Rossat-mignod, *J. Phys.* **5**, C5-95 (1979).
87. F. Damay, *J. Phys. D. Appl. Phys.* **48**, 504005 (2015).
88. J. Rodriguez-Carvajal, *Solid State Phenom.* **170**, 263 (2011).
89. M. I. Aroyo *et al.*, *Zeitschrift Fur Krist.* **221**, 15–27 (2006).
90. B. J. Campbell, H. T. Stokes, D. E. Tanner, D. M. Hatch, *J. Appl. Crystallogr.* **39**, 607–614 (2006).
91. R. Young, *The Rietveld Method* (Oxford University Press, 1993).
92. J. Rodríguez-Carvajal, *Phys. B.* **192**, 55–69 (1993).
93. J. Rodríguez-Carvajal, *FullProf 2000* (2001).
94. D. Orobengoa, C. Capillas, M. I. Aroyo, J. M. Perez-Mato, *J. Appl. Crystallogr.* **42**, 820–833 (2009).
95. B. K. Teo, *EXAFS : Basic Principles and Data Analysis* (Bell Telephone Laboratories, 1986).
96. J C Fuggle, J. E. Inglesfield, *Unoccupied Electronic States Fundamentals for XANES, EELS, IPS and BIS* (Springer-Verlag Berlin Heidelberg, 1992).
97. F. Baudelet *et al.*, *High Press. Res.* **31**, 136–139 (2011).
98. B. Ravel, M. Newville, *J. Synchrotron Radiat.* **12**, 537–541 (2005).
99. L. Palatinus, *Inst. Phys. AS CRPrague, Czechia* (2011).
100. V. Petricek, M. Dusek, L. Palatinus, Crystallographic computing system jana2006. *Inst. Physics, Acad. Sci. Czech Repub.* **229** (2006), pp. 345–352.
101. P. J. Goodhew, J. F. Humphreys, R. Beanland, *Electron Microscopy and Analysis* (Taylor & Francis, 2001).
102. S. J. Pennycook, L. A. Boatner, *Nature.* **336**, 565–567 (1988).
103. C. L. Jia, K. Urban, *Science (80-.).* **303**, 2001–2004 (2004).
104. R. Vincent, P. A. Midgley, *Ultramicroscopy.* **53**, 271–282 (1994).
105. E. O. Wollan, W. C. Koehler, *Phys. Rev.* **100**, 545–563 (1955).
106. I. S. Zheludev, *Physics of Crystalline Dielectrics* (Springer Science+Business Media, 1971).
107. F. Kremer, A. Schonhals, *Broadband Dielectric Spectroscopy* (2003).

108. V. Hardy, Y. Bréard, C. Martin, *J. Phys. Condens. Matter.* **21**, 075403 (2009).
109. B. Donkova, D. Mehandjiev, *Thermochim. Acta.* **421**, 141–149 (2004).
110. M. a. K. Ahmed, H. Fjellvåg, A. Kjekshus, *J. Chem. Soc. Dalt. Trans.*, 4542–4549 (2000).
111. H. R. Oswald, M. J. Wampetich, *Helv. Chim. Acta.* **50**, 2023–2034 (1967).
112. W. Hase, *Phys. Status Solidi.* **3**, K446–K449 (1963).
113. O. LINDQVIST, *Acta Chem. Scand.* **22**, 977–982 (1968).
114. M. C. Montmory, R. Newnham, *Solid State Commun.* **6**, 323 (1968).
115. B. Klobes, N. Barrier, B. Vertruyen, C. Martin, R. P. Hermann, *Hyperfine Interact.* **226**, 713–719 (2014).
116. W. Kunnmann, S. La Placa, L. M. Corliss, J. M. Hastings, E. Banks, *J. Phys. Chem. Solids.* **29**, 1359–1364 (1968).
117. T. Chatterji, B. Ouladdiaf, P. Mandal, B. Ghosh, *Solid State Commun.* **131**, 75–80 (2004).
118. J. Rodriguez-Carvajal *et al.*, *Phys. Rev. B.* **57**, R3189--R3192 (1998).
119. Z. Jirák *et al.*, *Phys. Rev. B.* **61**, 1181 (2000).
120. J. Goodenough, *Annu. Rev. Mater. Sci.* **28**, 1–27 (1998).
121. M. Imada, A. Fujimori, Y. Tokura, *Rev. Mod. Phys.* **70**, 1039–1263 (1998).
122. S. Series, *Solid-State Sciences* (Springer-Verlag Berlin Heidelberg, 2003).
123. W. H. Baur, *Acta Crystallogr. Sect. B Struct. Crystallogr. Cryst. Chem.* **32** (1976).
124. B. Bochu *et al.*, *Solid State Commun.* **36**, 133–138 (1980).
125. M. Saes, N. P. Raju, J. E. Greedan, *J. Solid State Chem.* **140**, 7–13 (1998).
126. V. Guillen-Viallet, J. F. Marucco, M. Ghysel, *J. Alloys Compd.* **317–318**, 127–131 (2001).
127. A. Golubev *et al.*, *Inorg. Chem.* **56**, 6318–6329 (2017).
128. A. Nakua, H. Yun, J. N. Reimers, J. E. Greedan, C. V. Stager, *J. Solid State Chem.* **91**, 105–112 (1991).
129. D. Kasinathan, K. Koepernik, H. Rosner, *Phys. Rev. Lett.* **100**, 237202 (2008).
130. A. Golubev *et al.*, *Inorg. Chem.* **56**, 6318–6329 (2017).
131. J. B. Goodenough, *J. Solid State Chem.* **3**, 490–500 (1971).

132. D. B. Rogers, R. D. Shannon, A. W. Sleight, J. L. Gillson, *Inorg. Chem.* **8**, 841–849 (1969).
133. D. B. McWhan, M. Marezio, J. P. Remeika, P. D. Dernier, *Phys. Rev. B.* **10**, 490–495 (1974).
134. V. Eyert, *Ann. der Phys.* **11**, 650–702 (2002).
135. C. Vecchini *et al.*, *Phys. Rev. B - Condens. Matter Mater. Phys.* **82**, 1–5 (2010).
136. C. R. Dela Cruz *et al.*, *Phys. Rev. B - Condens. Matter Mater. Phys.* **74**, 1–4 (2006).
137. J. S. O. Evans, *J. Chem. Soc. Dalt. Trans.*, 3317–3326 (1999).
138. K. Takenaka, *Sci. Technol. Adv. Mater.* **13**, 013001 (2012).
139. R. Przeniosło, I. Sosnowska, E. Suard, A. Hewat, A. N. Fitch, *Phys. B Condens. Matter.* **344**, 358–367 (2004).
140. V. H. Langhof, H Weitzel, E. Wölfel, W. Scharf, *Acta Crystallogr. Sect. A.* **36**, 741–746 (1980).
141. A. Y. Nikulin *et al.*, *Dalt. Trans.* **46**, 6059–6068 (2017).
142. E. Tokizaki, Y. Sugitani, K. Nagashima, *Mater. Res. Bull.* **21**, 231–236 (1986).
143. a. Aruga, E. Tokizaki, I. Nakai, Y. Sugitani, *Acta Crystallogr. Sect. C Cryst. Struct. Commun.* **41**, 663–665 (1985).
144. E. J. Kinast *et al.*, *J. Solid State Chem.* **163**, 218–223 (2002).
145. N. Matsubara *et al.*, *Inorg. Chem.* **56**, 9742–9753 (2017).
146. S. D. Kaushik, B. Sahu, S. R. Mohapatra, A. K. Singh, *AIP Conf. Proc.* **1731**, 130037 (2016).
147. M. Drillon, L. Padel, J. C. Bernier, *Physica.* **97B+C**, 380–382 (1979).
148. M. Drillon, L. Padel, J. C. Bernier, *J. Chem. Soc. Trans. Ii.* **76**, 1224–1233 (1980).
149. D. Kumar, A. Banerjee, *J. Phys. Condens. Matter.* **25**, 0–9 (2013).
150. I. G. Deac, J. F. Mitchell, P. Schiffer, *Phys. Rev. B - Condens. Matter Mater. Phys.* **63**, 1724081–1724085 (2001).
151. M. Regulski, R. Przeniosło, I. Sosnowska, D. Hohlwein, R. Schneider, *J. Alloys Compd.* **362**, 236–240 (2004).
152. F. Damay *et al.*, *Phys. Rev. B - Condens. Matter Mater. Phys.* **80**, 2–8 (2009).

153. D. D. Khalyavin, P. Manuel, W. Yi, A. A. Belik, *Phys. Rev. B.* **94**, 134412 (2016).
154. M. Matsukawa *et al.*, *Phys. Rev. B - Condens. Matter Mater. Phys.* **72**, 1–8 (2005).
155. J. Dho, W. S. Kim, N. H. Hur, *Phys. Rev. Lett.* **89**, 1–4 (2002).
156. M. Songvilay *et al.*, *Phys. Rev. B - Condens. Matter Mater. Phys.* **91**, 1–9 (2015).
157. J. Galy, S. Andersson, *J. Solid State Chem.* **3**, 525–528 (1971).

Abstract -Trirutiles and multiferroic properties: exploring tellurates-

Magnetoelectric (ME) multiferroic materials, which present simultaneously two coupled properties between ferromagnetism and ferroelectricity, have attracted much attention recently, not only owing to their application perspectives, e.g., next-generation magnetic RAM, but also for the rich physics associated with the understanding of this coupling. Inverse trirutiles are of particular interest here since ME properties have been reported in this family of compounds. This manuscript presents the study of inverse trirutile Mn_2TeO_6 and its Cr-substitution series $Mn_{2-x}Cr_xTeO_6$. Mn_2TeO_6 and Cr-substituted series were prepared by solid state reaction at relatively low-temperature (< 700°C). Thanks to an extensive use of different techniques performed in a large temperature range (1.5K to 700°C), encompassing synchrotron, neutron and electron diffraction experiments combined with physical properties measurements, the very complex behaviour of Mn_2TeO_6 was revealed. A structural transition at 400°C from tetragonal ($P4_2/mnm$) to monoclinic ($P2_1/c$) is observed first, and related to a cooperative Jahn-Teller effect. Further cooling the sample, a hysteretic structural transition is observed spanning more than 50K, which leads to the coexistence of two monoclinic phases. A series of magnetic transitions are also observed between 48K and 22K, with magnetization, heat capacity measurement and neutron diffraction. Cr-substituted ($x \geq 0.15$) samples crystallize in the tetragonal phase, implying the suppression of the cooperative Jahn-Teller effect, and involving a simpler, though short–range, magnetic order.

Résumé -Trirutiles et propriétés multiferroïques: exploration de tellurates-

Les matériaux multiferroïques magnétoélectriques (ME) présentant simultanément des propriétés couplées de ferromagnétisme et de ferroélectricité suscitent beaucoup d'attention, non seulement pour leurs applications (comme la RAM magnétique de nouvelle génération), mais aussi pour la compréhension de la physique relative à ce couplage. Le but de cette thèse était de découvrir et de caractériser de nouveaux composés potentiellement multiferroïques, d'où le choix des trirutiles inverses. Ce manuscrit présente l'étude détaillée du trirutile inverse Mn_2TeO_6 et quelques résultats sur la série substituée au chrome $Mn_{2-x}Cr_xTeO_6$. Les composés Mn_2TeO_6 et substitués sont préparés par réaction à l'état solide à relativement basse température (<700°C). De nombreuses expériences de diffraction de neutrons et de rayons-X ont été réalisées pour étudier les structures cristallines et magnétiques en fonction de la température (de 700°C à 1.5K), ces données ont été analysées en lien avec les caractérisations des propriétés magnétiques et électriques. Mn_2TeO_6 s'est révélé un matériau complexe et riche en transitions en fonction de la température. En température décroissante, Mn_2TeO_6 présente d'abord une transition d'une structure tétragonale ($P4_2/mnm$) à une double maille monoclinique ($P2_1/c$) vers 400°C due à l'effet Jahn-Teller. Une seconde transition très hystérétique apparait à plus basse température, avec la coexistence de deux phases monocliniques entre 45 et 100K. Des transitions magnétiques sont également observées par des mesures de susceptibilité magnétique et de diffraction neutronique. La structure cristalline à température ambiante met en évidence un ordre orbitalaire, dû au manganèse trivalent, complexe et inédit avec une alternance d'octaèdres MnO_6 allongés et aplatis décrivant des chevrons. L'impact de l'effet Jahn-Teller induit par le manganèse trivalent est confirmé dans les composés substitués au Cr (avec $x \geq 0,15$) qui conservent la structure quadratique sur toute la gamme de température.

Mots-clés: Structure cristalline, Magnétisme, Trirutile, ME-multiferroïque, Transition de phase, Diffraction

Discipline: CHIMIE DES MATERIAUX

Laboratoire d'accueil: Laboratoire CRISMAT, UMR6508, ENSICAEN, 6 Boulevard du Maréchal Juin, 14050 CAEN et Laboratoire Léon Brillouin, UMR12, CEA-CNRS, Bât. 563 CEA Saclay, 91191 Gif sur Yvette